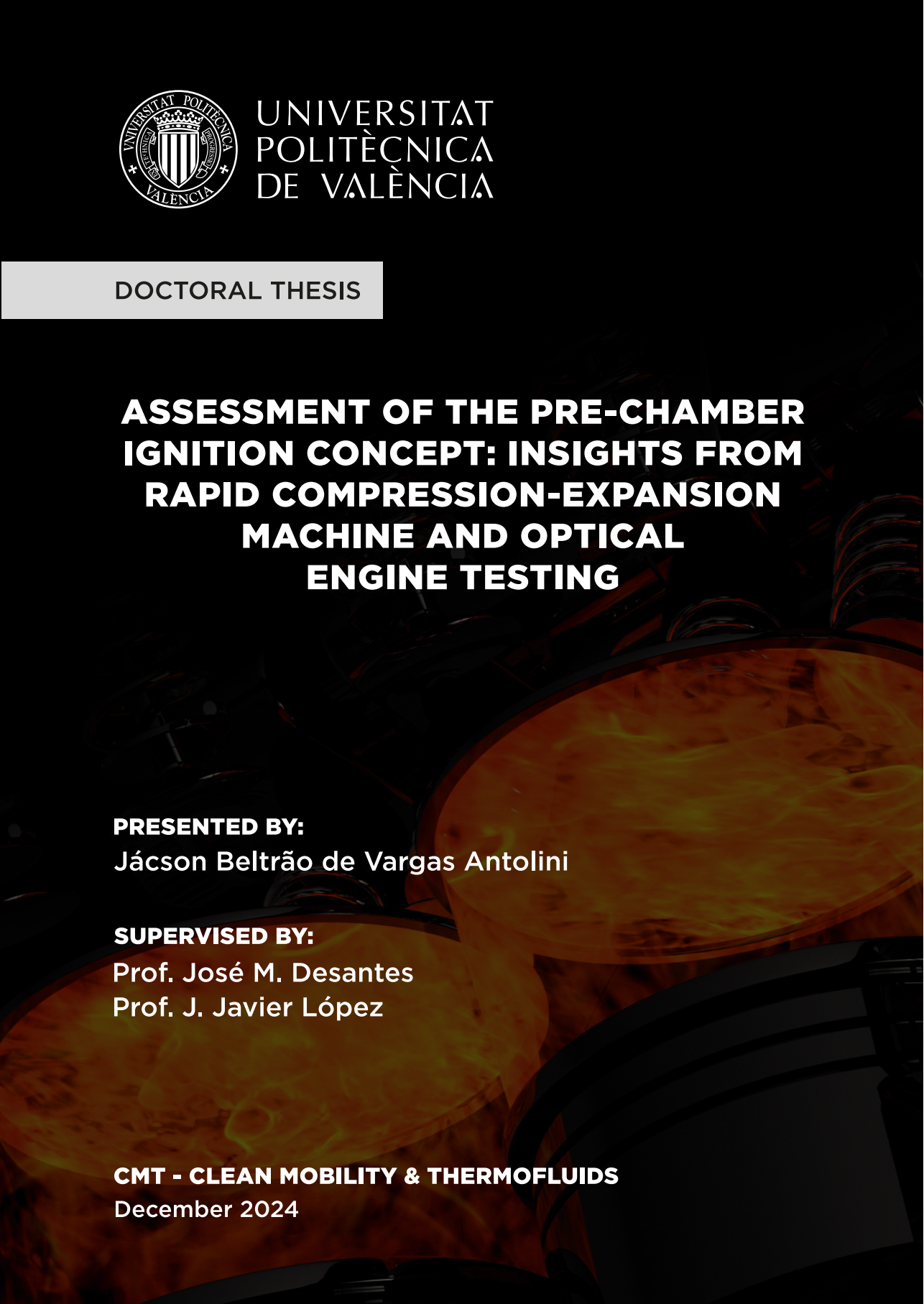

UNIVERSITAT POLITÈCNICA DE VALÈNCIA

DOCTORAL THESIS

ASSESSMENT OF THE PRE-CHAMBER IGNITION CONCEPT: INSIGHTS FROM RAPID COMPRESSION-EXPANSION MACHINE AND OPTICAL ENGINE TESTING

PRESENTED BY:
Jácson Beltrão de Vargas Antolini

SUPERVISED BY:
Prof. José M. Desantes
Prof. J. Javier López

CMT - CLEAN MOBILITY & THERMOFLUIDS

December 2024

UNIVERSITAT POLITÈCNICA DE VALÈNCIA
I.U.I. CMT - CLEAN MOBILITY & THERMOFLUIDS
PHD PROGRAM IN PROPULSION SYSTEMS FOR TRANSPORT

UNIVERSITAT
POLITÈCNICA
DE VALÈNCIA

Doctoral Thesis

ASSESSMENT OF THE PRE-CHAMBER IGNITION CONCEPT: INSIGHTS FROM RAPID COMPRESSION-EXPANSION MACHINE AND OPTICAL ENGINE TESTING

Presented by:
Jácson Beltrão de Vargas Antolini

Supervised by:
Prof. José M. Desantes
Prof. J. Javier López

in fulfillment of the requirements for the degree of
Doctor of Philosophy

Valencia, December 2024

Ph.D. Thesis

ASSESSMENT OF THE PRE-CHAMBER IGNITION CONCEPT: INSIGHTS FROM RAPID COMPRESSION-EXPANSION MACHINE AND OPTICAL ENGINE TESTING

Presented by: Jácson Beltrão de Vargas Antolini
Directed by: Prof. José M. Desantes
Prof. J. Javier López

Examination committee:

President: Prof. José M. García-Oliver
Secretary: Dr. Walter Vera-Tudela
Examiner: Dr. Christine Rousselle

Reviewing board:

Dr. Christine Rousselle
Dr. Walter Vera-Tudela

Valencia, December 2024

Abstract

The pursuit of carbon neutrality to mitigate the effects of climate change has been demanding research into alternative energy sources, as well as more efficient ways of using the current and future energy matrix in all sectors of the economy. In the transportation sector, which accounts for about 10% of the total greenhouse gas emissions, electrification and the use of carbon-free fuels are promising alternatives in the long term. In the meanwhile, however, highly efficient internal combustion engines still play an important role in the decarbonization of the transportation sector. In this context, the pre-chamber ignition system is an attractive method to increase the thermal efficiency of small engines for passenger cars and large-bore engines for power generation due to its high-energy ignition source, enabling lean operation and mitigating knock at low-speed and high-load operation. Within this framework, this present thesis aims to further understand the pre-chamber ignition concept, focusing on the jet ejection analysis by means of optical techniques and in-cylinder pressure data.

In order to fulfill this objective, the study of single-orifice pre-chambers on simplified experimental facilities was proposed as the first step for understanding such ignition method. Arising from the necessity to correctly determine the pre-chamber volume and orifice diameter of this simplified configuration, a theoretical and numerical study was carried out to identify the main geometrical parameters to reproduce as much as possible the jet characteristics of an existing PC geometry into a simplified pre-chamber geometry. In this sense, an one-dimensional engine model was used to provide the input data for the one-dimensional spray model used to predict the jet penetration for different PC geometries and operating conditions. Once the key geometrical parameters that drive the jet ejection were addressed, a Rapid Compression-Expansion Machine (RCEM) was redesigned for pre-chamber optical studies, and the effect of the pre-chamber geometry, equivalence ratio, and EGR rate on the jet ejection and MC ignition was assessed by means of in-cylinder pressure on both chambers and simultaneous Schlieren and OH* chemiluminescence optical techniques.

Finally, as a complement to the analysis of single-orifice pre-chambers on the RCEM, the effect of the diameter of the orifices and the engine operating parameters was assessed in a small optical engine. High-speed broadband chemiluminescence imaging and in-cylinder pressure data were used to evaluate the jet characteristics and the main chamber combustion development for three pre-chamber geometries under different mixture conditions.

Resumen

La búsqueda por la neutralidad de carbono para mitigar los efectos del cambio climático ha impulsado la investigación de fuentes de energía alternativas, así como de formas más eficientes de utilizar la matriz energética actual y futura en todos los sectores de la economía. En el sector del transporte, que representa alrededor del 10% de las emisiones totales de gases de efecto invernadero, la electrificación y el uso de combustibles libres de carbono son alternativas a largo plazo. Sin embargo, los motores de combustión interna de alta eficiencia aún siguen jugando un papel importante en la descarbonización del sector. En este contexto, el sistema de encendido por precámara es un método promisor para aumentar la eficiencia térmica de los motores para coches de pasajeros y los motores para la generación de energía debido a su fuente de ignición de alta energía, lo que permite una operación pobre y mitiga el *knock* en alta carga y baja velocidad. En este marco, esta tesis tiene como objetivo profundizar el conocimiento del método de encendido por precámara, centrándose en el análisis de la eyección del chorro por medio de técnicas ópticas y datos de presión de cilindro.

Para cumplir con este objetivo, se ha propuesto estudiar precámaras de un solo orificio en instalaciones experimentales simplificadas como el primer paso para mejor comprender dicho método de ignición. Partiendo de la necesidad de determinar correctamente el volumen y el diámetro del orificio de esta precámara simplificada, se ha llevado a cabo un estudio teórico y numérico para identificar los principales parámetros geométricos para reproducir lo más fielmente posible las características del chorro de una geometría de PC ya existente en una geometría simplificada. En este sentido, se ha utilizado un modelo numérico termodinámico para suministrar los datos de entrada para el modelo unidimensional de spray utilizado para predecir la penetración del chorro para diferentes geometrías de PC y condiciones de operación. Una vez conocidos los parámetros geométricos clave que gobiernan la eyección del chorro, se ha rediseñada una máquina de compresión-expansión rápida (RCEM) para estudios ópticos de precámaras y se ha evaluado el efecto de la geometría de la precámara, del dosado, y de la tasa de EGR en la eyección del chorro y la ignición de la cámara principal por medio de la presión en ambas cámaras y imágenes simultáneas de schlieren y quimioluminiscencia OH*.

Por fin, como complemento al análisis de precámaras de un solo orificio en la RCEM, se ha evaluado el efecto del diámetro del orificio y los parámetros de operación del motor en un motor óptico. Se han utilizado imágenes de alta velocidad de quimioluminiscencia de banda ancha y datos de presión en el cilindro para evaluar las características del chorro y el desarrollo de

la combustión en la cámara principal en tres geometrías de precámara bajo diferentes dosados.

Resum

La busca de la neutralitat de carboni per a mitigar els efectes del canvi climàtic ha impulsat la investigació de fonts d'energia alternatives, així com de formes més eficients d'utilitzar la matriu energètica actual i futura en tots els sectors de l'economia. En el sector del transport, que representa al voltant del 10% de les emissions totals de gasos d'efecte d'hivernacle, l'electrificació i l'ús de combustibles lliures de carboni són alternatives a llarg termini. No obstant això, mentrestant els motors de combustió interna d'alta eficiència continuen jugant un paper important en la descarbonització del sector del transport. En este context, el sistema d'encesa per precàmera és un mètode promissor per a augmentar l'eficiència tèrmica dels motors per a cotxes de passatgers i els motors per a la generació d'energia a causa de la seua font d'ignició d'alta energia, la qual cosa permet una operació pobra i mitiga el *knock* en operació a baixa velocitat i alta càrrega. En este marc, esta tesi té com a objectiu aprofundir el coneixement del procés d'encesa per precàmera, centrant-se en l'anàlisi de l'ejecció del doll per mitjà de tècniques òptiques i dades de pressió de cilindre.

Per a complir amb este objectiu, s'ha proposat estudiar precàmeres d'un sol orifici en installacions experimentals simplificades com el primer pas per a comprendre este mètode d'ignició. Partint de la necessitat de determinar correctament el volum de la precàmera i el diàmetre de l'orifici d'esta configuració simplificada, es va dur a terme un estudi teòric i numèric per a identificar els principals paràmetres geomètrics per a reproduir tan bé com siga possible les característiques del doll d'una precàmera amb múltiples orificis en una geometria de precàmera simplificada. Una vegada coneguts els paràmetres geomètrics clau que impulsen l'ejecció del doll, s'ha redissenyada una màquina de compressió-expansió ràpida (RCEM) per a estudis òptics de precàmeres i s'ha avaluat l'efecte de la geometria de la precàmera, del dosatge, i de la taxa de EGR en l'ejecció del doll i la ignició de la cambra principal per mitjà de la pressió en totes dues cambres i imatges simultànies de schlieren i quimioluminescència OH*.

Per fi, com a complement a l'anàlisi de precàmeres d'un sol orifici en la RCEM, s'ha avaluat l'efecte del diàmetre de l'orifici i els paràmetres d'operació del motor en un motor òptic. S'han utilitzat imatges d'alta velocitat de quimioluminescència de banda ampla i dades de pressió en el cilindre per a avaluar les característiques del doll i el desenrotllament de la combustió en la càmera principal en tres geometries de precàmera sota diferents dosatges.

À Thaís
Aos meus pais

Acknowledgements

At the end of this journey, it would be self-serving of me to believe that this work was an outcome exclusively of my own effort. Therefore, I would like to express my gratitude to the many people who supported me during this endeavor.

First of all, I sincerely thank my advisors, Javier López and José M. Desantes, for the opportunity to join this extraordinary research group and for giving me all the support necessary to conduct my PhD. thesis. Your guidance and the very fruitful discussions were undoubtedly essential for the development of this work. Thank you also for the daily motivation and assistance with many other matters.

I would also like to thank all the CMT members who contributed and helped me during these years, especially Ricardo Novella for sharing the learnings about pre-chambers, José M. García for the assistance with the jet penetration simulation, José Vicente Pastor for the tips during the design of the optical accesses, and José Enrique and Omar for the support during the experimental tests. In addition, thanks to all the professors, researchers, doctoral students, technicians, and the secretary board that somehow contributed to this work. Furthermore, thanks to the doctoral, master and undergraduate students who chose to do their final project or an internship within the framework of my thesis: Alessandro, Daniel, Hernando, and Isaac.

I would like to thank Paolo and Cinzia for the welcome during my stay at the Institute of Sciences and Technologies for Sustainable Energy and Mobility (STEMS). It was 3 months of a lot of learning that greatly contributed to my trajectory as a researcher. I also want to extend my thanks to the other researchers, technicians, and doctoral students who shared their knowledge and experiences during my research visit.

This task would have been much more difficult if I hadn't had someone so special by my side, my love Thaís. Even in the most challenging moments, you always had a word of encouragement and motivation. Thank you for the affection and patience and for giving up so many free days so that I could dedicate myself to the thesis. During these years, there have been so many goodbyes, longings, and moments when we couldn't be together, but I am sure it was all worth it in the end. I love you!

To Maria Iolanda and Vitorio, my parents and personal life examples, thank you so much for your support and unconditional love. My brother Jonas, thank you for being my best friend and for sharing great moments. Even far away, you were always willing to help with anything. I would like

to extend my gratitude to my in-laws Eliana and Thomé (In Memoriam), who were my point of refuge and spared no effort to help me with anything I needed.

I had the privilege of being surrounded by long-time friends and also of meeting new ones who became just as special: Álvaro, André, Augusto, Cássio, Diego, Douglas, Felipe, Rafael, Santiago, and Vitor, thank you so much. The daily work, breaks, lunches, weekends, and holidays were much easier with you.

I would also like to thank my colleagues from Instituto Mauá de Tecnologia for their support and motivation during the writing of the final document, especially Clayton Zabeu and Renato Romio, who trusted me and provided me with the assistance I needed to make this possible.

Finally, I am immensely grateful to God for providing me with health, peace, wisdom and for guiding me in every decision.

This thesis was developed with the assistance of the Universitat Politècnica de València through the predoctoral contract FPI-2019-20-545.

Contents

Contents **i**

List of Figures **v**

List of Tables **xi**

Nomenclature **xiii**

1 Introduction **1**
1.1 Introduction 1
1.2 Contextualization and motivations 1
1.3 Objectives 7
1.4 Document structure 8
References 9

2 Pre-chamber ignition systems applied in internal combustion engines **15**
2.1 Introduction 15
2.2 Spark-ignited engines 16
2.3 Historical review of the PC ignition system 19
2.4 Main processes on pre-chamber ignition systems 26
2.5 Fundamental studies on pre-chambers 28
2.5.1 Constant Volume Combustion Chambers 29
2.5.2 Rapid Compression Machines 33
2.5.3 Optical engines 39
2.6 Summary 44
References 45

3 Materials and methods 59
3.1 Introduction . . . 59
3.2 Rapid Compression-Expansion Machine . . . 60
3.2.1 RCEM redesign for pre-chamber optical studies . . . 61
3.2.2 Test cell instrumentation . . . 63
3.2.3 Mixture preparation . . . 64
3.2.4 Optical techniques . . . 66
3.2.5 Image processing . . . 69
3.3 Optical engine . . . 70
3.3.1 Test cell instrumentation . . . 72
3.3.2 Optical technique – Natural flame luminosity . . . 73
3.4 Numerical tools . . . 73
3.4.1 GT-Power . . . 74
3.4.2 DICOM . . . 74
3.4.3 CONVERGE . . . 75
3.5 Methodology . . . 75
References . . . 76

4 Fundamental aspects to reproduce a reference case in a simplified experimental facility 81
4.1 Introduction . . . 81
4.2 Research approach and validation tools . . . 82
4.2.1 Research approach . . . 82
4.2.2 Validation tools . . . 83
4.3 PC filling and ejection processes . . . 85
4.3.1 Theoretical development . . . 85
4.3.2 Validation and discussion . . . 91
4.4 Jet penetration . . . 98
4.5 Orifice flame quenching . . . 101
4.6 Summary and conclusions . . . 102
References . . . 104

5 The pre-chamber ignition concept applied in a Rapid Compression-Expansion Machine 107
5.1 Introduction . . . 107
5.2 Pre-chamber geometries . . . 108
5.2.1 Discharge coefficient . . . 111
5.3 Thermodynamic analysis . . . 116
5.3.1 Mass flow between chambers . . . 116
5.3.2 Heat transfer . . . 117

5.3.3 Leakage model . . . 118
5.3.4 Deformation model . . . 119
5.3.5 Heat released rate analysis . . . 120
5.4 Typical aspects of PC ignition in the RCEM . . . 122
5.5 Effect of PC geometry on its combustion and jet ejection . . . 125
5.5.1 Geometrical parameter ($A_e/V_{PC}N$) . . . 126
5.5.2 PC length . . . 134
5.5.3 Orifice length . . . 137
5.6 Effect of equivalence ratio . . . 140
5.7 Effect of EGR rate . . . 162
5.8 Summary and conclusions . . . 176
References . . . 181

6 Complementary studies on multi-orifices pre-chambers 185
6.1 Introduction . . . 185
6.2 Materials and methods . . . 186
6.2.1 Engine characteristics and optical setup . . . 186
6.2.2 Pre-chamber geometries . . . 187
6.2.3 Test cell instrumentation . . . 189
6.2.4 Image processing . . . 190
6.2.5 Fuel injection system . . . 192
6.2.6 Methodology . . . 193
6.3 Results . . . 194
6.3.1 SI and PCSI ignition method comparison . . . 195
6.3.2 Effect of orifice diameter and air-fuel ratio on the PCSI concept . . . 197
6.3.3 Spark timing sweep analysis . . . 204
6.4 Summary and conclusions . . . 210
References . . . 211

7 Conclusions and future works 213
7.1 Introduction . . . 213
7.2 Summary and conclusions . . . 213
7.2.1 Reproducing a reference PC under simplified conditions 215
7.2.2 Effect of the geometry on the pre-chamber ignition concept characteristics . . . 216
7.2.3 Effect of the global equivalence ratio on the pre-chamber ignition concept characteristics . . . 216
7.2.4 Effect of the EGR rate on the pre-chamber ignition concept characteristics . . . 218

7.2.5 Effect of orifice diameter and air-fuel ratio on multi-orifice PC geometries 219
7.3 Future works 220

Global Bibliography **223**

List of Figures

1.1 World's total energy supply (TJ-terajoules) by source, 1990-2021. Adapted from International Energy Agency (2023) [2]. 2
1.2 Evolution of the global temperature and the GHG emissions since 1850. Adapted from Intergovernmental Panel on Climate Change (2023) [4]. 3
1.3 Evolution of the global CO_2 emissions from transportation from 1990 to 2022. Adapted from International Energy Agency (2023) [11]. 4

2.1 New passenger cars by fuel type in the EU in 2022. Adapted from ACEA (2023) [2]. 17
2.2 Temporal evolution of the emission standards in the United States of America. Adapted from EPA (2023) [12]. 17
2.3 First concept of pre-chamber ignition system. Adapted from Ricardo, H. (1922) [22]. 20
2.4 Illustration of torch cell concept proposed by Toyota, Ford, and Volkswagen [26–28]. 21
2.5 Active torch cell architectures (3-valve design) [29–31]. 22
2.6 Active torch cell architectures (electronic injector design) [33, 34]. 23
2.7 Avalanche activated combustion [42] and Pulsed Jet Combustion (PJC) generator [36]. 23
2.8 MAHLE Turbulent Jet Ignition system [44]. 24
2.9 KAUST Narrow-throat pre-chamber system. Adapted from Almatraf, F. (2020) [48]. 25
2.10 Evolution of PC and MC pressures along with pressure-drop and HRR_{MC} [49] (left) and the different stages of the pressure-drop between chambers [50] (right). 27

2.11 Schematic view of different designs of CVCCs applied to pre-chamber ignition studies. Adapted from [53–56]. 30
2.12 Cross-sectional view of ETH-Zurich CVCC (left) and Schlieren image sequence for two different PC turbulence cases (right). Adapted from [64]. 33
2.13 Schematic view of different designs of RCMs and RCEMs applied to pre-chamber ignition studies. Adapted from [66, 92]. 35
2.14 RCM configuration for pre-chamber ignition studies used at Michigan State University. Source: [66]. 36
2.15 Optical engines employed for pre-chamber ignition studies. Adapted from: [51, 100]. 40
2.16 Two-row orifice pre-chamber arrangement proposed by the authors. Adapted from: [100]. 43

3.1 RCEM schematic view. 61
3.2 Fully optical accessible liner/cylinder head. 62
3.3 Pre-chamber internal geometry. 63
3.4 Schematic view of the optical setup. 67
3.5 Image outcome from the selected schlieren sensitivity for the RCEM operation. 68
3.6 Step-by-step schlieren post-processing methodology. a) raw image, b) background, c) jet binarization, d) image with the jet contour and the tip penetration (s). 70
3.7 Step-by-step chemiluminescence post-processing methodology. a) raw image, b) background and geometrical mask, c) final image. . 70
3.8 Schematic view of the optical engine setup. 72

4.1 Illustration of the control volumes for main and pre-chambers. . . 85
4.2 PC pressure, pressure difference to MC, and normalized mass flow rate during PC filling. * case at 4000 rpm. 94
4.3 PC temperature during the compression stroke (PC filling). * case at 4000 rpm. 94
4.4 PC pressure, pressure difference to MC, and normalized mass flow rate during the PC combustion process. * case at 4000 rpm ** case adiabatic. 95
4.5 Mach number (upper) and jet momentum (bottom). * case at 4000 rpm ** case adiabatic. 96
4.6 PC mean gas temperature during the PC combustion process. * case at 4000 rpm ** case adiabatic. 97

4.7 Effect of the combustion duration on the PC pressure, pressure difference to MC, and mass flow rate during the PC combustion process. 98
4.8 Simulated jet tip penetration. * case at 4000 rpm. ** Normalized by the distance to the walls (L). 100

5.1 Illustration of the pre-chamber internal geometry for RCEM operation (drawn to scale). 110
5.2 Pre-chamber silicon molds. 112
5.3 Surface geometry and boundary conditions during (a) filling and (b) jet ejection. 113
5.4 Computational domain and mesh details. 114
5.5 Discharge coefficient and calculation time (9 cores) of three different mesh configurations. 114
5.6 Discharge coefficient during jet ejection (filled triangles) and pre-chamber filling (empty squares). 115
5.7 Comparison between geometrical and corrected area for the geometrical relation calculation. 116
5.8 Temporal evolution of the PC jet ejection captured by schlieren and OH* chemiluminescence imaging. PC1 at Φ=1.0 and 0% EGR. 123
5.9 In-cylinder pressure and ΔP traces along with schlieren and OH* chemiluminescence images. 124
5.10 Pressure drop between PC and MC over few cycles for 4 different PC geometries during PC filling. ϕ=1.0 126
5.11 Pressure drop between PC and MC over few cycles for 4 different PC geometries during the jet ejection phase. ϕ=1.0 127
5.12 Pressure drop between PC and MC for PC1, PC2 and PC3 geometries after spark timing. $\phi = 1.0 - EGR = 0\%$ 128
5.13 Schlieren images of PC1, PC2, and PC3 on different time instants after spark timing. $\phi = 1.0 - EGR = 0\%$ 129
5.14 Pressure drop to MC and (a) jet tip penetration and (b) corrected jet tip penetration over time after SOE for PC1, PC2 and PC3. $\phi = 1.0 - EGR = 0\%$ 131
5.15 Jet tip penetration calculated via the DICOM software, along with experimental data, for PC1, PC2, and PC3. $\phi = 1.0 - EGR = 0\%$ 133
5.16 Corrected jet tip penetration from the calculated data (DICOM 1D spray model) for PC1, PC2, and PC3. $\phi = 1.0 - EGR = 0\%$. 134
5.17 PC and MC pressure & pressure drop from PC to MC for PC2+ and PC3. 135
5.18 schlieren images of PC2+ and PC3 at different time instants after spark timing. $\phi = 1.0 - EGR = 0\%$ 136

5.19 Elapsed time since ST of the unreactive and reactive jet ejection for PC1, PC2, PC2+, and PC3. 136
5.20 Jet tip penetration evolution taken from schlieren images of PC2+ and PC3. 137
5.21 Jet penetration evolution of PC1 and PC4, average image during the reactive phase, and an illustration of the PC geometries. 138
5.22 Normalized flame area for PC1 and PC4 cases. 139
5.23 Pressure difference between chambers (top) and jet tip penetration (bottom) after SOE for PC1 and PC4. 140
5.24 Effect of the equivalence ratio on the PC and MC pressure for PC1, PC2, and PC3. 142
5.25 Effect of the equivalence ratio on the ΔP between chambers and jet momentum for PC1, PC2, and PC3. 143
5.26 Graphical illustration of the pre-chamber characteristic times for different fuel-air equivalence ratios. 145
5.27 Effect of the fuel-air equivalence ratio on the interval between ST and SOE for PC1, PC2, and PC3. 146
5.28 Schlieren images of the PC1 operating with ϕ=1.0, 0.90, 0.80, and 0.75. 147
5.29 Chemiluminescence OH* images of the PC1 operating with ϕ=1.0, 0.90, 0.80, and 0.75. 148
5.30 Pressure rise rate for the PC1 operating with ϕ=1.0, 0.90, 0.80, and 0.75. 152
5.31 Schlieren images of the PC2 operating with ϕ=1.0, 0.90, 0.80, and 0.75. 153
5.32 Chemiluminescence OH* images of the PC2 operating with ϕ=1.0, 0.90, 0.80, and 0.75. 154
5.33 Pressure rise rate for the PC2 operating with ϕ=1.0, 0.90, 0.80, and 0.75. 156
5.34 Schlieren images of the PC3 operating with ϕ=1.0, 0.90, 0.80, and 0.75. 158
5.35 Chemiluminescence OH* images of the PC3 operating with ϕ=1.0, 0.90, 0.80, and 0.75. 159
5.36 Pressure rise rate for the PC3 operating with ϕ=1.0, 0.90, 0.80, and 0.75. 161
5.37 Illustration of the internal geometry of PC1 (left) and PC3 (right). 163
5.38 PC and MC in-cylinder pressure and ΔP curves for different EGR levels - PC1. 165
5.39 Pre-chamber chemical heat release rate for different EGR levels - PC1. 166

5.40 Schlieren images of the PC1 operating with 0 (left), 10 (center) and 20% (right) of EGR. 167
5.41 Chemiluminescence OH* images of the PC1 operating with 0 (left), 10 (center) and 20% (right) of EGR. 168
5.42 PC and MC pressure for different EGR levels - PC3. 170
5.43 Pre-chamber chemical heat release rate for different EGR levels - PC3. 171
5.44 Schlieren images of the PC3 operating with 0 (left), 10 (center) and 20% (right) of EGR. 172
5.45 Chemiluminescence OH* images of the PC3 operating with 0 (left), 10 (center) and 20% (right) of EGR. 173
5.46 Effect of the EGR rate on the interval between ST and SOE for PC1 and PC3. 175
5.47 Ratio between orifice diameter and laminar flame thickness, and Da number for different equivalence ratio and EGR rate. 181

6.1 Illustrative representation of (a) the optical engine setup and (b) the PC layout. 187
6.2 Steps during image processing. 190
6.3 Methodology to calculate the jet tip penetration. 191
6.4 Flame contour (left) and the grey value along the jet axis (right). . 192
6.5 In-cylinder pressure and RoHR comparative between SI and PCSI with 1.0, 1.2, and 1.5 mm orifice diameter at $\lambda = 1.0$ and MBT. . 195
6.6 Flame development comparison between SI and PCSI (1.5 mm orifice) at $\lambda = 1.0$ and ST=-20 CAD using broadband flame chemiluminescence. 196
6.7 Equivalent flame propagation velocity: a comparison between SI and PCSI with different diameter of orifices operating at $\lambda = 1.0$ and MBT, and advanced ST for 1.5 mm case. 197
6.8 Jet penetration and flame development: a comparison between different diameters of orifices of the PCSI operating at $\lambda = 1.0$ and ST=-18 CAD-ATDC using broadband flame chemiluminescence imaging. 198
6.9 Flame area normalized: a comparison between different diameters of orifices of the PCSI operating at $\lambda = 0.9$, 1.0 and 1.1 and MBT. 200
6.10 Equivalent flame propagation velocity: a comparison between different diameters of orifices of the PCSI operating at $\lambda = 0.9$, 1.0 and 1.1 and MBT. The instant in which part of the flame is outside the optical limit is indicated by dashed lines. 201

6.11 Jet tip velocity vs mean jet tip penetration: a comparison between different diameters of orifices of the PCSI operating at λ=0.9, 1.0 and 1.1 and MBT. 202
6.12 Flame development angle: a comparison between different diameters of orifices of the PCSI operating at λ=0.9, 1.0, and 1.1 at MBT condition. 203
6.13 Combustion duration and flame development angle for different orifice diameters of the PCSI operating at λ=1.0 and MBT condition. 204
6.14 In-cylinder pressure and RoHR for different spark timings for the PC 1.2 mm operating at lambda 0.9 (top), 1.0 (center), and 1.1 (bottom). Blue rectangle highlights 13-15 CAD. 205
6.15 In-cylinder pressure and RoHR for different spark timings for the PC 1.5 mm operating at lambda 0.9 (top), 1.0 (center), and 1.1 (bottom). Blue rectangle highlights 13-15 CAD. 207
6.16 Normalized flame area and flame development angle for different spark timings for the PC 1.0, 1.2, and 1.5 mm operating at lambda=1.0. 208
6.17 Effect of the spark timing and lambda on the CA50 for SI and PCSI with different diameters of orifices operating at lambda 0.9 (top), 1.0 (center), and 1.1 (bottom). 209

List of Tables

2.1 Historical overview of the pre-chamber technologies. 26

3.1 Technical characteristics of the RCEM. 60
3.2 Air/air-EGR tank composition for each EGR level. 65
3.3 Fuel characteristics. Source: [8, 9] 66
3.4 Optical engine specifications. 71

4.1 Engine geometry and boundary conditions 84
4.2 Dimensions and specifications of the simulated pre-chambers . . . 92
4.3 PC specifications for jet penetration assessment. *Suitable chamber length. 100

5.1 Pre-chamber dimensions for RCEM operation (measurements obtained using silicone molds). 109
5.2 CFD boundary conditions. 115
5.3 Pre-chamber characteristic times for different fuel-air equivalence ratios. 144
5.4 Damköhler number at 25mm downstream the orifice exit for different equivalence ratios - PC1. 151
5.5 Flame properties for different fuel-air equivalence ratios and thermodynamic conditions of PC1. 151
5.6 Flame properties for different fuel-air equivalence ratios and thermodynamic conditions of PC2. 157
5.7 Flame properties for different fuel-air equivalence ratios and thermodynamic conditions of PC3. 162
5.8 Mixture composition for each EGR level. 163
5.9 Pre-chamber characteristic times for different EGR rates. 164

5.10 Flame properties for different EGR rates and thermodynamic conditions of PC1. 169
5.11 Flame properties for different EGR rates and thermodynamic conditions of PC3. 175
5.12 Summary of the flame properties for the equivalence ratio and EGR rate sweep for PC1, PC2, and PC3. 180

6.1 Engine specifications. 186
6.2 Pre-chamber characteristics. 189
6.3 Fuel characteristics. 193
6.4 Matrix for optical engine experiments. 194

Nomenclature

Acronyms

ABDC	After bottom dead center.
AFR	Air-fuel ratio.
APIR	Self-ignition Triggered by Radical Injection.
ATDC	After top dead center.
BDC	Bottom dead center.
BEV	Battery Electric Vehicle.
BTDC	Before top dead center.
CA10-90	Main chamber combustion duration.
CA50	Combustion center.
CAD	Crank angle degree.
CFD	Computational Fluid Dynamics.
CI	Compression-ignited.
CNR	National Research Council of Italy.
CO_2	Carbon dioxide.
CO	Carbon monoxide.
CVCC	Constant Volume Combustion Chamber.
DI	Direct injection.
DOI	Duration of injection.
EGR	Exhaust gas recirculation.
ETU	Engine timing unit.
EU	Europe Union.

GDI Gasoline direct injection.
GHG Greenhouse gases.
HC Unbunred hydrocarbon.
HEV Hybrid Electric Vehicle.
ICE Internal combustion engine.
$IMEP_g$ Gross indicate Mean Effective Pressure.
IMEP Indicate Mean Effective Pressure.
ISFC Indicated Specific Fuel Consumption.
JISCE Jet ignition Stratified Charge Engines.
LAG Russian acronym for Avalanche Activated Combustion.
LHV Lower Heating Value.
LRT Likelihood ratio test.
MBT Maximum brake-torque.
MC Main chamber.
NOx Nitrogen oxides.
PCCI Premixed Charge Compression Ignition.
PCSI Pre-chamber ignition concept.
PC Pre-chamber.
PFI Port fuel injection.
PHEV Plug-in Hybrid Electric Vehicles.
PJC Pulsed Jet Combustion.
PLIF Planar Laser-Induced Fluorescence.
RCEM Rapid Compression-Expansion Machine.
RCM Rapid Compression Machine.
SI Spark ignition.
SOE Start of Ejection.
SOI Start of Injection.
ST-CA10 Flame development angle.
STEMS Institute of Sciences and Technologies for Sustainable Energy and Mobility.
ST Spark timing.
TDC Top dead center.
TGP Turbulence Generating Pot.
TJI Turbulent Jet Ignition.
TWC Three-way catalyst.

USA United States of America.
VVT Variable valve timing.

Greek symbols

$(F/A)_{stoich}$ Stoichiometric fuel-to-air ratio.
$\Delta\theta$ Duration of combustion (Wiebe).
ΔP Pressure difference.
δ Flame thickness.
δ_L Laminar flame thickness.
γ Specific heat ratio c_p/c_v.
λ Relative air/fuel ratio.
Φ Fuel/air equivalence ratio.
ρ Density (general).
τ_L Characteristic turbulent eddy turnover time.
τ_T Characteristic chemical reaction time.
θ Crank angle degree.
θ_o Start of combustion (Wiebe).
φ Flow compressibility function.

Latin symbols

a Wiebe constant.
A_e Effective flow area.
A_n Nozzle flow area.
C_D Discharge coefficient.
c_v Specific heat at constant volume.
CH_4 Methane.
CV_{MC} Main chamber control volume.
CV_{PC} Pre-chamber control volume.
d_o Orifice diameter.
E_{CV} Energy of a given control volume.
F_R F/A equivalence ratio.
h_k Enthalpy associated to the mass transfer.
$HRR_{CHEMICAL}$ Pre-chamber chemical heat released rate.
HRR_{MC} Main chamber heat released rate.
k_p Proportionality constant.

L	Distance between orifice exit and cylinder walls/piston surface.
l_I	Integral length scale.
L_o	Orifice length.
m	Mass transfer between control volumes.
m_{Wiebe}	Wiebe constant.
N	Engine speed (rpm).
n	Engine speed (rps).
N_2	Nitrogen.
O_2	Oxygen.
P_{CV}	Pressure in a given control volume.
P_{MC}	Main chamber pressure.
P_{PC}	Pre-chamber pressure.
Q_{ch}	Chemical energy released by combustion of the fuel.
Q_{CV}	Heat added in a given control volume.
R	Gas constant.
r_c	Compression ratio.
s	Jet tip penetration.
S_L	Laminar flame speed.
t	Time from start of injection.
T_{CV}	Temperature in a given control volume.
$T_{U,PC}$	Unburnt mixture temperature in the PC.
u'	Turbulence intensity.
U_{CV}	Internal energy of a given control volume.
V	Volume (general).
v	Flow velocity at the pre-chamber orifice.
V_c	Clearance volume.
v_f	Flame propagation velocity.
V_{CV}	Volume of a given control volume.
W_{CV}	Work done by a given control volume.
x_b	Fuel mass fraction burned.

Chapter 1

Introduction

1.1 Introduction

This chapter aims to give an overview of the current scenario of the energy sector, with a focus on the relevance of internal combustion engines in the transport and power generation sectors, as well as their important role in the decarbonization of these sectors. In addition, this chapter includes the objectives and the document structure, describing the way that the information is organized within each chapter.

1.2 Contextualization and motivations

The global demand for energy has been growing over the last decades, either due to population growth or to the economic development of countries [1]. In global terms, as depicted by Figure 1.1, the origin of the Total Energy Supply (TES, i.e. all the energy produced in or imported to a country, minus that which is exported or stored) is mainly from fossil fuels such as coal, oil, and natural gas, which are known sources of CO_2 emissions [2]. The share of renewable energy sources (e.g. hydro, wind, solar, biofuels, etc.) has been increasing over the last years, but it still represents a small fraction when compared to very polluting sources like coal and heavy oils.

The link between CO_2 emissions and the global rise in temperatures is widely known and discussed, as well as the contribution of human activities to the greenhouse gas (GHG) emissions [3]. As depicted by Figure 1.2, the global

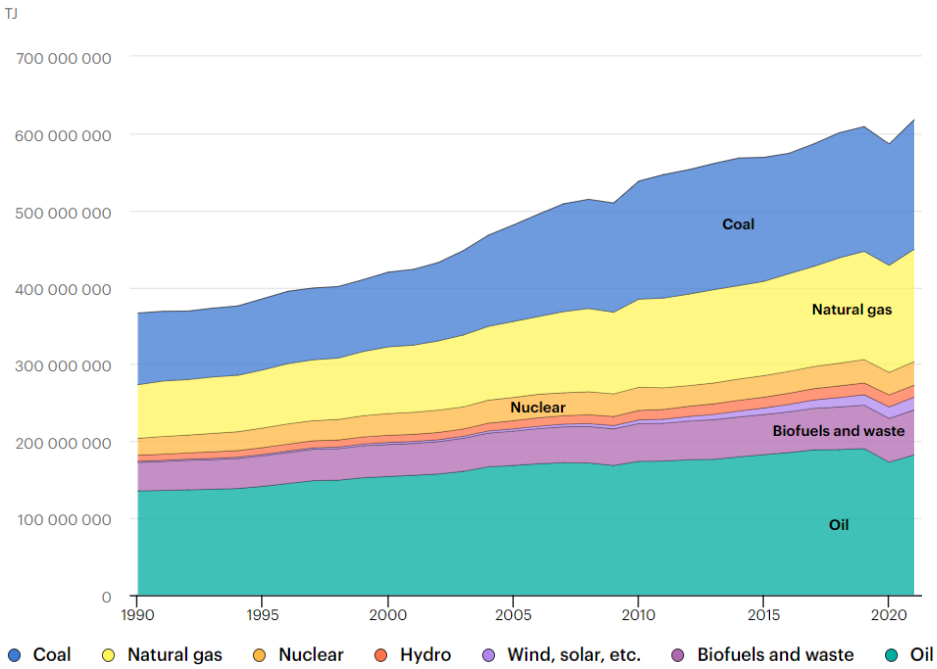

Figure 1.1: World's total energy supply (TJ-terajoules) by source, 1990-2021. Adapted from International Energy Agency (2023) [2].

surface temperature has increased by 1.1 °C in the last decade compared to 1850-1900 half-century, which correlates with the increase of the concentration of GHGs and the emission of GHG as a result of the human activities [4]. The CO_2 emissions from the use of fossil fuels for electricity production or to power the transportation sector can, therefore, be considered the main driver of the increase in temperature across the globe [5].

Climate change as a result of the global temperature rise is intensifying extreme weather events and can lead to significant variations in the sea ice, sea level, and precipitation patterns [6]. Such events might bring vulnerability to farming systems and population housing, as well as cause a direct impact on human health [7–9]. Therefore, there has never been a greater need for humanity to discover solutions for lowering the CO_2 emissions before reaching a point of no return.

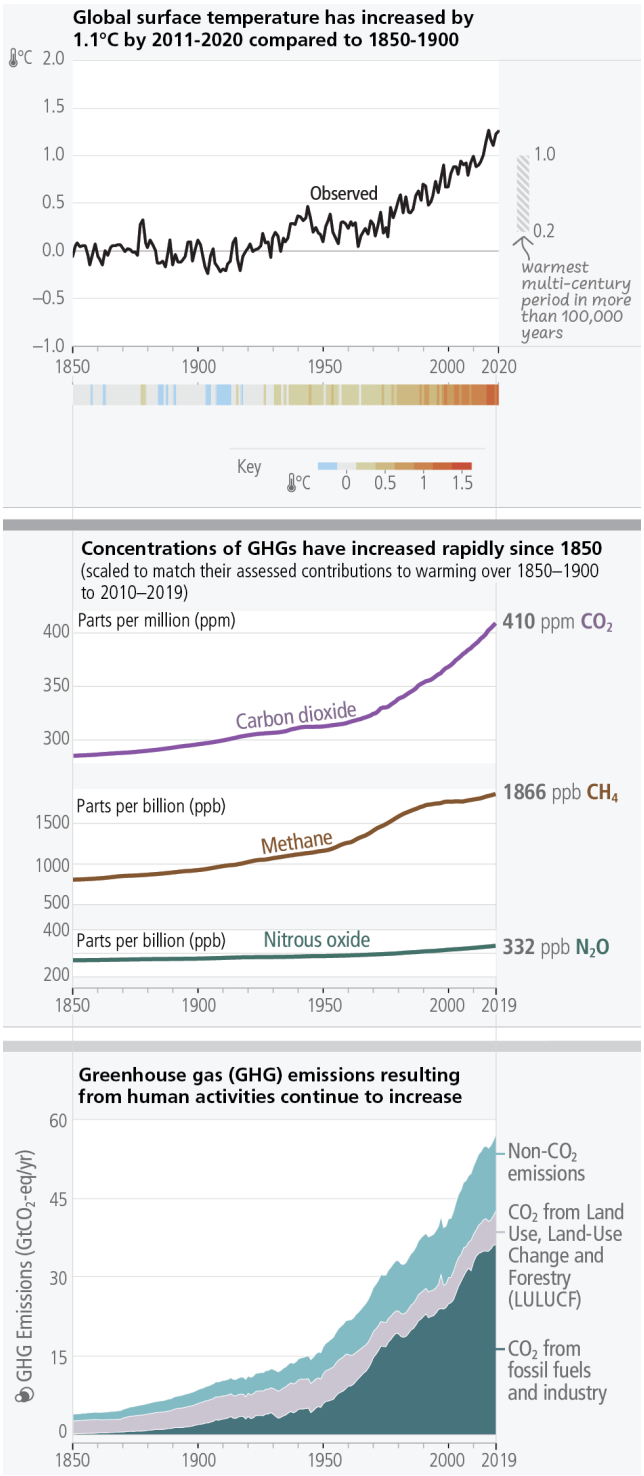

Figure 1.2: Evolution of the global temperature and the GHG emissions since 1850. Adapted from Intergovernmental Panel on Climate Change (2023) [4].

When the final energy consumption (a share of the total energy supply) is segregated into sectors, transportation is one of the most relevant, accounting for more than a third of CO_2 emissions from end-use sectors and around 10% of the total GHGs emissions, mainly because 91% of the total energy used in the transport sector relies on oil products [10–12]. During the last decades, special attention has been paid to the road and shipping sub-sectors due to their share of 85% of the total transportation CO_2 emissions. Figure 1.3 shows the contribution of each transportation sub-sector to the total CO_2 emission from 1990 to 2022, and the percentage of each one in 2022.

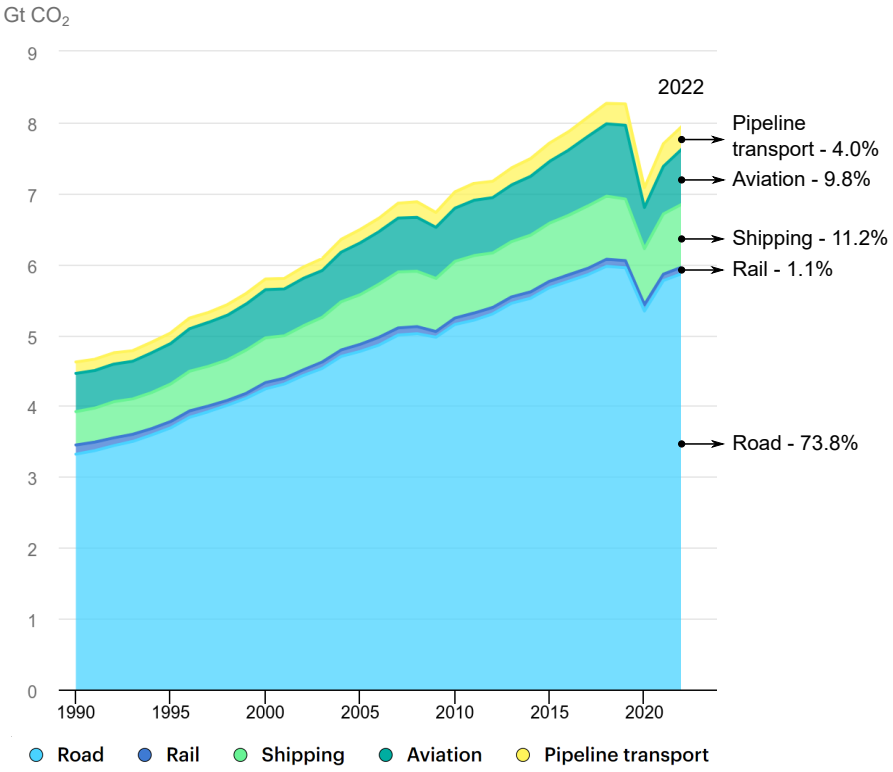

Figure 1.3: Evolution of the global CO_2 emissions from transportation from 1990 to 2022. Adapted from International Energy Agency (2023) [11].

In order to promote global CO_2 reduction and mitigate the effects of climate change, the policymakers, encouraged by the population, researchers, and companies, have announced nations' commitment to reach net-zero carbon emissions in the coming decades. The pledges include actions in all sectors (e.g., electricity, industry, transport, buildings) and encourage the use of less

carbon-intensive sources of energy, as well as more efficient ways of using the energy [13].

Focusing on the transportation sector, in addition to the concern with reducing CO_2 emissions, the reduction of pollutant emissions produced by any kind of transportation media has also been the subject of regulatory actions. The pollutant emissions (particulate matter, nitrogen dioxide, carbon monoxide, sulfur dioxide, volatile organic compounds, etc.), unlike GHG, have a local effect and are a concern primarily in large urban centers due to their potential to cause health issues. In this sense, several emission standards were implemented over the last years to restrict the internal combustion engine (ICE) tailpipe emissions for on-road and nonroad vehicles and marine engines, such as "Tier #" in the United States of America (USA), "EURO #" in the Europe Union (EU), "Proconve L# or P#" in Brazil, "China #" in China, and MARPOL for marine applications [14]. On the one hand, these legislations forced car manufacturers to develop and implement new technologies and control strategies to reduce pollutant emissions by vehicles, either by enhancing the combustion and mitigating the pollutant formation or reducing their concentration in a post-treatment system. On the other hand, marine vessels were required to operate with low-sulfur fuels within Emission Control Areas (ECA) or directly retrofit to fuels with a lower carbon footprint such as natural gas [15]. In addition to reducing CO_2 emissions, the measures adopted have helped to improve air quality in the US, EU, and Brazil according to World Health Organization's Air quality guidelines [16].

Besides the new technologies implemented on "conventional powertrains" (i.e. powered exclusively with ICEs), electrification is gaining ground in passenger cars due to its potential to improve the powertrain efficiency over a wide range of applications, whether on hybrid - Hybrid Electric Vehicles (HEV) and Plug-in Hybrid Electric Vehicles (PHEV) - or fully electric - Battery Electric Vehicles (BEV) - architectures [17, 18]. Moreover, given the current emission standards (focused on tank-to-wheel emissions), incentive mechanisms have been created to increase the commercialization of electrified vehicles, whether in the form of discounts on fees for the population or on fleet emissions abatement to car manufacturers. Nevertheless, life cycle analysis studies indicate that the well-to-wheel GHG emissions of electrified vehicles can substantially vary according to the electricity production matrix, and may be comparable to ICE GHG emissions where the energy matrix is highly dependent on fossil fuels [19, 20].

In terms of mobility, it is plausible to think that there will not be a single powertrain architecture, but a mix of solutions involving BEVs, HEVs,

PHEVs, fuel cell electric vehicles (FCEVs), and vehicles powered exclusively with ICEs, depending on the application (urban, highway, etc.), cost, tax incentives, use restrictions (e.g. low emission zones), charging infrastructure, and other aspects. As an example, sales projection for 2050 indicates that 79% of the US light-duty vehicles will be powered with ICEs [21]. Therefore, even with electrified powertrain configurations, the ICE will remain crucial for the mobility of people or goods for a significant period of time, whether to generate power in a hybrid powertrain or to power the vehicle itself.

In addition to the transportation sector, electricity production can be one of the most CO_2 emitters sectors in some countries, depending on the availability of renewable sources in their energy matrix. In the USA, for instance, about 60% of the electricity comes from burning fossil fuels, mostly coal and natural gas, representing 25% of the total US GHG emissions in 2022 [22]. In the case of Brazil, giving another example, where the non-renewable sources for electricity generation accounted only for 12.3% in 2022, the use of thermal power plants is still necessary to ensure electricity security during peak consumption periods or when the hydroelectric reservoir levels are low or the sunshine and wind are not available [23]. Thermal power plants are widely used due to their fast start-up time, flexible output range (by connecting multiple ICE units) without compromising efficiency, and excellent ramp load rate. Such characteristics make it a good option for balancing variations over the day and between seasons on electric power systems.

In this sense, due to the degree of dependence on fossil fuels and the high financial and temporal cost of transitioning to a carbon-free energy matrix, an intermediate and necessary step to reduce GHGs emissions is to increase the efficiency of the current fossil-based transportation sector without significant increases in purchase and operating costs in the short-to-medium term. The use of alternative fuels such as e-fuels, green hydrogen, and ammonia is another alternative for decarbonization, and has been the subject of substantial research over the last years due to their carbon neutrality. However, the cost and the availability of renewable sources for their production still is the main drawback for its large scale implementation [24–26].

With regard to improving efficiency, in recent years the pre-chamber ignition concept gained attention due to its capability to achieve high efficiency on small engines, whether extending the lean and EGR dilution limits of spark-ignited (SI) engines, or ensuring knock-safe operation on turbocharged/high-compression ratio SI engines, or when low knock-resistance fuels are used [27–30]. Especially on small engines, the high efficiency obtained with this concept makes it a promising candidate to be integrated into a Series-Hybrid vehicle

as a range-extender [31–33]. For large-bore engines (i.e. marine and power generation applications), the pre-chamber ignition enables high-load operation of natural gas engines under lean conditions, improving thermodynamic efficiency while maintaining low NOx emissions levels [34]. The pre-chamber concept consists of a small volume chamber (1 5% of the clearance volume), a so-called pre-chamber (PC), where the combustion is initiated by an external ignition source (usually a spark plug), once the combustion develops and the pre-chamber pressure increase, the hot combustion gases are ejected towards the main chamber (MC) through orifices, generating multi ignition sites and shortening the combustion duration [35]. The pre-chamber ignition concept is quite easily adapted to the current SI engine architecture by replacing the conventional spark plug with the PC kit. Despite these benefits, an optimal geometry that fits the full engine map is still one of the barriers to implementing this technology in passenger car engines [36].

Several studies have been reported in the literature aiming to optimize the pre-chamber geometry and study the effect of the different geometrical aspects (e.g. orifice diameter, PC volume, number and orientation of the orifices, etc.) or mixture conditions on the jet pattern. However, to convey this information (usually obtained under simplified conditions due to experimental convenience) to engine applications, it is mandatory that these PC configurations represent the same flow pattern (e.g. velocity, jet penetration, and turbulence) and thermodynamic conditions found in ICEs. In this sense, this PhD. thesis aims to further investigate the pre-chamber ignition system under engine-like conditions both using an experimental facility (Rapid Compression-Expansion Machine) with simplified conditions (single orifice PCs) and an optical engine with a prototype multi-orifice PC, being supported by the development of a methodology to design PCs to preserve as much as possible the jet characteristics of the reference pre-chamber.

1.3 Objectives

The present thesis was proposed to further investigate the pre-chamber ignition concept, within the scope of an emerging topic from the automotive sector to improve SI engine fuel conversion efficiency. Given the lack of optical studies using pre-chamber under engine-like conditions, the Rapid Compression-Expansion Machine (RCEM) was chosen as the experimental facility to conduct the first part of the experimental tests for allowing to associate an optically accessible combustion chamber to engine-like condition operation. To complement this first part, the pre-chamber ignition concept

was also studied in an optical engine, in which the thermodynamic conditions are closer to those found in a commercial engine, but optical techniques can still be applied.

In this context, this thesis includes some specific objectives, which are detailed here:

- To identify constructive parameters that affect the jet ejection process;
- To develop a methodology to reproduce the jet characteristics of a multi-orifice pre-chamber design into a single-orifice pre-chamber design, allowing to test engine-like PC geometries into simplified experimental conditions;
- To modify the existing RCEM facility available at the CMT Institute to obtain an optically accessible combustion chamber for pre-chamber ignition systems testing;
- To experimentally validate the effect of geometrical aspects on the PC combustion and jet ejection processes by using pressure-based and imaging analysis;
- To evaluate the effect of the fuel-air equivalence ratio and the EGR rate on the PC combustion, jet ejection characteristics, and MC ignition pattern;
- To assess constructive geometrical parameters of a multi-orifice PC, and the effect of the air-fuel ratio on the jet characteristics and MC combustion by using optical techniques and in-cylinder pressure measurements in a single-cylinder optical engine;

1.4 Document structure

The thesis is organized into seven chapters, starting with this brief introduction (**chapter 1**), which presents the general context and primary objectives of the work carried out.

Then, **chapter 2** focuses on describing the use of the pre-chamber ignition concept on internal combustion engines, from the first applications to the state-of-the-art, highlighting why much attention has been paid in recent years to this concept, and what are its benefits and drawbacks on ICE applications. In addition, the chapter includes, in a comprehensive literature review, the main gaps in terms of fundamental studies on simplified experimental facilities.

Chapter 3 presents the experimental facilities, equipment, numerical tools, and the methodology followed during the present thesis. Each experimental test-rig and its optical setup are described with the corresponding optical technique utilized. Furthermore, the modifications made to the RCEM experimental facility to carry out PC ignition studies with full optical access to the main combustion chamber are detailed.

Next, **chapter 4** reports a theoretical and numerical study about how the pre-chamber geometrical parameters affect the different pre-chamber processes: gas exchange, PC combustion, and jet ejection. The outcome of this study is a guideline of how to emulate as best as possible the jet ejection of a multi-orifice PC into a single-orifice PC, supporting the pre-chamber design of the geometries which would be experimentally tested later on the Rapid Compression-Expansion Machine (RCEM).

After that, **chapter 5** presents and discusses the results from the different pre-chamber geometries on the RCEM. The experimental results are divided into three main sections: (1) the effect of the PC geometry, (2) the effect of the equivalence ratio, and (3) the effect of the EGR rate. In the first part, modifications on the PC length, PC diameter, orifice diameter, and orifice length were proposed to evaluate their effect on the PC filling, PC combustion, jet ejection characteristics and MC ignition pattern. In the second part, the same features are evaluated with different fuel-air mixture equivalence ratios, from stoichiometric mixture up to the lean limit. Finally, the main parameters of the PC ignition concept are assessed for different EGR rates: from 0 up to 25%.

Later, **chapter 6** is centered on discussing the results obtained with a multi-orifice passive pre-chamber operating in a single-cylinder optical engine. The jet ejection and the MC combustion development were assessed by means of the in-cylinder pressure and natural flame luminosity optical technique in a parametric study varying the orifice diameter, the relative air-fuel ratio, and the spark timing.

Lastly, **chapter 7** presents a review of the work carried out, as well as the main conclusions. Additionally, some unexplored topics that emerged from the information and experience gathered during the development of this PhD. thesis are suggested for future works.

References

[1] Institute, Energy. “Statistical Review of World Energy 2023”. In: *BP Energy Outlook 2023* 70.73 (2023), pp. 8–20.

[2] IEA. *Energy Statistics Data Browser*. 2023.

[3] Lacis, Andrew A., Schmidt, Gavin A., Rind, David, and Ruedy, Reto A. "Atmospheric CO 2 : Principal Control Knob Governing Earth's Temperature". In: *Science* 330.6002 (2010), pp. 356–359. DOI: 10.1126/science.1190653.

[4] Calvin, Katherine et al. *IPCC, 2023: Climate Change 2023: Synthesis Report. Contribution of Working Groups I, II and III to the Sixth Assessment Report of the Intergovernmental Panel on Climate Change [Core Writing Team, H. Lee and J. Romero (eds.)]. IPCC, Geneva, Switzerland.* Tech. rep. Intergovernmental Panel on Climate Change, 2023, pp. 1–163. DOI: 10.59327/IPCC/AR6-9789291691647.

[5] Intergovernmental Panel on Climate Change (IPCC). *Climate Change 2022 - Mitigation of Climate Change*. Ed. by Intergovernmental Panel on Climate Change (IPCC). Cambridge University Press, 2023. DOI: 10.1017/9781009157926.

[6] Rounce, David R. et al. "Global glacier change in the 21st century: Every increase in temperature matters". In: *Science* 379.6627 (2023), pp. 78–83. DOI: 10.1126/science.abo1324.

[7] Hsiang, Solomon et al. "Estimating economic damage from climate change in the United States". In: *Science* 356.6345 (2017), pp. 1362–1369. DOI: 10.1126/science.aal4369.

[8] Albert, James S. et al. "Human impacts outpace natural processes in the Amazon". In: *Science* 379.6630 (2023). DOI: 10.1126/science.abo5003.

[9] Blöschl, Günter et al. "Changing climate shifts timing of European floods". In: *Science* 357.6351 (2017), pp. 588–590. DOI: 10.1126/science.aan2506.

[10] IEA. *Energy consumption in transport by fuel in the Net Zero Scenario, 1975-2030*.

[11] IEA. *Global CO2 emissions from transport by sub-sector in the Net Zero Scenario, 2000-2030*. 2023.

[12] Reitz, R. D. et al. "IJER editorial: The future of the internal combustion engine". In: *International Journal of Engine Research* 21.1 (2020), pp. 3–10. DOI: 10.1177/1468087419877990.

[13] International Energy Agency. *World Energy Outlook 2022*. Tech. rep. Paris, 2022, p. 524.

[14] Wallington, Timothy J., Anderson, James E., Dolan, Rachael H., and Winkler, Sandra L. "Vehicle Emissions and Urban Air Quality: 60 Years of Progress". In: *Atmosphere* 13.5 (2022). DOI: 10.3390/atmos13050650.

[15] Sys, Christa, Vanelslander, Thierry, Adriaenssens, Mathias, and Van Rillaer, Ive. "International emission regulation in sea transport: Economic feasibility and impact". In: *Transportation Research Part D: Transport and Environment* 45 (2016), pp. 139–151. DOI: 10.1016/j.trd.2015.06.009.

[16] Ribeiro, Camilo Bastos, Rodella, Fernando Henrique Cavalcante, and Hoinaski, Leonardo. "Regulating light-duty vehicle emissions: an overview of US, EU, China and Brazil programs and its effect on air quality". In: *Clean Technologies and Environmental Policy* 24.3 (2022), pp. 851–862. DOI: 10.1007/s10098-021-02238-1.

[17] Minarcin, Monika A., Rask, Eric, and Smith, Matthew R. "Challenges and Opportunities in Adoption of Hybrid Technologies in Medium and Heavy Duty Applications". In: *SAE Technical Papers*. Vol. 2711. 2011. DOI: 10.4271/2011-01-2251.

[18] Boretti, Alberto. "Plug-in hybrid electric vehicles are better than battery electric vehicles to reduce CO 2 emissions until 2030". In: *International Journal of Energy Research* 46.14 (2022), pp. 20136–20145. DOI: 10.1002/er.8313.

[19] Nordelöf, Anders, Messagie, Maarten, Tillman, Anne Marie, Ljunggren Söderman, Maria, and Van Mierlo, Joeri. "Environmental impacts of hybrid, plug-in hybrid, and battery electric vehicles—what can we learn from life cycle assessment?" In: *International Journal of Life Cycle Assessment* 19.11 (2014), pp. 1866–1890. DOI: 10.1007/s11367-014-0788-0.

[20] Bieker Georg. *A global comparison of the life-cycle greenhouse gas emissions of combustion engine and electric passenger cars - International Council on Clean Transportation*. 2021.

[21] U.S. Energy Information Administration. *Annual Energy Outlook 2022*. 2022.

[22] U.S. Energy Information Administration. *Electricity explained*. 2023.

[23] Empresa de Pesquisa Energética. *Brazilian Energy Balance 2023 Year 2022*. Rio de Janeiro, 2023.

[24] Pastor, José V., Micó, Carlos, Lewiski, Felipe, Tejada, Francisco J., and Tornatore, Cinzia. "A Synergic Application of High-Oxygenated E-Fuels and New Bowl Designs for Low Soot Emissions: An Optical Analysis". In: *Applied Sciences (Switzerland)* 13.14 (2023). DOI: 10.3390/app13148560.

[25] Sementa, Paolo et al. "Exploring the potentials of lean-burn hydrogen SI engine compared to methane operation". In: *International Journal of Hydrogen Energy* 47.59 (2022), pp. 25044–25056. DOI: 10.1016/j.ijhydene.2022.05.250.

[26] Tornatore, Cinzia, Marchitto, Luca, Sabia, Pino, and De Joannon, Mara. "Ammonia as Green Fuel in Internal Combustion Engines: State-of-the-Art and Future Perspectives". In: *Frontiers in Mechanical Engineering* 8.July (2022), pp. 1–16. DOI: 10.3389/fmech.2022.944201.

[27] Bunce, Michael and Blaxill, Hugh. "Sub-200 g/kWh BSFC on a Light Duty Gasoline Engine". In: *SAE Technical Papers*. Vol. 2016-April. April. 2016. DOI: 10.4271/2016-01-0709.

[28] Benajes, J. et al. "Evaluation of the passive pre-chamber ignition concept for future high compression ratio turbocharged spark-ignition engines". In: *Applied Energy* 248 (2019), pp. 576–588. DOI: 10.1016/j.apenergy.2019.04.131.

[29] Zhou, Lei et al. "Effects of different hole structures of pre-chamber with turbulent jet ignition on the flame propagation and lean combustion performance of a single-cylinder engine". In: *Fuel* 308.August 2021 (2022), p. 121902. DOI: 10.1016/j.fuel.2021.121902.

[30] Rohwer, Johannes, Han, Taehoon, Shah, Ashish, and Rockstroh, Toby. "Investigations into EGR dilution tolerance in a pre-chamber ignited GDI engine". In: *International Journal of Engine Research* (2022), p. 146808742210847. DOI: 10.1177/14680874221084777.

[31] Toulson, Elisa, Schock, Harold J., and Attard, William P. "A Review of Pre-Chamber Initiated Jet Ignition Combustion Systems". In: *SAE Technical Paper Series* (2010). DOI: 10.4271/2010-01-2263.

[32] Novella, R., Gomez-Soriano, J., Martinez-Hernandiz, P.J., Libert, C., and Rampanarivo, F. "Improving the performance of the passive pre-chamber ignition concept for spark-ignition engines fueled with natural gas". In: *Fuel* 290.December 2020 (2021), p. 119971. DOI: 10.1016/j.fuel.2020.119971.

[33] Frasci, Emmanuele et al. “Comprehensive model for energetic analyses of a series hybrid-electric vehicle powered by a passive Turbulent Jet Ignition engine”. In: *Energy Conversion and Management* 269.May (2022), p. 116092. DOI: 10.1016/j.enconman.2022.116092.

[34] Shah, Ashish, Tunestal, Per, and Johansson, Bengt. “Scalability Aspects of Pre-Chamber Ignition in Heavy Duty Natural Gas Engines”. In: *SAE Technical Papers*. group 1. 2016. DOI: 10.4271/2016-01-0796.

[35] Alvarez, Carlos Eduardo Castilla, Couto, Giselle Elias, Roso, Vinícius Rückert, Thiriet, Arthur Braga, and Valle, Ramon Molina. “A review of prechamber ignition systems as lean combustion technology for SI engines”. In: *Applied Thermal Engineering* 128 (2018), pp. 107–120. DOI: 10.1016/j.applthermaleng.2017.08.118.

[36] Bunce, Michael et al. “Pre-chamber Combustors: An Enabling Technology for High Efficiency, Low CO2 Engine Operation”. In: *Energy, Environment, and Sustainability*. Springer Singapore, 2022, pp. 133–173. DOI: 10.1007/978-981-16-8717-4_7.

Chapter 2

Pre-chamber ignition systems applied in internal combustion engines

2.1 Introduction

This chapter aims to give the state-of-the-art of pre-chamber spark-ignited engines and describe their contribution to thermal efficiency improvement in internal combustion engines, while maintaining low engine-out emission of greenhouse gases (GHG) and pollutant emissions. To accomplish this, a comprehensive literature review is carried out to characterize the use of internal combustion engines, and especially spark-ignited engines, in current times, their changes over the last years, and the challenges to meet future emission regulations.

In addition to the general aspects of pre-chamber spark-ignited engines, this chapter also aims to describe some relevant studies that further investigated pre-chamber combustion, whether from a more fundamental point of view in dedicated experimental facilities or evaluating the fuel conversion efficiency or pollutant emissions on metallic engines.

First, the relevance of internal combustion engines and some of the improvements introduced on spark-ignited engines over the last few years are presented. Then, the possible paths for thermal efficiency improvements and

their limitations are discussed. Next, the pre-chamber ignition concept is described and a brief historical review of the main findings on the pre-chamber ignition concept is presented. After that, some fundamental studies on pre-chamber ignition systems carried out on different experimental facilities are presented and discussed. To conclude, some fundamental aspects when operating with pre-chamber ignition systems are pointed out.

2.2 Spark-ignited engines

Among the different types of reciprocating internal combustion engines, spark-ignited (SI) engines along with compression-ignited (CI) engines are the most widespread engine configurations currently used due to their simplicity, reliability, efficiency, serviceability, low cost, and high power-to-weight ratio [1]. In SI engines, characterized by the combustion of a premixed and compressed air-fuel mixture, the combustion is initiated by an external ignition source (spark plug) and propagates along the combustion chamber through a flame front until reaching the chamber walls and consuming all the air-fuel mixture.

The relevance of SI engines in the current world scenario can be measured by their share on passenger and commercial vehicle registrations. For instance, as shown in Figure 2.1, 36.4% of all new cars registered in 2022 in the EU are powered exclusively with SI engines, in addition to 22.6% of hybrid electric vehicles (HEV) that likely have an SI engine as a range extender [2]. In the USA, 92.5% of the new light-duty vehicles (cars, sport utility vehicles, and small trucks) registered in 2022 were equipped with SI engines [3]. Despite light-duty vehicles, SI engines are also used on large-bore engines for marine applications or power generation, and nonroad small engines such as those for lawnmowers, chainsaws, pumps, etc.

Due to their worldwide relevance and use, the contribution of ICE engines to greenhouse gas (GHG) emissions is noticeable and has been the focus of discussion on how their emissions can be reduced. To illustrate in numbers, only road transportation represents around 20% of the total GHG emissions in the EU [4]. To reduce GHG emissions, therefore, a series of government measures have been implemented and imposed both for onroad and nonroad applications [5–8]. In the EU, for instance, since 1992 all new-model cars are required to meet emission standards, which have been periodically updated to more and more restrictive levels [4, 9–11]. To achieve such emission standards and fuel economy goals, new technologies and engine control strategies were being developed both to control its formation during combustion and/or

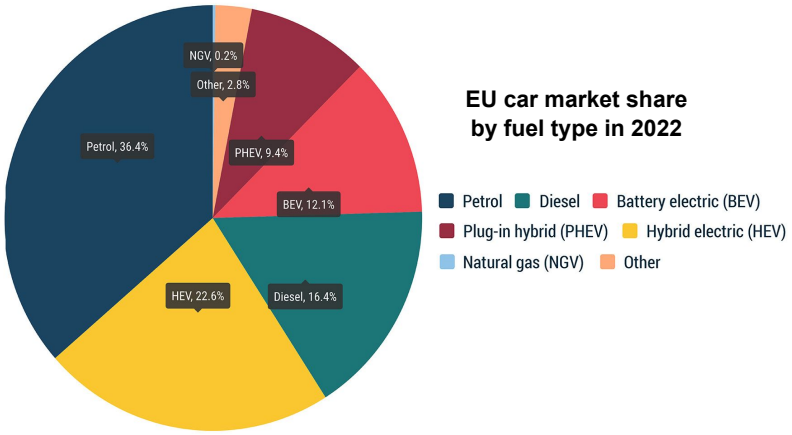

Figure 2.1: New passenger cars by fuel type in the EU in 2022. Adapted from ACEA (2023) [2].

to oxidize or reduce pollutants in the exhaust system. Figure 2.2 shows a temporal evolution of the emission standards in the USA.

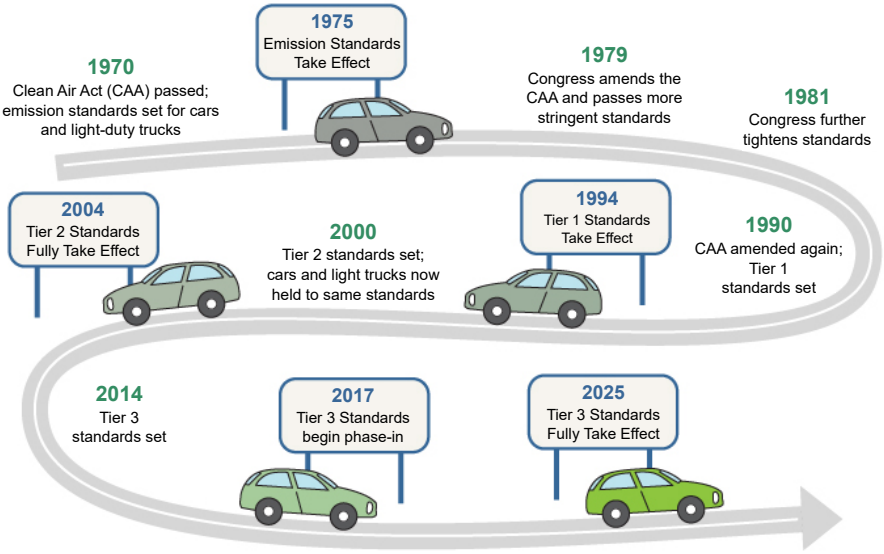

Figure 2.2: Temporal evolution of the emission standards in the United States of America. Adapted from EPA (2023) [12].

In SI engines, the prevailing exhaust aftertreatment system since the 1970s is the three-way catalyst (TWC) technology, which is able to efficiently convert

CO, HC, and NO_x emissions when the engine is operating with a stoichiometric air-fuel mixture [1]. In terms of engine-out emissions, the implementation of EGR usage strategies in gasoline engines allows for the reduction of HC and particulate emissions and fuel penalty at mid and high engine loads, where fuel enrichment strategies were applied to prevent engine knocking [13, 14]. In addition to these technologies that aim to reduce pollutants directly, other technologies such as turbocharging, direct injection, start-stop, and cylinder deactivation were being introduced to reduce fuel consumption and then meet the level of CO_2 emissions per kilometer imposed by the regulation [15].

From a thermodynamic point of view, the ideal fuel conversion efficiency of ICEs, calculated via Equation 2.1, can be increased by using higher compression ratios (r_c) and/or using lean air-fuel mixtures to increase the specific heat ratio (γ).

$$\eta_{f,ideal} = 1 - \frac{1}{{r_c}^{\gamma-1}} \tag{2.1}$$

Both modifications increase the pressure at the start of the expansion stroke, but beyond that, the former increases the expansion ratio (TDC to BDC volume ratio) and the latter increases the high temperature during the cycle, resulting in a larger area of the p-V diagram on both cases [1]. Along with these benefits, abnormal combustion (knock), and poor combustion stability are the most common drawbacks when using high compression ratios and lean mixture, respectively. The knock phenomenon is the auto-ignition of the end-gas before the flame front reaches this portion of the air-fuel mixture, and is caused by the temperature increase due to the piston displacement combined with the temperature built up as a result of the combustion development [16]. Poor combustion stability issues are related to lean operation due to its lower flame front propagation velocity and its greater propensity to misfire (no combustion event) compared to stoichiometric air-fuel mixtures [17].

To overcome such issues and promote faster and more stable combustion on SI engines, different advanced combustion and ignition concepts have been studied over the last years [18]. One promising technology to address knock-limited operating conditions and extend the lean-limit of SI engines is the pre-chamber (PC) ignition concept, where the combustion is initiated by a spark plug in a small volume chamber (so called pre-chamber) interconnected to the "main" combustion chamber via one or more orifices, through which hot gases are ejected creating a powerful ignition source with multiple ignition points. In the following sub-section, the pre-chamber ignition system will be described in detail.

2.3 Historical review of the PC ignition system

The pre-chamber ignition system consists of an extra volume chamber (known as pre-chamber, PC) connected to the combustion chamber by a set of orifices [19]. The combustion, initiated in the PC by a spark plug, builds up the PC pressure and eject its hot combustion gases to the main combustion chamber through the orifices, providing a very powerful ignition source capable of shortening the combustion duration in comparison to the conventional spark plug [20]. The main objectives are, therefore, to ignite and to reduce the cycle-to-cycle variability of premixed air-fuel mixtures under critical conditions such as diluted (with air or EGR) mixtures, and speed up the combustion under knock-limited operating conditions [21].

The first concept of a pre-chamber ignition system (Figure 2.3), presented by Harry R. Ricardo, is dated from 1922 [22]. The auxiliary combustion chamber, as it was called at the time, was fed with a rich air-fuel mixture by means of an auxiliary valve and was equipped with a spark plug to initiate the combustion. Once the combustion has taken place in this auxiliary combustion chamber, the hot gases pass through a convergent-divergent nozzle towards the main combustion chamber and ignite the leaner mixture. The author reported the capability to ignite a large volume of very lean mixture by igniting a small portion of rich mixture, as well as the wide engine operating range from idle up to 8.3 bar IMEP, the smoothness during operation, and the strategy to control engine load via AFR.

Since then, several pre-chamber configurations have been developed and the different types can be classified according to their volume, complementary fuel addition, and orifice diameter. Small pre-chambers are considered when their internal volume corresponds up to 5% of the clearance volume (V_c) [23]. Active pre-chambers incorporate an auxiliary fueling system or a dedicated fresh air-fuel mixture intake port, while passive pre-chambers rely on the air-fuel mixture coming from the main chamber through the orifices during the compression stroke [24]. In this sense, the scavenging (i.e. wiping out residual gases) process on active PCs is more effective than on passive PCs. Lastly, the orifice diameter can promote or not the quenching of the PC flame front when it reaches the orifice location. Small orifice diameter, for instance, extinguishes the flame front and increases gas velocity on the nozzle [25].

Some years after Ricardo's publication, car manufacturers developed and presented a simplified PC arrangement by removing the auxiliary fueling system but keeping the single orifice of large diameter design [26–28]. This concept, illustrated in Figure 2.4, was then known as torch cell system as a result of the flame passing through the orifice like a torch.

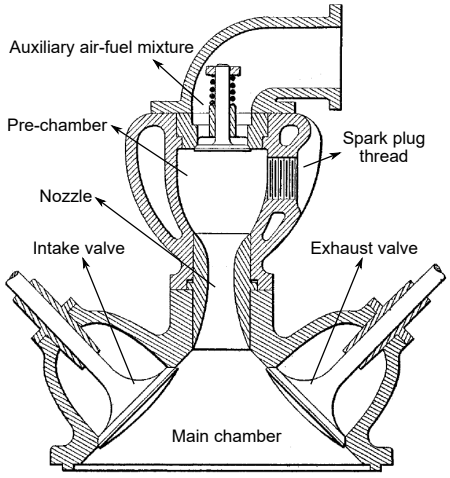

Figure 2.3: First concept of pre-chamber ignition system. Adapted from Ricardo, H. (1922) [22].

The torch cell architecture proposed by Toyota in 1976, named as Turbulence Generating Pot (TGP), is composed of a chamber of 4.6 cm^3 (9% of V_c) with an orifice diameter of 9.5 mm, and a spark plug located close to the orifice exit. The authors reported an improvement in the combustion of lean mixtures and an extension in the lean misfire limit, reducing the cycle-to-cycle variability under these situations while meeting the 1976 Japanese passenger car emission standard when equipped with a lean thermal reactor [26].

The design proposed by Ford Motor Co. comprises a PC volume of 5.7 cm^3 (5% of V_c) with an orifice diameter of 7.6 mm, and a spark plug at the top-end of the PC volume. The main outcomes when operating with this design revealed that, depending on the nozzle orientation, the Indicated Specific Fuel Consumption (ISFC) could be reduced in relation to the conventional spark ignition at the expense of a greater specific emission of HC and NO_x, or the specific emissions could be reduced without fuel consumption benefits [27].

The arrangement suggested by Volkswagen on its Lean Burn PC-Engine Concept is a PC volume between 10 and 15% of clearance volume (4.5 to 6.7 cm^3) and an orifice diameter (connecting port in this case) of 11 mm. According to the authors, this 1300 cm^3 engine concept was able to comply, at that time, with emission standards during the European driving cycle [28].

Also in the 1970s, other researchers continued investigating active torch cell architectures even with the necessity of including an additional intake valve, ducts, and a second carburetor [29–31]. One of the most successful designs

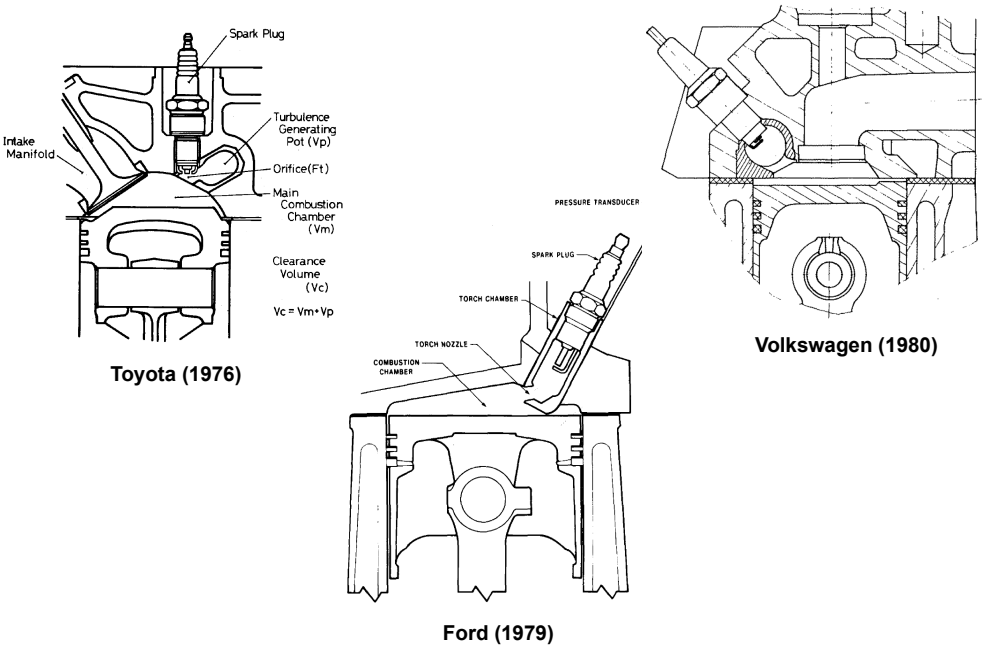

Figure 2.4: Illustration of torch cell concept proposed by Toyota, Ford, and Volkswagen [26–28].

was the one developed by Honda Research and Development Co. named as CVCC system, it could meet the 1975 emission standards from the USA and Japan on every vehicle where it was applied without any fuel penalty. Some examples of active torch cell architectures are depicted in Figure 2.5.

With advances in electronically controlled injection technology, the number of extra components and moving parts required to operate active pre-chambers has reduced to only an injector placed into the PC [32]. Some examples of such progress are the designs proposed by Porsche (SKS Engine) [33] and General Motors (EFI PC Torch Ignition) [34] in 1975, both schematically illustrated in Figure 2.6. The authors reported that the PC of the Porsche-SKS is able to ignite within the range of $\lambda = 0.4 - 1.5$, however, the greatest stability is reached when the PC is running at $\lambda = 0.6 - 0.7$. The global air-fuel equivalence ratio can be varied from $\lambda = 0.8 - 2.2$ under low load, but the maximum power is reached at $\lambda = 0.9$.

In addition to the torch ignition system characterized by large orifices, another PC design with a small volume and small orifices, known as jet ig-

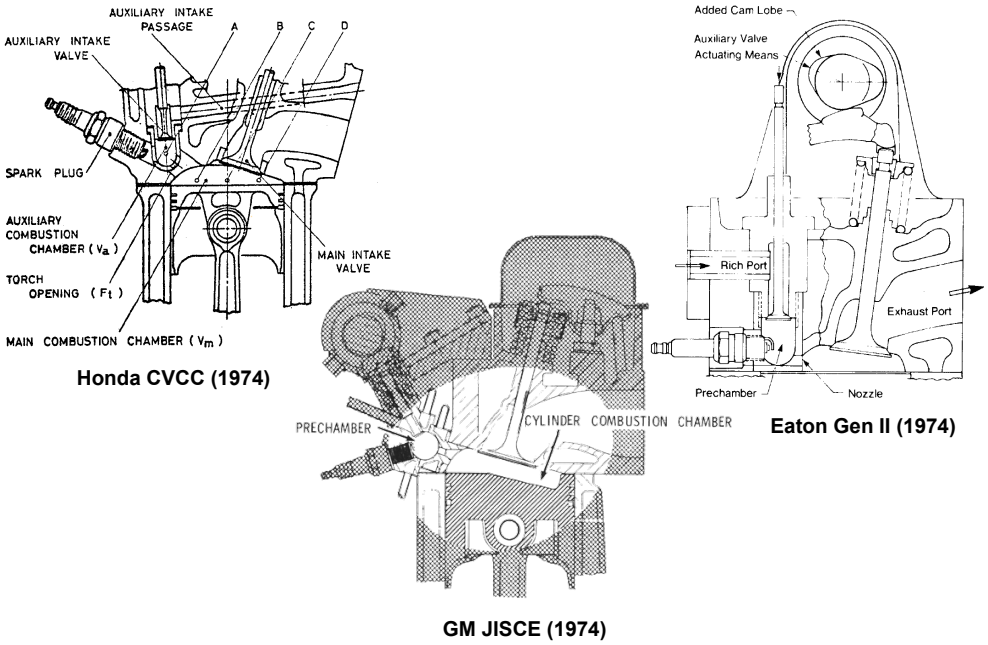

Figure 2.5: Active torch cell architectures (3-valve design) [29–31].

nition system, has been studied in parallel to the other architectures already discussed. This jet ignition concept was first introduced by Nikolai Semenov in the 50's decade and was further investigated by Gussak in the late 70's and 80's, then called LAG (Russian acronym for Avalanche Activated Combustion) [35]. The main characteristic of this concept is to increase the velocity of the ejecting gases while promoting flame quenching as the PC flame front reaches the orifices, thus spreading chemically active species from incomplete combustion into the main chamber. In the case of using multiple small orifices, there is a benefit of better spatial distribution of ignition sites. An illustration of the Avalanche Activated Combustion (LAG) process is shown in Figure 2.7.

Also during the late 70's, the so-called Pulsed Jet Combustion (PJC) was proposed by Professor Oppenheim (University of California, Berkeley) as an alternative to the conventional spark plug method to modulate the magnitude and distribution of the ignition energy source [36, 37]. The PJC generator, depicted in Figure 2.7, consists of a spark plug placed in a small volume with a dedicated fuel port and an orifice plate attached to the end of the chamber volume. The concept was then further investigated by Oppenheim and his

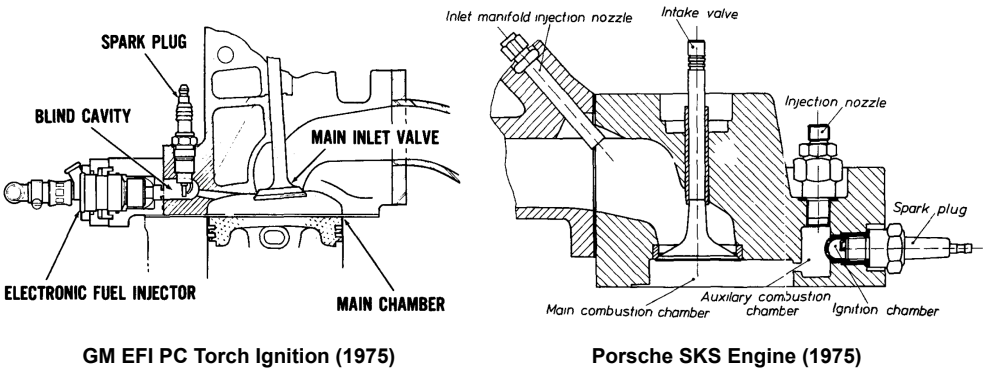

Figure 2.6: Active torch cell architectures (electronic injector design) [33, 34].

colleagues, as well as by Professor Wolanski from the Warsaw University of Technology, and the advantages of the PJC system (and its variations JPIC-Jet Plume Injection and Combustion- and PFJ-Pulsed Flame Jet) to enable lean and ultra-lean combustion were reported in several studies [38–41].

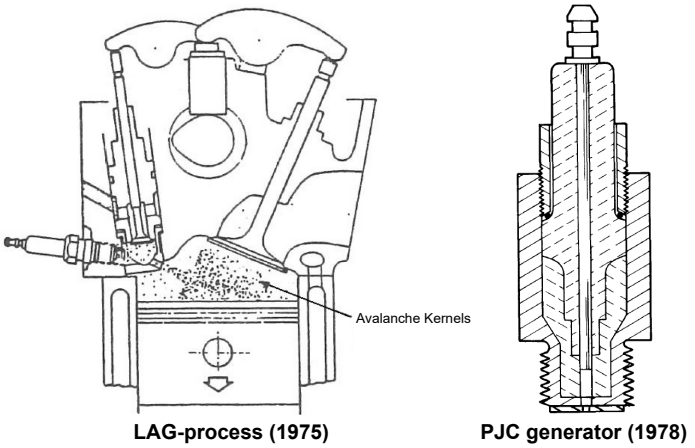

Figure 2.7: Avalanche activated combustion [42] and Pulsed Jet Combustion (PJC) generator [36].

Similarly to the PJC, but with smaller orifices (below 1 mm in diameter), researchers from the University of Orléans proposed a firing concept called APIR (French acronym for Self-ignition Triggered by Radical Injection) [43]. According to the authors, the smaller orifices are intended to promote flame

quenching at the orifice, as well as to ensure a high pressure rise to expel the radicals to the main chamber, and limit the backflow during the main chamber combustion. In addition, since the orifice diameter is reduced, their number can be increased up to about ten and improve the radical seeding distribution in the main combustion chamber. Once the intermediate combustion products from the pre-chamber are ejected into the main chamber, the compression stroke provide the thermodynamic conditions for the self-ignition of these high-content radical sites in the main chamber. The main conclusions reported are the reduction of the cycle variability and extension of lean operation, with the drawback of higher HC emissions probably due to the rich mixture used in the pre-chamber.

More recently, in 2010, MAHLE presented its jet ignition system (the so-called Turbulent Jet Ignition - TJI) installed on a modern engine design running with commercial fuels [44]. The main characteristic of this design, shown in Figure 2.8, is the use of a very small PC volume (1.3 cm^3 - 2% of V_c) associated with multiple small orifices (6 x 1.25 mm), a 10mm thread spark plug, and a fuel system with direct injection (DI) into the PC and DI/PFI into the main chamber. One of the objectives of the project was to build a TJI system to fit on a conventional spark plug thread and able to run with commercial fuels, reducing the time needed to implement this technology into the current passenger-car scenario [45, 46].

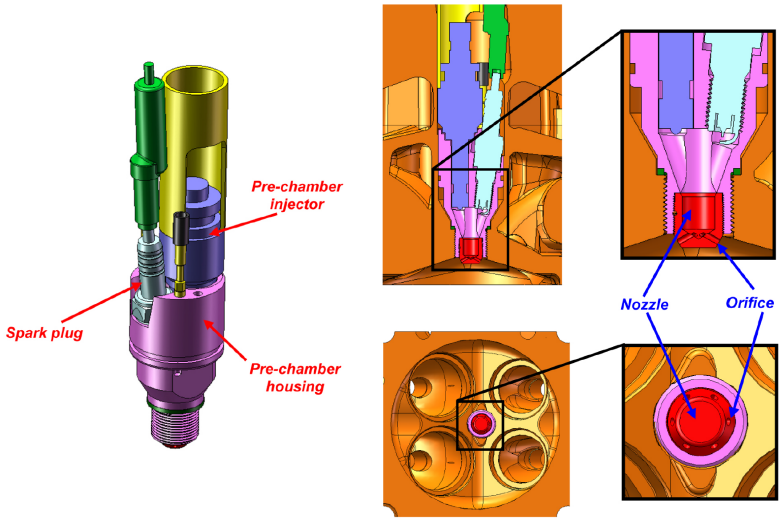

Figure 2.8: MAHLE Turbulent Jet Ignition system [44].

The MAHLE's TJI system was then experimentally tested on a single-cylinder, naturally aspirated, four-stroke engine equipped with 4 valves and a variable valve timing (VVT) system. The combustion chamber has a pent-roof shape and a central spark plug. The author's main conclusions from using MAHLE's TJI compared to the conventional spark ignition at low engine speed and low load were: (1) higher tolerance to air and EGR dilution, extending the lean limit from $\lambda = 1.4$ to 2.3 with CoV IMEPg $< 10\%$ and (2) 18% fuel consumption improvement thanks to de-throttling and improved combustion process [44]. In addition to performance parameters, the authors also experimentally tested different spark plug types, orientations, electrode gaps, and its depth into the PC to evaluate the lean and rich limits, as well as combustion parameters [45, 46].

Another example of an active jet ignition system is the narrow-throat design proposed by the Clean Combustion Research Center from KAUST [47]. Similar to the MAHLE TJI system (designed to fit on a conventional spark plug thread), the narrow-throat system was designed to fit on the central fuel injector housing of typical diesel engines. Due to this constraint, the narrow-throat PC design has a narrow and elongated channel ("neck") to connect the major volume of the PC to the orifices, then changing the smallest flow cross-section area, usually on the orifices, to this elongated channel. The main components of the narrow-throat design are depicted in Figure 2.9.

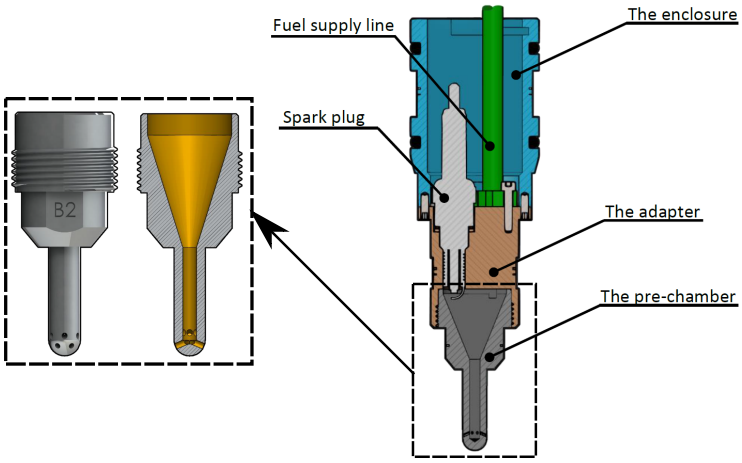

Figure 2.9: KAUST Narrow-throat pre-chamber system. Adapted from Almatraf, F. (2020) [48].

In summary, the research conducted at KAUST concluded that the throttling effect caused by the narrow-throat design promotes flame-quenching and

reduces the reactivity of the hot gases ejected to the main chamber [17].

To summarize the historical review of the PC ignition system, Table 2.1 shows a historical overview of the pre-chamber technologies along with some relevant references. The PC ignition systems are divided into four types: (1) auxiliary combustion chamber, (2) torch cell, (3) active torch cell, and (4) jet ignition. The first is characterized by a relative large volume and orifice diameter, and the examples are the first concepts of PC ignition. The second is characterized by a simplified version without extra fuel injection and lower PC volume and orifice diameter in relation to the first one, but sill relying on the flame passing through the orifice. The third type groups the PCs with extra fuel injection (either by a dedicated air-fuel mixture passage or an electronic fuel injector). In the fourth type group are the PCs with lower volume and smaller orifice diameter, usually with intentional flame quenching at the orifice.

Table 2.1: Historical overview of the pre-chamber technologies.

Type	Concept name	Ref.
Aux. Comb. Chamber	Stratified-charge engine	[22]
Torch cell	TGP - Turbulence Generating Pot	[26]
	Torch chamber	[27]
	PC-Combustion Process	[28]
Active torch cell	JISCE - Jet ignition Stratified Charge Engines	[29]
	CVCC - Compound Vortex Controlled Combustion	[30]
	SKS - Stratified-charge-chamber	[33]
	EFI Torch Ignition	[34]
Jet ignition	LAG - Avalanche Activated Combustion	[35]
	PJC - Pulsed Jet Combustion	[36–40]
	JPIC - Jet Plume Injection and Combustion	[41]
	APIR - Self-ignition Triggered by Radical Injection	[43]
	TJI - Turbulent Jet Ignition	[44–46]
	Narrow-throat	[47, 48]

2.4 Main processes on pre-chamber ignition systems

In addition to the numerous thermo-fluid processes taking place in a SI engine with conventional spark ignition, the pre-chamber ignition system also takes part in some well-defined processes during its operation. Understanding

these processes is crucial to comprehend the whole combustion process. In this sense, as pre and main chambers are, from a thermodynamic point of view, two open systems interconnected by the orifices, the different processes can be characterized by the energy exchange through mass transfer, and then, ultimately by the pressure-drop between chambers. Please refer to Figure 2.10 to better understand the several phases to be described in the following paragraphs. The left-hand side of Figure 2.10 shows the PC and MC pressure, the pressure difference between chambers (ΔP), the MC heat released rate (HRR_{MC}), and the jet discharge duration determined by optical techniques (highlighted rectangle). The right-hand side of Figure 2.10 exhibits the ΔP and the different stages for two operating conditions.

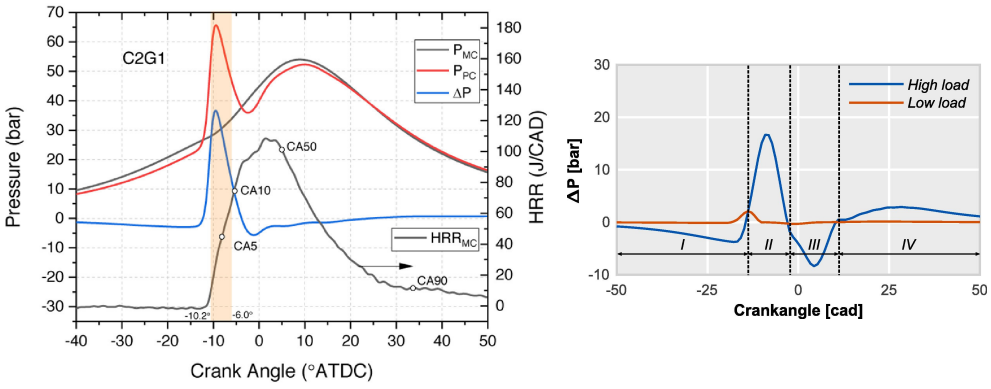

Figure 2.10: Evolution of PC and MC pressures along with pressure-drop and HRR_{MC} [49] (left) and the different stages of the pressure-drop between chambers [50] (right).

The first phase occurs during the compression stroke and is characterized by the introduction of a fresh mixture into the PC. The piston displacement starts to compress the MC mixture and build up its pressure, generating a pressure difference to the PC and then "filling" it with fresh mixture. This fresh mixture will dilute the residual gases trapped at the end of the exhaust stroke or, in the case of an active pre-chamber, dilute the additional fuel added to a near-to-stoichiometric mixture. The magnitude of the pressure-drop in the first phase is related to, besides the engine load, the PC geometrical aspects (e.g. total orifice area and volume), a topic that will be covered in 4.3.2.

Close to the end of the compression stroke, while the PC pressure is still slightly lower than MC pressure, the PC combustion is initiated by a spark

plug and the PC pressure starts to increase. The second phase starts when the PC exceeds the MC pressure and the PC components are ejected to the MC. As the PC combustion develops and the PC pressure rises, the mixture near the orifices is first ejected as a hot-unreacted fuel-air mixture [51]. Then, as the flame front reaches the orifices, the gases being ejected change to hot combustion products.

The ejection of the hot gases into the MC during the second phase then leads to the MC ignition, increasing its pressure as the PC pressure decreases by virtue of the end of PC combustion and mass transfer to MC [52]. As the MC combustion progresses, there is, once again, a reversal in the direction of mass flux between chambers, and then this is the beginning of the third phase, characterized by the back-flow of residual gases from MC combustion into the PC.

Finally, once the MC combustion has finished and the piston moves away from TDC during the expansion stroke, the MC volume expands and decreases its pressure, promoting PC emptying. In this fourth and last phase, the PC pressure is slightly higher than the MC pressure and, in the same way as in the first phase, the emptying process depends on both the operating conditions and some geometrical aspects.

2.5 Fundamental studies on pre-chambers

Collecting pre-chamber experimental data under real engine conditions may be a challenge due to the lack of physical space, making it difficult to place a pressure sensor or apply optical techniques. For this reason, to access such information, some studies are performed on dedicated experimental facilities with the drawback of reproducing the phenomenon under simplified conditions. The main differences between the conditions in a real engine and in an experimental facility can occur in several aspects and levels, such as: on the thermodynamic conditions, mixture composition (e.g. residual gas fraction), flow pattern (e.g. turbulence level and its local distribution), geometrical aspects (e.g. pre- to main chamber volume ratio, surface area to volume ratio and orifice diameter), etc. Nevertheless, experimental facilities are useful for validating and calibrating numerous models, for instance, chemical kinetic mechanisms, combustion models, etc.

As the literature reports a range of studies from the most simplified experimental facilities up to engines under representative operating conditions, where each experimental setup will assess different aspects of pre-chamber ignition systems, this section will group the review into experimental facilities,

starting with constant volume combustion chambers, then rapid compression machines, and finally optical engines. The studies reported in the literature give limited information about how the volume, orifice diameter, and number of orifices were defined in these simplified conditions, raising the question of whether the results are representative of engine-like conditions or not.

2.5.1 Constant Volume Combustion Chambers

A Constant Volume Combustion Chamber (CVCC), is an experimental facility comprising a combustion chamber with a constant volume with full optical access for line-of-sight or orthogonal optical diagnostics. Besides the optical access, the main advantages are the very precise mixture composition and well-controlled wall temperature. However, the disadvantages are the large volume, low temperature and pressure at the beginning of the combustion, and the low turbulence intensity due to the absence of the piston movement as in an engine. Therefore, its thermodynamic conditions are different from those found in engine applications, making it unfeasible to directly use this information on such applications. Some designs of CVCCs are schematically shown in Figure 2.11.

On the framework of his doctoral studies, Biswas and other researchers from Purdue's School of Aeronautics and Astronautics have investigated the physics of turbulent jet ignition on a CVCC using optical techniques (High-speed Schlieren, OH* chemiluminescence, schlieren PIV, and IR imaging) and numerical simulation [25]. A proportionally small volume pre-chamber ($100\,\mathrm{cm}^3$ - 1% of V_{CVCC}) was attached to the CVCC ($10\,000\,\mathrm{cm}^3$), and an orifice plate was used to divide both chambers. The use of a $25\mu m$ thick aluminum diaphragm allowed the use of different equivalence ratios on each chamber.

First, the researchers investigated the effect of several parameters on the ignition mechanism of CH_4 and H_2 using single orifice PC, such as orifice diameter (1.5, 2.5, 3, and 4.5 mm), MC equivalence ratio (0.45, 0.5, 0.6, 0.7, 0.8, 0.9, and 1.0), initial temperature (300 and 500 K) and pressure (0.1, 0.3, 0.4, 0.5 MPa), as well as spark position in the pre-chamber (bottom, middle, 1/3 from top, and top) [53]. Using simultaneous Schlieren and OH* chemiluminescence, the authors categorized two ignition mechanisms (1) flame ignition and (2) jet ignition. On the one hand, flame ignition is characterized by no flame quenching as the PC flame front passes through the orifices, and then the jet contains abundant flame kernels and intermediate species that speed up the main chamber ignition. On the other hand, the jet ignition is composed of hot combustion products only, with very little or no OH radicals, due to

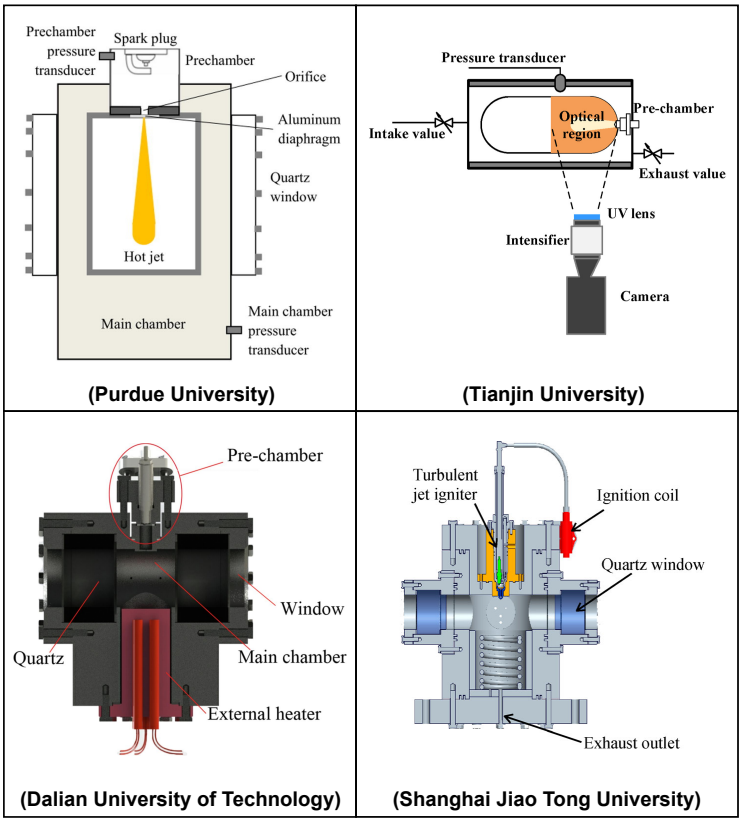

Figure 2.11: Schematic view of different designs of CVCCs applied to pre-chamber ignition studies. Adapted from [53–56].

the orifice quenching. The authors also categorized the different experimental tests in a Borghi-Peters diagram according to whether they ignited or not.

Complementing the studies carried out with a single orifice plate, Biswas et al. [57] also investigated the H_2 ignition process using a multi-orifice plate with straight and angled orifices, as well as different spark plug positions in the PC. In terms of lean flammability limit (mini- mum fuel condition that has an ignition probability of 100%), no improvement was observed with multiple jets in relation to a single jet (remaining at Φ=0.3 in the MC). However, as the mixture condition approaches the lean flammability limit, the probability of ignition increases substantially with multiple jets (but still with an ignition probability less than 100%). The spark plug location affects the main chamber ignition source, changing from the central jet (straight) for near-to-orifice

spark plug location, to side jets (either straight or angled) for far-to-orifice spark plug location.

In another study, Biswas & Qiao [58] assessed the lean limit, ignition mechanism, MC ignition delay, and combustion stability of H_2/air mixture for different types of orifice design: straight, convergent, and convergent-divergent. The key finding was the lean limit extension and lower ignition delay by using a convergent-divergent nozzle rather than a straight nozzle due to their better mixing with cold unburned H_2/air mixture. Moreover, the higher static temperature of the supersonic jet caused by the shock increases its ignition probability.

Moreover, Biswas [59] studied the ignition mechanism of a hot turbulent jet being impinged on six different impinging plates in the main combustion chamber. The results pointed out two ignition mechanisms: (1) the ignition taking place near the impingement point, and (2) the ignition where it typically occurs on turbulent jet ignition, on the "outside shell" of the jet. Finally, Biswas et al. [60] investigated the flame propagation on straight and convergent-divergent microchannels for different methane-air mixtures. The experimental tests were carried out with microchannels from 1 to 10 mm in diameter and different throat diameters and presented three propagation patterns: survival, partial extinction/re-ignition, and extinction, where extinction was the most frequently seen pattern in convergent-divergent microchannels due to the higher heat losses and flame stretch.

Li et al. [56] and Ju et al. [61] from Shanghai Jiao Tong University also studied the pre-chamber ignition system in a CVCC due to the impossibility of reproducing the diameter of a large-bore engine in a Rapid Compression Machine. In this sense, the authors used a CVCC with a diameter of 300 mm to assess the effect of the air-methane equivalence ratio (0.8, 1.0, and 1.2) and initial pressure (0.6, 1.0, and 1.5 MPa) with a six-orifice passive pre-chamber (6 x 2.9 mm) and a constant initial temperature of 300 K. The main results reported by the authors were the reduction of flame propagation rate as a result of increasing mixture dilution and increasing initial pressure, and the combustion time using the pre-chamber was up to 60% lower than the traditional spark ignition system.

Zhou et al. [62] and Liu et al. [54] from the State Key Laboratory of Engines of Tianjin University experimentally investigated the ignition characteristics of methane and hydrogen using a single orifice pre-chamber in a CVCC employing Schlieren and OH* chemiluminescence imaging. In both studies, a cylindrical-shaped CVCC with a diameter of 100 mm and volume of 2320 cm^3 was used in conjunction with a pre-chamber with a volume of

3.6 cm^3 (0.16% of V_{CVCC}) and an injector to operate both in passive or active modes. First, the lean flammability limit of the air-methane mixture was explored with different ignition methods: conventional spark plug, unfueled PC, CH_4 fueled PC, and H_2 fueled PC. The initial thermodynamic conditions were 3 bar and 363 K. The SI lean limit has not been extended beyond $\lambda = 1.9$ on the unfueled PC case, but it was extended to $\lambda = 2.2$ on the CH_4 fueled PC, and to $\lambda = 5.2$ on the H_2 fueled PC case. Moreover, the main chamber combustion development, the jet tip velocity, and the flame area were analyzed for the different ignition methods and PC orifice diameters (4 and 6 mm). In a second work, Liu et al. [54] studied smaller orifice diameter (2 and 3 mm) with the same passive and active PC using methane and hydrogen.

Tian et al. [55] performed a parametric study with different orifice diameters (1, 2, and 3 mm), pre-chamber volumes (4, 6, and 8 cm^3), initial pressures (0.8, 1.0, 1.4 and 1.6 MPa), initial temperatures (300, 350, 400, and 500 K), and pre- and main chamber equivalence ratio (Φ=1.0 and 0.8). The main findings reported were the different ignition positions depending on the orifice diameter: a small orifice diameter led to orifice flame quenching and ignition near the orifice, whereas a large orifice diameter did not lead to quenching and the ignition occurred far from the orifice. The PC volume did not show a clear trend regarding the delay between spark timing and jet ejection for all cases tested, being affected mainly by the initial temperature. Decreasing the fuel/air equivalence ratio resulted in a slower combustion rate and poor main chamber ignition. However, the PC fueling could boost ignition energy and ignite MC mixture with Φ=0.8. Using the same experimental facility and employing a similar testing methodology, Wei et al. [63] assessed the combustion characteristics of different orifice diameters and lean/ultra-lean air-methanol mixtures. The key conclusions were that (1) the pre-chamber ignition system speed-up combustion in comparison with the conventional spark ignition, (2) the smaller orifice diameter (1 mm) presented jet ignition failure at Φ=0.6, and (3) the lean-limit was achieved at Φ=0.4 with the 2 mm orifice diameter.

Vera-Tudela et al. [64], from ETH Zurich, designed a novel CVCC with full optical access to the main and pre- chambers (the first study reported in the literature to visualize the PC combustion). Moreover, the CVCC had a purge system in the PC to emulate the turbulence generated during the PC filling (occurring during the compression stroke in an ICE) and a customized dwell time between the end of the purging to the spark signal to set the turbulence level at the PC. A cross-sectional view and some schlieren images are shown in Figure 2.12. The PC volume was 3.6 cm^3 (1.9% of V_{CVCC}) and the orifice diameters tested were: 2.0, 2.5, and 4 mm. The fuel-air equivalence ratio (same in both chambers) varied from 0.5 to 1.5. The major conclusions were

that the orifice diameter has little effect on the PC combustion development, being more relevant on the flame quenching and the subsequent main chamber ignition and combustion (premixed-like HRR for the 2 mm case and diffusive-like HRR for the 4 mm case). Furthermore, the emulated PC turbulence showed a significant impact on the PC combustion development, shortening the combustion duration as the turbulence increased and then increasing the PC peak pressure. Finally, the fuel-air equivalence ratio basically affected the PC combustion velocity and main chamber ignition delay, not changing PC combustion development or the MC ignition mechanism.

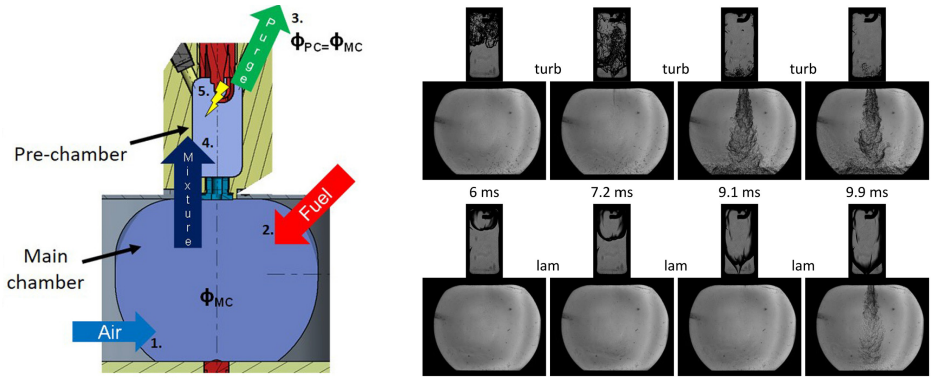

Figure 2.12: Cross-sectional view of ETH-Zurich CVCC (left) and Schlieren image sequence for two different PC turbulence cases (right). Adapted from [64].

In summary, some important ignition mechanisms could be identified and characterized using CVCCs in part of the engine thermodynamic conditions (low pressure and temperature). However, high-pressure/high-temperature thermodynamic conditions and other aspects such as the turbulence in the PC and MC cannot be fully reproduced in this experimental facility. To take it a step further in engine-like conditions, the use of a Rapid Compression Machine can address the turbulence topic and also increase the pressure and temperature conditions.

2.5.2 Rapid Compression Machines

A Rapid Compression Machine (RCM) is an experimental facility that reproduces engine-like thermodynamic conditions in a single piston stroke. Pneumatic and hydraulic-driven pistons push the experimental piston similarly to a crank-connecting rod system found in reciprocating engines. Typically, two variants can be found: (1) those where the piston reproduces the

compression stroke and remains static at TDC during combustion, and (2) those where the piston reproduces the compression stroke and the beginning of the expansion stroke. The latter is usually known as Rapid Compression-Expansion Machine (RCEM).

The main benefit of the RCMs and RCEMs is the possibility to vary the compression ratio and the initial conditions (equivalent to the conditions at IVC in ICEs) without relying on mechanical modifications and other subsystems such as turbocharger, air intercooler, EGR, cooling system, etc., making it easier to study each parameter separately. Compared to the CVCCs, the RCMs and RCEMs can reach higher pressure and temperature at the end of the compression, as well as reproduce the turbulence generated by the piston movement both in the MC and PC (in the case of PC ignition system studies).

Some research groups around the world have been investigating the prechamber ignition system on RCMs and RCEMs with different architectures. Michigan State University (USA) [65–79], Tsinghua University (China) [21, 80, 81], and Poznan University of Technology (Poland) [82] are some examples of universities that published pre-chamber-related studies using RCMs. Studies on RCEMs that have been published include those from ETH Zurich (Switzerland) [83–87], CMT-Universitat Politècnica de València (Spain) [52, 88–90], Waseda University (Japan) [91], and Oita University (Japan) [92]. Different designs of RCMs and RCEMs are shown in Figure 2.13.

Researchers from Michigan State University mounted the prechamber ignition system orthogonally to the piston top and used a quartz optical window to have a one-sided view of the jet from the top of the combustion chamber. This configuration, illustrated in Figure 2.14, allowed the maximum free-jet length as possible of the RCM used, but relies on the luminosity generated from the high-temperature reactions and combustion which makes it impossible to perform techniques with backlighting such as single-pass Schlieren. Gentz et al. [65, 66] studied the effect of the orifice diameter on single-orifice and multi-orifices PCs by means of natural luminosity, OH* and CH* radicals visualization, pressure-based analysis and numerical simulations. The passive PC has a volume of 1 cm^3 (2% of V_c) and the orifice diameters tested were: 1.0, 1.5, 2.0, and 2.5 mm for the single orifice PCs, and varied from 1.25 to 2.165 mm to the PCs with 2, 3 and 6 orifices. The 0-10% and 10-90% burn durations, the lean limit, and the initial penetration velocity were also assessed for propane-air mixtures. The key findings were the faster jet penetration as the orifice diameter is reduced, and the faster 0-10% burn duration as the higher the flame area is at 1.3 ms after the spark (i.e. inverse correlation between 0-10% burn duration and the ratio between flame area and total

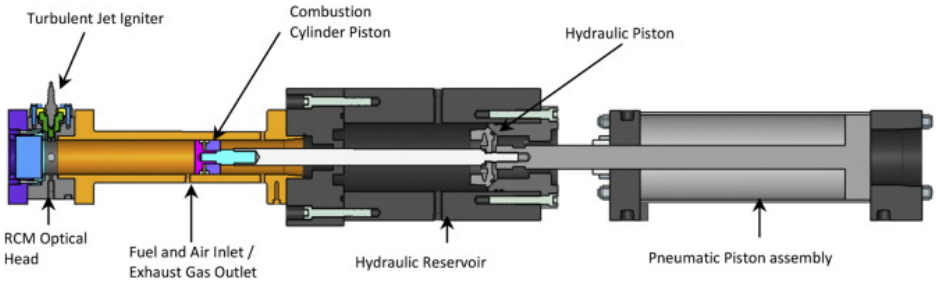

RCM - Michigan State University

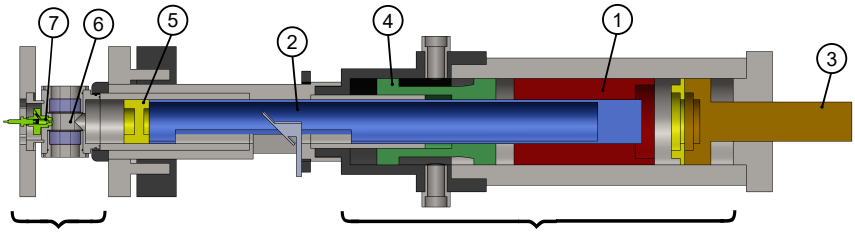

1	Pushing piston	4	Air piston	7	Pre-chamber
2	Driver piston	5	Experimental piston		
3	Displacement piston	6	Main chamber		

RCEM - CMT / Universitat Politècnica de València

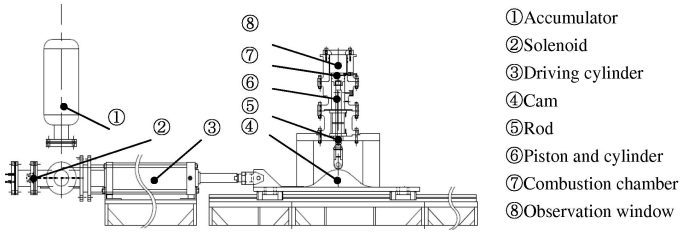

RCEM - Oita University

Figure 2.13: Schematic view of different designs of RCMs and RCEMs applied to pre-chamber ignition studies. Adapted from [66, 92].

combustion chamber area). Finally, a reduction in the initial jet penetration velocity as the orifice diameter increased was noticed, both for stoichiometric and lean cases.

Afterwards, purely experimental studies on RCM's Michigan State University evaluated the effect of the number of orifices, their diameter, and their

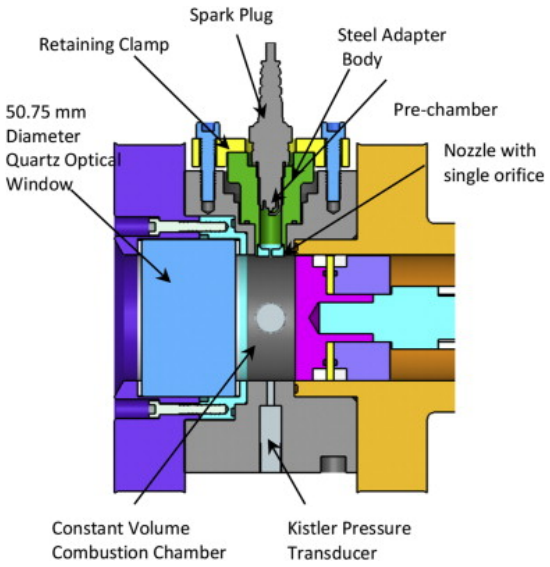

Figure 2.14: RCM configuration for pre-chamber ignition studies used at Michigan State University. Source: [66].

arrangement (straight, converging, or diverging) in active pre-chambers fueled with iso-octane [74] and methane [76, 79]. The results showed that the PC fuelling strongly affects the jet penetration velocity and the MC 0-10% burn duration.

Along with the experimental studies, Computational Fluid Dynamics (CFD) models were developed and validated for passive and active PCs using different chemistry-based-combustion (detailed - SAGE - and simplified mechanisms) and turbulence (RANS and LES) models for propane [65, 67], methane [69, 71, 77, 93], and iso-octane [78] air-fuel premixed mixtures. Gholamisheeri et al. [75], for instance, compared four detailed and one reduced methane chemical kinetic mechanisms against RCM experimental data. The authors conclude that despite having a reasonably good agreement in terms of burn rate, peak pressure, and ignition delay prediction, none of the mechanisms are in complete agreement with the experimental data. Exploratory CFD studies were also conducted to investigate different positions of the ignition source [68], and different orifice diameters [73].

Researchers from Tsinghua University also investigated the prechamber ignition system in an RCM using optical techniques and numerical CFD studies. Li et al. [80, 81] assessed the effects of different diameter orifices and synthetic EGR (CO_2/N_2) rates in a single orifice passive PC operating with

methane as a fuel. Similar to what was previously proposed by Biswas et al. [53], Li et al. also classified the jet ignition process in two ignition patterns: pre-chamber jet flame ignition (PJFI) when the jet has intense and uninterrupted OH radical emission, and pre-chamber jet auto-ignition (PJAI) when the jet has little or no OH radical emission. The authors observed that the ratio of the total effective cross-sectional area of orifices to pre-chamber volume (A_t/V_{PC}) was the most essential parameter to actually influence the ignition modes in the main chamber, regardless of the number of orifices, their diameter, and pre-chamber volume. Finally, Liu et al. [21] investigated knock characteristics and end-gas auto-ignition behaviors of the stoichiometric iso-octane-air mixture using a PC ignition system at different initial pressures and temperatures. When compared to the conventional spark ignition, the PC ignition reduced the combustion duration and knock intensity under the same initial conditions.

With a different RCM geometry from those previously mentioned, Poznan University of Technology researchers studied different architectures of passive and active multi-orifice PCs [82]. A novel PC geometry (so-called 3-stage) was compared to the "classical" passive and active configuration with lean air-methane mixtures ($\lambda = 1.5$) using natural flame luminosity and indicated pressure data. The authors concluded that the 3-stage and the "classical" active PC presented a shorter delay between the spark signal and the MC ignition and a higher flame development rate in comparison to the passive PC and the conventional spark ignition system.

Now addressing to RCEMs, the researchers from ETH Zurich (Swiss Federal Institute of Technology) designed a pre-chamber setup configuration similar to those found in ICEs (where a multi-orifice PC is placed centralized at the cylinder head and the jets are oriented towards the cylinder walls) [84]. Two optical windows at the liner provide side-view optical access to the region near the PC orifices, and one optical window at the piston provides a bottom view of the main combustion chamber (excluding the near-wall region).

First, Schlatter et al. [83] compared the behavior of ignition, inflammation, and combustion of methane-air mixtures using a pre-chamber ignition system and a pilot diesel injection. Then, Xu et al. [84] employed a RANS-CFD calculation along with a G-equation combustion model and other two sub-models (spark ignition and 1D flame-wall interaction models) to investigate passive PCs with two different inner volumes and five different operating conditions with methane as fuel. Simultaneous Schlieren and OH* chemiluminescence imaging combined with the main chamber pressure data were used to validate the computational models. The authors reported a good agreement

between the numerical models and experimental data in terms of main chamber pressure and RoHR, jet exit timing, and projected flame area. Moreover, the relevance of the initial hot jet speed and the peak of the pressure difference between chambers for the 0-5% MFB was emphasized.

In addition to the previous studies focused on the main chamber ignition, CFD studies were used to study the PC combustion development, turbulence intensity, and fuel distribution inside the PC for different orifice orientations and PC volumes [85–87]. The authors also concluded that a RANS model was able to reproduce the ensemble-averaged LES flow patterns quite effectively, and both qualitatively reproduce the OH* chemiluminescence experimentally measured in the main chamber.

Using an RCEM as well, researchers from CMT-Universitat Politècnica de València have assessed different multi-orifices active PCs [52, 88, 89] and single-orifice passive PCs [90] using two different RCEM optical configurations. First, Desantes et. al [88] explored under ultra-lean (Φ=0.3 - 0.8) isoctane-air mixtures with an active PC with a volume of 2.94 cm^3 (4.5% of V_c) and six 1.5 mm diameter orifices. The authors reported improvement in the combustion stability and reduction in the combustion duration in relation to the conventional spark ignition system, as well as the presence of OH* radicals in the jet coming out of the PC. Then, Macián et al. [52] analyzed the combustion process within the PC using a zero-dimensional turbulence model, 3D CFD calculations, a heat-released analysis, and OH* chemiluminescence imaging in the main combustion chamber. The authors validated the PC mean expansion speed (combination of the turbulent flame speed and gas expansion due to combustion) with the delay between spark and OH* intensity near the orifice exit and, based on this approximation, they found that the flame speed is stable if the PC equivalence ratio is preserved, and confirmed a thickened wrinkled flames regime in the PC combustion with a Damköhler number of around 40 and a flame speed ratio up to 25. Finally, using an active PC, Novella et al. [89] assessed the effect of straight (same orifice axes for opposite orifices) and tilted (opposite orifices with displaced orifice axes) nozzle orientations, as well as different numbers and diameters of orifices in the tilted orientation. Straight nozzles presented reasonably good combustion efficiency up to Φ=0.5, but as the mixture becomes leaner, the swirling flow generated by the jets with tilted nozzle orientation improved the main chamber flame propagation in the jet adjacent region. Regarding the number of orifices, the authors stated that, on the one hand, with few holes the main chamber combustion is impaired due to the low spatial distribution, causing a low flame propagation between jets especially at high dilution rates. On the other hand, if the number of orifices is increased, the momentum of

each jet is reduced and the jet penetration is negatively affected, thus reducing the main chamber propagation velocity.

Unlike the two-opposed piston movement design of the RCEM located at CMT and ETH, Oita University [92] and Waseda University [91] employed a different type of RCEM architecture based on a cam-follower movement. Tanoue et al. [92] first compared the combustion characteristics with two spark plug positions and then compared two passive PCs with the same inner volume and total nozzle area but with different numbers of orifices and diameters. The spark plug far from the orifice led to unburned and burned jet compositions, causing a sharp heat release rate, whereas the spark plug near the orifice led to practically only burned jet gases being ejected and produced a gradual rise in the heat released. Tanamura et al. [91] employed 3D CFD simulations with a chemical kinetic model which includes OH* chemiluminescence reaction kinetics to study the combustion characteristics of a passive pre-chamber. The numerical models were validated using OH* radical chemiluminescence imaging from the main chamber combustion.

In summary, good progress has been made by using RCMs and RCEMs coupled with numerical CFD studies in more relevant thermodynamic conditions (high pressure and temperature) and under engine-like charge motion patterns (induced by the piston movement). Nevertheless, the single combustion cycle precludes analysis of factors such as cycle-to-cycle variability and the degree of stratification of residual gases between PC and MC. The use of optical engines can further explore these factors under engine-like conditions while still being supported by optical techniques.

2.5.3 Optical engines

Optical engines are the experimental facilities that most represent engine-like conditions while allowing visualization of the phenomena taking place in the combustion chamber both using an optical piston (for a bottom-view) or a transparent liner (for a side-view) [94]. Usually based on a single-cylinder engine, the Bowditch design uses a hollow cylinder extensor to connect the metallic piston to the optical piston, generating a solidary movement between them and allowing to accommodate a 45º mirror below the optical piston [95]. Both small [96] and medium-to-large bore [51] optical engines have been used to validate and refine ICEs numerical models. The main advantage of optical engines in relation to the previously mentioned experimental facilities is the possibility to run consecutive cycles (then reproducing the heterogeneity between PC and MC in terms of residual gases) and conduct cycle-to-cycle assessments (combustion variability, jet penetration variability, etc.).

With regard to pre-chamber ignition studies, optical engines have been used to evaluate different engine-like pre-chamber architectures, focusing on the jet characteristics and extracting fundamental understanding about the pre-chamber combustion by means of broadband [97] and filtered OH* chemiluminescence [98], infrared imaging [51], and planar laser-induced fluorescence imaging (PLIF) [99]. Some examples of optical engines employed for pre-chamber ignition studies are shown in Figure 2.15.

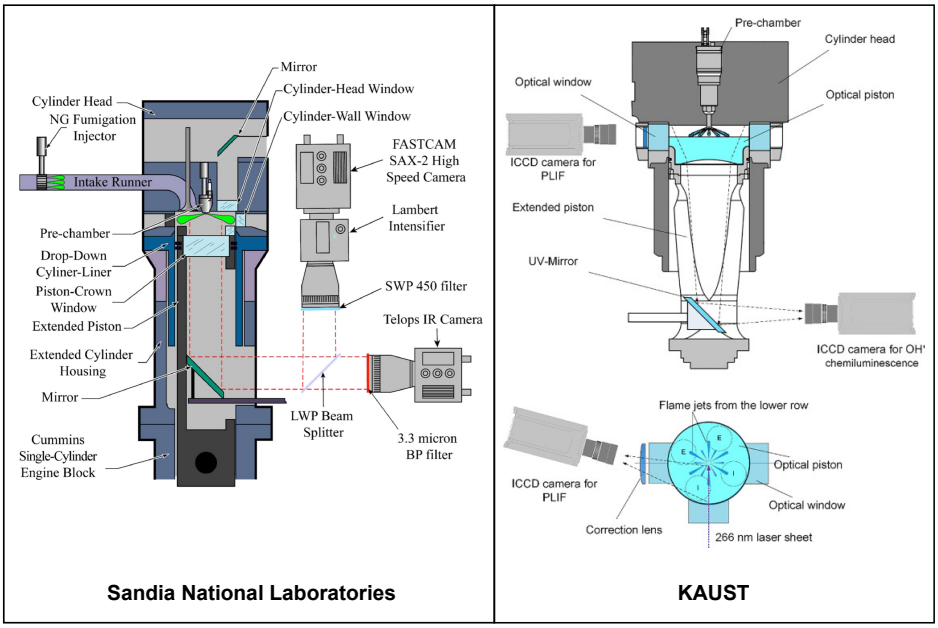

Figure 2.15: Optical engines employed for pre-chamber ignition studies. Adapted from: [51, 100].

Attard et al.[101] assessed the spark ignition natural gas combustion at different engine speeds and loads with stoichiometric as well as lean mixtures, and compared its results with an active pre-chamber ignition system (MAHLE TJI). The primary conclusions presented by the authors regarding PC combustion were the reduced jet-to-jet penetration variability, and the higher luminosity intensity of the pre-chamber combustion in comparison to the conventional spark ignition, even operating with a leaner mixture (λ=1.8 and 1.5, respectively). Also using a MAHLE TJI PC, Bureshaid et al. [102] investigated the effect of the quantity of auxiliary PC fuel and its injection timing both for gasoline and ethanol, comparing its results with no auxiliary PC fuelling. The authors concluded that by increasing the auxiliary PC fuel quantity, the pressure-drop to the main chamber increases and produces faster and

hotter jets capable of penetrating deeper into the main chamber and enlarging the ignition spots. Ethanol-fueled PC produced jets with greater momentum than gasoline as a result of its faster combustion. Within the range of 30 to 70 CAD-BTDC, the injection timing showed little influence on the combustion process.

Wellander et al. [99] investigated, for the first time, the ignition process of the main chamber by the pre-chamber jets in a Wärtsilä large-bore natural gas optical engine using PLIF. The PC was fueled with natural gas doped with acetone (fluorescent tracer for the PLIF), and no further details are given about the PC geometrical characteristics. The authors stated that the mixing between the rich-mixture inside the PC and the lean-mixture coming from the MC during compression stroke is low, and supported this assumption by no PLIF intensity during the initial phase of jet ejection (unburnt air-fuel mixture coming out). Moreover, although the PLIF imaging was not time-resolved, the authors concluded that the PC RoHR affects the MC combustion despite not detecting any change in the jet velocity.

Da Costa et al [103] first presented a methodology to determine the pre-chamber geometrical aspects (volume and orifice diameter) and then experimentally tested a prototype single-orifice passive pre-chamber in an optical engine equipped with a transparent liner. The experimental campaign, conducted with hydrous ethanol, showed the PC capability to shorten the combustion duration and improve the combustion stability. The optical images corroborate the indicated data, presenting a blue flame torch that impinges at the piston top and rapidly consumes the main combustion chamber mixture.

Researchers from the Institute of Sciences and Technologies for Sustainable Energy and Mobility (STEMS) carried out several studies regarding the pre-chamber ignition concept, using both active [104] and passive [19] configurations, and two different multi-orifice designs: large PC volume (9.4% of V_c) [105] and small PC volume (2.4% of V_c) [97]. Both gaseous (methane) [96] and liquid (gasoline) [106] fuels were used in the main chamber in PFI or DI modes, even if only methane was used in the active PC studies. In summary, the authors reported a comparison between PC and conventional spark ignition in terms of equivalent flame radius and flame speed, as well as in-cylinder pressure, RoHR, and exhaust emissions for stoichiometric and lean air-fuel mixtures, and different engine speeds. The orifice arrangement chosen to carry out the comparison was 4 holes with 1 mm diameter each, evenly distributed in the combustion chamber [19, 104–106]. The main conclusions drawn by the authors regarding the pre-chamber ignition system are the faster flame speed, shorter combustion duration, steeper RoHR, and the

lower cycle-to-cycle variability both for stoichiometric and lean conditions, regardless of the engine speed and fuel used in the main chamber. The 2D chemiluminescence images show a very fast combustion process when the jet emerges from the PC and moves towards the cylinder liner, presenting a slight reduction during mixture enleanment, unlike the conventional spark ignition which drastically reduces the combustion velocity. The optical engine data was also used to validate 3D CFD numerical models to further investigate the PC combustion process and extract valuable information about the internal PC flow field, mass exchange between chambers, evolution of chemical species, and pollutant formation [96, 107, 108].

Using an optical engine based on a heavy-duty commercial engine, researchers from KAUST and Saudi Aramco have investigated a new PC architecture using optical techniques. The optical engine includes a bottom view through an optical piston and a side view provided by three optical windows, allowing chemiluminescence and PLIF to be carried out simultaneously [109].

First, Tang et al. [98] examined the effect of the PC lambda (λ=0.99, 1.15 and 1.51) on the jet characteristics by fueling only the PC with methane and seeding the MC with acetone to create a "negative" image of the jet penetration. The main findings reported in this study were that the jet reaction zone (OH* chemiluminescence intensity) is located near the orifice exit, while the jet captured by the PLIF imaging impinges the piston wall and spreads to the cylinder wall. Moreover, the OH* intensity and the overall jet penetration increase as the PC mixture is enriched.

Then, in a similar study, Sampath et al. [109] assessed the PC jet characteristics and MC combustion by varying the PC lambda and fueling the MC with methane doped with acetone. Simultaneous OH* and "negative" PLIF images presented a good agreement due to the acetone combustion in the MC. The variation on the PC fueling (λ=0.86 and 0.97) did not present a substantial effect on the PC and MC behavior since the MC lambda was fixed at λ=2.

After that, in a complementary study using the same two-row PC orifice arrangement (shown in Figure 2.16) and optical setup for simultaneous OH* and "negative" PLIF images, Tang et al. [100] explored the effect of the MC fueling of an active PC operating under global lean air-fuel mixture (λ=1.8 and 2.3) and even without fueling to the MC. The authors reported a second "reactive" jet ejection both for the unfueled and ultra-lean (λ=2.3) cases, possibly caused by the pressure fluctuation after PC combustion and the MC pressure reduction due to the volume expansion during the expansion stroke. Moreover, the ultra-lean case presented two unburned regions: one close to

the PC and the other between the pre-chamber jets. Finally, the authors reported that the jet ejection is greatly affected by the orifice arrangement since the lower-row orifices produced jets able to penetrate until the near-wall region and the upper-row orifices did not produce any OH* chemiluminescence intensity. The optical experiments were used to validate a 3D-CFD model, and the results were presented in a different publication [110].

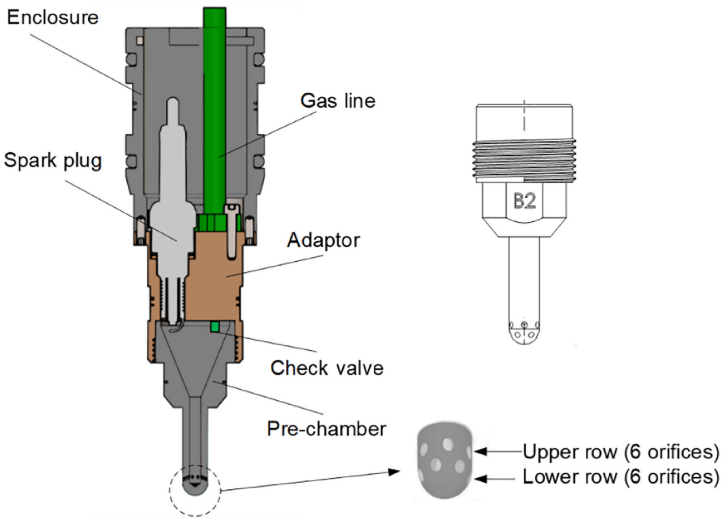

Figure 2.16: Two-row orifice pre-chamber arrangement proposed by the authors. Adapted from: [100].

Echeverri Marquez et al. [111] investigated the effect of the combustion chamber geometry on the pre-chamber jet characteristics and combustion development with a flat and a bowl-in piston. According to the authors, both pistons presented similar thermodynamic conditions during the jet ejection process, however, the shorter distance to the piston wall of the flat piston led to a combustion deceleration due to wall impingement and thus longer combustion duration. The bowl-in piston presented a lower chemiluminescence intensity on the squish area, possibly causing incomplete combustion and forming more HC emissions.

Using a dual formaldehyde PLIF imaging with a time interval of 10 µs, Tang et al. [49] could track the jet boundary and estimate a 2D jet/flame velocity for the first time. The methodology was used to characterize the jet ejection of different narrow-throat pre-chamber geometries, including different PC volumes, orifice diameters, and throat diameters. The authors concluded that the PC volume has little effect on the PC combustion, but the throat

diameter plays an important role in the PC pressure build-up and then in the jet penetration. A smaller throat diameter leads to a higher peak of ΔP, and then higher jet penetration velocity, and faster combustion, promoting high engine efficiency and the lean limit extension.

Lastly, Echeverri Marquez et al. [112] designed and experimentally tested an optically accessible pre-chamber under engine-like conditions. Copying the internal geometry of a metallic PC, the optical PC body is made of quartz and its tip (where the orifices are located) is made of stainless steel. Due to the constraints in terms of packaging into the metallic cylinder head, the optical PC was assembled where the lateral optical window was (without any impairment in terms of PC filling and jet ejection), and then synchronized with MC optical images of the metallic version on its original position (cylinder head). The PC combustion imaging confirmed the flame development process from the region close to the spark plug (upper part) towards the orifices (bottom part), and its faster velocity when passing through the throat area in comparison to the PC body. The OH* chemiluminescence intensity was proportional to the HRR at the beginning of the combustion process, being subsequently impaired by the CO_2* chemiluminescence.

Using the Sandia-Cummins single-cylinder heavy-duty optical engine, Rajasegar et al. [51] assessed the pre-chamber ignition system using simultaneous infrared (jet penetration extension) and filtered OH* chemiluminescence or broadband chemiluminescence (spatial and temporal combustion tracking) imaging. The experiments proposed by the authors first focused on the jet characteristics by deactivating the MC fuel injection, and then on the effect of the MC air-fuel equivalence ratio on the combustion development. The PC-only fueling experiments showed first the hot unreacting jets (IR), then an asymmetrical reacting jet in the near orifice region (OH* chemiluminescence) while the unreact jet penetrates towards the cylinder wall. The MC fuelling parametric study revealed that the MC equivalence ratio does not influence the PC combustion as long as the PC equivalence ratio is maintained, as the ΔP between chambers and the jet ejection timing was virtually identical for all cases.

2.6 Summary

Throughout this chapter, the relevance of SI engines in the current world scenario, as well as the possible paths for engine efficiency improvement were highlighted, and a detailed review of the pre-chamber ignition system was carried out. As described in this chapter, different pre-chamber aspects were

investigated both in experimental and numerical studies, employing different strategies to further understand the PC combustion, the jet characteristics, MC ignition by the jet, and MC combustion development.

It was noticed that the different studies reported aimed to investigate the effect of the PC volume, diameter and number of orifices, nozzle orientation, and inner PC geometry. Except for numerical studies, capable of predicting the internal flow pattern, the majority of the experimental studies focused on the effect of such parameters during and after jet ejection (i.e. all that takes place after the PC combustion). Despite the numerous studies varying the PC volume and the total orifice area (either by changing the diameter or number of holes), few studies [81, 90, 103, 113–118] reported the adoption of some geometrical relation when determining these parameters.

Due to the limited information about how the volume, orifice diameter, and number of orifices are defined in most studies, as well as the uncertainty about the representativeness of these pre-chambers in relation to commercial models (in the case of simplified PC geometries), one of the objectives of the present PhD. thesis is to define a methodology to determine the PC volume and total orifice area of a pre-chamber, whether to be used in an experimental facility or in an engine. Furthermore, it will be intended to experimentally validate this methodology in an RCEM and an optical engine under various equivalence ratios and EGR rates.

References

[1] Heywoood, John B. *Internal Combustion Engine Fundamentals*. Second ed. New York, N.Y.: McGraw Hill, 2018, p. 1056.

[2] European Automobile Manufacturers' Association (ACEA). *Fuel types of new passenger cars in the EU*. 2023.

[3] U.S. Department of Energy. *2022 Light-Duty Vehicle Registration Counts by State and Fuel Type*. 2023.

[4] European Parliament. *Amending Regulation (EU) 2019/631 as regards strengthening the CO2 emission performance standards for new passenger cars and new light commercial vehicles in line with the Union's increased climate ambition*. 2021.

[5] European Parliament. *Regulation (EC) No. 715/2007: on type approval of motor vehicles with respect to emissions from light passenger and commercial vehicles (Euro 5 and Euro 6) and on access to vehicle repair and maintenance information*. 2007.

[6] International Council on Clean Transportation. "European Stage V non-road emission standards". In: November (2016).

[7] Environmental Protection Agency (EPA). *Technical Amendments for Marine Spark-Ignition Engines and Vessels*. 2010.

[8] Environmental Protection Agency (EPA). *Revised 2023 and later model year light-duty vehicle greenhouse gas emissions standards*. 2021.

[9] Council Directive of the European Communities. *Directive 91/441: amending Directive 70/220/EEC on the approximation of the laws of the Member States relating to measures to be taken against air pollution by emissions from motor vehicles*. 1991.

[10] European Parliament. *Regulation (EC) No. 443/2009: setting emission performance standards for new passenger cars as part of the Community's integrated approach to reduce CO2 emissions from light-duty vehicles*. 2009.

[11] European Parliament. *Regulation (EU) 2019/631: setting CO2 emission performance standards for new passenger cars and for new light commercial vehicles*. 2017.

[12] Environmental Protection Agency (EPA). *Smog Vehicle Emissions*. 2023.

[13] Fischer, Michael, Kreutziger, Philipp, Sun, Yong, and Kotrba, Adam. "Clean EGR for Gasoline Engines – Innovative Approach to Efficiency Improvement and Emissions Reduction Simultaneously". In: *SAE Technical Papers*. Vol. 2017-March. March. 2017. DOI: 10.4271/2017-01-0683.

[14] Fernandes, Heder, Pimenta, Charles Quirino, Rodrigues, Wanderson Navegantes, De Souza Montemor, Raphael Bezerra, and Barros, José Eduardo Mautone. "Experimental Investigation of Internal Exhaust Gas Recirculation on a Variable Valve Actuation Spark Ignition Engine Operating with Gasoline and Ethanol". In: *SAE Technical Papers* Part F127082.October (2016). DOI: 10.4271/2016-36-0399.

[15] Environmental Protection Agency (EPA). *The 2020 EPA Automotive Trends Report: Greenhouse Gas Emissions, Fuel Economy, and Technology since 1975*. 2022.

[16] Tornatore, Cinzia, Marchitto, Luca, and Valentino, Gerardo. "Technologies for Knock Mitigation in SI Engines—A Review". In: *Engines and Fuels for Future Transport*. Springer Singapore, 2022. Chap. 13, pp. 325–349. DOI: 10.1007/978-981-16-8717-4_13.

[17] Marquez, Manuel Alejandro Echeverri et al. “A Pathway to Ultra-Lean IC Engine Combustion: The Narrow Throat Pre-chamber”. In: *Engines and Fuels for Future Transport*. 2022. Chap. 8, pp. 175–203. DOI: 10.1007/978-981-16-8717-4_8.

[18] Vedharaj, S. “Advanced Ignition System to Extend the Lean Limit Operation of Spark-Ignited (SI) Engines—A Review”. In: *Alternative Fuels and Advanced Combustion Techniques as Sustainable Solutions for Internal Combustion Engines*. Springer Singapore, 2021. Chap. 10, pp. 217–255. DOI: 10.1007/978-981-16-1513-9_10.

[19] Sementa, Paolo, Tornatore, Cinzia, Catapano, Francesco, Di Iorio, Silvana, and Vaglieco, Bianca Maria. “Custom-Designed Pre-Chamber: Investigating the Effects on Small SI Engine in Active and Passive Modes”. In: *Energies* 16.13 (2023), p. 5097. DOI: 10.3390/en16135097.

[20] Attard, William P. and Blaxill, Hugh. “A single fuel pre-chamber jet ignition powertrain achieving high load, high efficiency and near zero NOx emissions”. In: *SAE International Journal of Engines* 5.3 (2012), pp. 734–746. DOI: 10.4271/2011-01-2023.

[21] Liu, Wei, Qi, Yunliang, Zhang, Ridong, Zhang, Qihang, and Wang, Zhi. “Investigation on end-gas auto-ignition and knock characteristics of iso-octane over wide thermodynamic conditions under jet ignition using a rapid compression machine”. In: *Fuel* 313.September 2021 (2022), p. 122665. DOI: 10.1016/j.fuel.2021.122665.

[22] Ricardo, Harry R. “RECENT RESEARCH WORK ON THE INTERNALCOMBUSTION ENGINE”. In: SAE Technical Paper 220001, 1922. DOI: 10.4271/220001.

[23] Atis, Cyrus Ashok Arupratan, Ayele, Yidnekachew, Stuecken, Thomas, and Schock, Harold. “Effect of pre-chamber scavenging strategy on EGR tolerance and thermal efficiency of pre-chamber turbulent jet ignition systems”. In: *International Journal of Engine Research* (2022), p. 146808742211051. DOI: 10.1177/14680874221105162.

[24] Toulson, Elisa, Schock, Harold J., and Attard, William P. “A Review of Pre-Chamber Initiated Jet Ignition Combustion Systems”. In: *SAE Technical Paper Series* (2010). DOI: 10.4271/2010-01-2263.

[25] Biswas, Sayan. *Physics of Turbulent Jet Ignition*. Springer Theses. Springer International Publishing, 2018. DOI: 10.1007/978-3-319-76243-2.

[26] Noguchi, M., Sanda, S., and Nakamura, N. “Development of toyota lean burn engine”. In: *SAE Technical Papers* (1976). DOI: 10.4271/760757.

[27] Adams, Tim G. "Torch ignition for combustion control of lean mixtures". In: *SAE Technical Papers* (1979). DOI: 10.4271/790440.

[28] Brandstetter, Walter. "The Volkswagen lean burn PC-engine concept". In: *SAE Technical Papers* (1980). DOI: 10.4271/800456.

[29] Davis, G. C., Krieger, R. B., and Tabaczynski, R. J. "Analysis of the flow and combustion processes of a three-valve stratified charge engine with a small prechamber". In: *SAE Technical Papers* (1974), pp. 3534–3550. DOI: 10.4271/741170.

[30] Date, Tasuku, Yagi, Shizuo, Ishizuya, Akira, and Fujii, Isao. "Research and development of the Honda CVCC engine". In: *SAE Technical Papers* (1974). DOI: 10.4271/740605.

[31] Turkish, Michael C. "3 - Valve stratified charge engines: Evolvement, analysis and progression". In: *SAE Technical Papers* (1974), pp. 3483–3503. DOI: 10.4271/741163.

[32] Varde, K. S. and Lubin, M. J. "The roll of connecting nozzle and the flame initiation point in the performance of a dual chamber stratified charge engine". In: *SAE Technical Papers* (1974). DOI: 10.4271/741161.

[33] Gruden, Dusan. "Combustion and exhaust emission of an engine using the porsche-stratified- charge-chamber-system". In: *SAE Technical Papers* (1975). DOI: 10.4271/750888.

[34] Wyczalek, F. A., Harned, J. L., Maksymiuk, S., and Blevins, J. R. "EFI prechamber torch ignition of lean mixtures". In: *SAE Technical Papers* (1975). DOI: 10.4271/750351.

[35] Gussak, L. A. "High chemical activity of incomplete combustion products and a method of prechamber torch ignition for avalanche activation of combustion in internal combustion engines". In: *SAE Technical Papers* (1975). DOI: 10.4271/750890.

[36] Oppenheim, A. K., Teichman, K., Hom, K., and Stewart, H. E. "Jet ignition of an ultra-lean mixture". In: *SAE Technical Papers* (1978), pp. 2416–2428. DOI: 10.4271/780637.

[37] Oppenheim, A K et al. "Combustion by Pulsed Jet Plumes - Key to Controlled Combustion Engines". In: *SAE Technical Papers*. 1989. DOI: 10.4271/890153.

[38] Murase, E., Ono, S., Hanada, K., and Oppenheim, Antoni K. "Pulsed combustion jet ignition in lean mixtures". In: *SAE Technical Papers*. 412. 1994. DOI: 10.4271/942048.

[39] Lezanski, T., Kesler, M., Rychter, T., Teodorczyk, A., and Wolanski, P. "Performance of Pulsed Jet Combustion (PJC) System in a research engine". In: *SAE Technical Papers* 412 (1993). DOI: 10.4271/932709.

[40] Wolanski, Piotr, Gut, Zbigniew, Niedziela, Witold, Przastek, Janusz, and Siwiec, Stanislaw. "Study of combustion dynamics in the research engine". In: *SAE Technical Papers* 412 (1997). DOI: 10.4271/972829.

[41] Hensinger, D. M., Maxson, J. A., Hom, K., and Oppenheim, A. K. "Jet plume injection and combustion". In: *SAE Technical Papers*. 1992. DOI: 10.4271/920414.

[42] Oppenheim, A. K. "Prospects for combustion in piston engines". In: *SAE Technical Papers* 724 (2002). DOI: 10.4271/2002-01-0999.

[43] Robinet, C., Higelin, P., Moreau, B., Pajot, O., and Andrzejewski, J. "A new firing concept for internal combustion engines: "i'APIR"". In: *SAE Technical Papers* 724 (1999). DOI: 10.4271/1999-01-0621.

[44] Attard, William P., Fraser, Neil, Parsons, Patrick, and Toulson, Elisa. "A Turbulent Jet Ignition pre-chamber combustion system for large fuel economy improvements in a modern vehicle powertrain". In: *SAE Technical Papers* 3.2 (2010), pp. 20–37. DOI: 10.4271/2010-01-1457.

[45] Attard, William P. and Parsons, Patrick. "A normally aspirated spark initiated combustion system capable of high load, high efficiency and near Zero NOx emissions in a modern vehicle powertrain". In: *SAE International Journal of Engines* 3.2 (2010), pp. 269–287. DOI: 10.4271/2010-01-2196.

[46] Attard, William P., Kohn, Jacob, and Parsons, Patrick. "Ignition energy development for a spark initiated combustion system capable of high load, high efficiency and near zero NOx emissions". In: *SAE Technical Papers* 3.2 (2010), pp. 481–496. DOI: 10.4271/2010-32-0088.

[47] Hlaing, Ponnya et al. "A Study of Lean Burn Pre-Chamber Concept in a Heavy Duty Engine". In: *SAE Technical Papers* 2019-September (2019), pp. 1–13. DOI: 10.4271/2019-24-0107.

[48] Almatrafi, Fahad, Hlaing, Ponnya, Echeverri Marquez, Manuel, Ben Houidi, Moez, and Johansson, Bengt. "Narrow-Throat Pre-Chamber Combustion with Ethanol, a Comparison with Methane". In: *SAE Technical Paper Series* (2020). DOI: 10.4271/2020-01-2041.

[49] Tang, Qinglong et al. "Study on the effects of narrow-throat pre-chamber geometry on the pre-chamber jet velocity using dual formaldehyde PLIF imaging". In: *Combustion and Flame* 240 (2022), p. 111987. DOI: 10.1016/j.combustflame.2022.111987.

[50] Novella, R., Gomez-Soriano, J., Martinez-Hernandiz, P.J., Libert, C., and Rampanarivo, F. "Improving the performance of the passive pre-chamber ignition concept for spark-ignition engines fueled with natural gas". In: *Fuel* 290.December 2020 (2021), p. 119971. DOI: 10.1016/j.fuel.2020.119971.

[51] Rajasegar, Rajavasanth, Niki, Yoichi, García-Oliver, Jose Maria, Li, Zheming, and Musculus, Mark P.B. "Fundamental insights on ignition and combustion of natural gas in an active fueled pre-chamber spark-ignition system". In: *Combustion and Flame* 232.x (2021). DOI: 10.1016/j.combustflame.2021.111561.

[52] Macián, V., Salvador, F. J., De la Morena, J., and Pagano, V. "Combustion analysis of a stratified pre-chamber ignition system by means of a zero-dimensional turbulence and flame speed model". In: *Combustion and Flame* 232 (2021). DOI: 10.1016/j.combustflame.2021.111526.

[53] Biswas, Sayan, Tanvir, Saad, Wang, Haifeng, and Qiao, Li. "On ignition mechanisms of premixed CH 4 /air and H 2 /air using a hot turbulent jet generated by pre-chamber combustion". In: *Applied Thermal Engineering* 106 (2016), pp. 925–937. DOI: 10.1016/j.applthermaleng.2016.06.070.

[54] Liu, Peilin, Zhong, Lijia, Zhou, Lei, and Wei, Haiqiao. "The ignition characteristics of the pre-chamber turbulent jet ignition of the hydrogen and methane based on different orifices". In: *International Journal of Hydrogen Energy* 46.74 (2021), pp. 37083–37097. DOI: 10.1016/j.ijhydene.2021.08.201.

[55] Tian, Jiangping, Cui, Zechuan, Ren, Zhongyong, Tian, Hua, and Long, Wuqiang. "Experimental study on jet ignition and combustion processes of natural gas". In: *Fuel* 262.July 2019 (2020), p. 116467. DOI: 10.1016/j.fuel.2019.116467.

[56] Li, Xiang et al. "Pre-chamber turbulent jet ignition of methane/air mixtures with multiple orifices in a large bore constant volume chamber: effect of air-fuel equivalence ratio and pre-mixed pressure". In: *Frontiers in Energy* 13.x (2019), pp. 483–493. DOI: 10.1007/s11708-019-0631-1.

[57] Biswas, Sayan and Qiao, Li. "Prechamber Hot Jet Ignition of Ultra-Lean H2/Air Mixtures: Effect of Supersonic Jets and Combustion Instability". In: *SAE International Journal of Engines* 9.3 (2016), pp. 1584–1592. DOI: 10.4271/2016-01-0795.

[58] Biswas, Sayan and Qiao, Li. "A Numerical Investigation of Ignition of Ultra-Lean Premixed H2/Air Mixtures by Pre-Chamber Supersonic Hot Jet". In: *SAE International Journal of Engines* 10.5 (2017). DOI: 10.4271/2017-01-9284.

[59] Biswas, Sayan and Qiao, Li. "Ignition of ultra-lean premixed hydrogen/air by an impinging hot jet". In: *Applied Energy* 228.March (2018), pp. 954–964. DOI: 10.1016/j.apenergy.2018.06.102.

[60] Biswas, Sayan, Zhang, Pei, Wang, Haifeng, and Qiao, Li. "Propagation and extinction behavior of methane/air premixed flames through straight and converging-diverging microchannels". In: *Applied Thermal Engineering* 148.July 2018 (2019), pp. 1395–1406. DOI: 10.1016/j.applthermaleng.2018.07.049.

[61] Ju, Dehao, Huang, Zhong, Li, Xiang, Zhang, Tingting, and Cai, Weiwei. "Comparison of open chamber and pre-chamber ignition of methane/air mixtures in a large bore constant volume chamber: Effect of excess air ratio and pre-mixed pressure". In: *Applied Energy* 260.December 2019 (2020), p. 114319. DOI: 10.1016/j.apenergy.2019.114319.

[62] Zhou, Lei, Liu, Peilin, Zhong, Lijia, Feng, Zhonghui, and Wei, Haiqiao. "Experimental observation of lean flammability limits using turbulent jet ignition with auxiliary hydrogen and methane in pre-chamber". In: *Fuel* 305.March (2021), p. 121570. DOI: 10.1016/j.fuel.2021.121570.

[63] Wei, Fuxing et al. "Visualization study on lean combustion characteristics of the premixed methanol by the jet ignition of an ignition chamber". In: *Fuel* 308.July 2021 (2022). DOI: 10.1016/j.fuel.2021.122001.

[64] Vera-Tudela, Walter, Barro, Christophe, and Boulouchos, Konstantinos. "Investigations on spark pre-chamber ignition and subsequent turbulent jet main chamber ignition in a novel optically accessible test rig". In: *International Journal of Engine Research* (2021), pp. 1–13. DOI: 10.1177/14680874211019849.

[65] Gentz, Gerald, Thelen, Bryce, Toulson, Elisa, Litke, Paul, and Hoke, John. "Combustion Visualization, Performance, and CFD Modeling of a Pre-Chamber Turbulent Jet Ignition System in a Rapid Compression Machine". In: *SAE International Journal of Engines* 8.2 (2015), pp. 538–546. DOI: 10.4271/2015-01-0779.

[66] Gentz, Gerald et al. "A study of the influence of orifice diameter on a turbulent jet ignition system through combustion visualization and performance characterization in a rapid compression machine". In: *Applied Thermal Engineering* 81 (2015), pp. 399–411. DOI: 10.1016/j.applthermaleng.2015.02.026.

[67] Thelen, Bryce Charles, Gentz, Gerald, and Toulson, Elisa. "Computational Study of a Turbulent Jet Ignition System for Lean Burn Operation in a Rapid Compression Machine". In: *SAE Technical Papers*. Vol. 2015-April. April. 2015. DOI: 10.4271/2015-01-0396.

[68] Thelen, Bryce Charles and Toulson, Elisa. "A Computational Study of the Effects of Spark Location on the Performance of a Turbulent Jet Ignition System". In: *SAE Technical Papers* (2016). DOI: 10.4271/2016-01-0608.

[69] Gholamisheeri, Masumeh, Thelen, Bryce, Gentz, Gerald, and Toulson, Elisa. "CFD Modeling of an Auxiliary Fueled Turbulent Jet Ignition System in a Rapid Compression Machine". In: *SAE Technical Papers*. March. 2016. DOI: 10.4271/2016-01-0599.

[70] Gholamisheeri, Masumeh, Thelen, Bryce C., Gentz, Gerald R., Wichman, Indrek S., and Toulson, Elisa. "Rapid compression machine study of a premixed, variable inlet density and flow rate, confined turbulent jet". In: *Combustion and Flame* 169 (2016), pp. 321–332. DOI: 10.1016/j.combustflame.2016.05.001.

[71] Validi, AbdoulAhad, Schock, Harold, and Jaberi, Farhad. "Turbulent jet ignition assisted combustion in a rapid compression machine". In: *Combustion and Flame* 186 (2017), pp. 65–82. DOI: 10.1016/j.combustflame.2017.07.032.

[72] Song, Ruitao, Gentz, Gerald, Zhu, Guoming, Toulson, Elisa, and Schock, Harald. "A control-oriented model of turbulent jet ignition combustion in a rapid compression machine". In: *Proceedings of the Institution of Mechanical Engineers, Part D: Journal of Automobile Engineering* 231.10 (2017), pp. 1315–1325. DOI: 10.1177/0954407016670303.

[73] Thelen, Bryce C. and Toulson, Elisa. "A computational study on the effect of the orifice size on the performance of a turbulent jet ignition system". In: *Proceedings of the Institution of Mechanical Engineers, Part D: Journal of Automobile Engineering* 231.4 (2017), pp. 536–554. DOI: 10.1177/0954407016659199.

[74] Gentz, Gerald, Gholamisheeri, Masumeh, and Toulson, Elisa. "A study of a turbulent jet ignition system fueled with iso-octane: Pressure trace analysis and combustion visualization". In: *Applied Energy* 189 (2017), pp. 385–394. DOI: 10.1016/j.apenergy.2016.12.055.

[75] Gholamisheeri, Masumeh, Wichman, Indrek S., and Toulson, Elisa. "A study of the turbulent jet flow field in a methane fueled turbulent jet ignition (TJI) system". In: *Combustion and Flame* 183 (2017), pp. 194–206. DOI: 10.1016/j.combustflame.2017.05.008.

[76] Chinnathambi, Prasanna, Thelen, Bryce, Naylor, Michael, Cook, Dave, and Toulson, Elisa. "Performance Assessment of a Single Jet, Dual Diverging Jets, and Dual Converging Jets in an Auxiliary Fueled Turbulent Jet Ignition System". In: *SAE Technical Papers* 2018-April.x (2018), pp. 1–13. DOI: 10.4271/2018-01-1135.

[77] Gholamisheeri, Masumeh, Givler, Shawn, and Toulson, Elisa. "Large eddy simulation of a homogeneously charged turbulent jet ignition system". In: *International Journal of Engine Research* 20.2 (2019), pp. 181–193. DOI: 10.1177/1468087417742834.

[78] Gholamisheeri, Masumeh, Givler, Shawn, and Toulson, Elisa. "RANS and LES of a Turbulent Jet Ignition System Fueled with Iso-Octane". In: *Flow, Turbulence and Combustion* Ic (2019). DOI: 10.1007/s10494-019-00049-5.

[79] Chinnathambi, Prasanna, Thelen, Bryce, Cook, Dave, and Toulson, Elisa. "Performance metrics for fueled and unfueled turbulent jet igniters in a rapid compression machine". In: *Applied Thermal Engineering* 182.August 2020 (2021), p. 115893. DOI: 10.1016/j.applthermaleng.2020.115893.

[80] Li, Fubai, Zhao, Ziqing, Wang, Boyuan, and Wang, Zhi. "Experimental study of pre-chamber jet ignition in a rapid compression machine and single-cylinder natural gas engine". In: *International Journal of Engine Research* (2019), pp. 1–15. DOI: 10.1177/1468087419883783.

[81] Li, Fubai, Zhao, Ziqing, Wang, Zhi, and Wang, Boyuan. "Experimental and Numerical Study of a Methane-Fueled Pre-chamber System in Rapid Compression Machine". In: *Combustion Science and Technology* 193.9 (2021), pp. 1463–1494. DOI: 10.1080/00102202.2019.1699547.

[82] Bueschke, Wojciech, Szwajca, Filip, and Wislocki, Krzysztof. "Experimental Study on Ignitability of Lean CNG/Air Mixture in the Multi-Stage Cascade Engine Combustion System". In: *SAE Technical Papers* 2020 (2020), pp. 1–13. DOI: 10.4271/2020-01-2084.

[83] Schlatter, Stephanie, Schneider, Bruno, Wright, Yuri M., and Boulouchos, Konstantinos. "Comparative study of ignition systems for lean burn gas engines in an optically accessible rapid compression expansion machine". In: *SAE Technical Papers* 6 (2013). DOI: 10.4271/2013-24-0112.

[84] Xu, Guoqing, Kotzagianni, Maria, Kyrtatos, Panagiotis, Wright, Yuri M., and Boulouchos, Konstantinos. "Experimental and numerical investigations of the unscavenged prechamber combustion in a rapid compression and expansion machine under engine-like conditions". In: *Combustion and Flame* 204 (2019), pp. 68–84. DOI: 10.1016/j.combustflame.2019.01.025.

[85] Shapiro, Evgeniy et al. "Experimental and numerical analysis of prechamber combustion systems for lean burn gas engines". In: *SAE Technical Papers* 2019-April.April (2019), pp. 1–11. DOI: 10.4271/2019-01-0260.

[86] Bolla, Michele et al. "Numerical Simulations of Pre-Chamber Combustion in an Optically Accessible RCEM". In: *SAE Technical Paper Series* (2019). DOI: 10.4271/2019-01-0224.

[87] Bolla, Michele et al. "Numerical study of turbulence and fuel-air mixing within a scavenged pre-chamber using RANS and LES". In: *SAE Technical Papers* 2019-April.April (2019), pp. 1–11. DOI: 10.4271/2019-01-0198.

[88] Desantes, Jose Maria, Novella, Ricardo, De La Morena, Joaquin, and Pagano lng, Vincenzo. "Achieving Ultra-Lean Combustion Using a Pre-Chamber Spark Ignition System in a Rapid Compression-Expansion Machine". In: *SAE Technical Papers*. Vol. 2019-April. April. 2019. DOI: 10.4271/2019-01-0236.

[89] Novella, Ricardo, De la Morena, Joaquín, Pagano, Vincenzo, and Pitarch, Rafael. "Optical evaluation of orifice orientation and number effects on active pre-chamber spark ignition combustion". In: *Fuel* 338.December 2022 (2023), p. 127265. DOI: 10.1016/j.fuel.2022.127265.

[90] Desantes, José M, López, J Javier, Gil, Antonio, and Antolini, Jácson. "Theoretical development and experimental validation of a methodology to reproduce multi-orifice pre-chamber jets in an optical accessible RCEM". In: *SIA Powertrain & Power Electronics 2021*. 2021.

[91] Tanamura, Masashi et al. “A Fundamental Study on Combustion Characteristics in a Pre-Chamber Type Lean Burn Natural Gas Engine”. In: *SAE Technical Papers* (2019). DOI: 10.4271/2019-24-0123.

[92] Tanoue, Kimitoshi, Kimura, Takanori, Jimoto, Taishu, Hashimoto, Jun, and Moriyoshi, Yasuo. “Study of prechamber combustion characteristics in a rapid compression and expansion machine”. In: *Applied Thermal Engineering* 115 (2017), pp. 64–71. DOI: 10.1016/j.applthermaleng.2016.12.079.

[93] Gholamisheeri, Masumeh, Thelen, Bryce, and Toulson, Elisa. “CFD Modeling and Experimental Analysis of a Homogeneously Charged Turbulent Jet Ignition System in a Rapid Compression Machine”. In: *SAE Technical Paper Series* (2017). DOI: 10.4271/2017-01-0557.

[94] Pastor, José V., Olmeda, Pablo, Martín, Jaime, and Lewiski, Felipe. “Methodology for optical engine characterization by means of the combination of experimental and modeling techniques”. In: *Applied Sciences (Switzerland)* 8 (2018). DOI: 10.3390/app8122571.

[95] Benajes, J., Pastor, J. V., García, A., and Monsalve-Serrano, J. “Redesign and Characterization of a Single-Cylinder Optical Research Engine to Allow Full Optical Access and Fast Cleaning during Combustion Studies”. In: *Experimental Techniques* 42.1 (2018), pp. 55–68. DOI: 10.1007/s40799-017-0219-9.

[96] Distaso, Elia et al. “Analysis of the combustion process in a lean-burning turbulent jet ignition engine fueled with methane”. In: *Energy Conversion and Management* 223 (2020). DOI: 10.1016/j.enconman.2020.113257.

[97] Antolini, Jácson et al. “Effect of passive pre-chamber orifice diameter on the methane combustion process in an optically accessible SI engine”. In: *Fuel* 341 (2023), p. 126990. DOI: 10.1016/j.fuel.2022.126990.

[98] Tang, Qinglong et al. “Simultaneous Negative PLIF and OH* Chemiluminescence Imaging of the Gas Exchange and Flame Jet from a Narrow Throat Pre-Chamber”. In: *SAE Technical Papers*. 2020. DOI: 10.4271/2020-01-2080.

[99] Wellander, Rikard et al. “Study of the Early Flame Development in a Spark-Ignited Lean Burn Four-Stroke Large Bore Gas Engine by Fuel Tracer PLIF”. In: *SAE International Journal of Engines* 7 (2014), pp. 2014–01–1330. DOI: 10.4271/2014-01-1330.

[100] Tang, Qinglong et al. “Optical diagnostics on the pre-chamber jet and main chamber ignition in the active pre-chamber combustion (PCC)”. In: *Combustion and Flame* 228 (2021), pp. 218–235. DOI: 10.1016/j.combustflame.2021.02.001.

[101] Attard, William P. et al. “Spark Ignition and Pre-Chamber Turbulent Jet Ignition Combustion Visualization”. In: *SAE Technical Papers*. 2012. DOI: 10.4271/2012-01-0823.

[102] Bureshaid, Khalifa, Shimura, Ray, Feng, Dengquan, Zhao, Hua, and Bunce, Mike. “Experimental Studies of the Effect of Ethanol Auxiliary Fueled Turbulent Jet Ignition in an Optical Engine”. In: *SAE International Journal of Engines* 12 (2019). DOI: 10.4271/03-12-04-0026.

[103] Costa, Roberto Berlini Rodrigues da et al. “Development of a homogeneous charge pre-chamber torch ignition system for an SI engine fuelled with hydrous ethanol”. In: *Applied Thermal Engineering* 152 (2019), pp. 261–274. DOI: 10.1016/j.applthermaleng.2019.02.090.

[104] Sementa, Paolo, Catapano, Francesco, Di Iorio, Silvana, Todino, Michele, and Vaglieco, Bianca Maria. “Analysis of the Combustion Process of SI Engines Equipped with Non-Conventional Ignition System Architecture”. In: *SAE Technical Papers*. 2020. DOI: 10.4271/2020-37-0035.

[105] Sementa, Paolo, Catapano, Francesco, Di Iorio, Silvana, and Vaglieco, Bianca Maria. “Experimental Investigation of a Fueled Prechamber Combustion in an Optical Small Displacement SI Methane Engine”. In: *SAE Technical Papers*. 2019. DOI: 10.4271/2019-24-0170.

[106] Sementa, Paolo, Catapano, Francesco, Di Iorio, SILVANA, Todino, Michele, and Vaglieco, Bianca Maria. “Turbulent Jet Ignition Effect on Exhaust Emission and Efficiency of a SI Small Engine Fueled with Methane and Gasoline”. In: *SAE Technical Paper Series*. Vol. 1. 2020. DOI: 10.4271/2020-24-0013.

[107] Distaso, Elia et al. “Experimental and Numerical Analysis of a Pre-Chamber Turbulent Jet Ignition Combustion System”. In: *SAE Technical Papers*. Vol. 2019. 2019. DOI: 10.4271/2019-24-0018.

[108] Millo, Federico et al. “Experimental and Numerical Investigation of a Passive Pre-Chamber Jet Ignition Single-Cylinder Engine”. In: *SAE Technical Paper Series*. 2021. DOI: 10.4271/2021-24-0010.

[109] Sampath, Ramgopal et al. “Study on the Pre-Chamber Fueling Ratio Effect on the Main Chamber Combustion Using Simultaneous PLIF and OH* Chemiluminescence Imaging”. In: *SAE International Journal of Advances and Current Practices in Mobility* 3.1 (2020), pp. 2020–01–2024. DOI: 10.4271/2020-01-2024.

[110] Sanal, Sangeeth, Echeverri Marquez, Manuel, Silva, Mickael, Cenker, Emre, and Im, Hong G. “A Numerical Study on the Effect of a Pre-Chamber Initiated Turbulent Jet on Main Chamber Combustion”. In: *SAE Technical Paper Series* 1 (2022), pp. 1–8. DOI: 10.4271/2022-01-0469.

[111] Echeverri Marquez, Manuel et al. “Optical Diagnostics of Pre-Chamber Combustion with Flat and Bowl-In Piston Combustion Chamber”. In: *SAE Technical Papers*. 2021. DOI: 10.4271/2021-01-0528.

[112] Echeverri Marquez, Manuel et al. “Visualization of Pre-Chamber Combustion and Main Chamber Jets with a Narrow Throat Pre-Chamber”. In: *SAE Technical Paper Series* (2022). DOI: 10.4271/2022-01-0475.

[113] Valle, R. M., Cândido De Sá, D. C., and Ramalho Filho, F. A. “Constructive parameters analysis of combustion pre-chamber adapted in torch-ignition system of otto cycle engine”. In: *SAE Technical Papers* (2003). DOI: 10.4271/2003-01-3713.

[114] Moreira, T. A. A. et al. “Design and Construction Methodology of a Stratified Torch Ignition System”. In: *SAE Technical Papers*. 2013. DOI: 10.4271/2013-36-0562.

[115] Shah, Ashish, Tunestal, Per, and Johansson, Bengt. “Effect of Pre-Chamber Volume and Nozzle Diameter on Pre-Chamber Ignition in Heavy Duty Natural Gas Engines”. In: *SAE Technical Papers*. Vol. 2015-April. April. 2015. DOI: 10.4271/2015-01-0867.

[116] Shah, Ashish, Tunestal, Per, and Johansson, Bengt. “Scalability Aspects of Pre-Chamber Ignition in Heavy Duty Natural Gas Engines”. In: *SAE Technical Papers*. group 1. 2016. DOI: 10.4271/2016-01-0796.

[117] Cruz, Igor William Santos Leal, Alvarez, Carlos Eduardo Castilla, Teixeira, Alysson Fernandes, and Valle, Ramon Molina. “Zero-dimensional mathematical model of the torch ignited engine”. In: *Applied Thermal Engineering* 103 (2016), pp. 1237–1250. DOI: 10.1016/j.applthermaleng.2016.05.017.

[118] Desantes, José M., López, J. Javier, Novella, Ricardo, and Antolini, Jácson. "Pre-chamber ignition systems: A methodological proposal to reproduce a reference case in a simplified experimental facility for fundamental studies". In: *International Journal of Engine Research* 22.11 (2021), pp. 3358–3371. DOI: 10.1177/1468087420971115.

Chapter 3

Materials and methods

3.1 Introduction

This chapter describes the experimental facilities and their optical setups, the numerical tools, and the methodology followed during the present thesis to study the pre-chamber ignition system. In addition to a theoretical and numerical study to understand the relationship between geometrical and engine operating parameters (described in detail in the following chapter), this thesis relies on experimental data obtained in a Rapid Compression-Expansion Machine (RCEM) located at the Clean Mobility and Thermofluids - CMT Institute from the Universitat Politècnica de València. It is worth mentioning that this thesis also relies on experimental data obtained in an optical engine located at the Institute of Sciences and Technologies for Sustainable Energy and Mobility (STEMS) from the Italian National Research Council (CNR), during a doctoral research visit founded by the UPV mobility exchange program.

First, the RCEM components and its operation principle, as well as the redesign required to operate with pre-chambers, the instrumentation, the optical techniques, and the image processing methodology implemented are thoroughly presented and discussed. Then, the optical engine is presented, and its instrumentation and optical techniques employed are described. Next, the different numerical tools are reported. Finally, the methodology followed during the present thesis to further understand the pre-chamber ignition concept is explained.

3.2 Rapid Compression-Expansion Machine

The Rapid Compression-Expansion Machine (RCEM) is an experimental facility designed to reproduce a single combustion cycle under engine-like thermodynamic conditions in a well-controlled environment, allowing a complete combustion assessment, either with a pressure-based or optical analysis. Unlike conventional Rapid Compression Machines (RCM's), which can only reproduce the compression stroke and hold the piston at Top Dead Center (TDC), the RCEM available at CMT Institute also partially reproduces the expansion stroke, accurately emulating the piston position of a reciprocating internal combustion engine (ICE) during the combustion process. Table 3.1 indicates the main technical characteristics of the RCEM.

Table 3.1: Technical characteristics of the RCEM.

Parameter	**Value**	**Units**
Bore	84	mm
Stroke	120-223	mm
Compression Ratio	5-17	-
Initial pressure	1-5	bar
Maximum cylinder pressure	200	bar
Fuel system	PFI or DI with gaseous or liquid fuels	-

This kind of experimental facility is excellent for testing the combustion process individually, avoiding second-order effects arising from the modifications needed to achieve a certain operating condition, as for instance the possibility of greatly varying the compression ratio without mechanical modifications, or reaching high intake pressure without boosting system constraints.

The RCEM has four pistons hydraulically coupled to each other and can be divided into two different regions: the driving region where all the piston movement is generated, and the experimental region where an 84 mm piston (attached to the driver piston) delimits the combustion chamber volume. A schematic view of the pistons can be seen in Figure 3.1. The working principle is based on the opposed piston movement between the pushing (1) and the driver piston (2), which generates a nearly vibrationless operation. The air piston (4) is pneumatically driven by a user-defined pressure, and it rules the movement of the hydraulic coupled pushing (1) and driver (2) pistons, determining its velocity and, consequently, the clearance height between the

experimental piston and the cylinder head. The stroke is previously adjusted by the displacement piston (3), and it remains constant during the experiment.

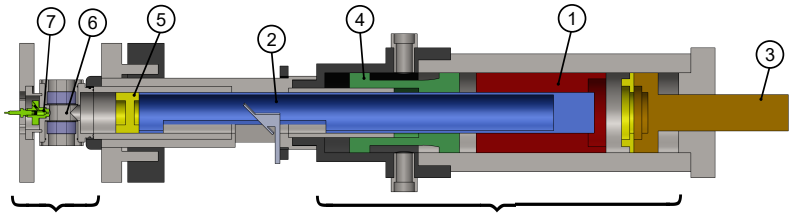

1	Pushing piston	4	Air piston	7	Pre-chamber
2	Driver piston	5	Experimental piston		
3	Displacement piston	6	Main chamber		

Figure 3.1: RCEM schematic view.

Unlike engines, this specific RCEM model utilized in this thesis presents a greater free area on the cylinder head due to the inexistence of moving parts such as valves and camshafts. This advantage allows for better-instrumented installations and increases the facility's flexibility. Moreover, the modular experimental region provides an easy geometry replacement to test several combustion methods such as autoignition of diesel and gasoline surrogates [1, 2], Premixed Charge Compression Ignition (PCCI) [3], Dual-Fuel [4], and passive and active pre-chambers [5, 6]. In terms of optical access, the RCEM has bottom and side-views. On the one hand, the bottom-view is obtained through a quartz insertion on the experimental piston, giving a central optical view of 46 mm of diameter (out of the total 84 mm). On the other hand, the side-view has three rectangular quartz accesses of 20x40 mm located on the cylinder liner at 0/90/180 degree.

3.2.1 RCEM redesign for pre-chamber optical studies

As previously commented, the RCEM on its stock configuration is equipped with two optical accesses: one gives a bottom-view (through an optical piston) and the other a side-view (through three small quartz insertions on the liner) of the combustion chamber. However, besides being small, the side-views are covered as the piston approaches TDC, limiting the available optical area. To overcome this limitation, a new liner/cylinder head with a fully accessible combustion chamber was designed to visualize the jet ejection into the main chamber.

Thus, the RCEM available at CMT Institute was modified to be able to assess single orifice pre-chambers with adequate free-length jet penetration and orthogonal optical accesses. This configuration, as can be seen in Figure 3.2, has a 32x32x64 mm rectangular-shaped main chamber, of which 52 mm (starting from the orifice exit) are optically accessible, being possible to see nearly all the jet penetration and main chamber combustion. In addition, this configuration enables the use of single-pass schlieren, natural luminosity, chemiluminescence, and laser-based optical techniques (e.g., PLIF).

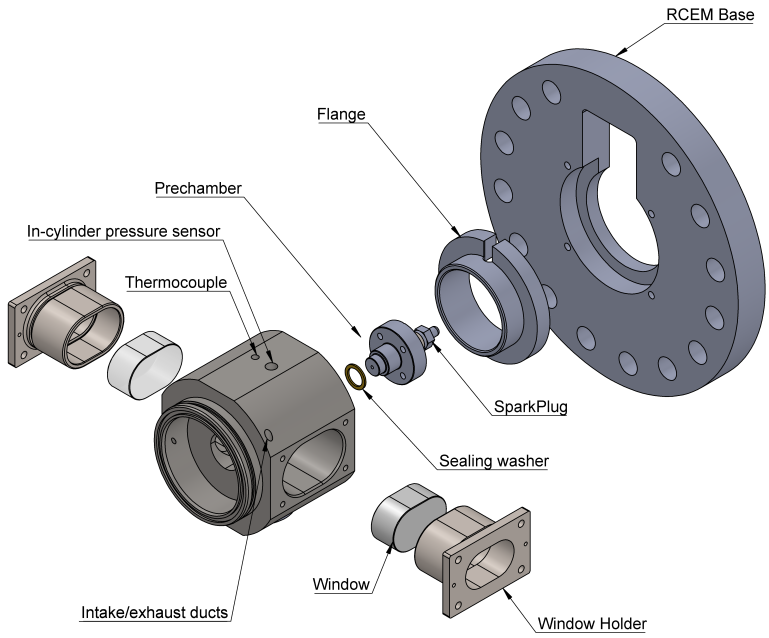

Figure 3.2: Fully optical accessible liner/cylinder head.

In this new setup, as the piston no longer crosses the visible area and does not reach the end of the combustion chamber, the dead volume when the piston is at the Top Dead Center (TDC) is significantly higher than in the previous configuration and in engines with similar bore and stroke dimensions. Another difference is that most of the combustion chamber volume is in the optically accessible main chamber, reaching up to 80% of the total volume at the maximum operating piston position (not the same as TDC). Nevertheless, due to the RCEM flexibility, an adequate compression ratio can be achieved with a longer piston stroke.

Completely designed in conjunction with the optically accessible RCEM cylinder head and liner, the proposed pre-chamber architecture allows the variation of the pre-chamber volume by changing the spark plug position. Additionally, its modular construction makes it easy to swap between different pre-chambers. The pre-chamber kit, as shown in Figure 3.3, is composed by the PC body, the spark plug (10 mm thread diameter) and the pressure transducer. The PC combustion chamber has a cylindrical shape and a conical section to connect to the orifice.

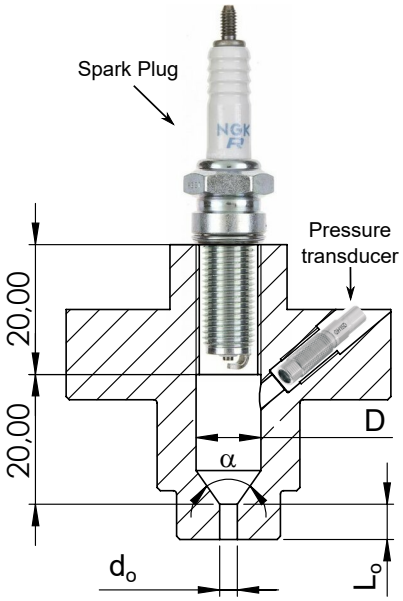

Figure 3.3: Pre-chamber internal geometry.

During the pre-chamber design process, one of the constraints that limited the most the pre-chamber packaging was the requirement (for a full PC monitoring) of installing a pressure transducer in such a small volume. Given this constraint and the arrangement of the PC on the cylinder head, the pre-chamber length (distance from the end of the spark plug thread to the beginning of the orifice) was set at 20 mm for all pre-chambers. Apart from the fixed minimum PC length, the pre-chamber internal diameter (D), orifice diameter (d_o), and orifice length-to-diameter ratio (L_o/d_o) were also varied.

3.2.2 Test cell instrumentation

For a proper combustion analysis, the pre- and main chambers were instrumented with uncooled piezoelectric pressure transducers. The main chamber

was equipped with a Kistler 6045A with a sensitivity of 47.5 pC/bar, and the pre-chamber with an AVL GH15D with a sensitivity of 18.81 pC/bar, both individually coupled to a Kistler 5018A charge amplifier. The experimental piston position is determined by an LM10 RLS high-speed magnetic incremental encoder with spatial resolution of 0.01 mm. All the indicated data are acquired and stored by a Yokogawa DL850V ScopeCorder equipped with one 10MHz-12 bits and five other 1MHz-16 bits Analog Voltage Modules.

In addition to the dedicated high-speed data measurement, the RCEM is equipped with a piezoresistive pressure sensor to monitor the chamber pressure during its filling procedure. This pressure is also recorded and used as a reference to the piezoelectric pressure sensors at the beginning of the cycle (pegging procedure).

To heat up and regulate the temperature of the optically accessible liner, four 150 W cartridge heaters controlled by a PID Watlow integrated controller were used. The target temperature (120 °C) was monitored by a k-type thermocouple placed 1.5 mm from the combustion chamber wall. An air compressor provides water- and oil-free compressed air to general machine operations.

3.2.3 Mixture preparation

The synthetic air or air-EGR mixture was previously prepared in a mixing tank and could vary in any proportion of oxygen (O_2), nitrogen (N_2), carbon dioxide (CO_2), and water (H_2O) to simulate air or any proportion of air and Exhaust Gas Recirculation (EGR). An in-house controller based on partial pressure fills the tank from the lowest to the highest molar concentration element to satisfy the composition defined by the user. The mixing tank temperature can be adjusted from ambient temperature up to 373 K thanks to electrical resistances and a PID controller.

Although the most representative air-EGR composition would be a mixture formed by O_2, N_2, CO_2, H_2O and Ar, this present study used a mixture of O_2 and N_2 to emulate a synthetic air-EGR mixture due to its simplicity to represent oxygen dilution [7]. On the one hand, the low mass fraction of Ar and CO_2 implies low partial pressures and, therefore, greater relative error due to the system accuracy. On the other hand, the water addition is complicated because it is in liquid phase at ambient temperature and pressure. Moreover, the CO_2 and H_2O addition have a greater impact in autoignition studies due to their chemical effect on generating OH radicals, but in terms of oxygen dilution, their effect is less representative.

Immediately before filling, the air/air-EGR tank is vacuumed and then filled up to 9 bar with the partial pressures of each component according to each EGR level, as described in Table 3.2.

Table 3.2: Air/air-EGR tank composition for each EGR level.

EGR level	**Molar fraction**		**Partial pressure**		**Tank pressure**
%	O_2	N_2	O_2	N_2	**[bar]**
0	0.2095	0.7905	1.886	7.114	9.000
10	0.1880	0.8120	1.692	7.308	
20	0.1666	0.8334	1.500	7.500	
25	0.1560	0.8440	1.404	7.596	

As a natural gas surrogate, the fuel used on all RCEM tests was methane G20 (CH_4>99 %). It was injected into the intake pipeline by a Zavoli commercial PFI natural gas injector with a 3 mm nozzle orifice diameter. The methane injection pressure was regulated at 2 bar (gauge) by means of a pressure reducer and regulator, ensuring chocked flow through the nozzle during injection (so the methane mass flow rate remains constant throughout the injection process). As only single combustion cycles can be reproduced at the RCEM, a continuous fuel mass flow rate measurement cannot be conducted during the experimental campaign. Therefore, a fuel mass per injection vs energizing time curve was previously determined by using the averaged mass flow rate of a 10 Hz injection frequency in a range of 4000 to 6000 µs of energizing time. Given the large displacement (piston stroke), combustion chamber and intake pipes volumes, 10 injections were needed to meet the fuel amount requirements. The mass flow meter used to characterize the injector was a BRONKHORST F-113AC-M50-AAD-44-V thermal mass flow meter. The fuel characteristics can be found in Table 3.3.

Before the fuel and air or air-ERG mixture enters the combustion chamber, the chamber and the pipelines are vacuumed to ensure the correct mixture composition at the end of the filling process. Thus, the filling procedure can be described as follows: first, the chamber and pipelines are vacuumed; then, the fuel is injected into the pipeline; next, the air or air-EGR mixture previously prepared in the mixing tank is introduced; and finally, when the target initial pressure is reached, the rapid compression stroke begins.

Table 3.3: Fuel characteristics. Source: [8, 9]

Parameter	**Value**	**Units**
Chemical formula	CH_4	-
Lower Heating Value	50.0	MJ/kg
Molecular weight	16.042	kg/kmol
Density @ 300 K and 6.5 bar	4.2269	kg/m3
Specific heat	2.20	kJ/kg K
Ratio of specific heats @ 300 K and 6.5 bar	1.3198	-
Gas constant	0.5182	kJ/kg K
Research Octane Number	120	-
Auto ignition temperature @ 1 atm and stoichiometric mixture	813	K
Stoichiometric air/fuel ratio	17.23	kg/kg

3.2.4 Optical techniques

In this sub-section, the optical techniques applied to the optical portion of the main chamber to visualize the jet ejection from the pre-chamber are presented and discussed. First the schlieren imaging and then the chemiluminescence imaging.

Schlieren

The schlieren optical technique relies on the refraction of the light in any direction other than the straight direction when passing through an inhomogeneous transparent media, creating refractive differences within the image background [10]. This optical technique can be used to identify temperature gradients, high-speed flows, or any other phenomenon that changes the refractivity of the medium.

In this study, a single-pass schlieren arrangement was utilized to both quantitatively and qualitatively describe the reacting and unreacting phases of the jet ejection. As schematically illustrated in Figure 3.4, on one side of the test area a Karl Storz Xenon Nova 300 light source coupled to a diaphragm produce a point light source. Placed at its focal distance far from the point light source, a UV Plano-Convex lens (f=200 mm, D=75 mm) was used to generate a collimated light beam passing through the combustion chamber. On the opposite side of the test area, an UV lens (f=750 mm, D=150 mm) refocuses the beam to an image of the point source, where a diaphragm is located to cutoff the refracted light. A Photron Nova S12 high-speed camera

coupled with a Carl-Zeiss Makro-Planar 100 mm f/2 collects the real inverted image. The shutter time of 0.3 µs was kept constant in all tests. A resolution of 512x256 pixels resulted on a projected pixel size of 5.7 pixels per millimeter. The frame rate was set at 80,000 FPS, which is equivalent to an angular resolution of 0.1 CAD at 1300 rpm.

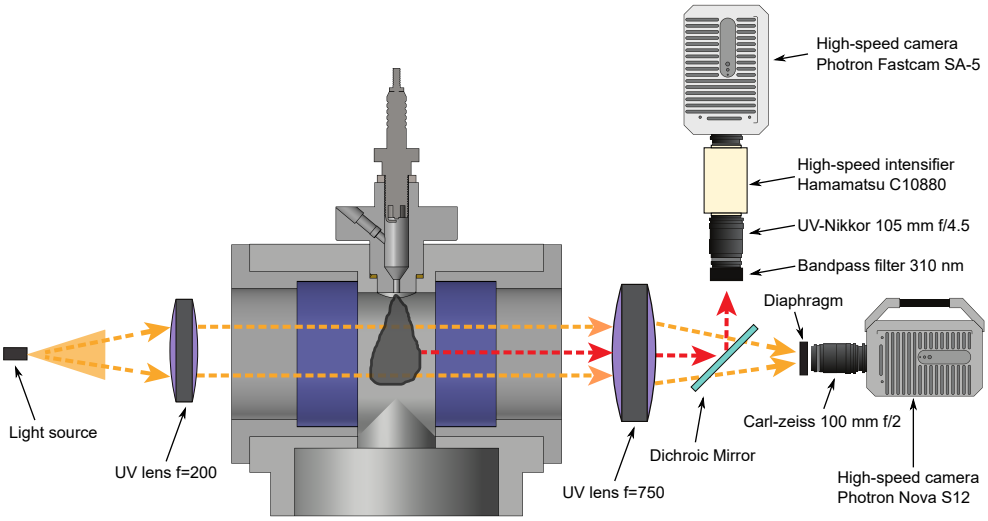

Figure 3.4: Schematic view of the optical setup.

The schlieren images can be more or less sensitive depending on the setup arrangement (e.g., single or double-pass [11]), the light source brightness, and the calibration of the knife edge (the diaphragm aperture in this case) before the high-speed camera [12]. In this sense, a very sensitive schlieren setup will capture even a slight temperature gradient due to the difference in the refractive index. The schlieren experimental setup prepared for the RCEM was configured to be very sensitive in order to capture the initial phase of the PC jet ejection, in which the temperature of the gases exiting the PC is close to the main combustion chamber temperature. The drawback of a more sensitive schlieren setup is the visualization of undesired phenomena, such as the in-cylinder turbulence vortex due to the diameter change from the piston bore to the optically accessible combustion chamber diameter, and the streamline flow boundary during the PC filling, as shown in Figure 3.5.

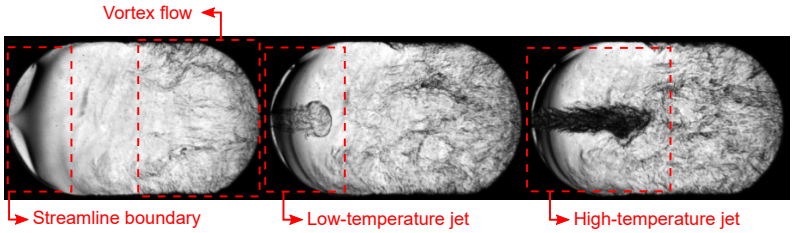

Figure 3.5: Image outcome from the selected schlieren sensitivity for the RCEM operation.

Chemiluminescence

During a chemical reaction, the energy released by a matter in the form of light is called chemiluminescence [13]. On the oxidation of methane and other higher-order hydrocarbons, several exothermal chain branching reactions occur, forming radicals such as OH, CH, O, and H, especially at high temperatures [14]. A typical approach to detect these radicals is the use of band-pass filters to capture the light emission on a specific wavelength, corresponding to the excited-state of the radical of interest [15]. On hydrocarbon combustion, the more important are OH and CH radicals, excited at 308 and 431 nm, respectively.

A widely accepted path of OH* formation, proposed by Gaydon [13], is given by:

$$CH + O_2 = CO + OH^* \tag{3.1}$$

being especially relevant in the reaction zone, where CH is found. Under engine-like conditions, the OH* formation is greatly affected by the fuel-air equivalence ratio, decreasing the OH* intensity as the fuel-air equivalence ratio decreases [16].

In the RCEM, the chemiluminescence images were acquired by a Photron FASTCAM SA-5 high-speed camera coupled to a Hamamatsu C10880-03F high-speed image intensifier and a UV-Nikkor 105 mm f/4.5 objective (Figure 3.4). As it was applied simultaneously with the schlieren technique, a Thorlabs shortpass dichroic mirror placed at 45 degrees was used to reflect the light spectrum below 400 nm to the chemiluminescence camera. A 310 nm band-pass filter with a 10 nm full width-half max was used to capture the wavelength correspondent to the hydroxyl radical (OH*), an important marker of combustion reactions. The resolution of 512x512 pixels resulted in a spatial

resolution of 6.1 pixels per millimeter. The frame rate was set at 20,000 frames per second (FPS), which is equivalent to an angular resolution of 0.4 CAD at 1300 rpm. The shutter speed was set at 49.75 µs, the maximum admissible for the frame rate chosen [17]. The relative gain of the image intensifier, an dimensionless number which varies from 600 to 999 and is nonlinear with the total luminous gain ($1x10^5$ $(lm/m^2)/lx$), was fixed at 780 for the stoichiometric cases and for the cases to evaluate the effect equivalence ratio, and 810 for the EGR ratio study.

3.2.5 Image processing

Once the images are obtained, a series of procedures can be done to facilitate the handling of images and improve their quality. The most common procedure is to apply a geometrical mask to ignore the area outside the region of interest and then crop the image to a given format. Aside from the qualitative information directly seen in the image, the sequence of images can provide quantitative information about the jet ejection and main chamber combustion development, depending on the optical technique employed.

For schlieren imaging, as it essentially detects temperature gradients, the mass flow coming out the pre-chamber after the start of combustion can be tracked frame-by-frame. To do so, from the raw image (Figure 3.6 a), first the origin of coordinates and the jet axis are set accordingly with the position of the pre-chamber orifice. Then, a background average image, taken before the jet ejection is initiated, is used to implement a so-called dynamic background, where the jet area from the previous frame is replaced by the background average image (Figure 3.6 b). Next, after the background subtraction, a threshold is defined based on the intensity of each image and a user defined sensitivity parameter, and the image is then binarized among the jet and the non-jet regions (Figure 3.6 c) [18]. After that, the jet contour is defined as the border line between the two regions (Figure 3.6 d). Finally, several parameters can be taken from these regions and jet contour, the most typical are the jet tip penetration and velocity, and the jet angle and area.

For chemiluminescence OH* imaging, the methodology to post-process the images was similar, but no jet segmentation was done and, therefore, no quantitative information about the jet/flame was obtained. In this context, the chemiluminescence OH* imaging can be seen as a complementary information to the schlieren imaging, indicating if the jet contents are chemically reacting or not. Starting from a raw image (Figure 3.7 a), the geometrical mask is applied and a background image considering the last 10 frames before the beginning of the jet ejection is collected (Figure 3.7 b). Finally, the

background and the geometrical mask are applied to remove the background luminosity noise (Figure 3.7 c).

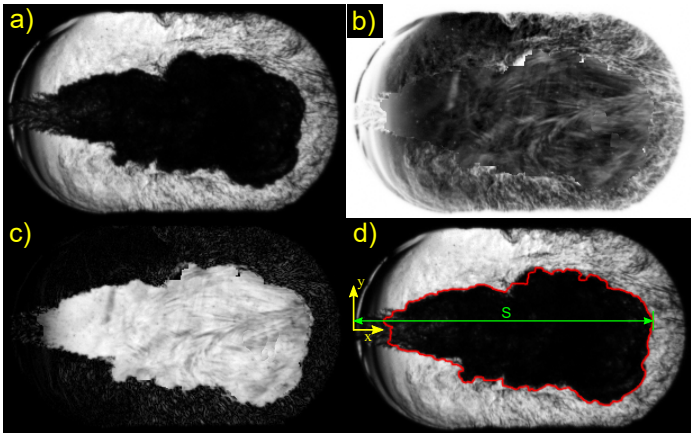

Figure 3.6: Step-by-step schlieren post-processing methodology. a) raw image, b) background, c) jet binarization, d) image with the jet contour and the tip penetration (s).

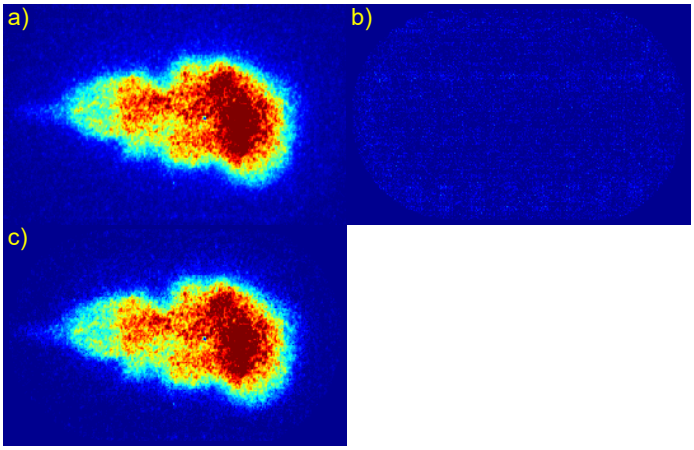

Figure 3.7: Step-by-step chemiluminescence post-processing methodology. a) raw image, b) background and geometrical mask, c) final image.

3.3 Optical engine

In a complementary way, the pre-chamber ignition concept was also assessed under more engine-like conditions in an optical engine available at

Institute of Sciences and Technologies for Sustainable Energy and Mobility (STEMS). This experimental facility gives the possibility to apply optical diagnosis tools in conjunction with the traditional heat released analysis (based on the in-cylinder pressure) while preserving the main characteristics of a metallic engine (consecutive combustion cycles, residual gas fraction, etc.).

The optically accessible engine was based on a 4-stroke single-cylinder SI engine typically used in motorcycles. The cylinder head has a central spark plug, four-valves and a pent-roof shaped combustion chamber. Direct fuel injection (DI) and port-fuel injection (PFI) for both liquid and gaseous fuels are available. Table 3.4 summarizes the main characteristics of the engine.

Table 3.4: Optical engine specifications.

Property	**Unit**	**Value**
Engine base type	–	4-stroke SI
Bore x Stroke	mm	72 x 60
Swept volume	cm^3	244.3
Compression Ratio SI	–	9.0:1
Compression Ratio PCSI	–	8.6:1
Fuel injection system	–	DI or PFI - liquid or gaseous
Valve timing @1mm lift	CAD	IVO = 6 BTDC IVC = 50 ABDC EVO = 41 BBDC EVC = 1 ATDC
Coolant temp.	$°C$	60
Lubricant temp. / pres.	$°C$ / bar	60 / 3

The bottom optical access is obtained through an elongation of the regular metallic piston with a hollow cylinder (Bowditch design) and the use of a cylindrical sapphire window with a diameter of 54 mm. Unlubricated Teflon-bronze composite piston-rings seals the combustion chamber while ensuring no window oil contamination. The one-side oblong opening on the extended piston allows to install a 45-degree UV coated mirror to redirect the image orthogonally to the piston axis. A schematic view of the optically accessible engine setup is illustrated in Figure 3.8.

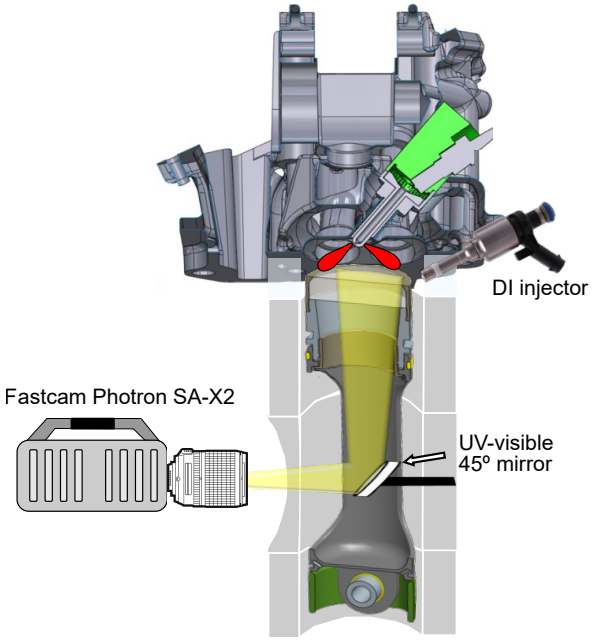

Figure 3.8: Schematic view of the optical engine setup.

3.3.1 Test cell instrumentation

The optical engine was installed in a fully instrumented test cell to allow appropriate engine monitoring and data capture of a wide range of pertinent information for engine testing. To control the load and speed, the engine was connected to an active dynamometer. Using an AVL FlexIFEM Piezo charge amplifier and an AVL GH12D piezoelectric pressure transducer, the in-cylinder pressure was measured and referenced with an encoder with a precision of 0.1 CAD. The intake pressure was measured using a manifold absolute pressure (MAP) sensor. Thermal mass flowmeters manufactured by Brooks SLA5861 and Sensyflow NW 25 were used to measure the fuel mass flow rate and air mass flow rate, respectively. The exhaust oxygen content was measured by a Bosch wide-band lambda sensor LSU 4.9, which was conditioned by an ETAS Lambda Meter LA4. This allowed the real air-to-fuel ratio to be calculated. The multi-channel AVL Engine Timing Unit (ETU) system managed the injection and ignition settings. An AVL IndiModul high-speed data aquisition unit was used to gather all the above sensors signals, enabling AVL IndiCom software to perform real-time combustion analysis. Quantitative information about the combustion process and its cycle-to-cycle variability was

obtained through a heat-release analysis of 400 consecutive cycles. Type-K thermocouples were employed in a low-frequency system to measure the temperatures of the exhaust and intake gases. Using an AVL DiGas 4000 gas analyzer, the concentrations of HC, CO, CO_2, O_2 and NO_x in the exhaust was measured.

Due to the composition of the piston rings, a precise cylinder wall temperature control is indispensable to guarantee its proper operation and durability. In this sense, an external cooling system control the engine coolant temperature at 60 °C. Additionally, two external lubrication systems guarantee the proper lubrication of the bottom (crankshaft, bearings, connecting rod, etc.) and upper (camshaft, valves, etc.) parts of the metallic engine, keeping its pressure and temperature at 3 bar and 60 °C, respectively.

3.3.2 Optical technique – Natural flame luminosity

The natural flame luminosity is the only optical technique used in this engine. As its name indicates, it relies on the luminosity generated naturally during the high-temperature exothermic chemical reactions of the combustion process, i.e., no external light source is employed. In flames with soot formation, especially in diffusion combustion, in addition to the light emitted from chemical reactions (chemiluminescence), the incandescence of the soot particles also emits thermal radiation. This optical technique can be used to obtain general information about the combustion process development, such as flame propagation velocity and flame structure.

The high-speed flame natural luminosity was recorded by a Photron FASTCAM SA-X2 high-speed camera mounted with a NIKKOR 18-105mm f/3.5-5.6 zoom lens (the focal length and aperture were set at 105 mm and f/5.6, respectively). The frame rate was set to 10,000 FPS, which is equivalent to 1.2 CAD resolution at 2000 rpm. The shutter speed was set at 99 µs, the maximum for the corresponding frame rate [19]. A resolution of 512x512 pixels resulted on a spatial resolution of 6.3 pixels per millimeter. Given the characteristic time of the jet penetration, an even higher temporal resolution would be desirable; however the trade-off between shutter speed and frame rate was the limiting factor due to the low luminosity intensity produced during the jet ejection process.

3.4 Numerical tools

This section will briefly introduce the numerical tools used in the different stages of this study. The full case setup will be described during the

corresponding section, in which the numerical study is presented.

3.4.1 GT-Power

The GT-Power software is a simulation tool suitable for analysis of a wide range of topics related to vehicle and engine performance. For engine applications, the system is discretized into finite volumes and the Navier-Stokes equations (conservation of continuity, momentum, and energy) are solved [20, 21]. The time integration method is, typically, explicit, which means that the current time step is calculated using values from the previous time step. Regarding the pre-chamber ignition concept, GT-Power is able to calculate the mass transfer between main chamber and pre-chamber and thus estimate the trapped mass, pressure, temperature, mixture composition and residual mass fraction all over the cycle. In addition, jet velocity and momentum during the jet ejection phase are also estimated based on the combustion profile specified by the user.

In this study, the GT-Power software was used as a calculation tool to understand the energy flow of multi-orifice and simplified single-orifice geometries during the closed cycle (from inlet valve closing – IVC, until exhaust valve opening – EVO). Due to its flexibility to vary the geometry, a methodology to reproduce the thermodynamic conditions of a multi-orifice configuration in a single-orifice configuration was first numerically validated with GT-Power before manufacturing any pre-chamber. Moreover, the information obtained with the numerical simulation was used as input data to the DICOM software for jet evolution simulation (see next sub-section).

3.4.2 DICOM

Developed by CMT Institute members, the DICOM software is a one-dimensional spray model that predicts the evolution of a steady or transient turbulent gas jet or liquid spray, either inert or reactive [22, 23]. Based on the jet mass flow rate and momentum flux, as well as on the density, pressure, and composition at the chamber in which the jet will be injected, DICOM can predict the jet tip penetration, velocity, and many other jet parameters. Although designed for fuel injection applications, the software also is applicable to the pre-chamber ignition concept due to the similar phenomenology between the processes.

In this present PhD. thesis, the jet ejected by the pre-chamber was modeled as an inert transient gas jet, where the time-resolved mass flow rate and

momentum flux are given either by a one-dimensional flow model or experimental data. The temperature and the composition of the gas being ejected were kept constant, an assumption based on a simplified scenario where a non-reactive gaseous jet can be considered as a flow of constant density [24]. More details about the development and validation of the DICOM spray model can be found in previous studies reported in the literature [22–24].

The DICOM software was initially employed to compare the jet penetration of the multi orifice and the single orifice configurations during the development of the methodology to reproduce the jet of a multi-orifice PC into a single orifice pre-chamber. In this study, the input data for the DICOM model was obtained via one-dimensional model (GT-Power).

Then, once the RCEM experimental data were available, the DICOM model was used to calculate the jet tip penetration, which was then compared to the jet penetration obtained via schlieren imaging.

3.4.3 CONVERGE

CONVERGE is a computational fluid dynamics (CFD) program to simulate incompressible or compressible, transient or steady flows in geometries with stationary or moving surfaces [25]. Equipped with several engine-related models for physical processes (turbulence, heat transfer, etc.), a vast of flow problems can be addressed. The simulations can be performed both on crank-angle or time basis. The automated grid generation and the straightforward geometry import from Computer-aided design (CAD) programs are also convenient for the user.

In this study, the CONVERGE software supported on the commissioning of the new RCEM configuration for pre-chamber optical application, identifying and quantifying the mass transfer between combustion chamber and part of the intake/exhaust ducts during the closed cycle (an inherent aspect of how the RCEM works), as well as to validate the CFD model with a motored condition. Moreover, the CONVERGE was used to calculate the discharge coefficient of the single orifice pre-chambers and qualitatively characterize the PC combustion.

3.5 Methodology

The study carried out in this present PhD. thesis aims to expand the know-how of the pre-chamber ignition concept, covering from the theoretical

development to engine testing, passing through tests with simplified geometries in different experimental facilities. First, given the valuable information that optical techniques can provide and the fact that some of them were still not used on PC studies under engine-like conditions, the RCEM was chosen as the first experimental facility to carry out the tests due to its flexibility in terms of setup modification. To do so with a sufficient free-jet length and favorable conditions to optical techniques, the single orifice arrangement was chosen in detriment of a multi-orifice arrangement (typically found in engine applications). The first hindrance was how to properly reproduce the jet ejection of a multi-orifice into a single-orifice pre-chamber, therefore an examination of the most representative design criteria (volume, orifice diameter, etc.) was conducted employing the energy conservation equation. This theoretical study pointed out the main variables that affect the energy flow during the pre-chamber filling and jet ejection processes, as well as their relationship with the pressure and temperature rise rate. After numerically validate the theoretical study using GT-Power, five single-orifice PC's were proposed to validate it with experimental data, as well as to evaluate other pertinent aspects of this ignition concept. To conclude and further understand the pre-chamber ignition concept under engine-like conditions, complementary studies with multi-orifices pre-chambers in an optical single-cylinder engine were conducted. In particular, the effect of three different orifice diameters was assessed by means of high-speed natural flame luminosity images and rate of heat released analysis. Once the methodological aspects and both experimental and numerical tools were presented, in the upcoming chapters the results will be presented and discussed, starting with the theoretical study to reproduce the jet of a multi-orifice into a single-orifice PC configuration.

References

[1] Desantes, José M., Bermúdez, Vicente, López, J. Javier, and López-Pintor, Darío. "Experimental validation of an alternative method to predict high and low-temperature ignition delays under transient thermodynamic conditions for PRF mixtures using a Rapid Compression-Expansion Machine". In: *Energy Conversion and Management* 129 (2016), pp. 23–33. DOI: 10.1016/j.enconman.2016.09.089.

[2] Desantes, José M, López, J Javier, Molina, Santiago, and López-Pintor, Darío. "Design of synthetic EGR and simulation study of the effect of simplified formulations on the ignition delay of isooctane and n-heptane". In: *Energy Conversion and Management* 96 (2015), pp. 521–531. DOI: 10.1016/j.enconman.2015.03.003.

[3] Martínez, María, Altantzis, Christos, Wright, Yuri M., Martí-Aldaraví, Pedro, and Boulouchos, Konstantinos. "Computational study of the Premixed Charge Compression Ignition combustion in a Rapid Compression Expansion Machine: Impact of multiple injection strategy on mixing, ignition and combustion processes". In: *Fuel* 318.February (2022), p. 123388. DOI: 10.1016/j.fuel.2022.123388.

[4] Salaun, Erwan et al. "Optical Investigation of Ignition Timing and Equivalence Ratio in Dual-Fuel CNG/Diesel Combustion". In: *SAE Technical Papers* 2016-April.April (2016). DOI: 10.4271/2016-01-0772.

[5] Desantes, Jose Maria, Novella, Ricardo, De La Morena, Joaquin, and Pagano lng, Vincenzo. "Achieving Ultra-Lean Combustion Using a Pre-Chamber Spark Ignition System in a Rapid Compression-Expansion Machine". In: *SAE Technical Papers*. Vol. 2019-April. April. 2019. DOI: 10.4271/2019-01-0236.

[6] Macián, V., Salvador, F. J., De la Morena, J., and Pagano, V. "Combustion analysis of a stratified pre-chamber ignition system by means of a zero-dimensional turbulence and flame speed model". In: *Combustion and Flame* 232 (2021). DOI: 10.1016/j.combustflame.2021.111526.

[7] Desantes, José M., López, J. Javier, Molina, Santiago, and López-Pintor, Darío. "Theoretical development of a new procedure to predict ignition delays under transient thermodynamic conditions and validation using a Rapid Compression–Expansion Machine". In: *Energy Conversion and Management* 108 (2016), pp. 132–143. DOI: 10.1016/j.enconman.2015.10.077.

[8] Lemmon, Eric W., McLinden, Mark O., and Friend, Daniel G. "Thermophysical Properties of Fluid Systems". In: *NIST Chemistry WebBook*. Ed. by P.J. Linstrom and W.G. Mallard. Gaithersburg MD: National Institute of Standards and Technology. Chap. NIST Stand. DOI: https://doi.org/10.18434/T4D303.

[9] Heywoood, John B. *Internal Combustion Engine Fundamentals*. Second ed. New York, N.Y.: McGraw Hill, 2018, p. 1056.

[10] Settles, G. S. *Schlieren and Shadowgraph Techniques*. Berlin, Heidelberg: Springer Berlin Heidelberg, 2001. DOI: 10.1007/978-3-642-56640-0.

[11] Payri, Raul, Salvador, F. J., Bracho, Gabriela, and Viera, Alberto. "Differences between single and double-pass schlieren imaging on diesel vapor spray characteristics". In: *Applied Thermal Engineering* 125 (2017), pp. 220–231. DOI: 10.1016/j.applthermaleng.2017.06.140.

[12] Prisacariu, Emilia et al. "Calculating and Setting Up A Schileren System". In: *Turbo* VII.2 (2020), pp. 25–34.

[13] Gaydon, A. G. *The Spectroscopy of Flames*. Vol. 80. 12. Dordrecht: Springer Netherlands, 1974, pp. 3169–3169. DOI: 10.1007/978-94-009-5720-6.

[14] Glassman, Irvin and Yetter, Richard A. *Combustion*. 4 ed. Vol. 59. Elsevier, 2008. DOI: 10.1016/B978-0-12-088573-2.X0001-2.

[15] Kalwar, Ankur and Agarwal, Avinash Kumar. "Optical Diagnostics for Gasoline Direct Injection Engines". In: *Energy, Environment, and Sustainability*. Ic. Springer Singapore, 2022, pp. 201–241. DOI: 10.1007/978-981-16-8418-0_7.

[16] Nori, Venkata and Seitzman, Jerry. "Evaluation of Chemiluminescence as a Combustion Diagnostic Under Varying Operating Conditions". In: *46th AIAA Aerospace Sciences Meeting and Exhibit*. Reston, Virigina: American Institute of Aeronautics and Astronautics, 2008, pp. 1–14. DOI: 10.2514/6.2008-953.

[17] Photron. *FASTCAM SA5 Hardware Manual*. 2014.

[18] Pastor, José V., Arrègle, Jean, and Palomares, Alberto. "Diesel spray image segmentation with a likelihood ratio test". In: *Applied Optics* 40.17 (2001), p. 2876. DOI: 10.1364/ao.40.002876.

[19] Photron. *FASTCAM SA-X2 Hardware Manual*. 2019.

[20] Technologies, Gamma. *Flow Theory Manual*. 2021.

[21] Technologies, Gamma. *Engine Performance Application Manual*. 2021.

[22] Pastor, J.V., Lopez, J. Javier, García-Oliver, J.M., and Pastor, José M. "A 1D model for the description of mixing-controlled inert diesel sprays". In: *Fuel* 87.13-14 (2008), pp. 2871–2885. DOI: 10.1016/j.fuel.2008.04.017.

[23] Desantes, J.M., Pastor, J.V., García-Oliver, J.M., and Pastor, J.M. "A 1D model for the description of mixing-controlled reacting diesel sprays". In: *Combustion and Flame* 156.1 (2009), pp. 234–249. DOI: 10.1016/j.combustflame.2008.10.008.

[24] Desantes, J. M., Payri, R., Salvador, F. J., and Gil, A. "Development and validation of a theoretical model for diesel spray penetration". In: *Fuel* 85.7-8 (2006), pp. 910–917. DOI: 10.1016/j.fuel.2005.10.023.

[25] Convergent Science. *CONVERGE 2.4 Manual*. 2020.

Chapter 4

Fundamental aspects to reproduce a reference case in a simplified experimental facility

4.1 Introduction

In this chapter, a methodology to reproduce a reference case under simplified experimental conditions is presented. This study arises from the necessity to correctly determine the pre-chamber volume and the orifice diameter of a simplified single-orifice pre-chamber based on a multi-orifice baseline pre-chamber, preserving as much as possible the jet characteristics of the baseline case. First, the methodology used in this study and the validation tools are described. Then, the effect of the geometrical aspects (i.e. volume and orifice diameter) and engine operating parameters (i.e. engine speed) during the PC filling and jet ejection processes are theoretically analyzed and a parameter relating them is proposed. Next, this relationship is validated in terms of the thermodynamic conditions at both pre and main chambers. After that, a jet penetration scalability factor is proposed and numerically validated. Then, orifice quenching is briefly discussed. Finally, the main findings of this fundamental study are summarized.

4.2 Research approach and validation tools

4.2.1 Research approach

The present study was divided in two parts: a theoretical development and a computational validation. The theoretical development presents some relations that governs the pre-chamber filling and jet ejection processes, as well as the jet tip penetration and the flame quenching in the orifices, whereas two computational tools were used to validate the thermodynamic and mass flow aspects (GT-Power) and the jet characteristics (DICOM), both explained in 4.2.2.

Looking at the pre-chamber ignition concept processes separately, it is possible to identify the crucial elements of each one, which are:

- Pre-chamber filing: During this phase, the fresh charge coming from the main chamber is transferred to the pre-chamber in a rate defined by the flow velocity (note that this one may be limited if sonic conditions at the orifice are reached) and the total orifice area. This mass flow causes an increase in PC pressure.

- Pre-chamber scavenging: Concomitant with the PC filling process, the proper scavenge depends on the flow pattern generated by the orifices. Therefore, it is a process completely related to three-dimensional phenomena.

- Pre-chamber combustion: Started by a sparkplug, it shares the same difficulties than a conventional SI engine, being highly affected by residual gases, equivalence ratio and local turbulent kinetic energy. Besides, the high surface to volume ratio implies non-negligible heat losses to the walls.

- Pre-chamber ejection: Overlapped with the PC combustion, this process consists of the ejection of gases into the main chamber. Initially the unburnt mixture acts as a turbulence source, then the hot gases act as both an ignition and a turbulence source [1]. The PC flame front can be quenched or not at the orifice, depending mainly on its diameter and equivalence ratio [2, 3].

- Jet penetration: It is reasonable to think that different engine sizes (i.e. cylinder bore) demand different penetration rates (mainly governed by the momentum at the orifice exit) to ensure a proper combustion

duration. Thus, the expectation is that the orifice diameter should be scaled with the distance between the PC and the cylinder walls.

Even though charge stratification (e.g. composition and temperature) and three-dimensional phenomena (e.g. turbulence) do play an important role in the pre-chamber combustion process, these factors are not going to be accounted for in the reasoning shown in this study. Moreover, thanks to the possibility of completely scavenge the combustion chamber before a combustion cycle on experimental facilities (e.g. Rapid Compression-Expansion Machine), the PC scavenge process will also not be accounted for. Therefore, this work is going to discuss exclusively 0D (and 1D for some aspects) phenomena, such as PC filling (section 4.3.2), PC ejection (section 4.3.2), jet penetration (section 4.4), and flame quenching (section 4.5).

4.2.2 Validation tools

Thermodynamic and mass flow validation

Based on the geometry and experimental data from a single-cylinder metallic research engine available at CMT Institute, a GT-Power model was build and used to solve the continuity, momentum and energy equations during the closed cycle (from inlet valve closing -IVC-, until exhaust valve opening -EVO-) and provide the numerical data used to compare the different PC geometries. Additionally, since the prediction of the main chamber ignitability is not necessary now, the main chamber combustion object was neglected, and the downstream jet condition during ejection is simply a non-ignited hot chamber. On the contrary, the pre-chamber combustion process needs to be correctly described, because of its vital influence on the pre-chamber behavior. In this study, it was represented by a Wiebe function, ensuring the same combustion profile for all cases, except when it was intentionally changed to highlight its effect on the pressure rise rate. The pre-chamber combustion duration and mass fraction burnt shape were determined based on experimental data. The heat transfer was modeled according to the Woschni correlation.

The initial conditions were imposed both in the main chamber and the pre-chamber at IVC, and one single cycle was calculated using the explicit solver. The composition chosen was a stoichiometric mixture between air and methane, and no residual or EGR gases were added. More details about the engine geometry and initial conditions are described in Table 4.1.

The discharge coefficient of the pre-chamber orifices was set to 1 for all cases, avoiding the effect of nozzle diameter variation in the discharge coefficient.

Table 4.1: Engine geometry and boundary conditions

Parameter	**Value**	**Units**
Engine type	4-stroke-SI	-
Stroke x Bore	80 x 80.5	mm
Compression Ratio	13.4	-
IVC	-120	CAD-ATDC
EVO	160	CAD-ATDC
Clearance volume	32.63	cm^3
Temperature at IVC	320	K
Pressure at IVC	1.0	bar
Composition at IVC	CH_4=0.055 O_2=0.220 N_2=0.725	molar fraction

Jet characteristics validation

In addition to orifice mass flow rate, jet velocity and momentum, a more complete assessment of the jet characteristics can be done by estimating a "hypothetical" jet penetration rate, which gives some idea about how far and fast the jet leading edge could go at a given time. The term "hypothetical" has been used intentionally because, in a real situation, the jet ignites the main chamber charge while it is penetrating and entraining fresh mixture, which greatly increases the complexity of the problem, requiring Computational Fluid Dynamics (CFD) calculations and detailed chemical kinetics to more accurately predict it [4].

To estimate this hypothetical jet penetration rate, a one-dimensional spray model was used. This code, developed at CMT Institute, predicts the evolution of a steady or transient turbulent jet or spray, either inert or reactive. The model development, solution procedure and more details about the model can be found in [5, 6].

In the current study, the transient input data to this spray model were imported from GT-Power and the same boundary conditions were imposed. The jet morphology (mainly cone angle) was considered the same for all prechamber geometries, since it is intended to test similar orifice geometries. Swirl and/or any other type of engine-induced air movement was not considered.

4.3 PC filling and ejection processes

4.3.1 Theoretical development

This section demonstrates some geometrical relations and combustion parameters that are important in the frame of pre-chamber design, especially for reciprocating internal combustion engine applications. At the same time, it develops a methodology to reproduce the same characteristics, in terms of pre-chamber filling and jet ejection, of a multi-orifice pre-chamber in a single-orifice pre-chamber, even if the engine speed is different.

Starting from the energy conservation equation, the objective is to point out the main variables that affect the energy flow during the pre-chamber filling and combustion processes, and how they are related to the pressure and temperature rise rate.

To perform this evaluation, two control volumes (open systems) were defined: the main chamber control volume (CV_{MC}) and the pre-chamber control volume (CV_{PC}). The CV_{MC} is surrounded by a moving control surface, which follows the piston movement, whereas the CV_{PC} is surrounded by a fixed control surface, due to its constant volume. No mass transfer beyond the pre-chamber and the main chamber is assumed. Figure 4.1 shows schematically the control volumes and their main properties.

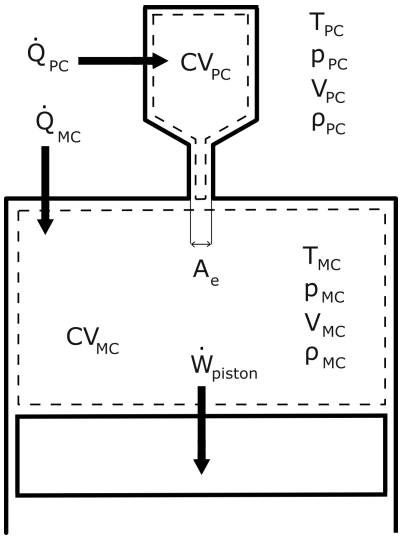

Figure 4.1: Illustration of the control volumes for main and pre-chambers.

Considering that the energy in both control volumes is essentially thermal energy (both kinetic and potential energy are neglected in the control volumes) and that the potential energy associated to the mass flow is negligible too (but here the kinetic energy is considered), the energy variation in the control volume (open system) can be defined as:

$$\frac{dE_{CV}}{dt} = \frac{dU_{CV}}{dt} = \frac{dQ_{CV}}{dt} - \frac{dW_{CV}}{dt} + \frac{dm_{CV}}{dt}\left(h_k + \frac{v^2}{2}\right) \tag{4.1}$$

where E_{CV} is the total energy in the control volume, U_{CV} is the internal energy in the control volume, Q_{CV} is the sum of heat added into the control volume, W_{CV} is the work done by the control volume, $\frac{dm_{CV}}{dt}$ is the mass flow rate across the control surface, h_k is the enthalpy corresponding to the mass being transferred, and v is the flow velocity at the orifice.

Moreover, the internal energy can be calculated as:

$$U = mc_vT \tag{4.2}$$

where c_v is the specific heat at constant volume. Deriving in time, the internal energy variation in a control volume is given by:

$$\frac{dU_{CV}}{dt} = c_{v,CV}T_{VC}\frac{dm_{CV}}{dt} + m_{CV}c_{v,CV}\frac{dT_{CV}}{dt} \tag{4.3}$$

The second term at the right-hand side can be rewritten using the equation of state (Equation 3.4) and its time derivative (Equation 3.5), as follows:

$$P_{CV}V_{CV} = m_{CV}RT_{CV} \Rightarrow T_{CV} = \frac{P_{CV}V_{CV}}{m_{CV}R} \tag{4.4}$$

$$\frac{dT_{CV}}{dt} = \frac{V_{CV}}{m_{CV}R}\frac{dP_{CV}}{dt} - \frac{P_{CV}V_{CV}}{Rm_{CV}^2}\frac{dm_{CV}}{dt} + \frac{P_{CV}}{m_{CV}R}\frac{dV_{CV}}{dt} \tag{4.5}$$

$$\frac{dU_{CV}}{dt} = c_{v,CV}T_{VC}\frac{dm_{CV}}{dt} + c_{v,CV}\left(\frac{V_{CV}}{R}\frac{dP_{CV}}{dt} - \frac{P_{CV}V_{CV}}{Rm_{CV}}\frac{dm_{CV}}{dt} + \frac{P_{CV}}{R}\frac{dV_{CV}}{dt}\right) \tag{4.6}$$

Thus, rearranging some terms, the internal energy variation in a control volume becomes:

$$\frac{dU_{CV}}{dt} = \frac{c_{v,CV}}{R}\left(V_{CV}\frac{dP_{CV}}{dt} + P_{CV}\frac{dV_{CV}}{dt}\right) \tag{4.7}$$

Now, Equation 4.1 can be rewritten as:

$$\frac{dE_{CV}}{dt} = \frac{c_{v,CV}}{R}\left(V_{CV}\frac{dP_{CV}}{dt} + P_{CV}\frac{dV_{CV}}{dt}\right) = \frac{dQ_{CV}}{dt} - \frac{dW_{CV}}{dt} + \frac{dm_{CV}}{dt}\left(h_k + \frac{v^2}{2}\right) \tag{4.8}$$

which represents the energy balance in a control volume. Now this equation will be applied to both control volumes, CV_{PC} and CV_{MC}, to obtain Eqs. 4.9 and 4.10, under the following hypotheses:

- No work is performed by CV_{PC}.
- No volume variation takes place in CV_{PC}.

$$\frac{dE_{PC}}{dt} = \frac{c_{v,PC}}{R}V_{PC}\frac{dP_{PC}}{dt} = \frac{dQ_{ch,PC}}{dt} - \frac{dQ_{ht,PC}}{dt} + \frac{dm_{CV}}{dt}\left(h_k + \frac{v^2}{2}\right) \tag{4.9}$$

$$\begin{aligned}\frac{dE_{MC}}{dt} &= \frac{c_{v,MC}}{R}\left(V_{MC}\frac{dP_{MC}}{dt} + P_{MC}\frac{dV_{MC}}{dt}\right) = \\ &= \frac{dQ_{ch,MC}}{dt} - \frac{dQ_{ht,MC}}{dt} - \frac{dW_{piston}}{dt} + \frac{dm_{CV}}{dt}\left(h_k + \frac{v^2}{2}\right)\end{aligned} \tag{4.10}$$

where, $Q_{ch,i}$ is the chemical energy released by the fuel combustion in the control volume i, $Q_{ht,i}$ are the heat losses to the walls in the control volume i and W_{piston} is the work done by the piston on the control volume. The enthalpy sub index k depends on the mass flow orientation: if it is a positive value (i.e. mass entering into the control volume) the reference are the conditions at the opposite control volume (for instance, when the mass is flowing to the pre-chamber, the enthalpy reference are the main chamber conditions).

In the following subsections, particularizations of Equations 4.9 and 4.10 are going to be presented for the pre-chamber filling process and the pre-chamber combustion (jet ejection) process.

Pre-chamber filling process

The pre-chamber filling process is defined by the period between the IVC and the angle were the PC pressure overcomes that in the MC. As a first approach, this last angle can be taken when the start of combustion (SOC)

in the PC takes place. Therefore, it comprises the period in which the pre-chamber is filled with fresh mixture coming from the main chamber, and no combustion at all occurs nor in the PC, nor in the MC. For this reason, the following additional hypotheses for the pre-chamber filling process can be taken:

1. No combustion occurs both in CV_{PC} and CV_{MC}.
2. The mass is flowing from CV_{MC} to CV_{PC}, thus the enthalpy sub index would be $k = MC$.

With these hypotheses, equations 4.9 and 4.10 become:

$$\frac{c_{v,PC}}{R} V_{PC} \frac{dP_{PC}}{dt} = -\frac{dQ_{ht,PC}}{dt} + \frac{dm_{MC}}{dt}\left(h_{MC} + \frac{v^2}{2}\right) \tag{4.11}$$

$$\frac{c_{v,MC}}{R}\left(V_{MC}\frac{dP_{MC}}{dt} + P_{MC}\frac{dV_{MC}}{dt}\right) = -\frac{dQ_{ht,MC}}{dt} - \frac{dW_{piston}}{dt} + \frac{dm_{MC}}{dt}\left(h_{MC} + \frac{v^2}{2}\right) \tag{4.12}$$

These equations can be numerically solved using either implicit or explicit methods. However, as the objective of the present study is to point out the main variables affecting the PC filing process, an approximation of the mass flow rate between chambers can be made assuming an isentropic flow through an orifice, calculated as:

$$\frac{dm}{dt} = A_e[2\rho_{up}(P_{up} - P_{down})]^{\frac{1}{2}}\varphi; A_e = C_D A_n \tag{4.13}$$

where A_e is the effective area, A_n is the nozzle area (i.e. the sum of orifice cross section areas), C_D is the discharge coefficient, ρ is the density, and φ is the compressibility factor, defined as follows:

$$\varphi = \left\{ \frac{\left(\frac{\gamma}{\gamma-1}\right)\left[\left(\frac{P_{down}}{P_{up}}\right)^{\frac{2}{\gamma}} - \left(\frac{P_{down}}{P_{up}}\right)^{\frac{\gamma+1}{\gamma}}\right]}{1 - \frac{P_{down}}{P_{up}}} \right\}^{\frac{1}{2}} \tag{4.14}$$

where γ is the specific heat ratio, and the subscript up and down refers to the conditions upstream and downstream of the orifice, respectively. Thus,

the mass flow rate from CV_{MC} to CV_{PC}, according to Equation 4.13, can be estimated as:

$$\frac{dm_{MC}}{dt} = A_e[2\rho_{MC}(P_{MC} - P_{PC})]^{\frac{1}{2}}\varphi; A_e = C_D A_n \tag{4.15}$$

Appling Equation 4.15 into Equation 4.11 and rearranging terms, the pre-chamber pressure rise rate can be expressed in terms of the effective flow area and the PC volume:

$$\frac{dP_{PC}}{dt} = \frac{A_e}{V_{PC}}\frac{R}{c_{v,PC}}[2\rho_{MC}(P_{MC}-P_{PC})]^{\frac{1}{2}}\varphi\left(h_{MC}+\frac{v^2}{2}\right) - \frac{R}{V_{PC}c_{v,PC}}\frac{dQ_{ht,PC}}{dt} \tag{4.16}$$

The equations presented until now are all described in terms of time. However, in reciprocating internal combustion engine applications, it might be more useful to describe them in crank angle basis, which introduces an important characteristic time: the engine speed (N, in rpm; n, in rps). Thus, the time variation can be written in terms of crank angle degrees (θ) as follows:

$$t = \theta\frac{1}{n(rps)}\frac{1}{360} = \theta\frac{1}{N(rpm)}\frac{1}{6} \tag{4.17}$$

If Equation 4.17 is differentiated, the relationship between dt and $d\theta$ can be found:

$$dt = d\theta\frac{1}{N(rpm)}\frac{1}{6} \tag{4.18}$$

Rewriting Equation 4.16 in crank angle basis:

$$\frac{dP_{PC}}{d\theta} = \frac{1}{6N}\left\{\frac{A_e}{V_{PC}}\frac{R}{c_{v,PC}}[2\rho_{MC}(P_{MC} - P_{PC})]^{\frac{1}{2}}\varphi\left(h_{MC}+\frac{v^2}{2}\right) - \frac{R}{V_{PC}c_{v,PC}}\frac{dQ_{ht,PC}}{d\theta}\right\} \tag{4.19}$$

Therefore, the pre-chamber pressure rise rate is a function of the thermodynamic conditions of both chambers, as well as the heat losses to the wall, the effective flow area, the pre-chamber volume and the engine speed. Assuming that a given pre-chamber pressure rise rate is intended to be reproduced in a new engine or a new PC configuration, and that the heat losses term is small compared to the other term in the equation (this will be demonstrated

later, during the validation section), the following actions might be taken. First, to preserve the angular evolution of the main chamber thermodynamic conditions (ρ, h and P, all of them appearing in the equation), the engine compression ratio must be kept the same. Then, to preserve the thermodynamic conditions at the pre-chamber (P and $dP/d\theta$), it is necessary to keep the parameter $A_e/V_{PC}N$. With this last criterion the mass flow rate is scaled according to the pre-chamber volume and engine speed, by introducing a variation in the effective flow area. Thereby, the energy flux in terms of enthalpy and kinetic energy associated to the mass flow is scaled, and a similar pressure rise rate is achieved in both pre-chambers with this new configuration.

Pre-chamber ejection process

As a complement to the previous sub-section, where the pre-chamber filling process was studied, the following analysis will evaluate the period from the pre-chamber SOC until the EVO. This phase comprises the period in which the pre-chamber mixture is ignited and the hot combustion products are ejected to the main chamber.

Now, the following additional hypotheses for the pre-chamber combustion process can be assumed:

1. No combustion occurs in CV_{MC}.
2. The mass is flowing from CV_{PC} to CV_{MC}, thus the enthalpy sub index would be $k = PC$.

If the previous hypotheses are considered in Eqs. 4.9 and 4.10, they become, respectively:

$$\frac{c_{v,PC}}{R} V_{PC} \frac{dP_{PC}}{dt} = \frac{dQ_{ch,PC}}{dt} - \frac{dQ_{ht,PC}}{dt} + \frac{dm_{PC}}{dt} \left(h_{PC} + \frac{v^2}{2} \right) \tag{4.20}$$

$$\begin{aligned} \frac{c_{v,MC}}{R} \left(V_{MC} \frac{dP_{MC}}{dt} + P_{MC} \frac{dV_{MC}}{dt} \right) = \frac{dQ_{ch,MC}}{dt} - \frac{dQ_{ht,MC}}{dt} \\ - \frac{dW_{piston}}{dt} + \frac{dm_{PC}}{dt} \left(h_{PC} + \frac{v^2}{2} \right) \end{aligned} \tag{4.21}$$

Using the approximation to the mass flow rate as an isentropic flow through an orifice (Equation 4.13), the energy variation in CV_{PC} becomes:

$$\frac{c_{v,PC}}{R}V_{PC}\frac{dP_{PC}}{dt} = \frac{dQ_{ch,PC}}{dt} - \frac{dQ_{ht,PC}}{dt} - A_e[2\rho_{PC}(P_{PC}-P_{MC})]^{\frac{1}{2}}\varphi\left(h_{PC}+\frac{v^2}{2}\right) \tag{4.22}$$

Rewriting in a crank angle basis and rearranging terms, the pre-chamber pressure rise rate during pre-chamber combustion can be expressed as:

$$\begin{aligned}\frac{dP_{PC}}{d\theta} &= \frac{R}{c_{v,PC}}\rho_{PC}(F/A)_{stoich}F_R LHV\frac{dx_{b,PC}}{d\theta} \\ &- \frac{A_e}{V_{PC}N}\frac{R}{c_{v,PC}}\frac{1}{6}[2\rho_{PC}(P_{PC}-P_{MC})]^{\frac{1}{2}}\varphi\left(h_{PC}+\frac{v^2}{2}\right) \\ &- \frac{R}{V_{PC}c_{v,PC}}\frac{dQ_{ht,PC}}{d\theta}\end{aligned} \tag{4.23}$$

where R is the gas constant, F_R is the fuel-to-air equivalence ratio, LHV is the Lower Heating Value of the fuel, and $x_{b,PC}$ is the fuel mass fraction burned at CV_{PC}, which can be approximated by a Wiebe function [7]:

$$x_b = 1 - exp\left[-a\left(\frac{\theta-\theta_0}{\Delta\theta}\right)^{m_{wiebe}+1}\right] \tag{4.24}$$

where θ is the current crank angle, θ_0 the start of combustion, $\Delta\theta$ the total combustion duration in CAD and m_{wiebe} and a are tuning parameters. It is worth to indicate that this approximation to the combustion profile is completely unnecessary for the conclusions derived from Equation 4.23 presented in the next paragraph, but it will be a very helpful choice to analyze the effect of the combustion duration on the PC behavior, as will be shown later.

To conclude this theoretical development, Equation 4.23 is quite similar to Equation 4.19, already seen in the previous subsection. The pressure rise is now represented by two terms: a new term related to the heat introduced by the combustion process, and an energy flux associated to the mass transfer (already presented in Equation 4.19). Therefore, to reproduce the jet characteristics after the pre-chamber combustion, it is necessary to preserve both the relation $A_e/V_{PC}N$ previously discussed, as well as the pre-chamber mass fraction burning rate.

4.3.2 Validation and discussion

In the current section, the relation between geometrical and operating parameters presented and discussed in the previous section will be validated.

The pressure and temperature rise rate, pressure drop and mass flow rate will be evaluated both during the pre-chamber filling and ejection processes.

As depicted in the theoretical development, a similar pressure rise rate in the pre-chambers that comply with the relation $A_e/V_{PC}N$ and exhibit a similar combustion process is expected to be obtained. Therefore, changes in (a) the pre-chamber volume, (b) the effective flow area and (c) engine speed will be performed to prove this assumption. Moreover, there will be one case that purposely will not comply with the relation $A_e/V_{PC}N$, highlighting the discrepancy.

As already discussed, the PC combustion process is greatly affected by the local turbulence and residual gas fraction, which in turn are affected by the PC shape and orifice arrangement. However, these phenomena will not be accounted for in this first approach. For this reason, the center of combustion (CA50) is fixed at 10 crank angle degrees (CAD) before top dead center (BTDC) and the combustion duration, defined as the crank angle degrees between 10 and 90% of the PC burned fuel mass (CA10-90), is set to 5 CAD.

A multi-orifice pre-chamber configuration was taken as the baseline case, and it was tested (with the calculation tools presented in Section 2) along with another four single-orifice pre-chambers. Except for pre-chamber PC 2, all geometries comply with the aforementioned relation: $A_e/V_{PC}N$. Additional pre-chamber specifications are shown in Table 4.2.

Table 4.2: Dimensions and specifications of the simulated pre-chambers

Parameter	**Pre-chamber**				
	Baseline	PC 1	PC 2	PC 3	PC 4
Nozzle diameter [mm]	0.70	1.71	0.70	2.10	2.42
Number of nozzles [-]	6	1	1	1	1
V_{PC} $[mm^3]$	600	600	600	900	600
A_e $[mm^2]$	2.31	2.31	0.38	3.46	4.62
N [rpm]	2000				4000
$A_e/(V_{PC}\, n)$ $[(m/s)^{-1}]$	0.115	0.115	0.019	0.115	0.115
V_{PC}/V_{MC} [%]	1.84	1.84	1.84	2.76	1.84
Combustion duration (CA10-90) [CAD]	5				

The baseline multi-orifice pre-chamber geometry was chosen as being a representative one of a passenger car engine, and has already been extensively tested in a research engine at CMT Institute [8]. The single-orifice

pre-chamber configurations (PC 1 to 4) were chosen as follows: PC 1 preserve the baseline volume and the effective flow area. PC 2 preserve the nozzle diameter and the baseline volume, evidencing the error when a multi-orifice pre-chamber is tried to be reproduced in this manner. PC 3 increase both volume and flow area. PC 4 preserve the baseline volume and adjust the effective flow area to compensate the engine speed variation. The engine speed of 2000 and 4000 rpm were chosen arbitrarily as they fall in the typical operating range of passenger car engines. The choice of other engine speeds would not impair the validation of the proposed relationships.

Pre-chamber filling process

Figure 4.2 shows the pre-chamber pressure, pressure drop between chambers and the mass flow rate (in kilograms per CAD) divided by the pre-chamber volume during the filling process. The use of kilograms per CAD instead of per second helps not to confuse the interpretation under different engine speed, since the energy flux and the thermodynamic properties are given in terms of CAD. It is clearly seen that PC 2, the only geometry that do not satisfy the aforementioned relation, presents a disparate pressure profile. This occurs due to the lower mass transfer to the pre-chamber than the needed to increase its pressure in the same rate as the baseline. Therefore, the energy associated to the mass flowing into the pre-chamber (here in terms of enthalpy and kinetic energy) needs to be scaled with the pre-chamber volume. In other words, to reproduce with a given pre-chamber the same pressure rise rate than a baseline, the mass flow rate (in kilograms per CAD) to the pre-chamber (which is a function of the flow area and engine speed) must be scaled with its volume and/or engine speed: this is the reason why when the mass flow rate through the PC holes is divided by the PC volume, the same pattern is found for all PC's that satisfy the aforementioned relation (third column of Figure 4.2).

Since the same initial conditions in the main and pre- chamber are imposed at IVC, and the pressure rise rate is kept the same too, the temperature evolution in the pre-chamber, shown in Figure 4.3), will naturally be reproduced for the scaled pre-chambers.

Pre-chamber ejection process

Since the geometrical aspects that govern the mass flow between chambers have just been discussed in the previous subsection, here only the results regarding the pre-chamber combustion and jet ejection will be presented. It is

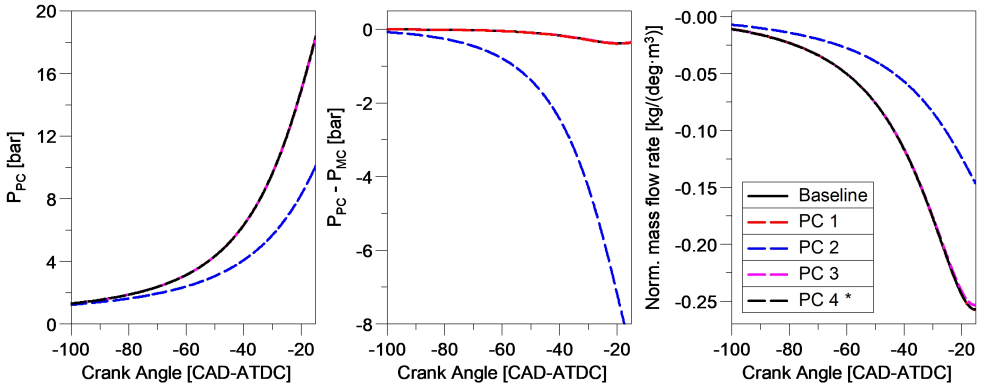

*Figure 4.2: PC pressure, pressure difference to MC, and normalized mass flow rate during PC filling. * case at 4000 rpm.*

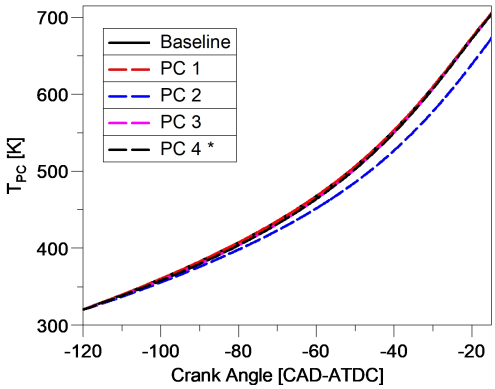

*Figure 4.3: PC temperature during the compression stroke (PC filling). * case at 4000 rpm.*

important to note that the mass fraction burning rate ($dx_b/d\theta$) from Equation 4.20) was equally imposed in all pre-chambers, i.e. the center of combustion (CA50) and combustion duration (CA10-90) are equal in all cases.

Figure 4.4 shows the pre-chamber pressure, the pressure drop from PC to main chamber and the mass flow rate (in kilograms per CAD) divided by the pre-chamber volume during the pre-chamber ejection process. Once again, the pre-chambers that are designed with the same $A_e/V_{PC}N$ relation present a similar pressure rise rate. As well as in the filling process, the energy exchange between chambers is associated to the mass transfer, which is governed by this

geometrical relation previously presented.

Thus, since the rate of mass fraction burned is preserved, the volume necessary to satisfy the relation $A_e/V_{PC}N$ to a given pre-chamber ensures that the amount of total heat released by the fuel (given by the fuel mass) was the one needed to compensate the energy loss associated to the mass flow rate to the main chamber. This can be seen in Figure 4.4 to the right, where the mass flow rate divided by the pre-chamber volume ($kg/(deg\,m^3)$) is preserved in all pre-chambers, except PC 2, evidencing that the heat released by the fuel is counteracted by the mass flow rate, preserving the rate of pressure rise in the pre-chamber during the combustion process.

Although crucial for early flame kernel development and wall-induced quenching, the PC heat losses represents a small fraction of the total energy available in the pre-chamber. Consequently, small differences in terms of PC geometry that could affect the heat transfer coefficient (surface area to volume ratio, turbulence intensity, and so on) should not influence the pressure rise rate as much as not satisfying the $A_e/V_{PC}N$ relation, which is depicted by PC 1 adiabatic in Figure 4.4.

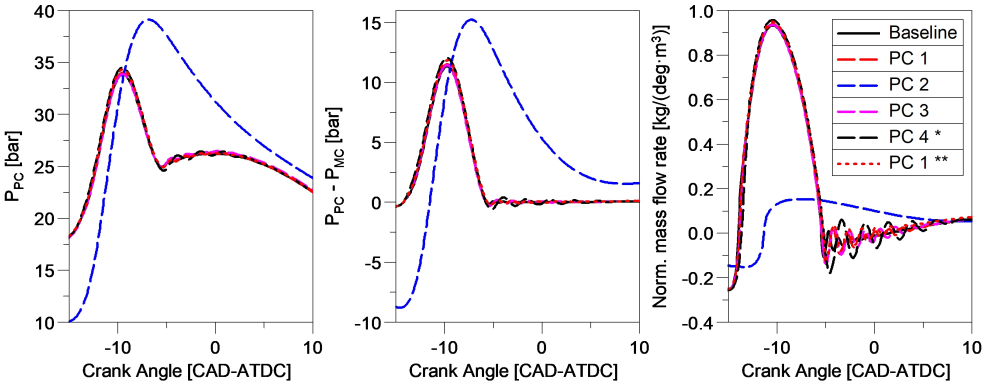

*Figure 4.4: PC pressure, pressure difference to MC, and normalized mass flow rate during the PC combustion process. * case at 4000 rpm ** case adiabatic.*

The disparate PC pressure profile obtained for PC 2 already seen in the previous figure, leads to a dissimilar jet velocity and momentum pattern, as can be seen in Figure 4.5, where the pre-chambers that satisfy the relation $A_e/V_{PC}N$ present the same curve shape for these parameters, merely multiplied with a factor given by the orifice cross-section area in the case of the jet momentum.

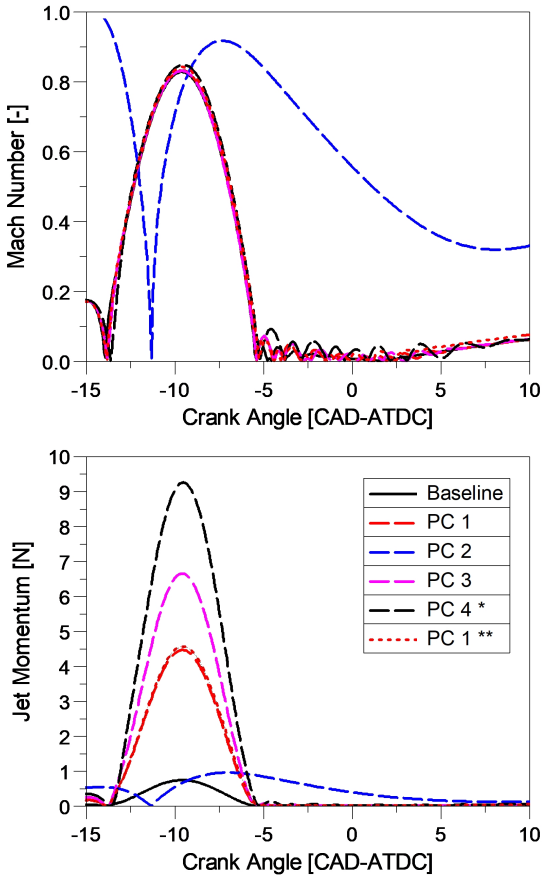

*Figure 4.5: Mach number (upper) and jet momentum (bottom). * case at 4000 rpm ** case adiabatic.*

Likewise to the filling process, if the pressure rise rate is kept constant, the temperature evolution in the pre-chamber during the combustion process, shown in Figure 4.6, will naturally be reproduced for the scaled pre-chambers. Obviously, the adiabatic pre-chamber case presents a higher post-combustion temperature. However, during jet ejection (concomitant with PC combustion), the heat transfer does not seem to have a substantial effect.

Effect of pre-chamber combustion duration

Here, a brief discussion about the effect of the pre-chamber combustion process is presented. In the previous sub-section, the pre-chamber mass fraction burning rate was assumed to be equal in all cases. However, this might

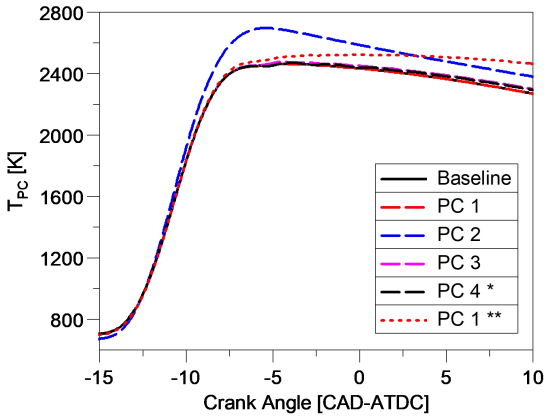

*Figure 4.6: PC mean gas temperature during the PC combustion process. * case at 4000 rpm ** case adiabatic.*

not be the case in some conditions or for some designs. Thus, to highlight the contribution of the combustion term to the pre-chamber pressure rise rate, as presented in Equation 4.23, a comparison between two combustion durations for the same pre-chamber geometry was done.

Figure 4.7 presents the pre-chamber pressure, pressure drop and mass flow rate of the two combustion duration cases. The rate of mass fraction burned was changed by means of the combustion duration (the CA50 of this combustion, however, is kept the same), evidencing that a lower rate of mass fraction burned (longer combustion duration) provokes a lower rate of pressure rise in the pre-chamber. Since the total heat released by the fuel is preserved, the energy delivered to the main chamber is preserved too, and only the rate at which this energy is released changes. Thus, different start of jet ejection, ejection velocity and penetration rate are expected.

It can be concluded that the combustion duration must be kept constant when trying to emulate a given reference PC configuration. However, how to ensure this is well beyond the scope of the present research, since this parameter is governed by the local turbulence in the PC, the PC scavenging process, the residual mass fraction, etc., which are not easy to be determined, nor controlled.

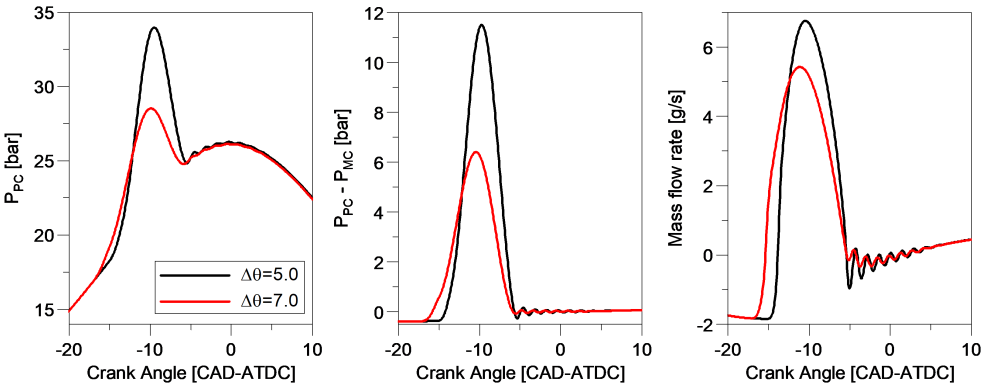

Figure 4.7: Effect of the combustion duration on the PC pressure, pressure difference to MC, and mass flow rate during the PC combustion process.

4.4 Jet penetration

Since how to preserve the pre-chamber thermodynamic conditions was already discussed and validated in previous sections, in this section the jet penetration issue is going to be discussed. Conjointly with the pre-chamber thermodynamic conditions, the jet penetration do play an important role during the main chamber ignition process. Therefore, when a given pre-chamber is emulated under simplified conditions (e.g. single orifice), the relative jet penetration (i.e. normalized by the distance from the orifice to the walls) rate (i.e. penetration per CAD) should be also reproduced.

As proposed by Desantes et al. [9] the jet-tip penetration (s) for a turbulent iso-dense gas jet (i.e. with the same density in both the injected and the ambient gas) can be described as:

$$s = k_p(d_o u_o t)^{1/2} \tag{4.25}$$

where k_p, d_o, u_o and t are a proportionality constant, the orifice diameter, the initial axial velocity at the orifice exit and the time from start of injection, respectively. This equation is valid when the environment is quiescent, the effective Schmidt number is 1, and the jet velocity, the cone angle, the air density, and the jet density are constant during the injection process.

In order to preserve the relative jet penetration rate (per CAD), even under different engine speed, the jet-tip penetration can be normalized by

the distance to the walls (L), and the time dependency can be transformed into angular dependency introducing the engine speed (N, in rpm), so the of Equation 4.25) can be rewritten as:

$$\frac{s}{L} = k_p \left(\frac{d_o u_o}{L^2} \frac{\theta}{6\,N} \right)^{1/2} \tag{4.26}$$

Since the jet velocity u_o is preserved when the relation $A_e/V_{PC}N$ is satisfied, to preserve the relative jet penetration rate (s/L), it is necessary to preserve the relation $d_o/(L^2N)$. Thus, even not knowing the exact value of the jet-tip penetration of a baseline PC, it is possible to design a scaled pre-chamber according to the main chamber geometry and engine speed of both configurations: the PC emulated and the PC to be studied in the experimental facility.

As previously discussed in section 4.2.2, a hypothetical inert jet penetration rate was calculated using a one-dimensional spray model. In this study a constant and equal angle was assumed for all pre-chambers, as well the Schmidt number was assumed as equal to 1. The jet penetration was estimated for a baseline and two other pre-chambers, all satisfying the relation $A_e/V_{PC}N$. The PC 1 corresponds to the single orifice configuration with the same volume as baseline. The PC 5 corresponds to the single orifice configuration that reproduces the same relative jet penetration rate as the baseline with twice the engine speed, defined by means of the relation $d_0/(L^2N)$. Additional pre-chamber specifications are shown in Table 4.3.

Figure 4.8 shows the jet penetration for the three tested geometries. Comparing the baseline and PC 5, it is noticed that it is feasible to adequate the orifice diameter and the PC volume to achieve the same jet penetration as a reference PC at a different engine speed. The requirements are: (1) to apply the relation $d_0/(L^2N)$ to identify the orifice diameter that compensates the engine speed variation and (2) apply the relation $A_e/V_{PC}N$ to determine the pre-chamber volume. Moreover, if it is necessary to adjust the total penetration according to the size of the combustion chamber, the relation $d_0/(L^2N)$ demonstrates that it is proportional to the square root of the increment in orifice diameter, as verified by the case PC 1 ** in Figure 4.8, which is the penetration of PC 1 divided by the square root of $d_{PC\,1}/d_{baseline}$.

*Table 4.3: PC specifications for jet penetration assessment. *Suitable chamber length.*

Parameter	**PC geometry**		
	Baseline	PC 1	PC 5
Nozzle diameter [mm]	0.70	1.71	1.40
Number of nozzles [-]	6	1	1
L [mm]	40	62.6*	40
V_{PC} $[mm^3]$	600	600	200
A_e $[mm^2]$	2.31	2.31	1.54
N [rpm]	2000		4000
$A_e/(V_{PC}\, n)$ $[(m/s)^{-1}]$	0.115		
$d_0/(L^2 N)$ $[(m/s)^{-1}]$	0.0131		
V_{PC}/V_{MC} [%]	1.84	1.84	0.61
Combustion duration (CA10-90) [CAD]	3		

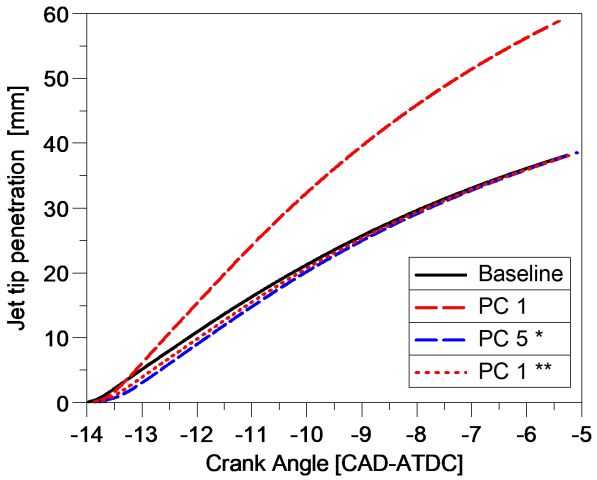

*Figure 4.8: Simulated jet tip penetration. * case at 4000 rpm. ** Normalized by the distance to the walls (L).*

4.5 Orifice flame quenching

In addition to the physical characteristics, the jet chemical characteristics are crucial to the main chamber ignition process. The question here is whether the flame front can survive or not to the high stretch rate as it passes through the orifice: if the flame can pass through, the jet would be composed by active species that quickly promote the chain-branching in the main chamber; on the contrary, if the flame is quenched, the jet would be composed by hot combustion products with a lower content of radicals.

The approach traditionally used in SI engines to determine the quenching distance in close to walls regions or in crevices, which is estimated from the balance between the heat released within the flame and the heat loss to the walls [7, 10], seems to be not valid to estimate the quenching diameter in pre-chamber applications due to the very large velocity gradients.

Mastorakos et al. [11] observed, by means of experimental data and CFD Large Eddy Simulation, that the flame quenching may be more related to the excessive stretch than to the wall heat transfer in the orifice. In addition, the orifice diameter may lead to exceed the maximum curvature tolerated by the flame front. Although the exact numerical relationship between radius of curvature of the cylindrical flame and flame thickness is not clear at present, the orifice diameter needed to prevent flame extinction is proposed to be at least twice the flame thickness [11].

T. Adams [12] suggested that for a flame to pass through the orifice without being extinguished, the characteristic time of turbulence must be greater than the characteristic time of combustion, leading to a relation between flame thickness (δ), flow velocity at the nozzle (v) and flame propagation velocity (v_f), given by:

$$d_o \geq \frac{\delta\, v}{2\, v_f} \tag{4.27}$$

S. Biswas et al. [3] do not correlated the flame quenching at the orifice directly with its diameter. However, they proposed to evaluate the Damköhler number at the orifice exit to characterize the main chamber ignition mechanism. The two mechanisms proposed by the authors are based on the presence of active radicals (e.g. OH), which evidence that flame quenching do not occur at the orifice. For methane, the authors found that the transition between mechanisms occur at a Damköhler number range between 300 and 350. The use of a non-dimensional number such as the Damköhler number, allows to transfer this knowledge from test rigs to engine-like conditions.

Therefore, the Damköhler number calculated based on the orifice exit conditions can be used as a flame quenching quantification parameter. For torch ignition systems, where there is no flame quenching at the orifice, the Damköhler number should be at least equal or greater than the reference case, whereas for jet ignition systems, where there is flame quenching at orifice, the Damköhler number should be at least less or equal than the reference case.

The Damköhler number is the ratio of the characteristic eddy turnover time τ_T to the characteristic chemical reaction time τ_L, as described by:

$$Da = \frac{\tau_T}{\tau_L} = \frac{\frac{l_I}{u^{'}}}{\frac{\delta_L}{S_L}} \tag{4.28}$$

where l_I, $u^{'}$, δ_L and S_L are the integral scale (proportional to the orifice diameter), the turbulence intensity (proportional to the jet velocity), the laminar flame thickness and the laminar flame speed (both depend on the composition and thermodynamic conditions), respectively.

When reproducing a multi-orifice reference PC into a single orifice PC using the methodology presented at the previous sections, it is expected that the jet velocity would be preserved and the orifice diameter would be increased. This approach leads to increasing the characteristic turbulent eddy turnover time in comparison to the reference case and, in some cases, could prevent the flame quenching at orifice when it should occur. Therefore, one of the possibilities to preserve the flame quenching at orifice is to proportionally increase the characteristic chemical reaction time by adjusting the equivalence ratio. In the previous example, a lower equivalence ratio would provide a thicker and slower laminar flame, increasing the characteristic chemical reaction time and recovering the Damköhler number of the reference case. However, it is worth to mention that modifying the equivalence ratio also has some secondary, but important, effects (i.e. worse conditions to flame propagation at pre- and main chambers) that could affect the PC pressure rise rate.

4.6 Summary and conclusions

In this section three relations between the geometrical and the engine operating parameters have been identified and presented: $A_e/V_{PC}N$, $d_0/(L^2N)$ and the Damköhler number. The conservation of the first relation between two pre-chambers, assuming a similar pre-chamber combustion process, ensures an identical pre-chamber pressure rise rate in both cases, whereas the conservation of the second relation allows the preservation of the relative jet

penetration rate even at a different engine speed. This is possible as a result of a scaled mass flowing in and out of the pre-chamber according to its volume, engine speed, and distance to the walls, given by the effective flow area determined from those relations. The fulfillment of the third relation, the Damköhler number, guarantees that the flame-quenching phenomenon is reproduced.

Moreover, the following conclusions can be deduced from this study:

- The design criteria presented in this work serve as a guideline to reproduce reference pre-chamber geometries under simplified conditions, keeping as much as possible the flow conditions, the thermodynamic parameters, and the jet characteristics.
- For torch ignition systems the Damköhler number should be at least equal or greater than the reference case, whereas for jet ignition systems the Damköhler number should be at least less or equal than the reference case.
- The most convenient situation is when a "sector" (i.e. the volume and flow area are divided by the number of orifices) of a multi-orifice PC is reproduced. Only in this way, the Damköhler number and the thermodynamic conditions are preserved simultaneously, maintaining the turbulence intensity and the integral scale, as well as the characteristic chemical time. For any other choice, there will always be a compromise between faithfully reproducing the thermodynamic conditions (preserving $A_e/V_{PC}N$) and the relative jet penetration (preserving $d_0/(L^2N)$) or the flame quenching phenomenon (preserving the Damköhler number). A possible way to address this problem is to play with the PC parameters so as to correctly reproduce both the thermodynamic conditions and the relative jet penetration, paying also attention to increasing the Damköhler number if the reference case works in the flame ignition regime, or decreasing this number if the reference case operates in the jet ignition regime.
- Although it was not the main objective of this research, the methodology approach presented in this work can be used to transfer information among different engine sizes. For instance, the knowledge of pre-chambers for large bore engines can be transferred to pre-chambers of passenger cars, and vice versa, serving as a design tool to new pre-chamber geometries, regardless of its application.

References

[1] Malé, Quentin et al. "Large Eddy Simulation of Pre-Chamber Ignition in an Internal Combustion Engine". In: *Flow, Turbulence and Combustion* 103.2 (2019), pp. 465–483. DOI: 10.1007/s10494-019-00026-y.

[2] Tian, Jiangping, Cui, Zechuan, Ren, Zhongyong, Tian, Hua, and Long, Wuqiang. "Experimental study on jet ignition and combustion processes of natural gas". In: *Fuel* 262.July 2019 (2020), p. 116467. DOI: 10.1016/j.fuel.2019.116467.

[3] Biswas, Sayan, Tanvir, Saad, Wang, Haifeng, and Qiao, Li. "On ignition mechanisms of premixed CH 4 /air and H 2 /air using a hot turbulent jet generated by pre-chamber combustion". In: *Applied Thermal Engineering* 106 (2016), pp. 925–937. DOI: 10.1016/j.applthermaleng.2016.06.070.

[4] Qin, Fei et al. "Detailed numerical simulation of transient mixing and combustion of premixed methane/air mixtures in a pre-chamber/main-chamber system relevant to internal combustion engines". In: *Combustion and Flame* 188 (2018), pp. 357–366. DOI: 10.1016/j.combustflame.2017.10.006.

[5] Pastor, J.V., Lopez, J. Javier, García-Oliver, J.M., and Pastor, José M. "A 1D model for the description of mixing-controlled inert diesel sprays". In: *Fuel* 87.13-14 (2008), pp. 2871–2885. DOI: 10.1016/j.fuel.2008.04.017.

[6] Desantes, J.M., Pastor, J.V., García-Oliver, J.M., and Pastor, J.M. "A 1D model for the description of mixing-controlled reacting diesel sprays". In: *Combustion and Flame* 156.1 (2009), pp. 234–249. DOI: 10.1016/j.combustflame.2008.10.008.

[7] Heywoood, John B. *Internal Combustion Engine Fundamentals*. Second ed. New York, N.Y.: McGraw Hill, 2018, p. 1056.

[8] Benajes, J. et al. "Evaluation of the passive pre-chamber ignition concept for future high compression ratio turbocharged spark-ignition engines". In: *Applied Energy* 248 (2019), pp. 576–588. DOI: 10.1016/j.apenergy.2019.04.131.

[9] Desantes, Jose M., Arregle, Jean, Lopez, J. Javier, and Cronhjort, Andreas. "SCALING LAWS FOR FREE TURBULENT GAS JETS AND DIESEL-LIKE SPRAYS". In: *Atomization and Sprays* 16.4 (2006), pp. 443–474. DOI: 10.1615/AtomizSpr.v16.i4.60.

[10] Turns, Stephen R. *An introduction to combustion: concepts and applications*. 2nd. Vol. 499. McGraw-Hill, 2000, p. 411.

[11] Mastorakos, Epaminondas et al. "Fundamental Aspects of Jet Ignition for Natural Gas Engines". In: *SAE International Journal of Engines* 10.5 (2017), pp. 2017–24–0097. DOI: 10.4271/2017-24-0097.

[12] Adams, T. G. "Theory and Evaluation of Auxiliary Combustion (Torch) Chambers". In: *SAE Prepr.* 780631. 1978, pp. 2328–2339. DOI: 10.4271/780631.

Chapter 5

The pre-chamber ignition concept applied in a Rapid Compression-Expansion Machine

5.1 Introduction

Chapter 4 has demonstrated the fundamental aspects to reproduce a reference case in a simplified experimental facility, highlighting the effect of the PC volume, diameter and number of orifices, as well as PC combustion development, on the main drivers of jet ejection and its effect on the hypothetical inert jet penetration calculated using a one-dimensional spray model. From this theoretical study, an important geometrical parameter was derived: $A_e/V_{PC}N$, which represents the ratio between the effective flow area (i.e. geometrical area multiplied by the discharge coefficient) of the orifices and the product of PC volume and engine speed. In this chapter, therefore, the parameters suggested by the theoretical studies are used to design five PC geometries to be experimentally tested in a Rapid Compression-Expansion Machine (RCEM).

In this sense, a comprehensive assessment of the pre-chamber ignition system will be carried out by means of schlieren and OH-chemiluminescence optical techniques, as well as in-cylinder pressure measurements for both PC and MC, supported by 1D and 3D simulations. First, the design motivation

of each PC along with its geometrical characteristics are described. Then, the assumptions and main equations used in the PC and MC thermodynamic analysis are presented. Next, the typical aspects found with the pre-chamber ignition system in the RCEM are detailed, explaining what can be seen from the different optical techniques employed, and how it is linked to the indicated pressure data. After that, the effect of the geometrical parameters of each PC is assessed in terms of the $A_e/V_{PC}N$ parameter, PC length, and orifice length. Finally, the effect of the fuel-air equivalence ratio and the EGR rate on the jet ejection and MC ignition are reported.

Given the operating principle of the RCEM, collecting a sample size large enough (e.g. 30 cycles) to conduct a statistical study on every PC geometry and operating condition would be unfeasible for the proposed study. Therefore, both the imaging and indicated data presented in this chapter refer to the most representative cycle among those performed/registered. The most representative cycle was determined based on the maximum piston position (thus compression ratio), spark timing, and the location of the maximum main chamber pressure of each cycle, aiming to compare the most similar cases to avoid secondary effects caused by factors that are not related to the pre-chamber.

5.2 Pre-chamber geometries

Five different single orifice pre-chamber geometries were proposed to validate the governing relations, as well as to evaluate separately the effect of (1) the orifice diameter and its length-to-diameter ratio, and (2) the pre-chamber volume and its length. All the pre-chamber dimensions as well as an illustration of the internal PC geometry are found in Table 5.1 and Figure 5.1.

Aiming to use a pre-chamber configuration as close as possible to those found on ICE, a six-orifice pre-chamber configuration designed and experimentally tested at the CMT Institute was chosen as the baseline case [1, 2]. Based on its dimensions and taking into account the manufacturing constraints due to the instrumentation, the PC1 orifice diameter and volume were determined employing the geometrical relations presented in chapter 4. This PC1 retains the same PC pressure evolution as the six-orifice baseline pre-chamber, conserving at the same time the flow velocity at the orifice during PC filling and jet ejection. It is worth mentioning that the designed PC body diameter was 10 mm, but it was discovered after experimental tests that, due to a manufacturing flaw, the diameter is 9 mm.

Table 5.1: Pre-chamber dimensions for RCEM operation (measurements obtained using silicone molds).

Parameter	**Units**	**PC 1**	**PC 2**	**PC 2+**	**PC 3**	**PC 4**
Orifice diameter (d_o)	mm	2.72	2.22	2.22	2.24	2.87
Orifice length (L_o)	mm	5.0	4.1	4.1	3.3	6.8
Length-to-diameter orifice ratio (L_o/d_o)	-	1.8	1.8	1.8	1.5	2.4
Cone angle	deg	120	72	72	72	72
Pre-chamber body diameter	mm	9	8	8	10	10
Pre-chamber volume (V_{pc})	mm^3	1461	1071	1610	1564	1626
Equivalent engine speed (N)	rpm			1290		
$A_n/(V_{pc}\, n)$	$(m/s)^{-1}$	0.185	0.168	0.112	0.117	0.185
Distance from orifice exit to chamber wall (L)	mm			64		
$d_o/(L^2\, n)$	$(m/s)^{-1}$	0.047	0.038	0.038	0.039	0.049

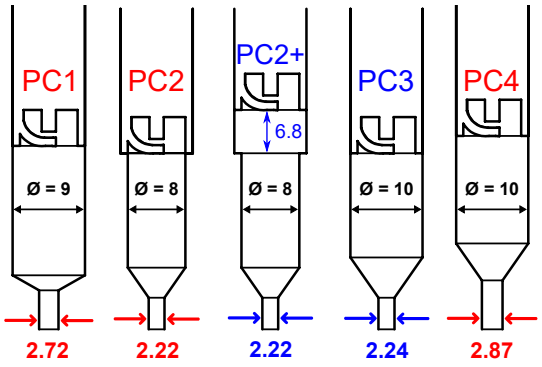

Figure 5.1: Illustration of the pre-chamber internal geometry for RCEM operation (drawn to scale).

For PC2, however, the objective is to reduce the PC volume by changing the internal diameter from 9 to 8 millimeters and scale the orifice diameter to keep the same value for the $A_e/V_{PC}N$ parameter. Once again, preserving this parameter between PC1 and PC2, the PC pressure evolution during PC filling and jet ejection is also preserved.

Taking advantage of the flexibility of the spark plug position, PC2+ uses the PC2's body with a spacer on the spark plug seat. By doing this, the PC volume is restored to PC1's level and the $A_e/V_{PC}N$ relation is no longer preserved. The primary effect expected is a higher pressure difference between chambers during PC filling and jet ejection due to the higher energy amount (i.e. mass with enthalpy) to be transferred through the same orifice area. The secondary effect is that the distance from spark plug to orifice is also increased, that is, the flame travel length inside the pre-chamber will be longer for PC2+.

PC3 adopts the same approach of PC2+ in terms of $A_e/V_{PC}N$ relation, but brings back the inner PC diameter to 10 millimeters (conserving the PC length of PC1 and PC2). Hence, the effect of the lower value for the $A_e/V_{PC}N$ relation is evaluated separately and at an equivalent PC length in relation to PC1 and PC2.

Lastly, the PC4 geometry was designed to assess the effect of the orifice length-to-diameter ratio (L_o/d_o) on the jet ejection characteristics. It preserves the same volume and orifice diameter as PC1, but has a larger orifice length. The main differences expected are in the jet penetration angle, but the heat transfer through the orifice can also be affected due to the higher residence time.

The equivalent engine speed presented in Table 5.1 is an estimation based on the time-elapsed during the rapid compression stroke, and is shown for the sake of reference of the RCEM conditions to those found in a reciprocating ICE. The target in-cylinder pressure and temperature conditions at TDC are, respectively, 34 bar and 850 K, similar to those found in a high-compression ratio turbocharged engine under high load [1]. Due to the large TDC volume as a result of the new RCEM arrangement for PC optical studies, the initial pressure of 2 bar (absolute) and the piston stroke of 150 mm were set to achieve the TDC thermodynamic conditions in the RCEM. As presented in section 3.2, the RCEM experimental facility does not relies on a crankshaft to drives the piston up and down, but rather on a hydraulic-pneumatic system to push the piston towards TDC, and the counter pressure from the combustion chamber to push the piston towards BDC during the expansion stroke. Given the RCEM operating constrains, it was unable to modify the equivalent engine speed preserving the compression ratio, impairing the experimental validation of the engine speed factor on the $A_e/V_{PC}N$ relation.

Because of the impossibility of accessing conventional measuring equipment, the internal geometry of the pre-chambers was characterized after the experimental campaign by using a non-destructive methodology based on silicon mold impressions [3]. This technique allowed the accurate measurement of the orifice characteristics such as diameter, length, and cylindricity, as well as the pre-chamber body characteristics as cone angle, diameter, volume, and length by means of microscope images of the silicon molds, as shown in Figure 5.2. A manufacturing flaw was then detected in the PC1, which had a smaller internal diameter and a larger cone angle to the orifice. Table 5.1 already reflect the measurements using the silicone molds.

5.2.1 Discharge coefficient

One of the variables that influence the application of the geometrical relations previously presented is the effective nozzle area (A_e): the product of the geometrical area and the discharge coefficient (C_D) of the orifice. Unfortunately, this last variable cannot be directly measured during the experimental campaign, and flow rate test benches cannot reproduce the thermodynamic conditions found during the jet ejection. To circumvent this difficulty, a three-dimensional (3D) computational fluid dynamic (CFD) parametric study was conducted to evaluate the discharge coefficient in both flow directions: from the main chamber to the pre-chamber (filling), and from the pre-chamber to the main chamber (jet ejection).

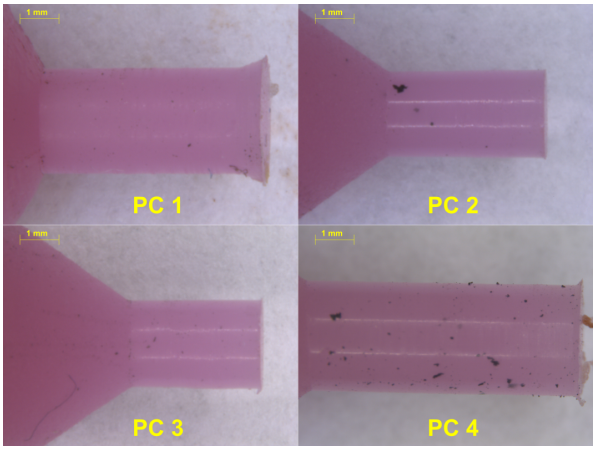

Figure 5.2: Pre-chamber silicon molds.

From a computer-aided design (CAD) program, the 3D pre-chamber model was coupled to a reservoir with the objective of stabilizing the flow on the orifice interface, mimicking the MC thermodynamic conditions. Then, the geometry was imported into CONVERGE Studio 2.4, where the surface geometry was checked for errors or inconsistencies and the boundary conditions, the initial conditions, the physical models, and the grid were set. A schematic view of the surface geometry and the boundary conditions can be seen in Figure 5.3.

To avoid the elevated computational cost of simulating the entire closed cycle and the variability coming from the experimental data, the methodology chosen was to discretize the time-resolved phenomenon in representative steady-state instants. In other words, evaluate the mass flow rate through the orifice by imposing an inlet and an outlet pressure boundary condition, while assuming the same orifice upstream and downstream thermodynamic conditions for all pre-chamber geometries.

The mesh grid is one of the most important elements to consider during a CFD calculation, being the balance between computational cost and accuracy. Based on previous works [4–6], the cell size was set to 2 mm at the reservoir and 0.5 mm at the pre-chamber. To properly capture the flow characteristics and the wall interaction effect, further refinements were applied to the orifice channel (0.125 mm), the pre-chamber walls (0.25 mm), and the orifice exit (0.25 mm). Additionally, an Adaptative Mesh Refinement (AMR) strategy was implemented to automatically increase the grid resolution (up to 0.125 mm) based on the velocity sub-grid of 1 m/s. The final mesh grid for the PC1

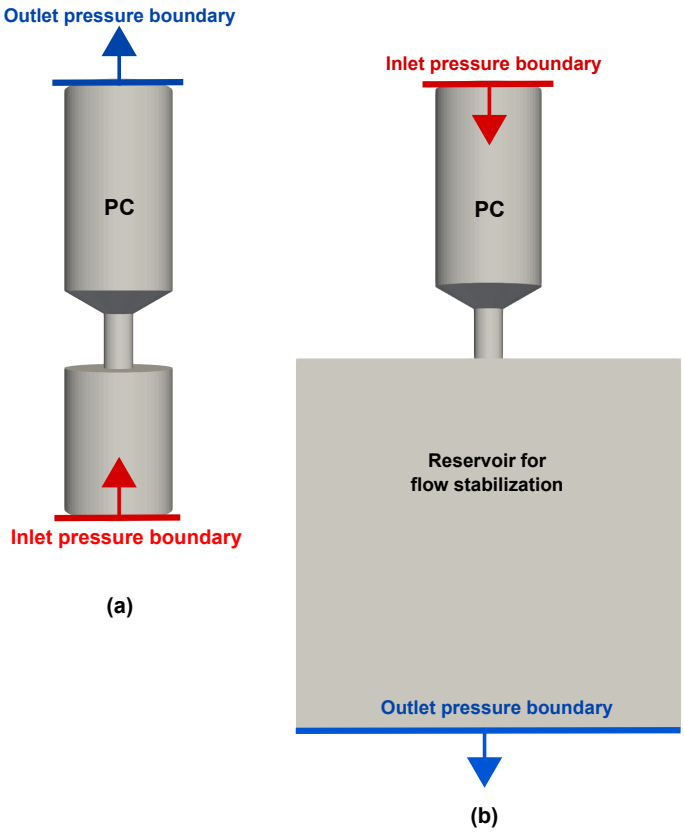

Figure 5.3: Surface geometry and boundary conditions during (a) filling and (b) jet ejection.

geometry during jet ejection, depicted in Figure 5.4, contains around 80,000 cells.

Two other mesh grids were used to estimate the differences in the C_D calculation and the computational cost of the chosen mesh: (1) a coarser mesh with a cell size of 2 mm at the reservoir and 0.5 mm at the pre-chamber, PC boundary, orifice, and orifice exit; (2) a finer mesh in the orifice (0.625 mm) compared to the mesh grid chosen, but the same cell size at the PC (0.5 mm), and at the orifice exit and PC boundary of 0.25 mm. The results in terms of discharge coefficient and calculation time (using 9 cores) are depicted in Figure 5.5. The calculation time grows practically linearly with the number of cells, while the C_D tends to follow a logarithm trend. Based on the results found, on the one hand, the gain in computational cost does not justify the use of the coarse mesh given the difference of 4.9% when compared to the

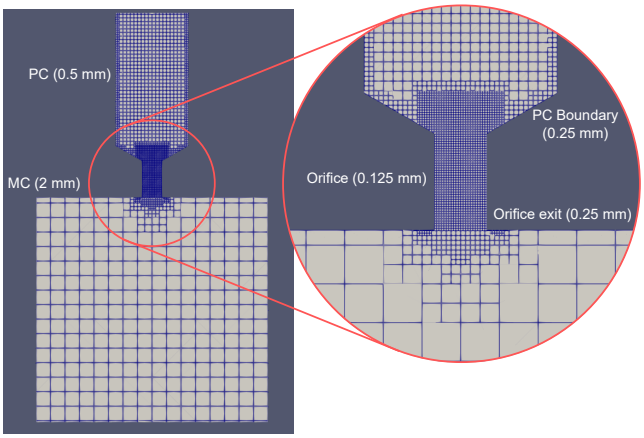

Figure 5.4: Computational domain and mesh details.

chosen mesh. On the other hand, the difference of 1.2% in C_D does not worth the 4 times higher calculation time required for the finer mesh.

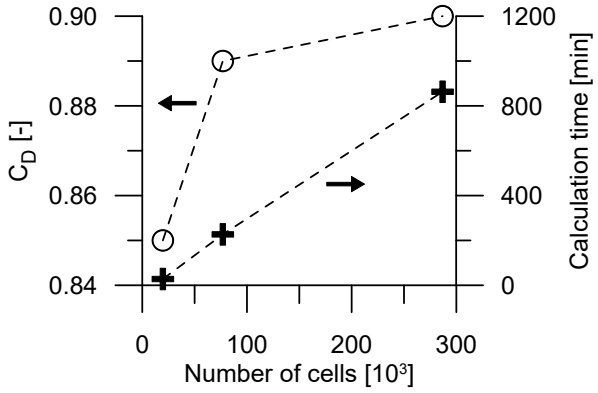

Figure 5.5: Discharge coefficient and calculation time (9 cores) of three different mesh configurations.

Since the thermodynamic properties during the pre-chamber filling do not vary substantially over the entire process, the discharge coefficient was estimated based on one thermodynamic condition only and, consequently, one pressure difference. For the jet ejection process, however, three different thermodynamic conditions were used to estimate the discharge coefficient. The boundary conditions used for the calculations are presented in Table 5.2.

Table 5.2: CFD boundary conditions.

Flow condition	ΔP [bar]	P_{pc} [bar]	P_{mc} [bar]	T_{inflow} [K]
Jet ejection	16.5	54	37.5	1200
	8.3	44	35.7	1100
	4.1	39	34.9	1000
Pre-chamber filling	0.5	30	29.5	900

Figure 5.6 shows the discharge coefficient for the pre-chamber filling and the three jet ejection conditions. Despite the manufacturing flaws of PC1 (incorrect cone angle before the orifice and countersunk at the orifice exit), the discharge coefficient does not vary significantly during the PC filling, with an amplitude of 0.04 between the minimum and maximum value of the discharge coefficient. During the jet ejection, however, the cone angle had a greater impact on the result, showing a clear difference between PC1 and the other geometries. Regarding the different pressure difference for jet ejection, a slight increment of the discharge coefficient is observed as the pressure difference is increased.

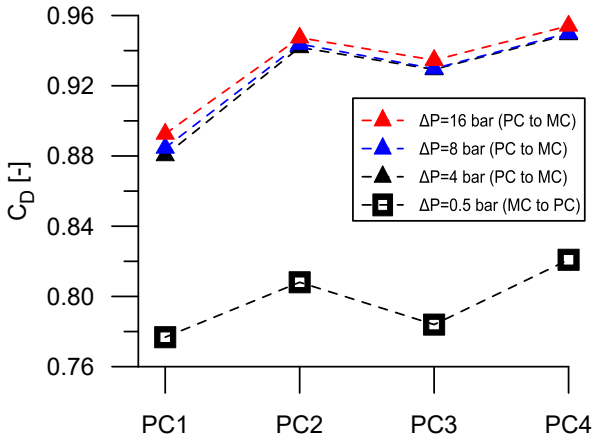

Figure 5.6: Discharge coefficient during jet ejection (filled triangles) and pre-chamber filling (empty squares).

Since the initial relation between geometrical parameters and operating conditions assumed the same discharge coefficient for all pre-chambers, the discharge coefficient calculated by CFD is now used to correct the geometrical

area and obtain the effective area to calculate the $A_e/V_{PC}N$ relation. Once again, the objective was to reproduce the same $A_e/V_{PC}N$ on two groups: (a) PC1, PC2 and PC4, and (b) PC2+ and PC3. As shown in Figure 5.7, the lower C_D for the PC1 contributed to decrease the difference between PC1 and PC2/PC4 caused by the manufacturing flaws on PC1. However, PC4 still presents some discrepancy in relation to PC1 and PC2.

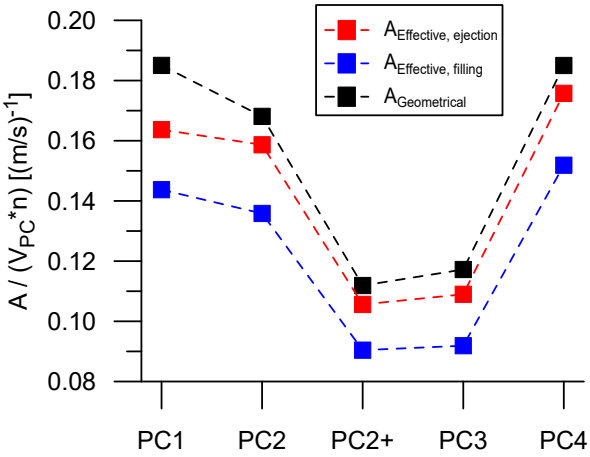

Figure 5.7: Comparison between geometrical and corrected area for the geometrical relation calculation.

5.3 Thermodynamic analysis

This section describes the thermodynamic model used to analyze the combustion process (via a heat release analysis) on both pre and main chambers, as well as to estimate valuable parameters, such as instantaneous gas temperature, mass, composition, and flow velocity through the orifice. In the following, each sub-model will be described separately.

5.3.1 Mass flow between chambers

The mass transfer between chambers was estimated based on the mass flow rate through a restriction of an ideal gas, as can be seen in Equation 5.1:

$$\frac{dm}{dt} = C_D A_n [2\rho_{up}(P_{up} - P_{down})]^{\frac{1}{2}} \varphi \tag{5.1}$$

where C_D is the discharge coefficient, A_n is the nozzle area (orifice cross-section area), ρ is the density, P is the pressure, φ is the compressibility factor, and

the *up* and *down* sub-indexes refer to the upstream and downstream position in relation to the orifice.

In addition to the measurable variables (A_n, P_{up} and P_{down}), some variables (C_D, ρ_{up} and φ) are estimated taking into account previous time steps. The C_D, for example, varies according to the flow Reynolds number (Re):

$$C_D = A - \frac{B}{\sqrt{Re}} \tag{5.2}$$

where A and B are fitting parameters, adjusted separately for filling and ejection processes. The Reynolds number is estimated based on the following equation:

$$Re = \frac{\rho_{pc}\, u\, d_o}{\mu_{air}} \tag{5.3}$$

where u is the flow velocity, d_o is the orifice diameter, and μ_{air} is the air dynamic viscosity.

It is worth noting that the upstream condition varies according to the instant of the cycle, being fresh air-fuel mixture (during the PC filling and the first part of the jet ejection) or hot burned combustion products (when the PC flame front reaches the orifice during the jet ejection). The correct determination of this state is important not only for the composition of the incoming/outgoing mass, but mainly for the correct computation of the mass flow rate due to the significant difference in temperature and density of unburned and burned states. Specifically during the jet ejection, the instant when the transition from unburnt to burnt gases occurs is imposed from the experimental data, taking advantage of the ability to capture temperature gradients with schlieren imaging.

5.3.2 Heat transfer

The heat transfer to the combustion chamber walls, a mandatory component to estimate the chemical heat release (Q_{ch}) and the rate of fuel mass burnt, must be approximated considering the in-cylinder conditions. Given the experimental configuration used in the RCEM for this thesis, the heat transfer coefficients for MC and PC were determined by two different methods.

In the main chamber, as the charge motion resembles an SI engine, the heat transfer was estimated by the Woschni correlation [7, 8], which is an empirical expression to determine the time-discretized heat transfer coefficient given by:

$$h_{mc} = 0.013\, B^{-0.2}\, P_{mc}^{0.8}\, T_{mc}^{-0.53}. \left[C_1 S_p + C_2 \frac{V_s\, T_{ref}}{P_{ref}\, V_{ref}} (P_{mc} - P_{mc,mot}) \right]^{0.8} \tag{5.4}$$

where B is the cylinder bore, P and T are, respectively, the in-cylinder pressure and temperature, S_p is the mean piston speed, C_1 and C_2 are fitting parameters, V_s is the swept volume, and T_{ref}, P_{ref} and V_{ref} are the temperature, pressure and volume at the reference state (start of the compression stroke). In summary, the Woschni correlation is based on the Nusselt-Reynolds number relationship, and is divided into two source terms: (1) the first related to the charge motion induced by the piston movement, and (2) the second related to the gas velocity induced by the combustion process.

In the pre-chamber, however, since the flow field is not exclusively driven by the piston velocity, a different approach is necessary to determine the pre-chamber heat transfer coefficient. Bardis, K. et al. [9] developed and numerically validated a heat transfer model specifically for the in-pre-chamber heat transfer based on the correlation proposed by Chiodi, M. and Bargende, M. [10]. This correlation is also based on a Reynolds-Nusselt correlation but uses the inlet flow velocity at the orifice as characteristic velocity. The pre-chamber heat transfer coefficient is calculated as follows:

$$h_{pc} = C_{BR} \,.\, V_{pc}^{-0.073} \,.\, P_{pc}^{0.8} \,.\, T_{pc}^{-0.53} \,.\, \left[\frac{1}{2} \sqrt{C_{B,k} \,.\, \frac{8}{3} k + C_{B,u} \,.\, u_{e,in}^2} \right]^{0.78} \tag{5.5}$$

where C_{BR}, is a global tuning constant, $C_{B,k}$ is a tuning constant for the contribution of the pre-chamber turbulence to the heat transfer, $C_{B,u}$ is a tuning constant for the contribution of the inlet pre-chamber orifice velocity to the heat transfer, k is the mass average pre-chamber turbulent kinetic energy, and $u_{e,in}$ is the velocity at nozzle inlet. Once the heat transfer coefficients are known, the heat transfer rate for pre-chamber and main chamber are given by:

$$\dot{Q}_{ht,mc} = h_{mc}\, A_{walls,mc}\, (T_{mc} - T_{walls,mc}) \tag{5.6}$$

$$\dot{Q}_{ht,pc} = h_{pc}\, A_{walls,pc}\, (T_{pc} - T_{walls,pc}) \tag{5.7}$$

5.3.3 Leakage model

Despite having numerous sealing rings, the RCEM (as well as ICE's) still requires some estimation of the mass flowing out of the combustion chamber

through the piston ring gaps, which is also called blow-by. In the case of the RCEM equipped with pre-chamber, since the PC has no clearances other than the connection with the main chamber, only blow-by from the main chamber was considered. These leakages are usually estimated by approximating the piston ring gap area to an orifice and calculating the mass flow through an orifice of an ideal gas. Assuming the ambient air condition as the downstream conditions ($P_{ambient} = 1bar$) and the critical pressure ratio of 0.528 ($\gamma = 1.4$, being γ the ratio of specific heats) the in-cylinder pressure will be greater than the critical pressure practically in the whole cycle. Therefore, the equation used for this condition is the equation for a chocked flow:

$$\dot{m}_{leakage} = A_{leakage} \cdot \rho_{throat} \cdot a_{throat} \tag{5.8}$$

where $A_{leakage}$ is the clearance area between piston rings and liner, and ρ_{throat} and a_{throat} are the density and velocity of sound at the leakage throat, whose equations are:

$$\rho_{throat} = \frac{P_{critical}\, MW}{R\, T_{critical}} \tag{5.9}$$

$$a_{throat} = \sqrt{\gamma \, \frac{R}{MW} \, T_{critical}} \tag{5.10}$$

where R is the universal gas constant, MW is the molecular weight of the mixture, and the critical conditions are given by:

$$P_{critical} = P_{mc} \left(\frac{2}{\gamma + 1} \right)^{\frac{\gamma}{\gamma - 1}} \tag{5.11}$$

$$T_{critical} = T_{mc} \left(\frac{2}{\gamma + 1} \right) \tag{5.12}$$

where the subscript mc stands for Main Chamber. The mass lost by leakages is estimated in each time step and then deducted from the current MC mass.

5.3.4 Deformation model

As a result of its oversized dimensions and the distance between piston position sensor and piston top, the real position of the piston top is possibly affected by the deformation of the piston rod tube. To account for this, a deformation model based on a beam under compression strain is adjusted

considering the physical properties of the moving parts and the mechanical stress originated by both pressure and inertia. The piston deformation (δ) is calculated by:

$$\delta = K_{def}(F_{pressure} + F_{inertia})(0.455 - x) \tag{5.13}$$

where K_{def} is the stiffness constant, $F_{pressure}$ is the force component associated with the in-cylinder pressure, $F_{inertia}$ is the force component associated with the inertia of the moving parts, and $(0.455 - x)$ is the distance between the piston position sensor and the piston top. The pressure and inertia forces are calculated as:

$$F_{pressure} = P_{mc}\frac{\pi}{4}d^2 \tag{5.14}$$

$$F_{inertia} = [m_{piston} + \lambda(0.3275 - x)]\, a_{piston} \tag{5.15}$$

where d is the piston bore, m_{piston} is the piston mass, λ is the lineal density of the piston rod tube, and $(0.3275 - x)$ is the length of the piston rod tube that exceeds the piston position sensor.

To calibrate K_{def}, an extension with known size was fitted to the piston head, and the real piston position in relation to the cylinder head was measured during a motored cycle by using a high-speed camera.

5.3.5 Heat released rate analysis

Once all the sub-models used were described, now it is possible to calculate the temperature and the rate of heat released in both chambers by using a first-order explicit method and the time-resolved ($10^{-5}\,s$) pressure and volume measurements. To do so, the combustion chamber was divided into two open systems: pre-chamber and main chamber (from now on called PC and MC, respectively), which exchange mass between them as detailed in subsection 5.3.1.

An important aspect is that the RCEM, unlike ICE's, includes a slow and a rapid compression phase, followed by a partial expansion. The slow compression phase goes from 0 to 29 mm of the piston stroke, whereas the rapid compression phase goes from 29 mm to TDC. The expansion follows a movement equivalent to a crank-and-connecting-rod mechanism just around 40 CAD after TDC, and then the piston moves slowly due solely to pressure difference. The piezoeletric pressure transducer, due to its measuring principle, needs to be referenced (pegged) with the absolute pressure (measured via

a piezoresistive pressure sensor) at the end of the filling process. The thermodynamic model starts at 29 mm of piston stroke and, therefore, the $t = 0s$ represents the beginning of the rapid compression phase. Its temperature (at $t = 0s$) is determined based on an extrapolation of the temperature at the end of the filling process (prior to the slow compression phase) by using the equation of state for ideal gases and the updated pressure and volume.

The mean temperature on MC and PC over the cycle is estimated using the equation of state:

$$T_{mc} = \frac{P_{mc} V_{mc} MW}{R\, m_{mc}} \tag{5.16}$$

$$T_{pc} = \frac{P_{pc} V_{pc} MW}{R\, m_{pc}} \tag{5.17}$$

where m_{mc} and m_{pc} are, respectively, the current mass in the MC and PC (calculated as the initial mass plus the instantaneous variation between chambers), V_{mc} and V_{pc} are the instantaneous volume at the MC and PC, R is the universal gas constant, and MW is the molecular weight of the mixture.

Both pre- and main chamber control volumes are modeled based on a zero-dimensional thermodynamic model, and the following hypotheses are assumed:

- Pressure is considered spatially homogeneous in each volume.
- The working fluid (air and fuel mixture) is considered as an ideal gas.
- The specific heat capacities (c_p and c_v) of each species varies with temperature according to the NASA polynomials [11].
- The mixture composition is homogeneous within each mixture state, when and where applicable.
- The temperature at the beginning of the slow compression phase is equal to the wall temperature.

The rate of chemical heat released (Q_{ch}) is then estimated by:

$$\begin{aligned} \frac{Q_{ch,mc}}{dt} = \frac{c_{p,mc}}{R} P_{mc} \frac{dV_{mc}}{dt} + \frac{c_{v,mc}}{R} V_{mc} \frac{dP_{mc}}{dt} + \\ + \frac{Q_{ht,mc}}{dt} + \frac{dm}{dt} \left(\frac{h_k}{MW} + \frac{1}{2} v^2 \right) \end{aligned} \tag{5.18}$$

$$\frac{Q_{ch,pc}}{dt} = \frac{c_{v,pc}}{R} V_{pc} \frac{dP_{pc}}{dt} + \frac{Q_{ht,pc}}{dt} - \frac{dm}{dt}\left(\frac{h_k}{MW} + \frac{1}{2}v^2\right) \tag{5.19}$$

where h_k is the enthalpy in the control volume where the mass is coming from ($k = mc$ during pre-chamber filling or $k = pc$ during jet ejection), dm/dt is the mass flow rate between chambers (positive when exiting the PC and entering into the MC), and v is the mass flow velocity at the PC orifice.

Integrating the rate of heat released, the cumulative heat release $Q_{ch,cumulative}$ is obtained, and the fuel mass burned ($mass_{fuel,burned}$) in both chambers can be estimated considering the Lower Heating Value (LHV) of the fuel:

$$mass_{fuel,burned} = \frac{Q_{ch,cumulative}}{LHV} \tag{5.20}$$

Since the physical properties of the jet vary significantly during its ejection, affecting the correct estimation of mass flow between chambers, a two-zone combustion model is implemented in the pre-chamber control volume, so the temperature, ratio of specific heats, density, and composition are estimated for each mixture state along the cycle. Therefore, as the PC fuel mass burnt is being calculated, the temperature of the burnt gases can be estimated according to (assuming the same c_p for the average, fresh and burnt components):

$$T_{burnt,i} = \frac{(mass_{pc} \cdot T_{pc}) - (mass_{pc,unburnt} \cdot T_{pc,unburnt})}{mass_{pc,burnt}} \tag{5.21}$$

and the temperature of the remaining unburnt mixture is estimated based on an isentropic compression of the fresh mixture:

$$T_{unburnt,i} = T_{unburnt,i-1} \cdot \left(\frac{P_{pc,i}}{P_{pc,i-1}}\right)^{\frac{\gamma_{pc}-1}{\gamma_{pc}}} \tag{5.22}$$

5.4 Typical aspects of PC ignition in the RCEM

This section intends to describe the typical aspects found with the pre-chamber ignition system in the RCEM, explaining what can be seen from the different optical techniques employed, and how it is linked to the indicated pressure data. Please refer to Figure 5.8 and Figure 5.9 to understand the reasoning set out in the following paragraphs, where the PC1 operating with a stoichiometric mixture and no EGR was taken as an example. Figure 5.8 shows the crank angle resolved schlieren and OH* chemiluminescence images, and Figure 5.9 illustrates the in-cylinder pressure for both MC and PC, the ΔP between chambers, and some schlieren and OH* chemiluminescence images at specific events of the combustion process.

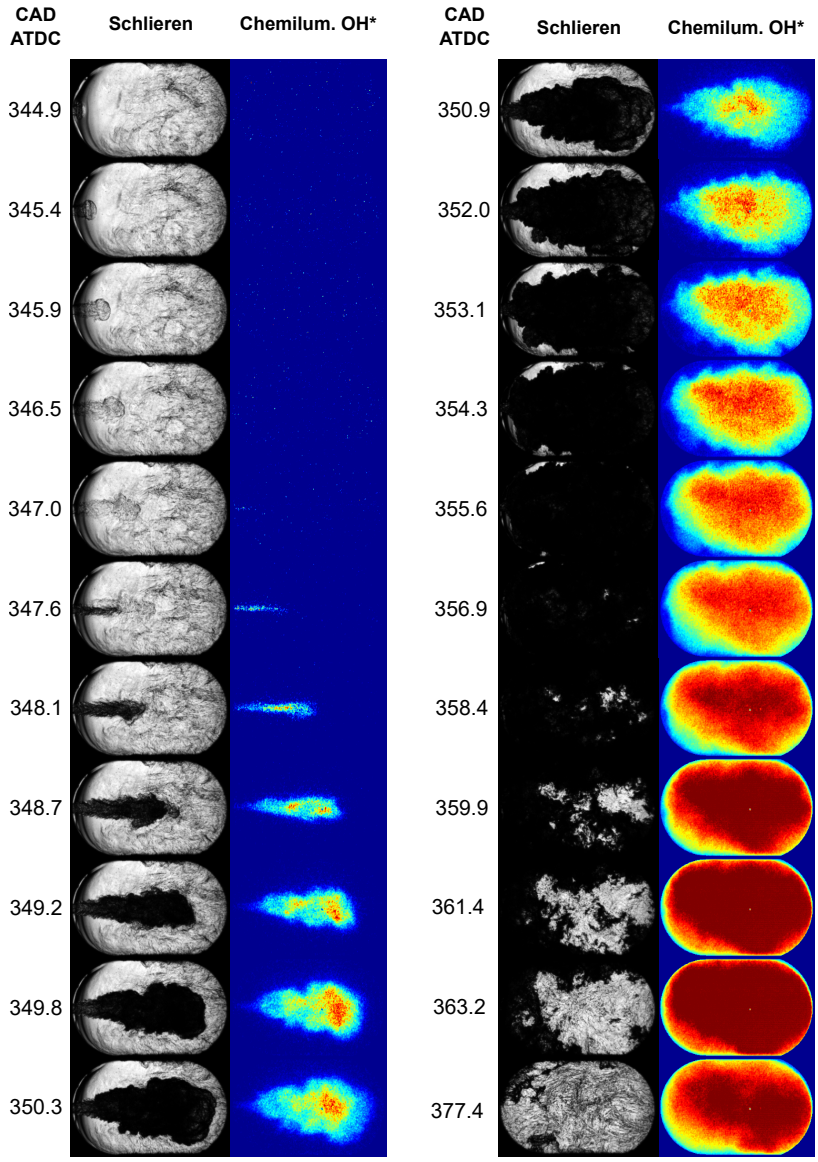

Figure 5.8: Temporal evolution of the PC jet ejection captured by schlieren and OH chemiluminescence imaging. PC1 at Φ=1.0 and 0% EGR.*

It is important to mention that, unlike chapter 4 and chapter 6 where the TDC firing is referenced at 0 CAD, in this chapter the TDC firing is referenced at 360 CAD. From 344.9 to 347.0 CAD (first five pairs of images), the ejection of a low-contrast jet can be observed via schlieren imaging, indicating that

the jet is composed of gases with a temperature close to that of the gases in the main combustion chamber, and probably is unburned mixture from the vicinity of the orifice. This hypothesis is corroborated by the lack of intensity observed in the OH* chemiluminescence images (an important tracer of high-temperature combustion reactions).

Then, at 347.6 CAD, while the low-contrast jet can still be seen, a high-contrast jet emerges from the orifice in the schlieren imaging, and OH* intensity is observed for the first time at the same region, indicating that the gases being expelled are now hot combustion products.

Next, this high-contrast (so-called "reactive") jet penetrates faster than the low-contrast (so-called "unreactive"), rapidly reaching the unreactive jet tip. This higher penetration velocity is linked to the pressure difference between chambers (ΔP), shown in Figure 5.9. Note that the ΔP is greater and rises faster when the reactive jet appears (bullet marker 2).

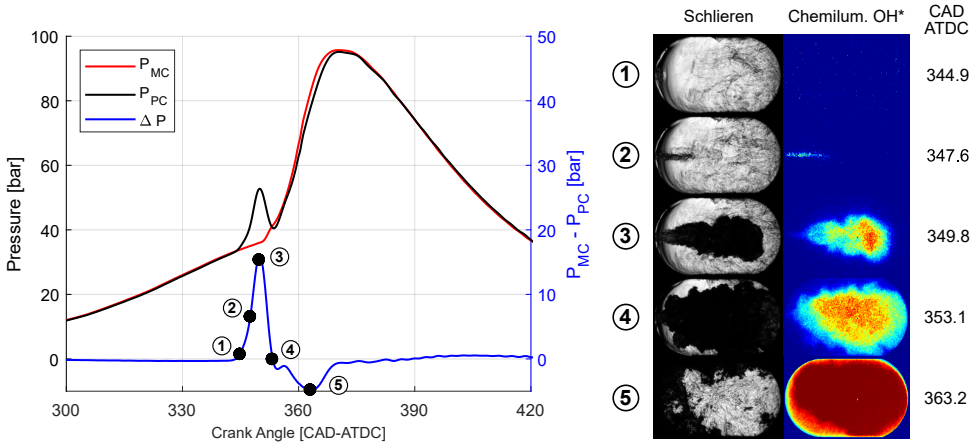

Figure 5.9: In-cylinder pressure and ΔP traces along with schlieren and OH chemiluminescence images.*

After that, it can be seen that the reactive jet penetrates almost to the end of the optical window and, at the same time, ignites the MC mixture. The MC ignition can be inferred by the inflection of the MC pressure trace and visualized in the images by the "jet widening" (showing that combustion starts to propagate in the orthogonal direction of the jet - i.e. from the jet to the top and bottom ends-), approximately in the bullet marker 3 in Figure 5.9, and coinciding with the point of maximum ΔP.

Then, while the PC combustion is approaching its end (dropping pressure), the MC combustion progresses and there is a reversal in the ΔP (bullet marker 4). The MC combustion thus continues and reaches its maximum OH* chemiluminescence intensity at the "minimum" ΔP (bullet marker 5). The fact that the peak intensity in OH* occurs when the contrast in schlieren pictures decreases once more suggests that the last portions of unburned mixture (probably located near the walls) are then ignited, and the temperature is approaching the burn gas temperature throughout the whole combustion chamber and becoming uniform again.

Finally, the OH* chemiluminescence intensity starts to decrease and gradually the ΔP returns to near zero (still with MC pressure slightly below PC pressure due to piston movement, removing burnt gases from PC).

It is important to highlight that the OH* chemiluminescence imaging captures the integral of the intensity through the entire "depth" of the optical combustion chamber, whereas the collimated beams used in the schlieren imaging can be refracted in any "depth". Thus, the OH* chemiluminescence provides complementary information on the internal region of the jet, such as where the higher heat release rate is located [12, 13]. Furthermore, once the combustion at MC ends, there are no different refraction indexes in the entire optical region and the schlieren images return to low-contrast format, where the OH* chemiluminescence still presents some intensity.

5.5 Effect of PC geometry on its combustion and jet ejection

Once the PC geometries and the motivation to design each one are known, this sub-section will further assess the effect of the different geometrical parameters purposely changed on the filling (gas exchange), combustion development and jet ejection processes taking place in the pre-chamber ignition system. In summary, the PC length and/or the PC diameter (therefore changing the PC volume), the orifice diameter and/or the orifice length were varied in such a manner that each factor could be individually assessed. The spark timing (ST) was adjusted to achieve the main chamber maximum pressure at 12 CAD ATDC. The global equivalence ratio (ϕ) and fraction of synthetic exhaust gas recirculation (EGR) were kept at 1.0 and 0%, respectively. The following subsections will address each factor, namely: geometrical parameter ($A_e/V_{PC}N$), PC length (i.e. distance from spark plug to orifice), and ratio between orifice length and diameter (L_o/d_o).

5.5.1 Geometrical parameter ($A_e/V_{PC}N$)

The first indicative parameter to be analyzed is the pressure evolution in both chambers. The pressure is the outcome of all the energy exchange processes (either thermal, piston work or enthalpic) that take place in the PC and MC control volumes. Since the main chamber pressure may vary slightly from cycle to cycle and the variation in the pre-chamber pressure caused by the geometry is small compared to the nominal pressure, the geometry effects during the pre-chamber filling and ejection processes are assessed with the pressure drop between chambers. Moreover, the pressure drop between chambers is also the main driver of the mass transfer.

As can be seen in Figure 5.10, in addition to the repetitiveness of the pressure drop between chambers over cycles for each geometry, the pressure drop is related to the constructive parameter $A_e/V_{PC}N$, where PC2+ and PC3 presents a very similar pressure behavior due to their similar $A_e/V_{PC}N$ number. When the spacer is removed from PC2+ (then PC2), the PC volume is reduced and then the $A_e/V_{PC}N$ parameter is increased, reducing the pressure drop between chambers. This occurs because the same orifice area allows more mass flow rate per PC volume, increasing the PC pressure by an increment of mass. The PC1 was designed to have the same $A_e/V_{PC}N$ parameter as PC2. However, due to manufacturing flaws, the PC1 has a slightly greater $A_e/V_{PC}N$ parameter than PC2, and therefore a lower pre-chamber pressure drop during PC filling.

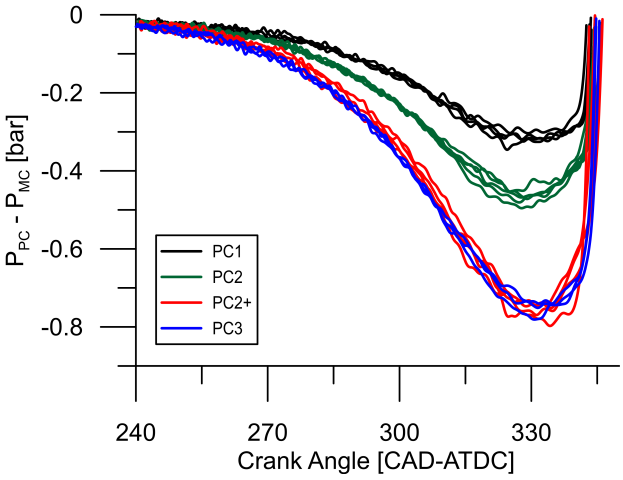

Figure 5.10: Pressure drop between PC and MC over few cycles for 4 different PC geometries during PC filling. ϕ=1.0

During the jet ejection process, the energy source term associated to combustion plays an important role in the pre-chamber pressure evolution. Therefore, the hypothesis of similar pre-chamber pressure evolution during jet ejection based on a similar $A_e/V_{PC}N$ parameter will also depend on the combustion development for each PC geometry and cycle. Since the pre-chamber is an open thermodynamic system, it is important to note that there is a competition between the pressure rise by combustion and the pressure reduction by mass (i.e. enthalpy) loss to the main chamber. In this sense, geometrical parameters such as pre-chamber diameter and spark plug-to-orifice distance can affect the PC combustion development and may cause one of the terms to be more relevant than the other. Taking as an example the geometries tested, despite having similar $A_e/V_{PC}N$, the PC pressure (and consequently the pressure drop between PC and MC) during jet ejection for PC2+ and PC3 are not similar. As can be seen in Figure 5.11, PC2+ presented a lower and later peak of pressure difference in relation to the PC3, possibly due to its narrow and longer PC geometry than PC3, which increases the time needed to burn the same amount of air-fuel mixture, and simultaneously gives more time for mass transfer to the MC.

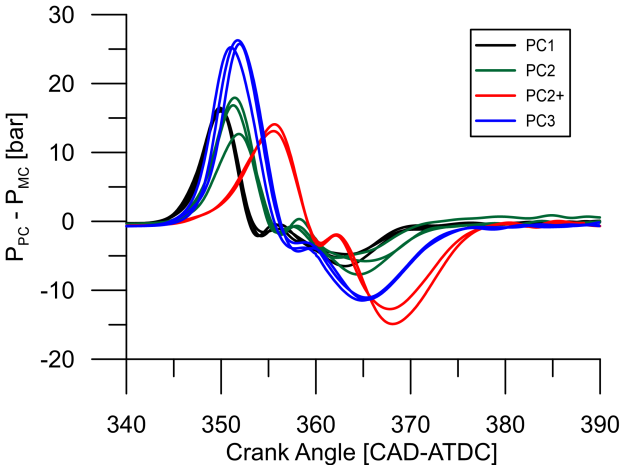

Figure 5.11: Pressure drop between PC and MC over few cycles for 4 different PC geometries during the jet ejection phase. ϕ=1.0

In terms of PC combustion and jet penetration, the analysis will focus on PC1, PC2, and PC3, because PC1 and PC2 have close $A_e/V_{PC}N$ parameters, whereas PC3 has intentionally a different value of this parameter. First, focusing on the PC combustion, both the pressure and imaging data will be

referenced at ST to illustrate the event of interest at the same time elapsed from the spark. Then, focusing on jet penetration, the start of ejection (SOE) will be the time reference to synchronize all the jets at the beginning of the mass flow delivery rate (SOE is defined as the instant when the mass flow direction is leaving the PC).

Figure 5.12 shows the pressure drop between PC and MC for PC1, PC2, and PC3 along with a schematic view of the internal volume of each PC. It can be seen that the pressure drop peak value and its position are, respectively, higher and retarded as the $A_e/V_{PC}N$ parameter decreases. When comparing PC1, PC2, and PC3, the two drivers of PC pressure rise must be taken into account: PC heat release rate and mass flow exiting the PC. The former may be affected by three-dimensional phenomena such as the flame-front propagation area, and the latter is related to the restriction imposed by the orifice. PC1 and PC3, for instance, have the same amount of fuel to burn, but the PC3 orifice is more restrictive than the one of PC1, causing a higher pressure rise rate. PC1 and PC2 curves tend to be more similar due to the similar $A_e/V_{PC}N$ parameter. However, due to the slightly lower $A_e/V_{PC}N$ parameter, the PC2 orifice is slightly more restrictive than PC1. To conclude, the lower the $A_e/V_{PC}N$ parameter, the higher the restriction to the flow exiting the PC, and the higher the pressure drop from PC to MC.

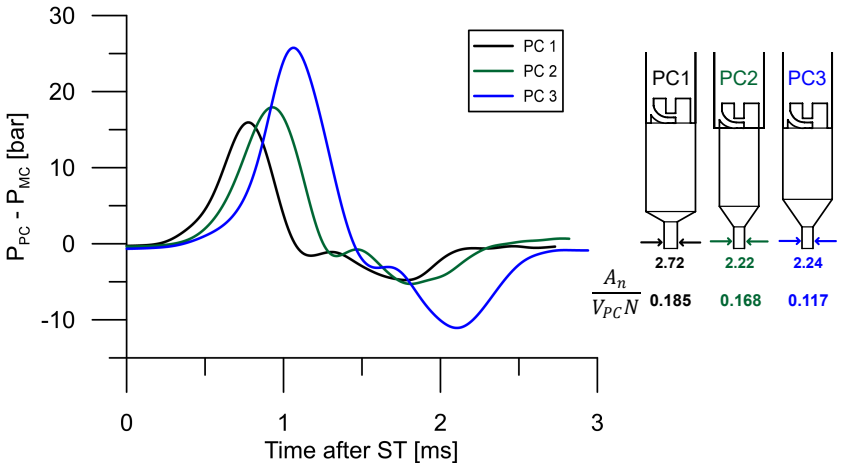

Figure 5.12: Pressure drop between PC and MC for PC1, PC2 and PC3 geometries after spark timing. $\phi = 1.0 - EGR = 0\%$

Figure 5.13 depicts the schlieren images of PC1, PC2, and PC3 on different time instants after spark timing, illustrating the jet resulting from the pressure

curve previously presented. The figure shows first a lighter and then a darker jet penetrating into the main chamber, representing jets with low or high temperature gradients in relation to the main chamber, possibly classifiable as low-temperature unburned gases and high-temperature burnt gases. Based on the comparisons made in Figure 5.12, it can be seen that the flame first reaches the PC1 orifice, then PC2, and then PC3.

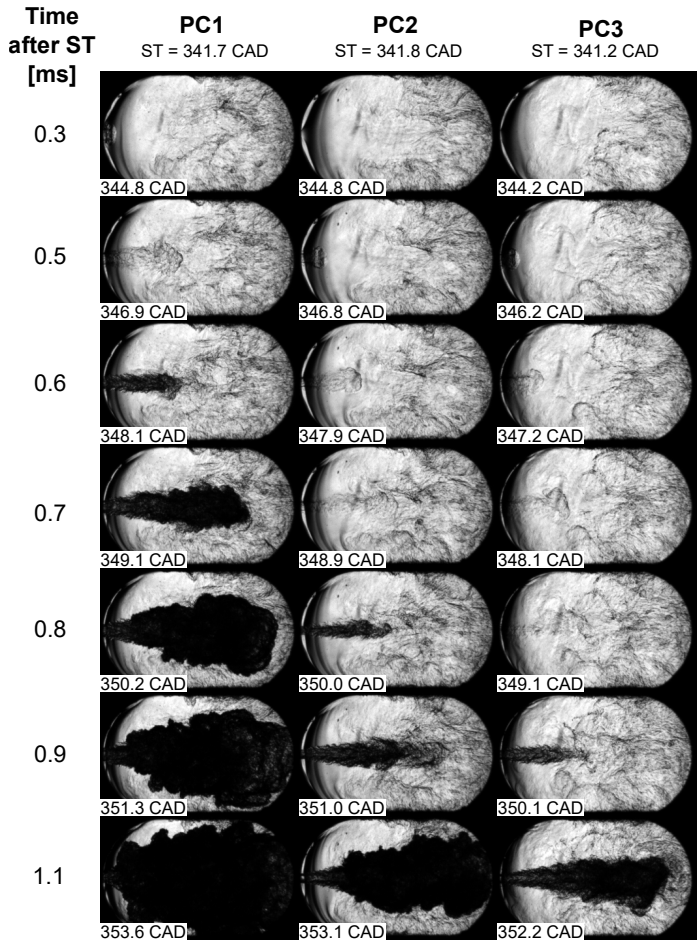

Figure 5.13: Schlieren images of PC1, PC2, and PC3 on different time instants after spark timing. $\phi = 1.0 - EGR = 0\%$

Regarding the elapsed time for the flame front (or hot burnt gases) to reach the PC orifice, two drivers can be mentioned: (1) PC flame-front propagation and (2) flame-drag by the bulk flow coming out of the PC. Once again,

the combustion chamber shape and the $A_e/V_{PC}N$ parameter are determining factors on the resulting jet to the main chamber. Comparing PC1 and PC3, due to their similar PC volume, it can be seen that the less restrictive orifice of PC1 leads to a shorter time between ST and the flame reaching the orifice. The PC3, although having the same orifice diameter as PC2, presented a longer time between ST and flame reaching the orifice, precisely because it represents a more restrictive situation given the higher volume of PC3 (lower $A_e/V_{PC}N$ parameter). Therefore, the flame-drag component is also related to the elapsed time between ST and the ejection of hot burnt gases, as well as the distance from the spark to the orifice.

Now the indicated and image data will be presented synchronized from the start of ejection (SOE), i.e. when the mass flow direction is from the PC to the MC, thus minimizing eventual mismatches at the beginning of the pressure-drop curve, focusing on the jet penetration. On the left-hand side of Figure 5.14, it can be observed the pressure drop from PC to MC, as well as the jet tip penetration (extracted from schlieren images) over time after SOE for PC1, PC2, and PC3. Since the jet characteristics change during the ejection from unburned gases (low contrast) to hot-burned gases (high contrast), each phase of the jet penetration is depicted separately for each PC. There is a good agreement among the different curves during the beginning of the first penetration phase, mainly due to the synchronization at the SOE and therefore a similar shape of pressure-drop curve. At the end of the first phase, the jet tip of PC2 reaches its maximum position slightly after PC1, and the jet tip of PC3 reaches this limit even later. On the one hand, although PC1 and PC2 present a similar pressure-drop, the larger PC1 orifice diameter leads to a higher mass flow through the orifice and therefore a higher jet momentum. On the other hand, due to the lower $A_e/V_{PC}N$ parameter, PC3 presented a lower pressure drop than PC1 and PC2 approximately until the end of its first ejection phase (0.5 ms after the SOE), leading to a lower jet momentum and a slower jet tip penetration. From the beginning of the second penetration phase, PC3 presented a higher pressure drop compared to PC1 and PC2. However, its effect on the jet penetration cannot be noticed in the experimental tests due to the "delay" between the orifice exit flow condition and the jet tip, and the proximity of the jet tip to the optical limit.

On the right-hand side of Figure 5.14 the pressure drop from PC to MC, and the corrected jet tip penetration (based on schlieren images) over time after SOE for PC1, PC2, and PC3 are depicted. The correction, based on Equation 5.23, considers the same engine speed (N) and flow velocity at the orifice exit (v) for all PC's, along with the same chamber length (L). There-

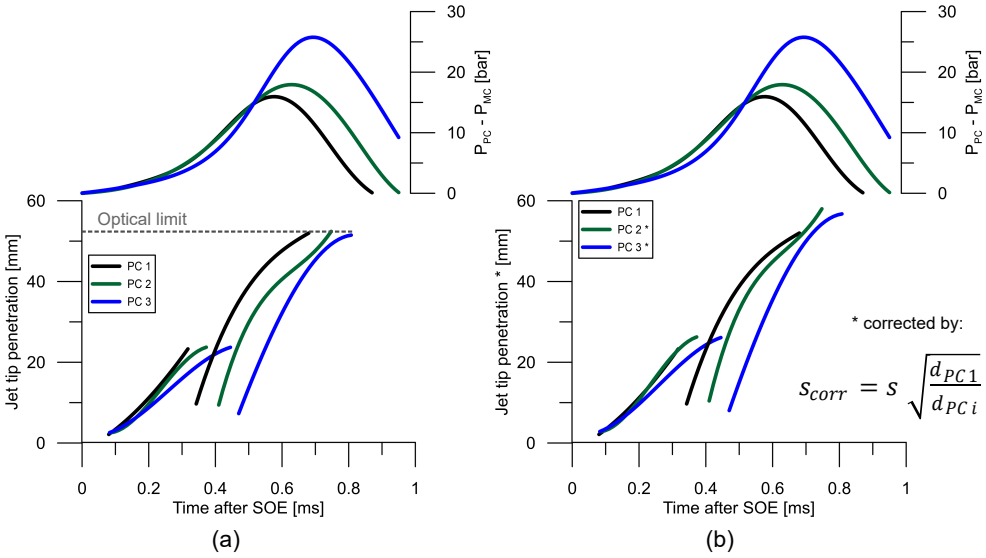

Figure 5.14: Pressure drop to MC and (a) jet tip penetration and (b) corrected jet tip penetration over time after SOE for PC1, PC2 and PC3. $\phi = 1.0 - EGR = 0\%$

fore, the penetration can be corrected in relation to PC1 exclusively with PC2 and PC3 orifice diameter using the expression below:

$$s_{corr} = s\sqrt{\frac{d_{PC1}}{d_{PCi}}} \tag{5.23}$$

where s is the jet tip penetration d_{PC1} and d_{PCi} are the PC1 orifice diameter, and the orifice diameter of the PC to be corrected (PC2 and PC3 in this case), respectively.

Now, when comparing the corrected penetration of PC1 and PC2, it can be observed that PC2 jet tip penetration reproduces that of PC1 during the first phase. In contrast, the PC3 jet tip penetration is slower than PC1 and PC2 even after the correction. These behaviors were expected due to the similar $A_e/V_{PC}N$ parameter for PC1 and PC2, and different for PC3. The expressions to correct the jet tip penetration previously validated numerically (subsection 4.3.2) have been experimentally validated now for the first ejection phase.

Over the second visible phase of jet penetration, the differences in the PC combustion lead to a time shift between PC1, PC2, and PC3, harming

the jet penetration comparison. In addition, the proximity of the jet tip to the optical limit impairs the correct assessment of the effect of the $A_e/V_{PC}N$ parameter on the corrected jet tip penetration. To circumvent this limitation and to expand the field of view, a 1D numerical spray model (DICOM) was adjusted to the experimental data to predict the jet tip penetration beyond the optical limit based on the experimental data. Figure 5.15 shows the jet tip penetration calculated by the DICOM software, along with the experimental data, for PC1, PC2, and PC3. The 1D spray model correctly reproduces the first phase of ejection and fits the experimental jet tip penetration at the end of the optical window. In contrast, the transition between the first and second visible phases cannot be reproduced by DICOM due to the fact that they are not two different jets, but a sudden and very relevant change in the characteristics (e.g. temperature and density) of the "injected" fluid during the ejection of a single jet. However, the second penetration curve ("reactive" jet) observed experimentally matches quite well the DICOM prediction once this jet reaches the "unreactive" jet tip (once the slope of the penetration curve clearly decreases, because of the enhanced jet - ambient interaction when the "reactive" jet reaches the tip of the jet).

In the lower right quadrant of Figure 5.15, the hypothetical jet tip penetration is depicted for PC1, PC2, and PC3 in the case of no chamber walls or optical limit restrictions. The PC1 jet tip penetrates faster than PC2 and PC3, mostly due to the larger orifice diameter while conserving a similar pressure-drop from PC to MC. The time shift between PC1, PC2, and PC3 found in the experimental data during the transition from the first to the second ejection phase is also found in the 1D spray model calculations. As previously done to the experimental data, the PC2 and PC3 hypothetical (predicted) jet tip penetrations must be corrected to be equivalent to PC1 orifice diameter, making use of the expression given by Equation 5.23.

Figure 5.16 shows the corrected jet tip penetration calculated via 1D spray model for PC1, PC2, and PC3 using the experimental data as input to the model. It can be noted that when correcting the jet tip penetration of PC2 (green dashed line), it matches the penetration of PC1. Moreover, even with a higher pressure drop from PC to MC, the jet tip penetration of PC3 does not overcome that of PC1 or PC2, but is able to recover the PC3's delay of the second ejection phase.

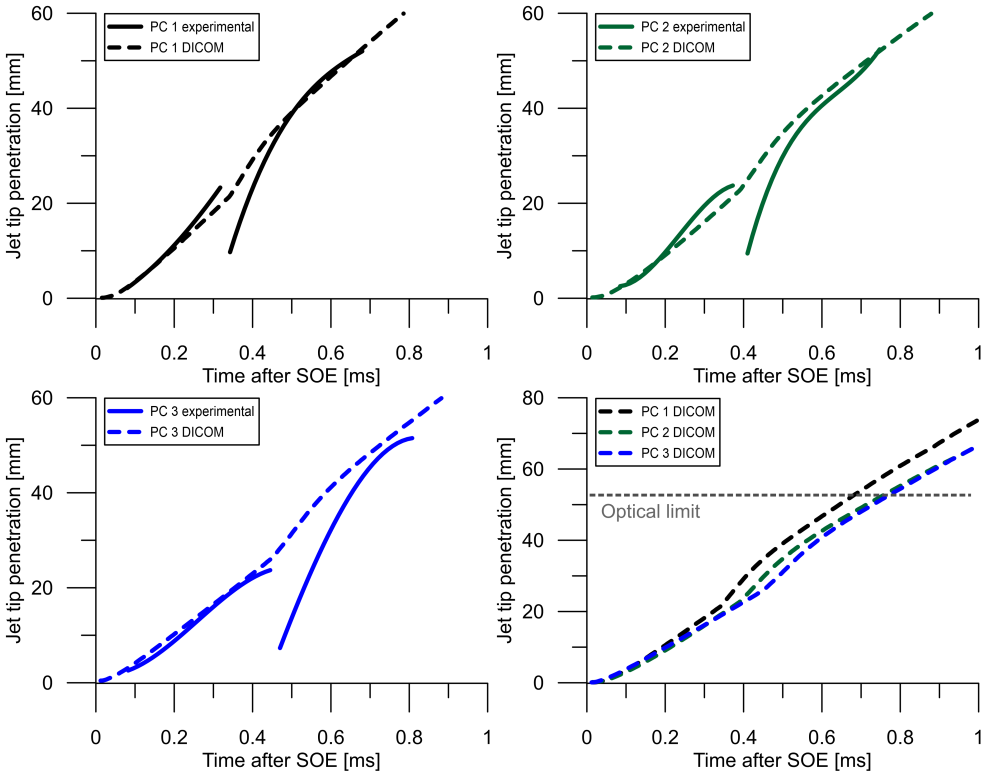

Figure 5.15: Jet tip penetration calculated via the DICOM software, along with experimental data, for PC1, PC2, and PC3. $\phi = 1.0 - EGR = 0\%$

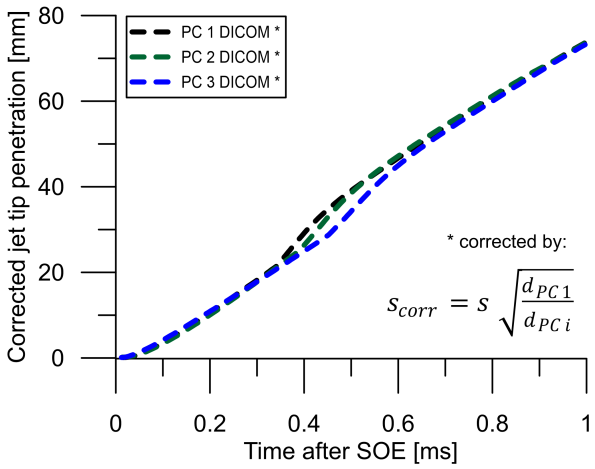

Figure 5.16: Corrected jet tip penetration from the calculated data (DICOM 1D spray model) for PC1, PC2, and PC3. $\phi = 1.0 - EGR = 0\%$

5.5.2 PC length

In order to assess the effect of the PC length (or, in other words, the distance between the spark plug and the PC orifice) on the combustion development and jet ejection, the most suitable pre-chambers to be compared are PC2+ and PC3 due to the same $A_e/V_{PC}N$ parameter and, consequently, identical pre-chamber pressure during PC filling, as previously discussed. As a reminder, PC2+ and PC3 have the same orifice diameter and volume. However, PC2+ has a smaller PC body diameter and a higher spark plug-to-orifice length to achieve the same volume as PC3.

First, assuming a flame-front-like combustion starting at the top of the PC (spark plug position), it can be deduced that the flame front would take more time to sweep the longer and narrower PC2+ than PC3, due to the same amount of air-fuel mixture to be burned in a reduced flame front area. This can be experimentally observed, both in the PC pressure curves (Figure 5.17) and on the imaging data (Figure 5.18). In Figure 5.17, it can be seen that the PC3 pressure (blue dashed line) rises faster than PC2+ pressure (red dashed line). As discussed in detail in chapter 4, the PC pressure rise during PC combustion is driven basically by two interconnected factors: (1) rate of net heat released (accounting for combustion and heat transfer to the walls) and (2) mass (i.e enthalpy) flow exiting PC through the orifice, where the latter goes in the opposite direction to the former. Therefore, as the mass flow should

be similar due to the same $A_e/V_{PC}N$ parameter, the slower pressure rise rate of PC2+ is probably caused by the slower air-fuel mixture burning rate than PC3, leading to a higher PC combustion duration, and a later and lower peak of PC pressure. Additionally, Figure 5.17 also depicts the pressure-drop from PC to MC, reflecting the earlier and higher peak for PC3 than PC2+, as occurred to the PC pressure itself.

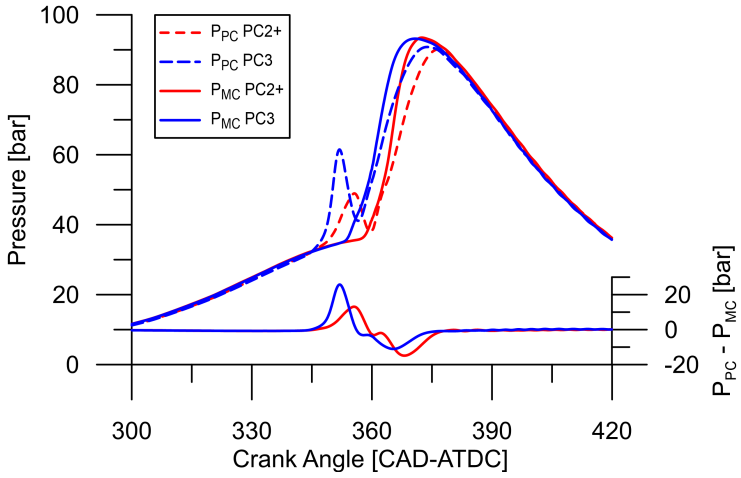

Figure 5.17: PC and MC pressure & pressure drop from PC to MC for PC2+ and PC3.

Figure 5.18 depicts schlieren images on different instants after spark timing for PC2+ (first row) and PC3 (second row). As can be seen in the first two frames, the elapsed time since ST for the unreactive jet to exit the PC is a little longer for PC2+ compared to PC3, roughly 0.1 ms or 1 CAD. Regarding, the reactive jet, representing burned fuel (i.e. flame front) exiting the PC, it takes even longer for PC2+ compared to PC3, with a difference of approximately 0.4 ms or 4 CAD. This corroborates, together with the PC pressure data, that the slower pressure rise rate of PC2+ is caused by the longer time for the flame front to sweep the entire pre-chamber. Figure 5.19 summarizes in a column chart the elapsed time from ST of the unreactive and reactive jet events for PC1, PC2, PC2+, and PC3.

Regarding the jet tip penetration, Figure 5.20 depicts the evolution of the jet tip penetration (taken from the schlieren images) over the time elapsed after ST for PC2+ and PC3, both for the unreactive and the reactive phase. As expected and previously seen on the schlieren images, the jet tip penetration of PC2+ starts slightly after in the unreactive phase and even later in the

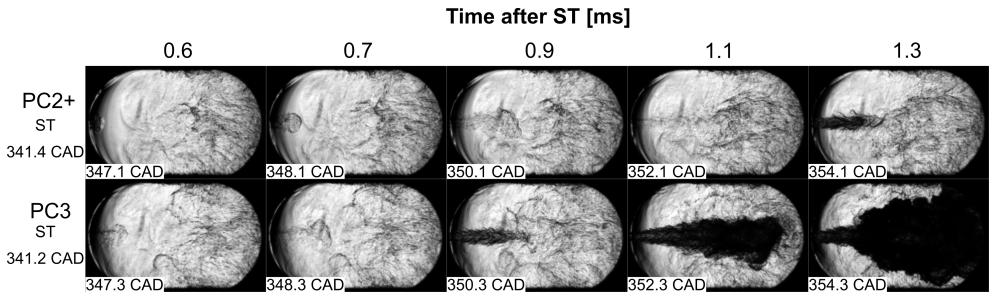

Figure 5.18: schlieren images of PC2+ and PC3 at different time instants after spark timing. $\phi = 1.0 - EGR = 0\%$

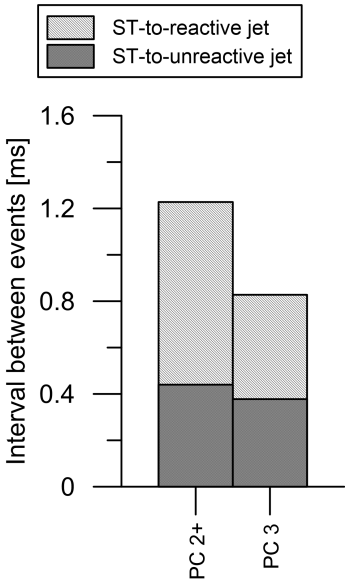

Figure 5.19: Elapsed time since ST of the unreactive and reactive jet ejection for PC1, PC2, PC2+, and PC3.

reactive phase as a result of the different PC pressure traces, and thus jet momentum.

In fact, as already indicated, there are not two different jets (reacting and unreacting) being ejected from the PC, but rather a significant change in the properties (e.g. temperature and density) of the fluid being ejected. However, since both schlieren and OH* chemiluminescence are not able to trace the entirety of the unreactive jet (since the reactive jet overlaps the unreactive

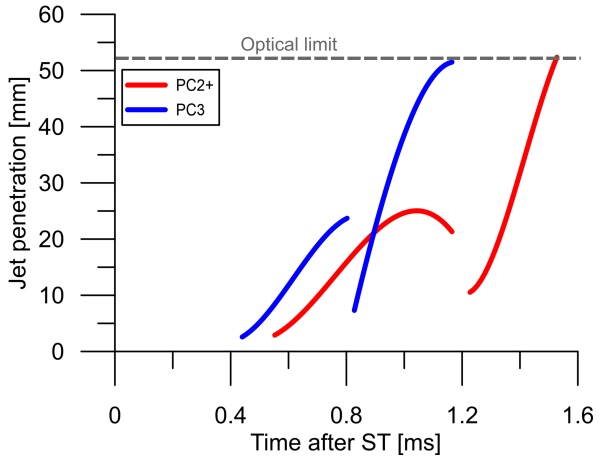

Figure 5.20: Jet tip penetration evolution taken from schlieren images of PC2+ and PC3.

jet), from the optical techniques point-of-view, the jets are segregated into unreactive and reactive phases.

5.5.3 Orifice length

In addition to the other geometric aspects already addressed, one of the parameters analyzed during this thesis was the effect of the length-to-diameter orifice ratio (L_o/d_o) on the jet ejection process. To do so, the PC1 and PC4 geometries were manufactured to have the same orifice diameter, PC body diameter, PC length, differing only by the length of the hole. Therefore, even with minor flaws in the manufacturing process, both PCs would have similar PC pressure (given by the $A_e/V_{PC}N$ parameter) and are the most suitable geometries to be compared when evaluating the effect of orifice length in terms of jet characteristics.

The inner orifice geometry affects the flow characteristics and has been extensively studied, especially in fuel injector applications [14–16]. As reported in the literature, the major effect of varying the length-to-diameter ratio (L/d) on GDI or diesel injectors is the spray cone angle, increasing the spray cone angle as the L/d ratio decreases.

Figure 5.21 shows the evolution of the jet penetration for PC1 and PC4 captured by schlieren images, the average image during the reactive ejection phase, and an illustration of the PC geometries for better understanding. The images are referenced by the Start of Ejection (SOE) and are shown from 0.1

to 0.65 ms after SOE. The average image of 8 frames was taken during the reactive jet ejection and before the flame front started to propagate in the jet orthogonal direction, which would impair the determination of the jet angle. In addition to the similar temporal jet penetration, it can be noted that the jet angle is wider for the PC1 case in relation to the PC4 case, reflecting the same behavior found in fuel injectors: a wider angle with a lower L/d ratio.

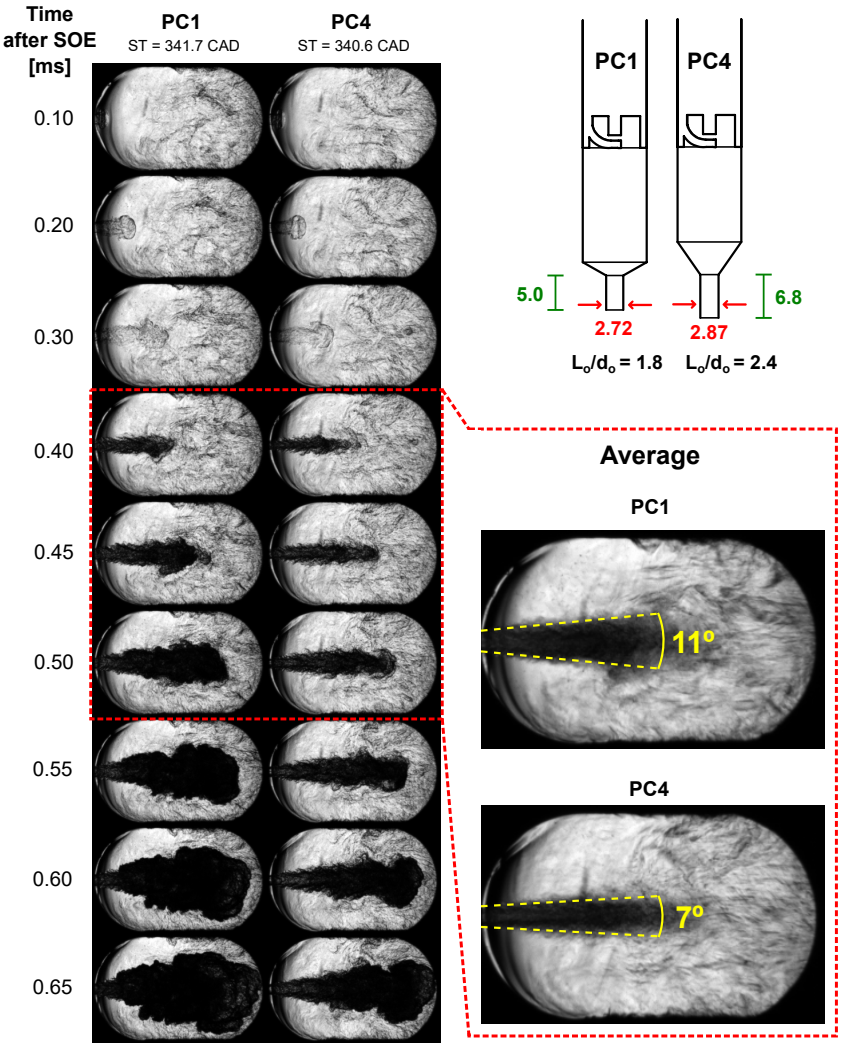

Figure 5.21: Jet penetration evolution of PC1 and PC4, average image during the reactive phase, and an illustration of the PC geometries.

The wider angle of PC1 reflects in faster flame propagation, as can be seen in Figure 5.22, where the 2D flame area normalized by the total optical area is plotted over time after SOE. The area that represents effectively the jet (approximately up to 0.5 ms) is similar for PC1 and PC4 cases (with minor differences arising from the angle of the jet), but the PC1 flame area grows faster immediately after the ejection event and reaches the entire optical area before PC4, which is consistent with the larger ignition spot produced by the wider PC1 jet angle.

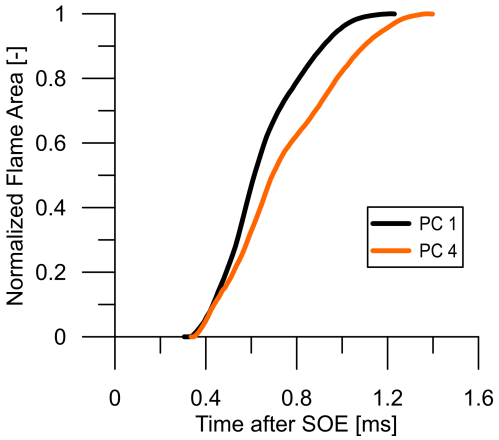

Figure 5.22: Normalized flame area for PC1 and PC4 cases.

Figure 5.23 shows the pressure difference between chambers and the evolution of the jet tip penetration over the time after the SOE. It is worth mentioning that the SOE is the instant at which the PC pressure is higher than the MC pressure, and it is linked to the frame in which it is possible to see the beginning of the jet ejection. The similar $A_e/V_{PC}N$ parameter and the similar PC combustion ensured a similar curve of pressure difference between chambers, a key factor for the jet ejection. Therefore, given the similarity in terms of jet ejection and PC combustion, the differences observed in MC combustion actually come from the distinct jet angle caused by the length-to-diameter orifice ratio (L_o/d_o).

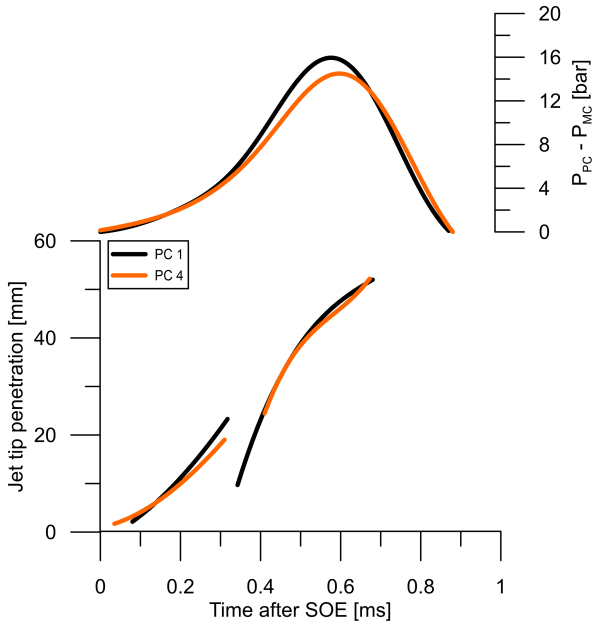

Figure 5.23: Pressure difference between chambers (top) and jet tip penetration (bottom) after SOE for PC1 and PC4.

5.6 Effect of equivalence ratio

After determining the influence of the PC geometry on the main events taking place in the PC ignition system, this section aims to further investigate the effect of the fuel/air equivalence ratio (ϕ) in the PC combustion, jet ejection, and MC ignition of different PC geometries. For this study, the PC1, PC2, and PC3 geometries were selected to evaluate (1) PCs with different PC volume and orifice diameter but a similar $A_e/V_{PC}N$ parameter (PC1 and PC2), and (2) PCs with only similar volume (PC1 and PC3) or orifice diameter (P2 and PC3) but with a different $A_e/V_{PC}N$ parameter.

Preliminary experimental tests point out that, although with delayed combustion, the lean limit is ϕ=0.75 for the PC1 geometry (i.e. no ignition with ϕ=0.70). Therefore, for this present study, the PCs were operated from stoichiometric up to this lean limit in four steps of fuel-air equivalence ratio: ϕ=1.00, 0.90, 0.80, 0.75 by preserving the initial charge pressure and reducing the fuel injected. As the fuel-air mixture is homogeneous between MC and PC, and given the low interest in operating rich fuel-air mixtures on the MC,

only stoichiometric and lean mixtures were tested. The spark timing (ST) was adjusted to achieve the main chamber maximum pressure at 10 CAD ATDC, or as close as possible on misfire-limited conditions. This combustion phasing criterion resembles the MBT condition in a reciprocating internal combustion engine and was chosen to facilitate the transfer of information to commercial applications.

Figure 5.24 shows the PC and MC pressure for PC1, PC2, and PC3 for different fuel-air equivalence ratios. It can be observed that the maximum in-cylinder pressure decreases as the fuel-air equivalence ratio is decreased, due to the lower fuel energy available. Specifically for the ϕ=0.75 case, it can be noted that the PC1 and PC2 geometries could not achieve the combustion phasing criterion due to the combustion deterioration caused by the leaner fuel-air mixture. On the one hand, the PC1 and PC2 cases presented misfire when the ST was further advanced in an attempt to phase the combustion. On the other hand, the PC3 generated a jet able to sustain the MC combustion duration despite the lower laminar flame velocity of the leaner mixture, and not needing to advance the ST even further. Finally, in terms of maximum in-cylinder pressure, the cases operating with ϕ=1.00, 0.90, and 0.80 presented similar behavior regardless of the PC geometry. Taking a closer look at the indicated data, Figure 5.25 shows the ΔP between chambers (left-hand side) and the jet momentum (right-hand side) for the three PC geometry and the different fuel-air equivalence ratio tested. The jet momentum is plotted only for the jet ejection period, so the period of PC filling (with fresh charge) and re-filling (with burnt gases from the MC combustion) are ignored. Both variables are plotted against the crank angle after ST to emphasize the effect of the equivalence ratio on the PC combustion. Except for the PC3 ϕ=0.90 case, a clear trend of decreasing the ΔP and the jet momentum as the equivalence ratio decreases is observed. In addition, the interval between the ST and the maximum ΔP and jet momentum increases as the equivalence ratio decreases. Such behaviors are derived from (1) the lower amount of fuel injected and (2) the lower flame propagation velocity inherent to the leaner fuel-air mixture, leading to a lower pressure rise rate and, consequently, lower PC peak pressure during PC combustion. Finally, as the ΔP is the primary driver of the jet momentum by means of the jet velocity, the jet momentum decreases as the equivalence ratio decreases.

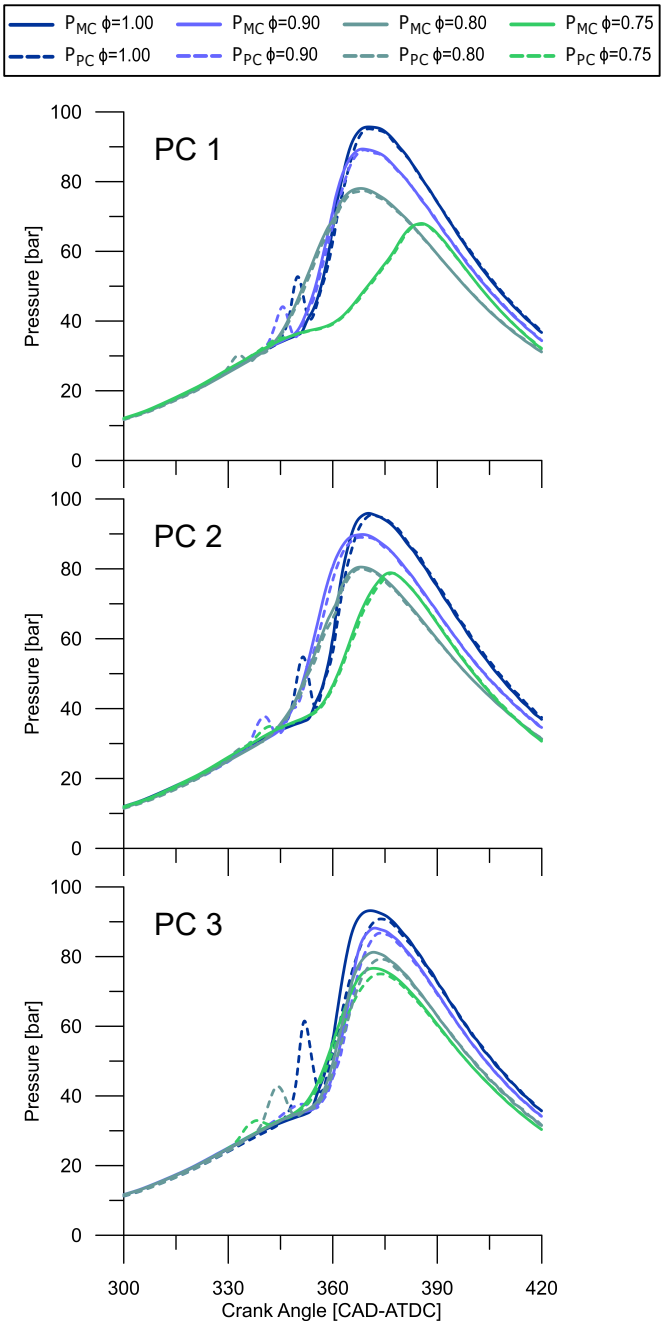

Figure 5.24: Effect of the equivalence ratio on the PC and MC pressure for PC1, PC2, and PC3.

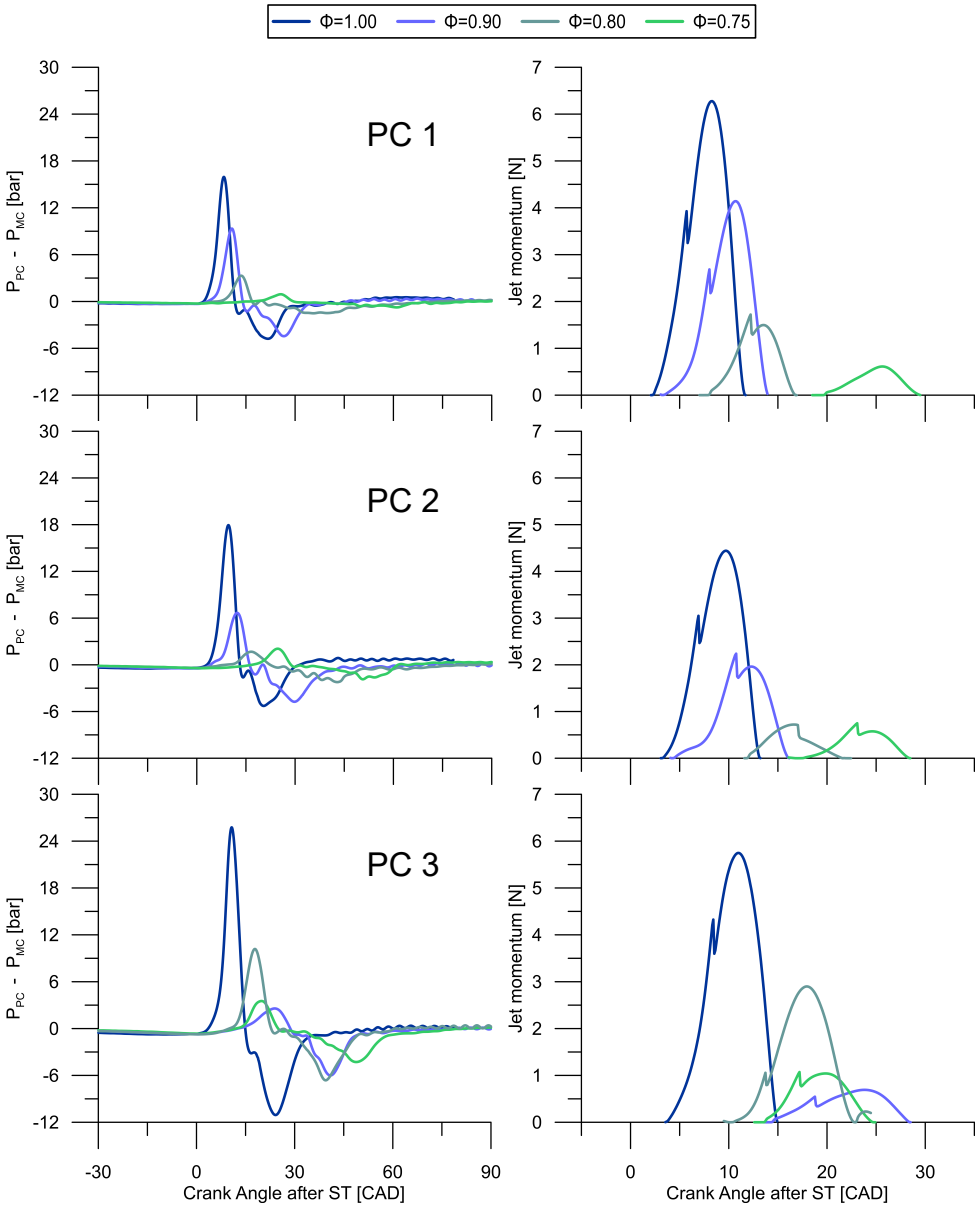

Figure 5.25: Effect of the equivalence ratio on the ΔP between chambers and jet momentum for PC1, PC2, and PC3.

When comparing the different PC geometries, it can be observed that, except for the PC3 ϕ=0.90 and PC2 ϕ=0.80 cases, the ΔP increases as the $A_e/V_{PC}N$ parameter decreases for all tested conditions. In this sense, the PC3 geometry proved to be beneficial to the lean operation due to its higher ΔP, possibly favoring the jet penetration into the MC (which will be seen later) and decreasing the MC combustion duration when compared to the PC1 and PC2 geometries.

Table 5.3 shows the pre-chamber characteristic times taken from the indicated data shown in Figure 5.24, where the Start of Ejection (SOE), the End of Ejection (EOE) and the Duration of Ejection (DOE) for PC1, PC2 and PC3 are exhibited for each fuel-air equivalence ratio tested. To facilitate data visualization, the same data presented in Table 5.3 is graphically presented in Figure 5.26. As expected due to the combustion deterioration, the advance of the ST and the longer DOE as the mixture becomes leaner is observed both for PC1, PC2 and PC3, except for PC3 ϕ=0.90 and PC2 ϕ=0.90 cases. The DOE will be especially important during the schlieren and OH* chemiluminescence imaging analysis presented below to detect the jet content.

Table 5.3: Pre-chamber characteristic times for different fuel-air equivalence ratios.

PC	ϕ	**ST**	**SOE**	**EOE**	**DOE**	
	[-]	[CAD]	[CAD]	[CAD]	[CAD]	[ms]
PC1	1.00	341.7	343.9	353.4	9.5	0.87
	0.90	334.8	339.3	350.0	10.7	1.00
	0.80	319.0	325.7	336.2	10.5	1.04
	0.75	317.8	334.3	347.5	13.2	1.32
PC2	1.00	341.8	344.9	354.9	10.0	0.95
	0.90	327.7	331.8	343.7	11.9	1.09
	0.80	317.0	325.7	339.3	13.6	1.33
	0.75	316.2	333.1	344.9	11.8	1.16
PC3	1.00	341.2	344.8	356.0	11.2	1.07
	0.90	326.2	338.8	354.8	16.0	1.59
	0.80	326.1	336.2	348.8	12.6	1.26
	0.75	317.2	329.3	342.2	12.9	1.31

Figure 5.27 presents the effect of the fuel-air equivalence ratio on the interval between ST and SOE for PC1, PC2, and PC3. This parameter indicates (1) the PC's ability to build up pressure and (2) the inherent delay between

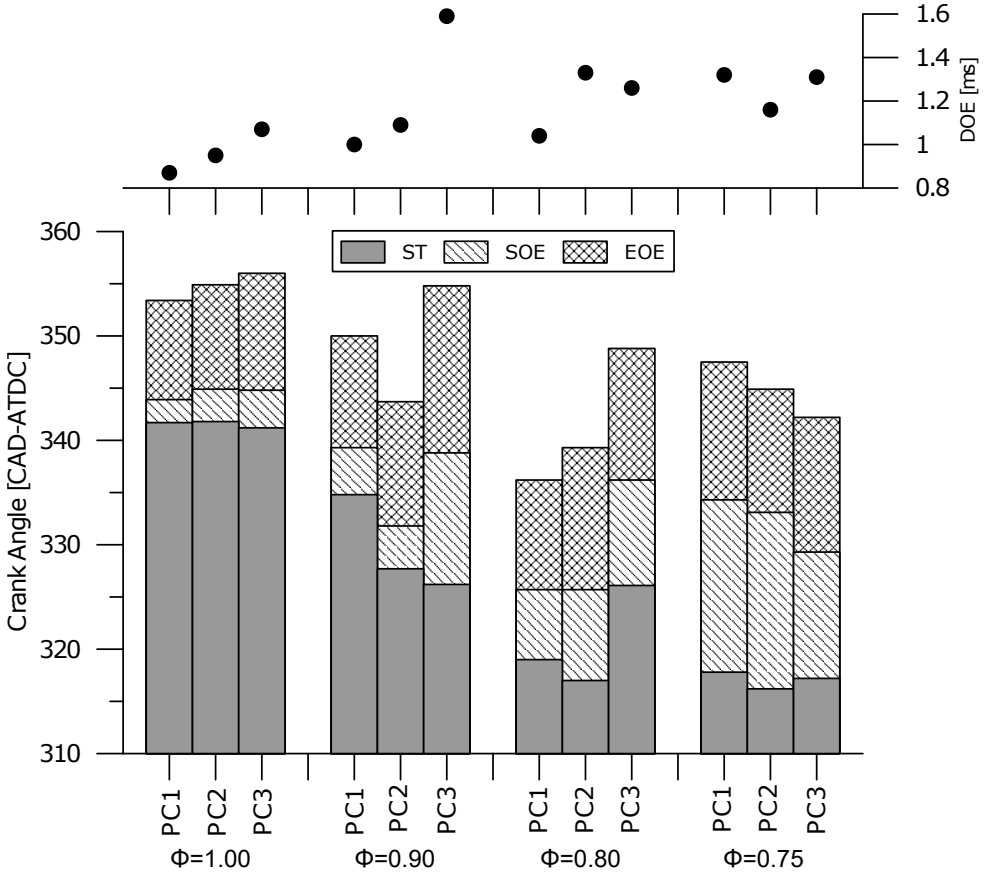

Figure 5.26: Graphical illustration of the pre-chamber characteristic times for different fuel-air equivalence ratios.

the ST and the energy delivery to the MC ignition. A clear trend of increasing the interval between ST and SOE can be noticed as the fuel-air equivalence ratio is increased, except for the PC3 ϕ=0.90 case, likely due to the reduced laminar flame speed of lean mixtures. The exacerbated delay between ST and SOE strongly contributed to the non-fulfillment of the MBT criterion for combustion phasing for PC1 and PC2 geometries operating at ϕ=0.75.

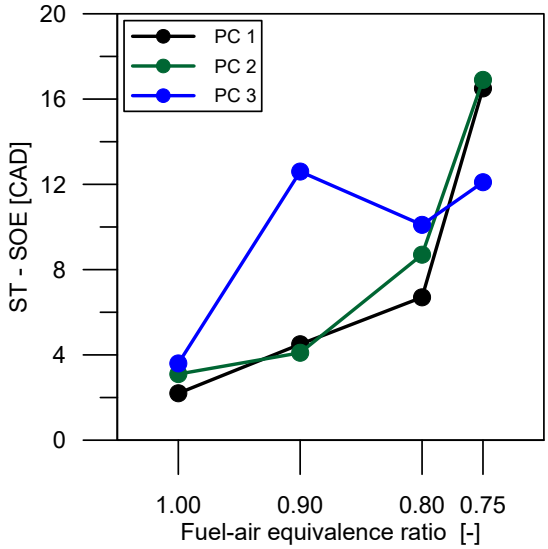

Figure 5.27: Effect of the fuel-air equivalence ratio on the interval between ST and SOE for PC1, PC2, and PC3.

Figure 5.28 and Figure 5.29 shows the temporal evolution of the jet penetration and MC ignition captured by the schlieren and OH* chemiluminescence imaging, respectively, for the PC1 geometry. The frames are synchronized from the SOE to highlight the characteristics of each jet and its effect on the MC ignition and flame propagation, then isolating the already discussed effects of the lean fuel-air equivalence ratio on the PC combustion (e.g. different intervals between ST and jet ejection). The respective ST and SOE crank angles are indicated for each case exhibited. Due to the shorter recording time of the ϕ=1.00 and ϕ=0.90 cases, there are no OH* chemiluminescence images for 4.5 ms and 5.5 ms after SOE time instants in Figure 5.29.

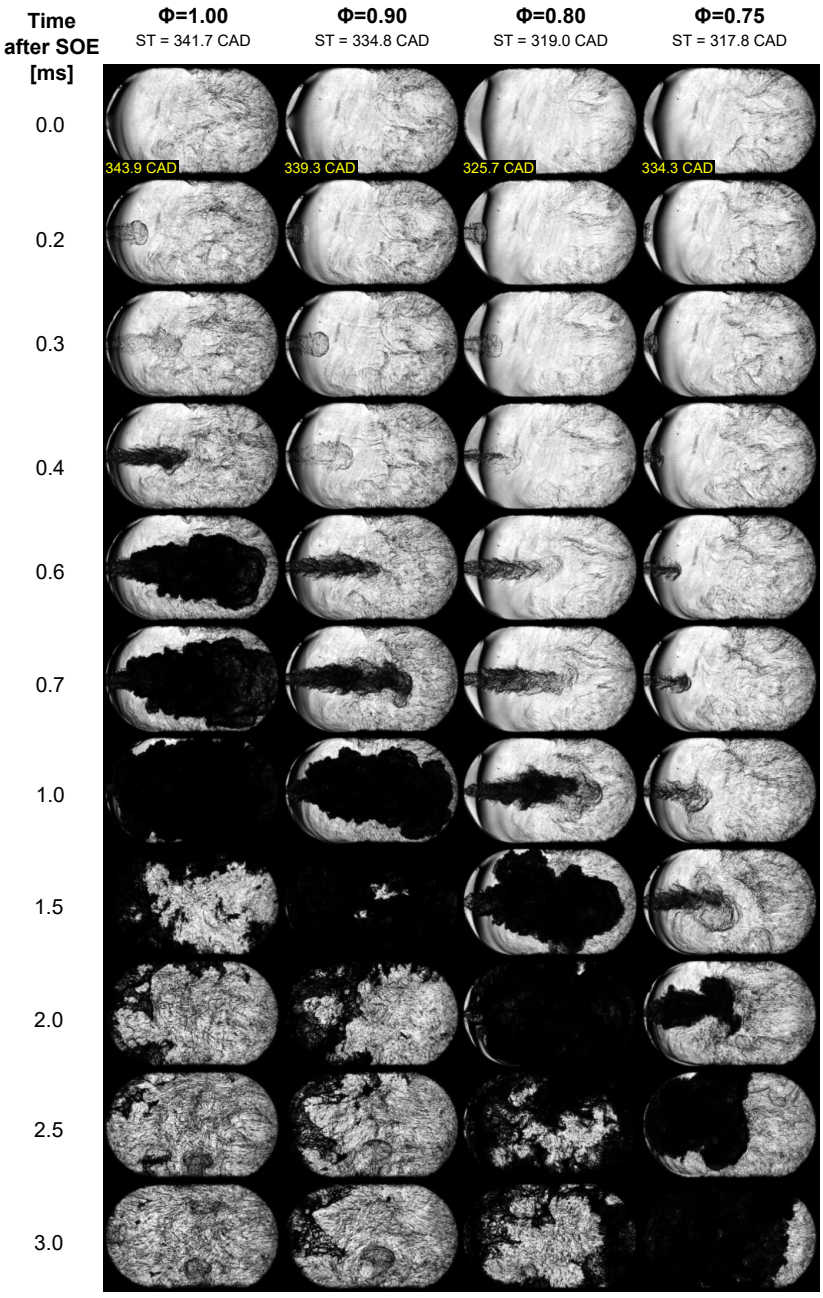

Figure 5.28: Schlieren images of the PC1 operating with ϕ=1.0, 0.90, 0.80, and 0.75.

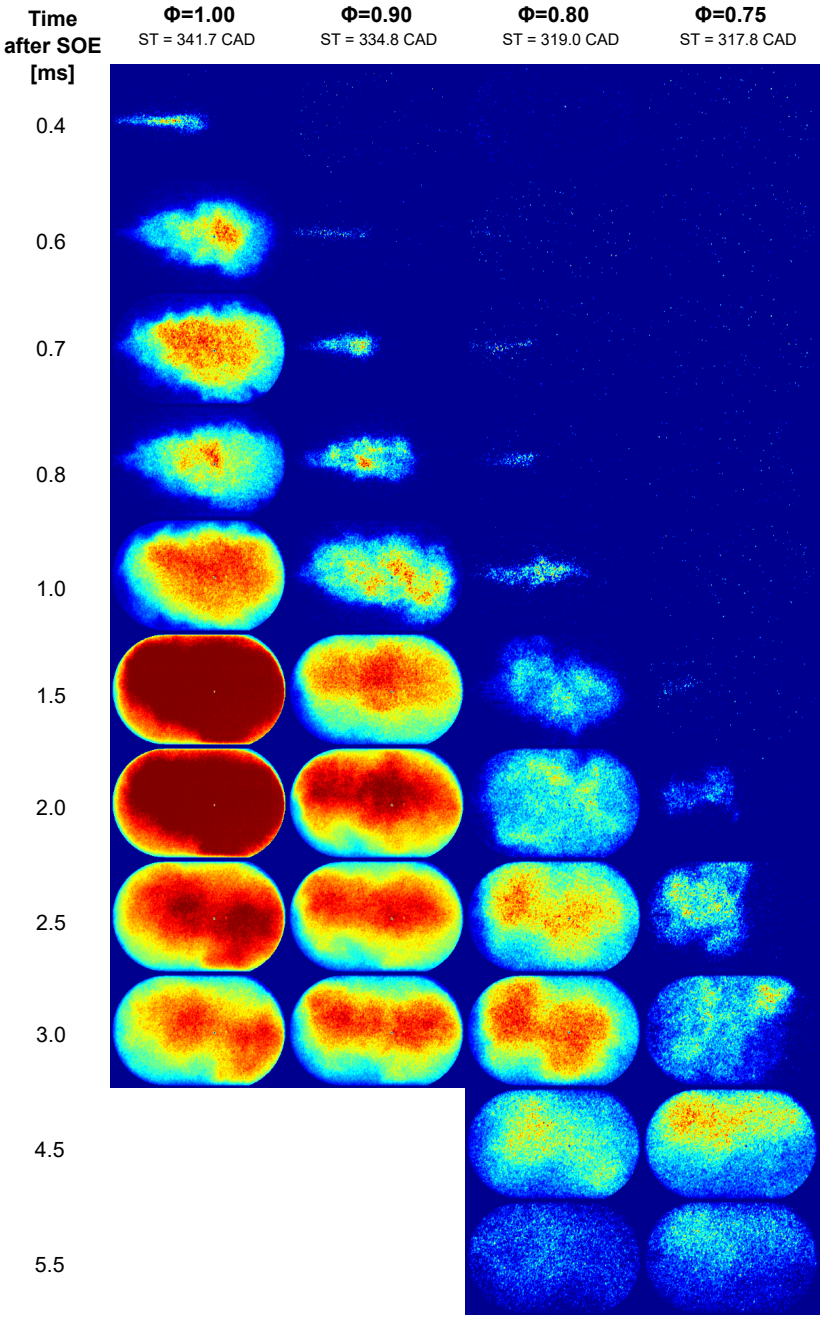

Figure 5.29: Chemiluminescence OH images of the PC1 operating with ϕ=1.0, 0.90, 0.80, and 0.75.*

Starting with the analysis of the schlieren images (Figure 5.28), it can be observed in the first three rows that the penetration rate of the low-contrast (so-called "unreactive") jet decreases as the ϕ decreases, as a result of the lower rate of PC pressure rise as the mixture becomes leaner. Note that this "unreactive" (i.e., low-temperature) jet is composed of unburned air-fuel mixture from the vicinity of the orifice that is expelled by virtue of the start of combustion at the other end of the PC (spark plug location). From the 0.4 ms after SOE, it can be observed the transition from an "unreactive" to a "reactive" jet for the ϕ=1.00 case, and, at 0.6 ms after SOE, for the ϕ=0.90 case. For the ϕ=0.80 and ϕ=0.75 cases, this transition is less apparent and is likely related to the MC ignition by the jet than the presence of high-temperature gases in the jet being ejected.

The OH* chemiluminescence images for the PC1 (Figure 5.29) corroborate that the transition from an unreactive to a reactive jet in the ϕ=1.00 and ϕ=0.90 cases is, indeed, due to high-temperature reacting gases being ejected from the PC. For the ϕ=0.80 and ϕ=0.75 cases, despite a contrast level change in the schlieren images at 0.4 ms and 0.6 ms, respectively, the OH* chemiluminescence images does not indicate any intensity before 0.7 ms for the ϕ=0.80 case, and 1.5 ms for the ϕ=0.75 case.

To further investigate the jet properties, the instant of the first noticeable OH* chemiluminescence intensity can also be checked whether it occurred before or after the main chamber start of combustion and the end of jet ejection (EOE), verifying if the OH* intensity is from a reactive jet or is a result of the MC ignition by an unreactive/quenched jet. Table 5.3 shows the EOE and Figure 5.30 shows the MC pressure rise rate against the time after SOE for all fuel-air equivalence ratios tested with the PC1 and, pointed out with a dashed arrow, the indication of the MC start of combustion detected by the slope change in the curve. It can be observed that the MC start of combustion of ϕ=1.00 and ϕ=0.90 cases occurs, respectively, at 0.6 ms and 0.9 ms after the SOE, which takes place later than the appearance of a significant OH* chemiluminescence intensity in both cases, suggesting that the jet is composed by hot-reacting gases. For the ϕ=0.80 case, the MC start of combustion occurs around 1.2 ms, just after the jet exhibits a weak OH* intensity, indicating that the jet reactivity is greatly reduced and occurs close to the EOE (1.04 ms). Lastly, the ϕ=0.75 case presents the slope change around 2.0 ms, with an even lower OH chemiluminescence intensity from 1.5 ms (i.e. after the EOE), indicating that the OH* intensity seen from 2.0 ms originates not from the jet but from the MC ignition.

There is, therefore, a shift in the MC ignition mechanism as the equiva-

lence ratio decreases. On the one hand, for the ϕ=1.00, 0.90, and 0.80 cases the OH* intensity is observed during the jet ejection, thus confirming that the jet is composed of active radicals that probably come from the wrinkled turbulent flame front that was not quenched when passing through the orifice. On the other hand, the ϕ=0.75 case did not present detectable OH* intensity before the MC ignition, corroborating that the flame front initiated in the PC was quenched at the orifice. Despite not containing active radicals and intermediate species, the hot gases coming out of the PC mix with the unburned MC mixture and locally raise its temperature up to the ignition temperature. The reasoning for the flame quenching at the orifice for the ϕ=0.75 case lies in the thicker flame thickness for the lean case, increasing, therefore, the flame quenching distance.

As proposed in section 4.5, one approach for addressing the flame quenching phenomenon is through the determination of the Damköhler (Da) number at a given position downstream of the orifice exit. The Da number can be calculated as

$$Da = \left(\frac{l_I}{\delta_L}\right)\left(\frac{S_L}{u'}\right) \tag{5.24}$$

where l_I is the integral length scale, δ_L is the laminar flame thickness, S_L is the laminar flame velocity, and u' is the turbulence intensity. However, obtaining this data experimentally is very complicated, and the calculation from the in-cylinder pressure data depends on additional assumptions and may lead to very large uncertainty. Table 5.4 shows the laminar flame thickness (δ_L), the laminar flame velocity (S_L), the turbulence intensity (u'), the integral length scale (l_I), and the Da number estimated at 25mm downstream the orifice exit (center of the main chamber). The components to calculate the characteristic chemical reaction time (δ_L and S_L) were estimated using the open-source Cantera software, and the components to calculate the characteristic turbulent eddy turnover time (u' and l_I) were estimated, respectively, using the correlation $u' = v0.16Re_d^{-1/8}$ of turbulence intensity for internal flows [17], and $l_I = d_o(0.052x + 0.0145)$ for compressible round jets [18], where x is the distance downstream of the orifice exit. A trend of decreasing the Da as the equivalence ratio decreases was observed for the ϕ=1.00, 0.90, and 0.80 cases. For the ϕ=0.75 case, however, the trend is not valid and the Da is similar to the ϕ=1.00 case. As previously mentioned, the estimation of the local flow parameters based on the in-cylinder pressure measurements may be imprecise and can lead to an incorrect local Damköhler number.

Table 5.4: Damköhler number at 25mm downstream the orifice exit for different equivalence ratios - PC1.

PC	ϕ [-]	δ_L [µm]	S_L [cm/s]	u' [m/s]	l_I [mm]	Da [-]
PC1	1.00	14.9	58.0	14.3	1.34	3.64
	0.90	20.1	41.5	12.4	1.34	2.23
	0.80	32.4	34.5	8.5	1.34	1.68
	0.75	35.8	30.1	3.1	1.34	3.62

An alternative approach for addressing the flame quenching phenomenon is by relating the orifice diameter to the quenching distance. By definition, the quenching distance is the minimum distance between two parallel plates in which a flame cannot propagate and can be assumed proportional to the flame thickness [19]. Table 5.5 shows the laminar flame thickness (δ_L) and the laminar flame velocity (S_L) calculated with the pressure (P_{PC}) and temperature ($T_{U,PC}$) of the unburnt air-fuel mixture at PC1 with all equivalence ratios tested. As the PC thermodynamic conditions vary along the jet ejection, the instant chosen for calculating the flame characteristics was the instant of maximum delta pressure during the jet ejection. It can be noticed that the flame thickness and, consequently, the quenching distance is enlarged as the equivalence ratio decreases. This thicker flame, therefore, is more susceptible to flame quenching when passing through the orifice.

Table 5.5: Flame properties for different fuel-air equivalence ratios and thermodynamic conditions of PC1.

PC	ϕ [-]	P_{PC} [bar]	$T_{U,PC}$ [K]	δ_L [µm]	S_L [cm/s]	d_o [mm]	d_o/δ_L [-]
PC1	1.00	52.7	793.1	14.9	58.0	2.72	182
	0.90	44.1	725.5	20.1	41.5		135
	0.80	30.2	682.4	32.4	34.5		84
	0.75	34.7	705.5	35.8	30.1		76

The relation between the orifice diameter (d_o) and the laminar flame thickness (δ_L), presented in Table 5.5, gives a dimensionless parameter that can be used to quantify the orifice flame-quenching phenomenon. In the case of the PC1, the threshold for the flame to quench when passing through the orifice seems to be somewhere between 76 and 84 d_o/δ_L.

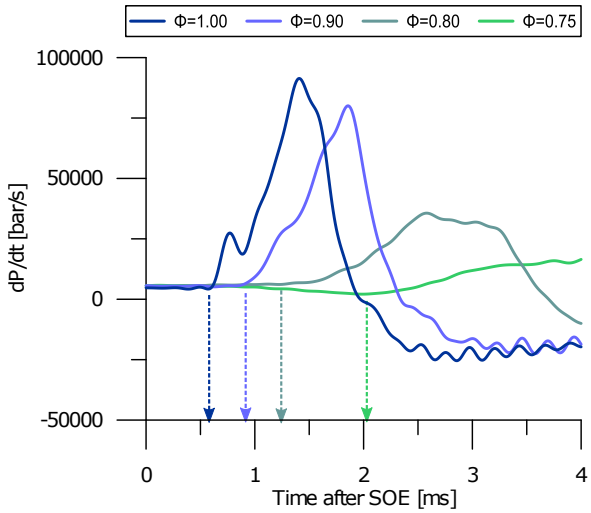

Figure 5.30: Pressure rise rate for the PC1 operating with ϕ=1.0, 0.90, 0.80, and 0.75.

In terms of jet penetration, it is clear that the lower ΔP as the mixture becomes leaner reduces the jet penetration into the MC, and consequently impairs its combustion and flame propagation. The MC ignition pattern significantly changes from the stoichiometric to the leanest case tested due to its dependence on the area covered by the jet, its temperature, and its turbulence induced. First, for the ϕ=1.00 case, the jet angle associated with the full jet penetration leads to a great area covered by the jet at the region opposite the orifice exit, causing this portion to be burned before the region close to the orifice. Then, for the ϕ=0.90 case, the MC flame propagates in an orthogonal direction to the jet practically at the same time as the jet momentum favors the combustion in the axial direction. Next, for the ϕ=0.80 case, the behavior is similar to that of ϕ=0.90 case, but with a lower contribution from the axial jet momentum. Finally, for the ϕ=0.75 case, the short jet penetration significantly decreases the "ignition area" and the MC combustion occurs in the region close to the orifice exit up to the middle of the optical combustion chamber, first propagating in the orthogonal direction of the jet axis and then towards the region opposite the orifice exit.

Figure 5.31 and Figure 5.32 shows the temporal evolution of the jet penetration and MC ignition captured by the schlieren and OH* chemiluminescence imaging, respectively, for the PC2 geometry. The frames are synchronized from the SOE, and the respective ST and crank angle reference for the first set of frames are indicated for each case exhibited.

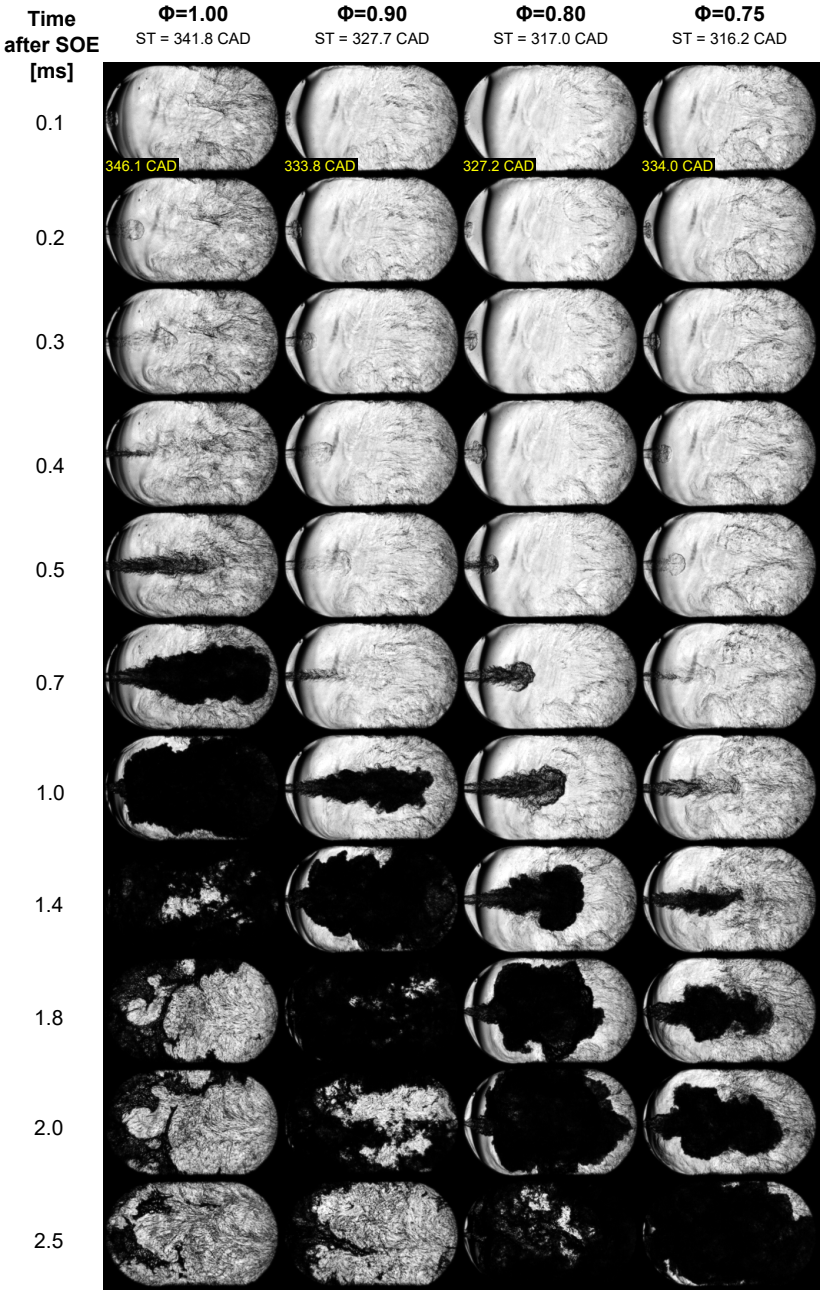

Figure 5.31: Schlieren images of the PC2 operating with ϕ=1.0, 0.90, 0.80, and 0.75.

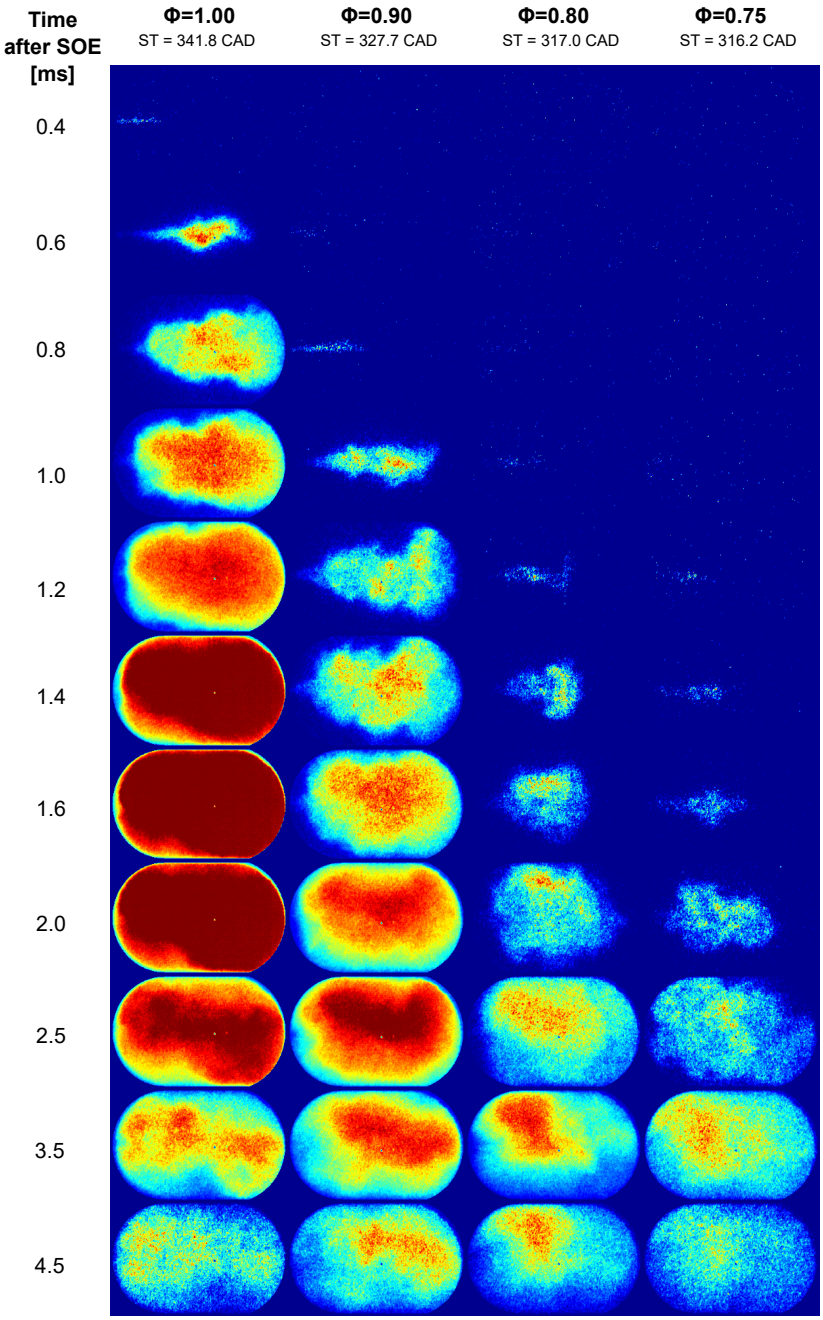

Figure 5.32: Chemiluminescence OH images of the PC2 operating with ϕ=1.0, 0.90, 0.80, and 0.75.*

Regarding the schlieren images, similarly to that observed with the PC1 geometry, the PC2 geometry also presents a reduction of the penetration rate of the unreactive jet phase (first frames of Figure 5.31) as the fuel-air equivalence ratio decreases. The penetration rate also decreases as the fuel-air equivalence ratio decreases for the high-contrast jet, but with some differences that will be discussed below. As previously mentioned for the PC1 geometry, the reduction of the penetration rate can be explained by the lower rate of PC pressure rise as the mixture becomes leaner, reducing the ΔP during the jet ejection (Figure 5.25). In addition to changing the penetration rate, the lower ΔP (and consequently lower jet momentum) also decreases the maximum jet tip penetration and, at some extent, decreases the MC turbulence induced by the jet. The reduced jet tip penetration associated with the lower temperature of the gases being ejected (directly proportional to the PC pressure) changes the location of the MC ignition and the MC flame propagation pattern.

When qualitatively comparing the schlieren images obtained with PC1 and PC2 geometries, a similar trend in the transition between the low- and high-contrast jet is obtained. For the ϕ=1.00 and ϕ=0.90 cases, the transition is well-defined and coincides with the appearance of OH* chemiluminescence intensity. However, for the ϕ=0.80 and ϕ=0.75 cases, the transition is gradual and differs from the instant when the OH* chemiluminescence intensity can be observed. On the one hand, for the PC2 ϕ=1.00 and ϕ=0.90 cases, this transition occurs, respectively, at 0.4 ms and 0.7 ms after the SOE. On the other hand, for the PC2 ϕ=0.80 and ϕ=0.75 cases, a change in the contrast between the jet and background is observed in the schlieren images before any noticeable intensity in the OH* chemiluminescence images. For the PC2 ϕ=0.80 case, some difference in the contrast is observed from 0.5 ms after SOE, but the OH* intensity starts to be detectable only from 1.0 ms. For the PC2 ϕ=0.75 case, the jet contrast starts to change from 0.7 ms after SOE. Nevertheless, the OH* intensity is first detectable at 1.2 ms.

In regard to the presence of hot-reacting gases in the jet, the PC2 presented a great reduction in the OH* intensity for the ϕ=0.80 and 0.75 cases, similar to that observed with the PC1 geometry. Using the same approach of comparing the OH* intensity to the EOE (Table 5.3) and the MC start of combustion by means of the inflection of its pressure rise rate curve (shown in Figure 5.33), it can be noticed that the ϕ=1.0 and 0.90 cases presented a high-intensity OH* signal in the jet region even before the MC start of combustion, suggesting the presence of hot-reacting gases in the jet's composition. In numerical terms, the ϕ=1.0 case presented the first OH* intensity at 0.4 ms, the MC start of combustion at 0.7 ms, and the EOE at 0.95 ms after the SOE. The ϕ=0.90 case presented the first OH* intensity at 0.8 ms, the MC

start of combustion at 1.0 ms, and the EOE at 1.09 ms after the SOE. For the ϕ=0.80 case, however, the OH* intensity was greatly reduced before the MC start of combustion (1.2 ms), indicating that the jet is now composed of high-temperature and low-OH* content gases from a quenched flame front. Lastly, there was no detectable OH* intensity during the jet ejection (up to 1.16 ms after the SOE) for the ϕ=0.75 case, suggesting that the jet is composed of high-temperature burnt gases with undetectable OH*, and the very-low OH* intensity observed from 1.2 ms is originated from the early flame development of the MC combustion instead of the jet ejection. Similar to that observed in the PC1 geometry, the absence of OH* intensity in the PC2 ϕ=0.75 case suggests that the flame quenched at the orifice due to its thicker flame thickness as a result of the diluted mixture.

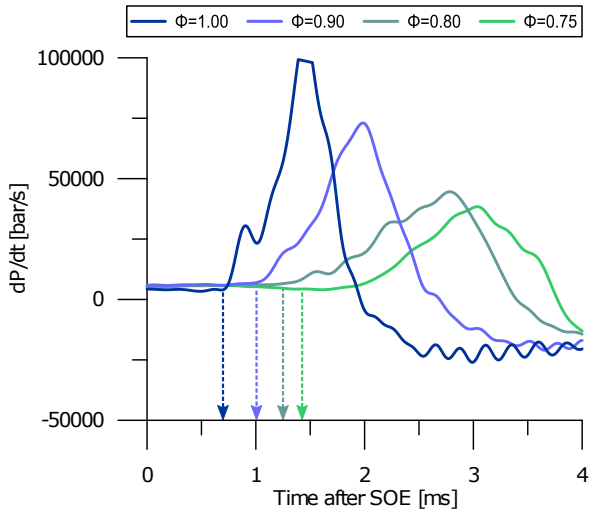

Figure 5.33: Pressure rise rate for the PC2 operating with ϕ=1.0, 0.90, 0.80, and 0.75.

Table 5.6 presents the laminar flame thickness (δ_L) and the laminar flame velocity (S_L) calculated with the pressure (P_{PC}) and temperature ($T_{U,PC}$) of the unburnt mixture at the PC, as well as the dimensionless d_o/δ_L parameter used to quantify the orifice flame-quenching phenomenon. From the data presented in Table 5.6, it is clear that the flame front thickness increases and the flame front velocity decreases as the mixture is diluted. Moreover, the calculated d_o/δ_L parameter for the PC2 suggests that the threshold for the flame quench at the orifice is between 92 and 64 d_o/δ_L, which is in line with the results obtained with the PC1 geometry.

Table 5.6: Flame properties for different fuel-air equivalence ratios and thermodynamic conditions of PC2.

PC	ϕ [-]	$\mathbf{P_{PC}}$ [bar]	$\mathbf{T_{U,PC}}$ [K]	$\boldsymbol{\delta_L}$ [µm]	$\mathbf{S_L}$ [cm/s]	$\mathbf{d_o}$ [mm]	$\boldsymbol{d_o/\delta_L}$ [-]
PC2	1.00	54.8	736.4	15.8	47.1	2.22	141
	0.90	37.6	680.2	24.1	35.2		92
	0.80	28.7	664.9	34.6	32.8		64
	0.75	34.6	627.8	36.6	22.7		61

Concerning the MC ignition location and the flame propagation pattern, Figure 5.32 suggest a significant change as the mixture becomes leaner. First, for the ϕ=1.0 case, the MC ignition occurs along the entire area covered by the jet, and, due to the full jet tip penetration, the flame propagates from the orifice center-line to the optical window borders (symmetrically to the jet axis) and the region near the orifice exit being the last portion to be burnt. Then the ϕ=0.9 case follows a similar trend with a slightly lower jet tip penetration and less OH* chemiluminescence intensity than the ϕ=1.0 case. Next, the MC ignition of the ϕ=0.8 case occurs at the center of the optical windows due to the low jet tip penetration, and the flame propagation goes from the jet location to the optical window borders, and lastly to the region on the opposite side of the orifice exit. Finally, for the ϕ=0.75 case, the MC ignition is located at the jet area and limited to the center of the optical window due to the low jet penetration. The OH* intensity is even lower than the observed in the other cases, and the flame front moves from the jet centerline toward the borders and lastly to the region on the opposite side of the orifice exit.

The temporal evolution of the jet penetration and MC ignition for the PC3 geometry captured by the schlieren and OH* chemiluminescence imaging are shown in Figure 5.34 and Figure 5.35, respectively. The frames are synchronized from the SOE in order to mitigate the mismatches caused by the different ST and jet ejection timing, and the corresponding ST and crank angle reference for the first set of frames are indicated for each case presented. It is important to keep in mind that the PC3 ϕ=0.90 case did not follow the trend observed in the ΔP between chambers, presenting the lower and later ΔP among all cases tested (Figure 5.25).

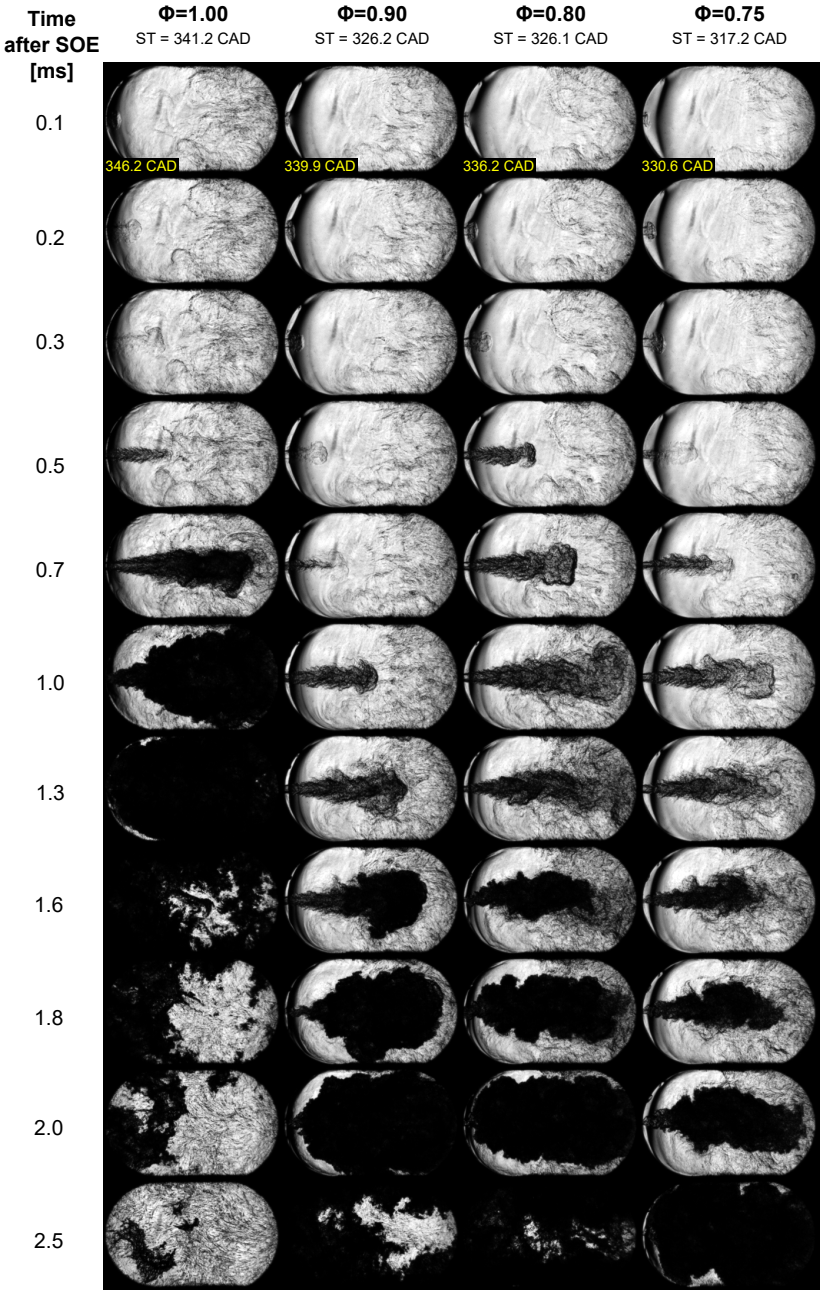

Figure 5.34: Schlieren images of the PC3 operating with ϕ=1.0, 0.90, 0.80, and 0.75.

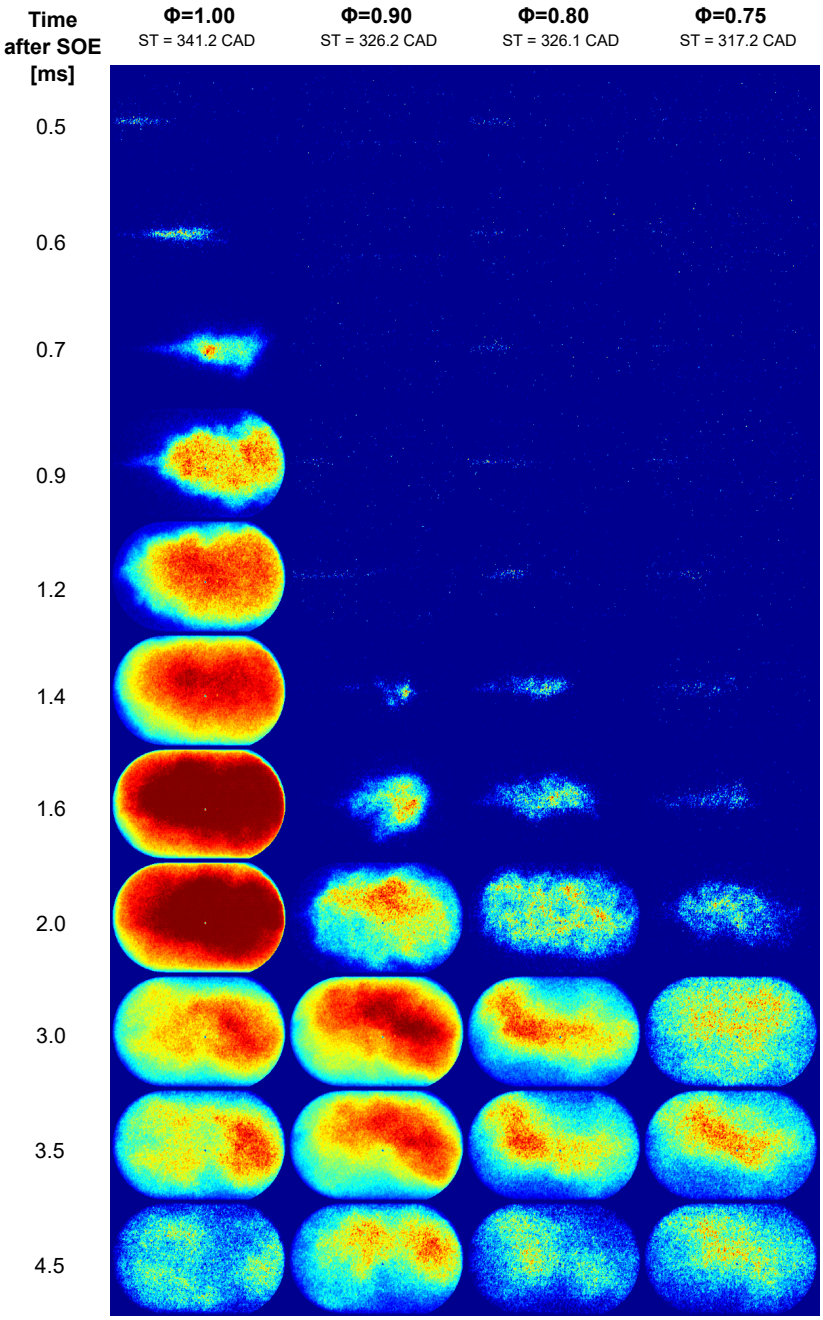

Figure 5.35: Chemiluminescence OH images of the PC3 operating with ϕ=1.0, 0.90, 0.80, and 0.75.*

As shown in Figure 5.34, following the behavior observed for PC1 and PC2 geometries, the PC3 presents a trend of reduction of the penetration rate as the mixture becomes leaner both for the low- and high-contrast jet, except for the ϕ=0.90 case. When compared with PC1 and PC2, the jet generated with the PC3 geometry was able to penetrate practically the entire optical chamber, even in the leanest case, which contributed to an adequate main chamber combustion phasing. This behavior can be explained by the higher delta pressure between chambers due to the higher restriction imposed by the smaller orifice diameter, i.e., in the competition between pressure drop by exiting mass flow and build-up pressure by combustion, the lower $A_e/V_{PC}N$ parameter (smaller orifice diameter) reduces the pressure drop by exiting mass flow in comparison to the PC1 and PC2 geometries.

Further analyzing the Schlieren images (Figure 5.34), it can be noticed that the transition from a low-contrast to a high-contrast jet is clear for the ϕ=1.00 case, coinciding with the appearance of OH* intensity at 0.5 ms after SOE (Figure 5.35) still during the jet ejection (from 0 to 1.07 ms). For the ϕ=0.90 case, however, a change in the jet contrast is noticed in the Schlieren images from 0.7 ms after SOE, but practically no OH* intensity is detected until 1.4 ms after SOE, the instant in which the MC is ignited (please refer to Figure 5.36). This behavior suggests that the PC flame front was quenched at the orifice, and the MC was ignited by a jet of hot gas (evidenced by Schlieren images) with a low OH* content (revealed by chemiluminescence images). Moreover, the hypothesis that the OH* intensity originates from the MC's ignition rather than the jet is further supported by the location of the initial observation of OH* intensity, which is on the opposite side of the orifice exit; otherwise, it would have been seen as it exited the orifice.

Continuing the qualitative analysis of the images for the PC3 geometry, the ϕ=0.80 case presents a change in the jet contrast (i.e. temperature) from 0.5 ms after SOE, but very low OH* intensity up to 1.4 ms after SOE, which coincides with the MC ignition (please refer to the inflection of the pressure rise rate curve in Figure 5.36) and is just after the EOE (1.26 ms). Furthermore, the ϕ=0.75 case also presents very low OH* intensity during the jet ejection (from 0 to 1.31 ms) even with a change in the jet temperature captured by the Schlieren images from 0.7 ms after SOE. The increase in the OH* intensity noticed from 1.4 ms, in the ϕ=0.75 case, is then likely from the MC early flame propagation. In conclusion, the images and the pressure trace for both PC3 ϕ=0.80 and ϕ=0.75 cases suggest that the PC flame front is quenched at the orifice, and the MC ignition source is a high-temperature and low-OH* content gas jet resulted from burnt air-fuel mixture.

When compared to the PC1 and PC2 geometries, the PC3 has a greater tendency to flame quenching at the orifice due to its higher flow velocity at the orifice in virtue of the higher ΔP. The higher flow velocity increases the flame stretch, leading to the flame quenching when the flame is passing through the orifice. Nevertheless, even though the flame was quenched at the orifice for the ϕ=0.80 and ϕ=0.75 cases, the higher PC peak pressure as a result of the more restrictive orifice increased the temperature of the gases exiting the PC and enhanced the MC ignition capabilities.

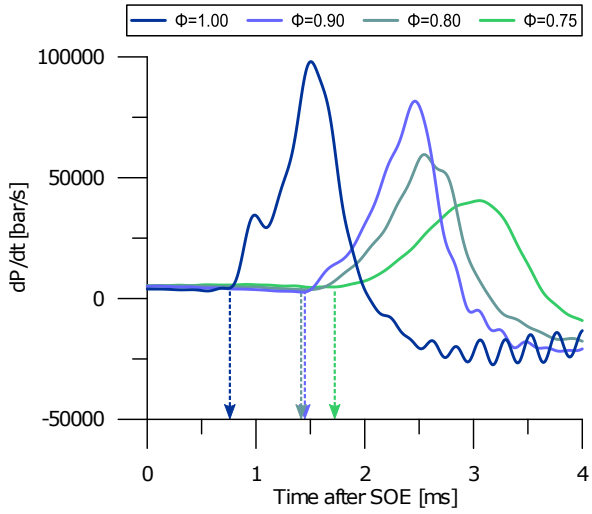

Figure 5.36: Pressure rise rate for the PC3 operating with ϕ=1.0, 0.90, 0.80, and 0.75.

Table 5.7 shows the laminar flame thickness (δ_L) and the laminar flame velocity (S_L) calculated with the pressure (P_{PC}) and temperature ($T_{U,PC}$) of the unburnt mixture into the PC3, as well as the dimensionless d_o/δ_L parameter used to quantify the orifice flame-quenching phenomenon. Similar to PC1 and PC2, the tendency to thicken the flame front and decrease the laminar flame speed as the mixture is diluted is also observed in PC3, supporting the reasoning employed in the analysis of the results. Finally, the calculated d_o/δ_L parameter for the PC3 suggests that the threshold for the flame to quench at the orifice is between 153 and 93 d_o/δ_L, slightly above the range observed in PC1 and PC2 geometries.

Table 5.7: Flame properties for different fuel-air equivalence ratios and thermodynamic conditions of PC3.

PC	ϕ [-]	P_{PC} [bar]	$T_{U,PC}$ [K]	δ_L [µm]	S_L [cm/s]	d_o [mm]	d_o/δ_L [-]
PC3	1.00	61.5	735.6	14.7	46.4	2.24	153
	0.90	37.4	685.1	24.0	36.0		93
	0.80	37.3	664.3	29.1	29.8		77
	0.75	32.6	643.8	36.9	24.9		61

5.7 Effect of EGR rate

To further understand the effect of the EGR dilution on the PC combustion, jet characteristics, and MC ignition and combustion, the PC ignition system was tested under four EGR levels: 0, 10, 20, and 25%. It is worth mentioning that EGR composition is considered N_2 only, and the EGR dilution rate is given by the ratio between EGR (N_2 only) and air (a mixture of O_2 and N_2). The EGR rate can be defined taking into account the oxygen fraction as follows:

$$EGR\,rate = \frac{x_{O_2,mixture} - x_{O_2,air}}{x_{O_2,EGR} - x_{O_2,air}} \tag{5.25}$$

where $x_{O_2,mixture}$, $x_{O_2,air}$, and $x_{O_2,EGR}$ is the molar fraction of mixture, air, and EGR, respectively. To ensure no contamination with the residual gas from the previous cycle, nor with the air used in the RCEM automatic procedures during the preparation for the operation, the cylinder was vacuumed before the fuel and air-EGR mixture entered into the cylinder on each combustion cycle.

As the mixture was kept stoichiometric ($\phi = 1.0$) in terms of oxygen, the fuel injected was decreased as the EGR increased due to the oxygen reduction. The mixture composition in molar and mass basis for each EGR level is presented in Table 5.8.

Two PC geometries were selected to evaluate the EGR effect: PC1 and PC3 (Figure 5.37). Both geometries have the same inner volume but different orifice diameters, which results in different values for the $A_n/V_{PC}N$ parameter. The objective when comparing two different PC geometries is to identify if some geometrical factor can be beneficial for EGR-diluted applications. For instance, as previously seen on section 5.5, the PC1 has a shorter time between

Table 5.8: Mixture composition for each EGR level.

EGR rate	**Molar fraction**			**Mass fraction**		
%	CH_4	O_2	N_2	CH_4	O_2	N_2
0	0.0948	0.1897	0.7155	0.0549	0.2197	0.7253
10	0.0859	0.1719	0.7422	0.0497	0.1989	0.7514
20	0.0769	0.1538	0.7693	0.0444	0.1777	0.7778
25	0.0724	0.1447	0.7829	0.0418	0.1671	0.7911

ST and the reacting jet, which may be beneficial to the combustion phasing on EGR-diluted conditions.

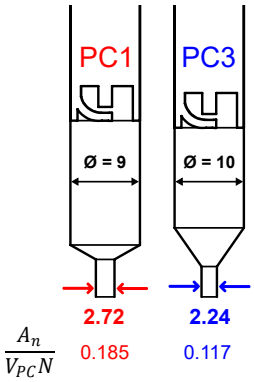

Figure 5.37: Illustration of the internal geometry of PC1 (left) and PC3 (right).

The spark timing was adjusted to achieve the peak of MC pressure at 10 CAD-ATDC, which corresponds to the MBT condition in a reciprocating internal combustion engine. In the event that the MBT criterion cannot be met due to misfiring, the ignition timing was adjusted as close as possible to MBT.

Table 5.9 shows the pre-chamber characteristic times taken from the indicated data shown in Figure 5.38 and Figure 5.42, where the Start of Ejection (SOE), the End of Ejection (EOE) and the Duration of Ejection (DOE) for PC1 and PC3 are exhibited for each EGR rate tested. As expected due to the combustion deterioration, the advance of the ST and the longer DOE are observed both for PC1 and PC3 as the EGR increases, except for the PC1 EGR20% case. In particular, the DOE will be essential for estimating the

jet content in the schlieren and OH* chemiluminescence imaging assessment shown below.

Table 5.9: Pre-chamber characteristic times for different EGR rates.

PC	EGR	ST	SOE	EOE	DOE	
	[%]	[CAD]	[CAD]	[CAD]	[CAD]	[ms]
PC1	0	337.6	339.5	348.9	9.4	0.87
	10	316.4	324.2	333.9	9.7	1.03
	20	318.5	332.7	346.0	13.3	1.37
PC3	0	341.2	344.8	356.0	11.2	1.07
	10	318.7	334.8	348.6	13.8	1.40
	20	311.3	331.5	343.5	12.0	1.23

The PC and MC in-cylinder pressure curves of some cycles for different EGR levels (0, 10, 20, and 25%) are shown in Figure 5.38 for the PC1 geometry. As can be observed, the 0% EGR case presents the higher in-cylinder pressure both for pre- and main chambers, followed by 10, 20, and 25% EGR cases, definitely caused by the higher fuel amount injected. Furthermore, as the EGR rate increases, the peak of ΔP during PC combustion likewise decreases, reducing the available momentum for the jet to penetrate into the MC. Additionally, the repeatability of the combustion cycles is impaired with the increase of EGR, especially for the 20% EGR case, including some misfired cycles (not represented in the graph). The MBT-like condition could not be achieved for the 20% EGR case due to the misfire when further advancing the spark timing. Finally, the 25% EGR case presented misfired cycles in all tested cycles for a wide range of spark timings.

For the sake of clarity, from now on the data regarding each EGR level will only be from the most representative cycle (defined in section 5.1). Figure 5.39 presents the pre-chamber chemical heat release rate (HRR) obtained with the PC1 geometry when operating with 0, 10, 20, and 25% of EGR. The HRR curves are synchronized with the ST to highlight the variation in the delay between the ST and the start of heat release as the EGR rate increases. As evidenced by Figure 5.39, when there is no addition of EGR, the PC heat release takes place during the first 10 CAD after the ST, and reaches a higher peak value when compared to the cases where some EGR is added. Additionally, a tendency to delay the start and to extend the duration of the PC heat release is observed as EGR is added to the mixture, which is most

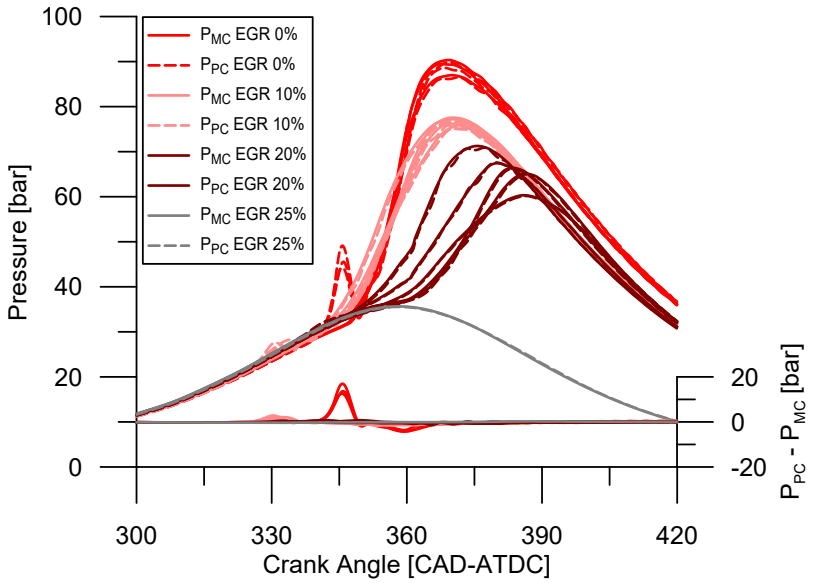

Figure 5.38: PC and MC in-cylinder pressure and ΔP curves for different EGR levels - PC1.

probably explained by the decrease in the flame propagation speed within the PC.

The effect of the EGR rate in the PC1 geometry is shown by the schlieren and chemiluminescence images in Figure 5.40 and Figure 5.41, respectively, synchronized from the Start of Ejection (SOE) of each case. It can be observed that the 0% EGR case presented the fastest transition between the SOE and the first detectable OH* chemiluminescence among the tested cases, occurring at 0.4 ms after the SOE, temporally coinciding with the instant in which the jet transitions from a low-contrast to a high-contrast appearance in the schlieren images. For the 10% and 20% EGR scenarios, however, this transition is not remarkable in the schlieren images and it takes around 1.0 and 1.5 ms after the SOE, respectively, for the first detectable intensity in the OH* chemiluminescence images to be noticed. Relating the images to the characteristic times presented in Table 5.9, it can be stated that the first detectable OH* intensity occurred during the jet ejection for the 0% EGR case, but after the end of the jet ejection for the 10% and 20% EGR cases, indicating that the PC flame front quenched when passing through the orifice and the jet does not contain active radicals for these latter cases.

One of the motivations for the “intermediate” contrast jet observed in the

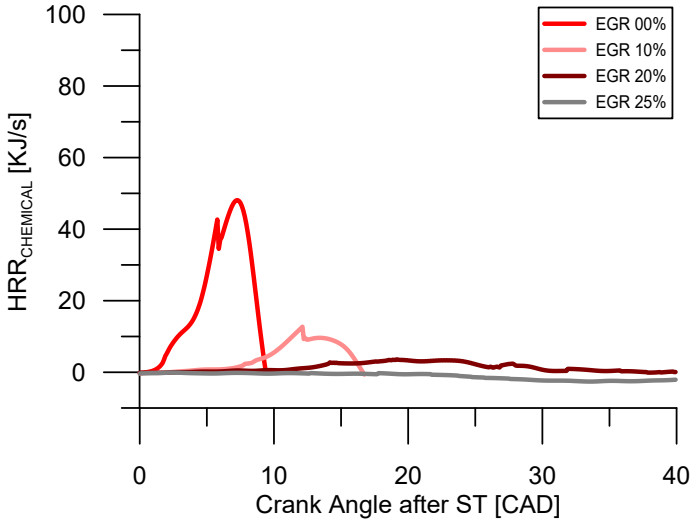

Figure 5.39: Pre-chamber chemical heat release rate for different EGR levels - PC1.

schlieren images for PC1 is the lower PC temperature due to the lower PC pressure when the EGR is added. Additionally, the thicker flame thickness as a result of the EGR may cause flame quenching as the flame front crosses the orifice, then mitigating the appearance of OH* chemiluminescence and thus supporting the hypothesis of low-temperature gases by the lack of flame kernels. Finally, the reduction of the ΔP between chambers during PC combustion also supports the lack of a "cold-unreacted jet" by the reduction of the available momentum to expel the unburned mixture near the orifice right after the PC combustion starts.

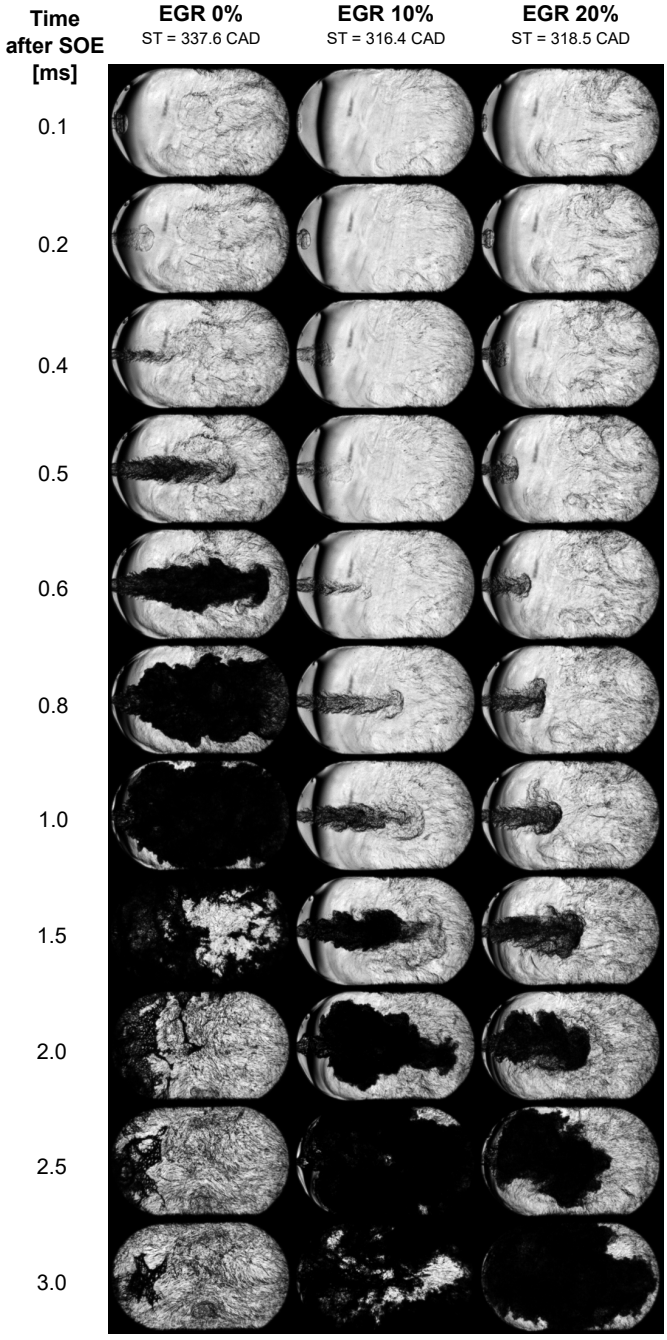

Figure 5.40: Schlieren images of the PC1 operating with 0 (left), 10 (center) and 20% (right) of EGR.

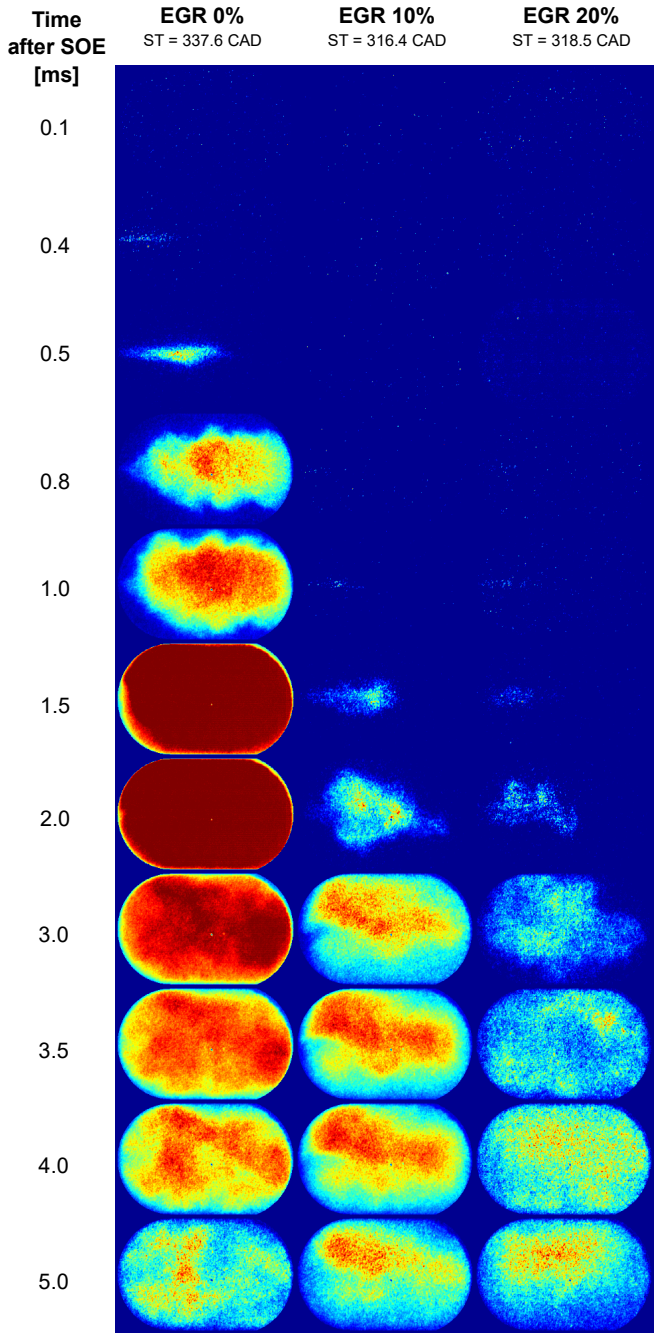

Figure 5.41: Chemiluminescence OH images of the PC1 operating with 0 (left), 10 (center) and 20% (right) of EGR.*

As already discussed in the previous section, the quenching distance is proportional to the laminar flame thickness. Table 5.10 shows the laminar flame thickness (δ_L) and the laminar flame velocity (S_L) calculated with the pressure (P_{PC}) and temperature ($T_{U,PC}$) conditions at PC1 with all EGR rates tested. Comparing the laminar flame thickness of the 0% EGR case with the 10% EGR case, it folds when the EGR is added to the mixture. Given the higher pressure and temperature for the 20% EGR case in comparison to the 10% EGR case due to the retarded spark timing, no significant increase in the flame thickness was noticed for the 20% EGR case. The calculated laminar flame thickness supports the behavior observed in the imaging data for the PC1: flame quenching for the 10% and 20% EGR cases.

Table 5.10: Flame properties for different EGR rates and thermodynamic conditions of PC1.

PC	**EGR** [%]	$\mathbf{P_{PC}}$ [bar]	$\mathbf{T_{U,PC}}$ [K]	$\boldsymbol{\delta_L}$ [µm]	$\mathbf{S_L}$ [cm/s]	$\mathbf{d_o}$ [mm]	$\boldsymbol{d_o/\delta_L}$ [-]
	0	45.5	645.6	21.3	36.2		128
PC1	10	26.8	587.0	45.9	23.7	2.72	59
	20	31.8	663.6	48.9	20.7		56

Table 5.10 also shows the relation between the orifice diameter (d_o) and the laminar flame thickness (δ_L) for all EGR rates tested. This dimensionless parameter is a parameter proposed by the author to quantify the orifice flame-quenching phenomenon. For the PC1 geometry, assuming that the cases with 10 and 20% of EGR presented flame quenching at the orifice, the threshold should be in the range between 59 and 128, which is in line with the results obtained with PC1 and PC2 when the equivalence ratio was swept.

In terms of the MC ignition pattern obtained with PC1, some differences are observed when the EGR is added to the mixture. First, without EGR addition, the hot-gas reacting jet penetrates into the MC almost to the end of the optical window, and only then it is possible to observe a flame front propagating from the optical window center-line towards the walls (from 0.6 ms after the SOE), and finally propagating to the region close to the orifice exit. The MC mixture, therefore, is ignited throughout the entire jet region and quickly consumes the entire optical volume. Then, with the addition of 10% of EGR, the jet momentum is significantly reduced due to the lower ΔP, causing a slow and reduced penetration. In this case, the MC ignition takes place locally in the middle of the optical window (jet center-line) and then slowly propagates towards the periphery closer to the orifice exit, and finally

burns the mixture on the opposite side of the orifice exit. To conclude, the 20% EGR case presents a similar MC ignition pattern to that of the 10% EGR case, initiating the combustion close to the orifice exit, propagating towards the periphery, and finally to the opposite region of the orifice exit.

Figure 5.42 shows the MC and PC in-cylinder pressure for PC3 geometry and different EGR levels (0, 10, 20, and 25%). Similarly to the PC1, four glaring characteristics can be noticed in the PC3 as the EGR rate increases: (1) reduction in the in-cylinder peak pressure; (2) lower ΔP during PC combustion; (3) higher "cycle-by-cycle" variation; (4) no MC ignition was achieved with 25% of EGR. These behaviors are fundamentally caused by the lower amount of fuel and the reduced laminar flame speed caused by the EGR. On the one hand, as shown in Figure 5.43, the reduction of the PC heat release rate caused by the EGR implies a reduction of the PC peak pressure. On the other hand, the longer PC combustion duration contributes to a gradual expulsion of the PC gases, which also implies a reduction of the PC peak pressure.

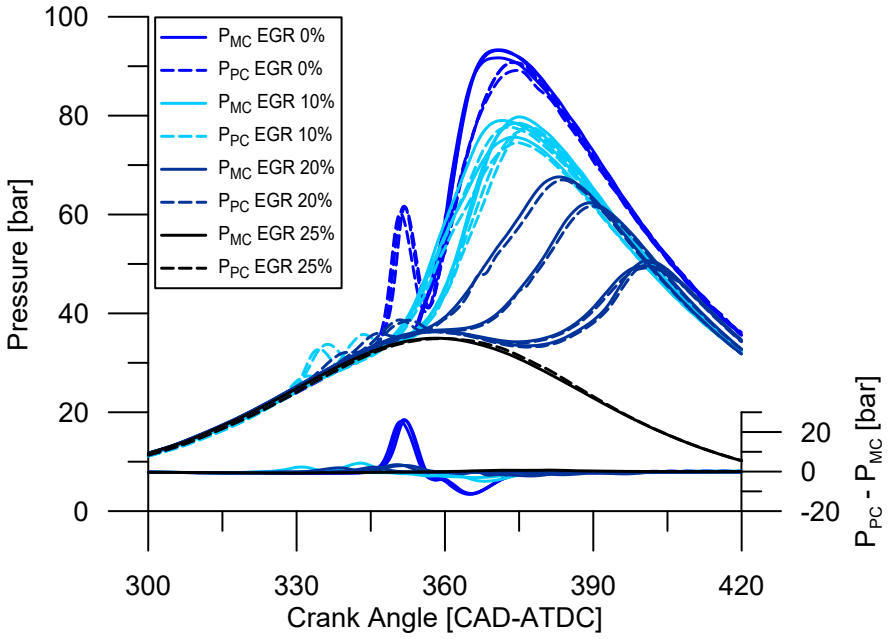

Figure 5.42: PC and MC pressure for different EGR levels - PC3.

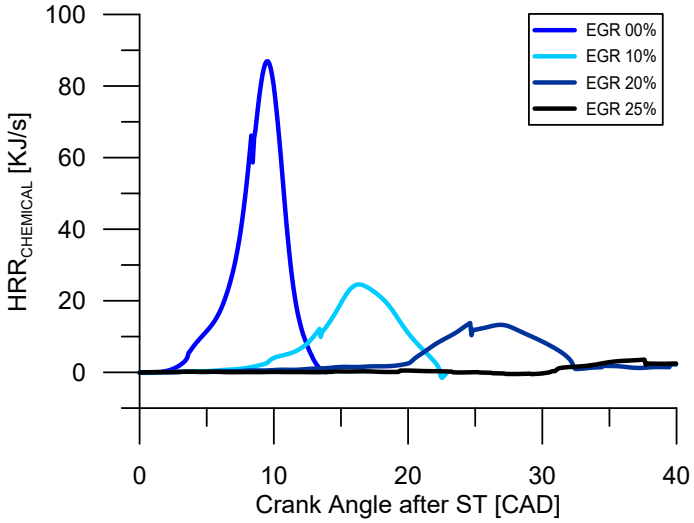

Figure 5.43: Pre-chamber chemical heat release rate for different EGR levels - PC3.

In addition to the magnitude of the HRR in the PC, Figure 5.43 also highlights the differences in terms of combustion velocity and the "delay" between ST and the beginning of heat release. As the EGR rate increases, the PC HRR curve becomes wider and further away from the ST. To compensate for the lower flame propagation velocity and preserve the MBT condition under EGR-diluted conditions, the spark timing was advanced as the EGR was increased. Nevertheless, for the 20% of EGR condition, further advancing the spark timing to achieve MBT condition resulted in misfiring, probably due to the low PC turbulence intensity when moving too far from TDC, as indicated by numerical studies [20].

Figure 5.44 and Figure 5.45 show the effect of the EGR rate on PC3 by means of schlieren and chemiluminescence images, respectively, synchronized from the SOE. Just as pointed out for the PC1 geometry, the clear distinction between a low-contrast (unreactive) first jet and a high-contrast (reactive) second jet is also not seen in the PC3 geometry for the cases with EGR addition.

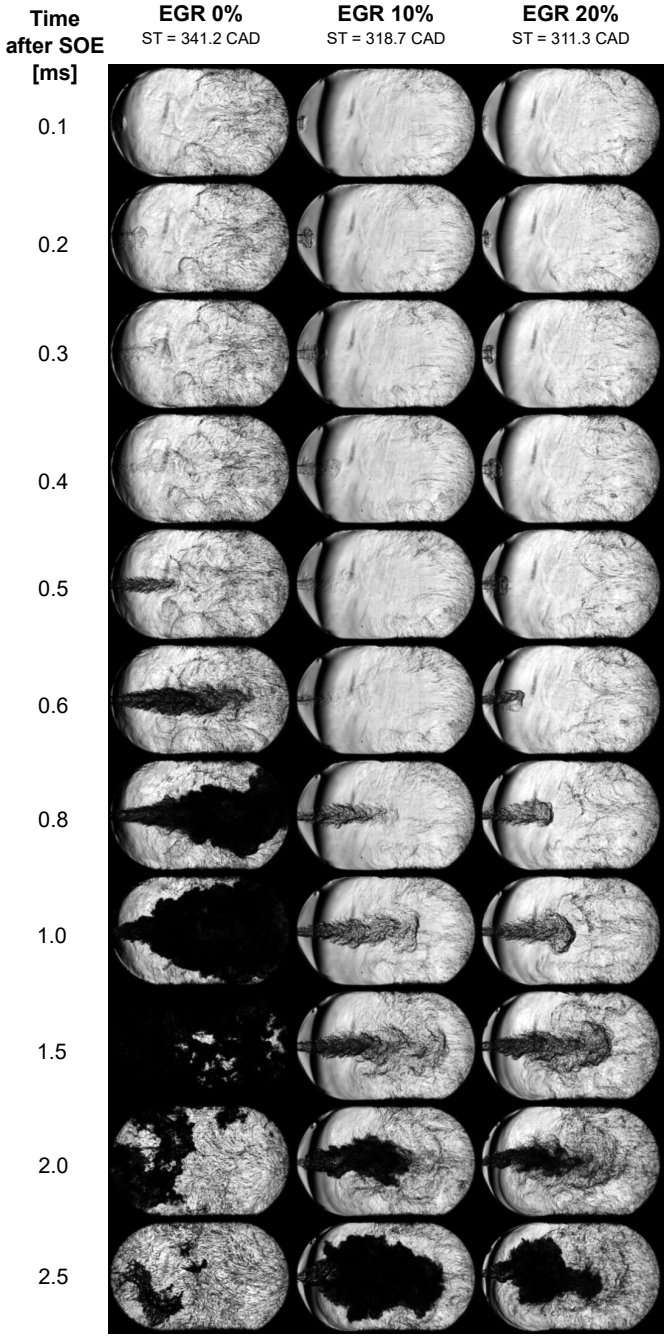

Figure 5.44: Schlieren images of the PC3 operating with 0 (left), 10 (center) and 20% (right) of EGR.

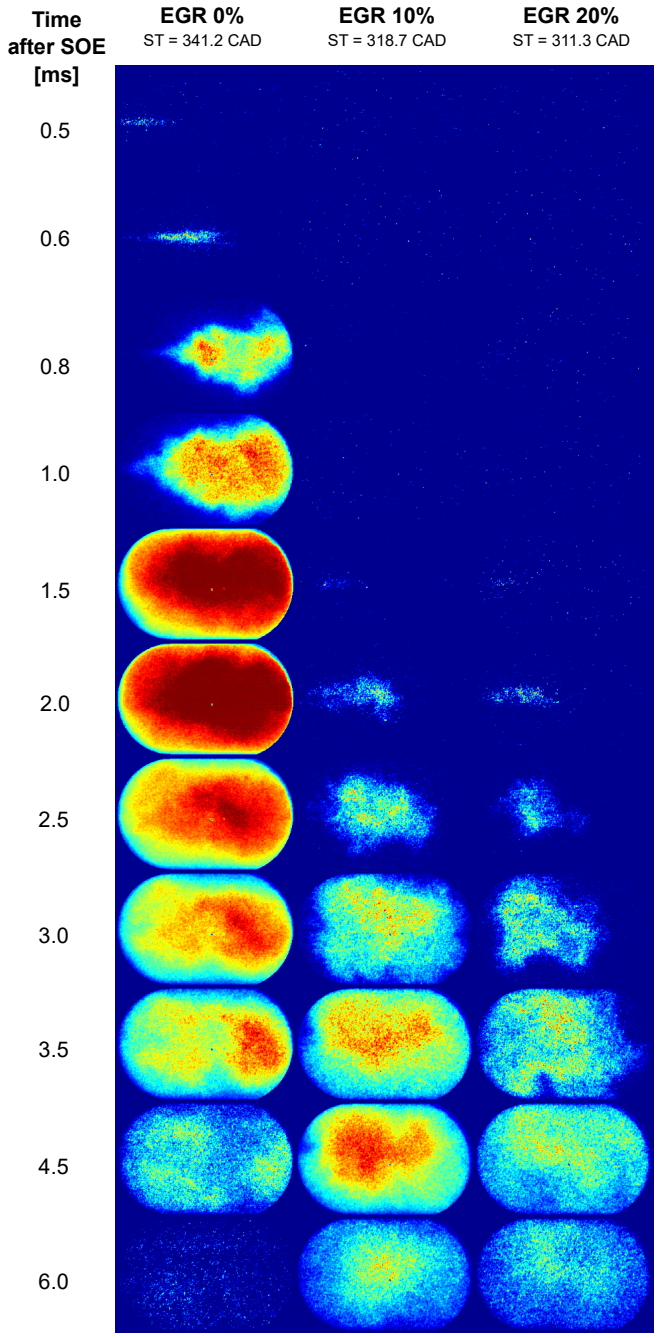

Figure 5.45: Chemiluminescence OH images of the PC3 operating with 0 (left), 10 (center) and 20% (right) of EGR.*

In the 0% EGR case, the low-contrast jet seen in the schlieren images (Figure 5.44) up to 0.4 ms after the SOE does not present any intensity on the OH* chemiluminescence images (Figure 5.45). Once the high-contrast jet appears in the schlieren images (0.5 ms after the SOE), OH* chemiluminescence intensity is also detected in the jet region. Linking the images to the characteristic times derived from the pressure traces shown in Table 5.9, it can be seen that the OH* chemiluminescence intensity is observed during the jet ejection period (up to 1.07 ms after the SOE, indicating that the PC flame front was not quenched at the orifice. Regarding the MC ignition pattern, it was observed in the OH* chemiluminescence imaging a sort of "lift-off length" (typically detected in diesel sprays and combustion [21]), and the MC combustion propagating from the jet tip to the walls and the region close to the orifice exit. This sort of lift-off length is probably caused by the high jet velocity, which leads to a high local turbulence that impairs the flame propagation. In addition, the bulk momentum also pushes the reacting mixture towards away from the orifice exit.

In the 10 and 20% EGR cases, the gases being ejected present an "intermediate" contrast (when compared to the low and high-contrast jets of the 0% EGR case) during the entire jet ejection period. The main difference lies, therefore, in the absence of OH* chemiluminescence intensity up to the end of the jet ejection (1.40 and 1.23 ms after the SOE for 10 and 20% EGR cases, respectively), suggesting that the PC flame front was quenched at the orifice. Only from 1.5 ms onwards OH* chemiluminescence intensity is detected in the inner region of the jet, which likely is from the MC ignition and not from the jet itself. The combustion then propagates from the center of the MC to the peripheries for the 10% EGR case, and from the region close to the orifice to the region opposite to the orifice (right-hand of Figure 5.45) for the 20% EGR case.

Table 5.11 presents the laminar flame thickness (δ_L) and the laminar flame velocity (S_L) calculated with the pressure (P_{PC}) and temperature ($T_{U,PC}$) conditions of the unburnt mixture at the PC3, as well as the dimensionless flame-quenching phenomenon parameter (d_o/δ_L) for all EGR rates tested in the PC3. From the data presented, it is clear that the flame front thickness increases, and the flame front velocity decreases as the EGR is added to the air-fuel mixture. Moreover, given the flame quenching for the 10 and 20% EGR cases suggested by the imaging data, the calculated d_o/δ_L parameter for the PC3 indicates that the threshold for the flame quench at the orifice is between 153 and 66 d_o/δ_L, which is in line with the range observed both with the PC3 geometry in the EGR dilution tests and the PC1 and PC2 geometries at different equivalence ratios.

Table 5.11: Flame properties for different EGR rates and thermodynamic conditions of PC3.

PC	EGR [%]	P_{PC} [bar]	$T_{U,PC}$ [K]	δ_L [µm]	S_L [cm/s]	d_o [mm]	d_o/δ_L [-]
	0	61.5	735.6	14.7	46.4		153
PC3	10	35.6	641.6	34.0	27.1	2.24	66
	20	31.6	640.1	51.7	18.8		43

Figure 5.46 shows the effect of the EGR rate on the interval between ST and SOE for PC1 and PC3. This parameter indicates (1) the PC's ability to build up pressure and (2) the inherent delay between the ST and the energy delivery to the MC ignition. Since the laminar flame speed of mixtures diluted with EGR is lower, there is a clear trend of increasing intervals between ST and SOE as the EGR rate is increased. The PC3 geometry presented a higher delay between ST and SOE for all EGR rates tested, which can be explained by the higher flow restriction caused by the lower $A_e/V_{PC}N$ parameter. For both PC geometries operating at 20% EGR, the non-fulfillment of the MBT criteria for combustion phasing was largely due to the increased delay between ST and SOE.

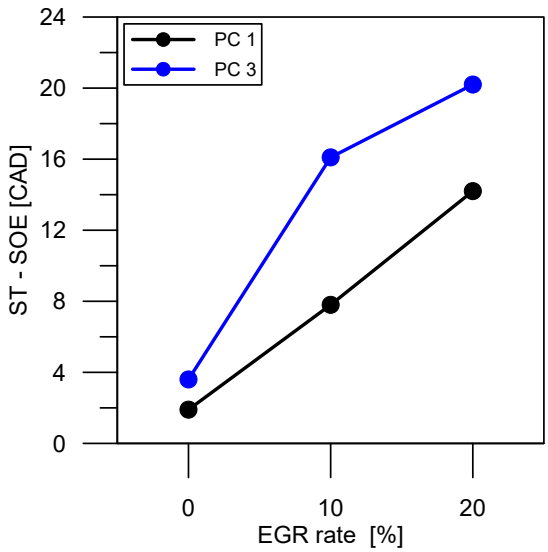

Figure 5.46: Effect of the EGR rate on the interval between ST and SOE for PC1 and PC3.

Summarizing the results obtained with PC1 and PC3 with different EGR rates, both PC geometries presented the EGR limit to the combustion at 20%, but without fulfilling the MBT criteria of maximum pressure at 10 CAD-ATDC. When the EGR rate was increased to 25%, no combustion was achieved regardless of the spark timing used. In terms of $A_e/V_{PC}N$ parameter, it can be highlighted that the PC geometry with the lower $A_e/V_{PC}N$ parameter (i.e. PC3) presented: (1) higher ΔP between chambers; (2) higher and early peak of PC heat release rate, but without enhancement of the MC ignition capabilities, and (3) greater delay between ST and SOE for all EGR conditions tested. Finally, the 10 and 20% EGR cases presented flame quenching at the orifice for both PC1 and PC3 geometries, all of them with a d_o/δ_L parameter below 66.

5.8 Summary and conclusions

This chapter has presented an evaluation of the pre-chamber ignition concept in an RCEM experimental facility by using optical techniques and in-cylinder pressure for both PC and MC. The experimental tests started from a PC geometry that replicated the geometrical parameter that controls the mass flow between MC and PC of a multi-orifice in a single-orifice PC geometry, thus emulating the delta pressure between chambers and preserving as much as possible the jet characteristics from the multi-orifice on the single-orifice geometry. From this single-orifice baseline geometry, other 4 PC configurations were experimentally tested, varying the PC volume, PC inner diameter, orifice diameter, distance between the spark plug and orifice, and orifice length to assess its individual contribution to the jet characteristics.

After presenting the PC geometries tested, as well as the thermodynamic model used to carry out the heat-released analysis, and the fundamental processes linked with the typical images obtained with the optical technique used, the experimental results were presented in three main sections: (1) the effect of the PC geometry, (2) the effect of the fuel-air equivalence ratio, and (3) the effect of the EGR rate.

First, the aspects regarding the PC geometry were assessed in terms of pressure drop between chambers, PC combustion development, jet ejection, and jet tip penetration, allowing to conclude that:

- The relation between the geometrical parameter $A_e/V_{PC}N$ and the pressure drop during the PC filling previously proposed and numerically validated is now experimentally validated.

- Despite the PC volume or orifice diameter, the pressure drop between chambers during the PC filling is preserved as long as the $A_e/V_{PC}N$ is preserved.
- During the PC combustion, however, a different PC length (i.e. distance from spark plug to orifice) leads to a different PC pressure rise rate even preserving the $A_e/V_{PC}N$ parameter. The longer PC combustion duration for the longer PC leads to a lower and late peak of delta pressure, and a late reactive ejection.
- Preserving all the geometric characteristics of the PC and only changing the orifice length, the jet tip penetration is preserved, but the higher the length-to-diameter orifice ratio (L_o/d_o), the lower the jet angle, and the slower the 2D flame area grows as the jet penetrates into the MC.

Then, once the effects of the PC geometry were addressed, the effect of the fuel-air equivalence ratio on the PC combustion, jet ejection, and MC ignition was thoroughly discussed, and the following conclusions can be drawn:

- The lean limit for operating with PC1, PC2 and PC3 under the same mixture condition was ϕ=0.75, but only PC3 met the criteria for the combustion phasing at this condition.
- Despite the PC geometry, the PC pressure rise rate decreased as the fuel-air equivalence ratio decreased, which impaired the jet penetration into the MC. However, the higher restriction to the mass flow caused by the lower $A_e/V_{PC}N$ parameter of PC3 was beneficial to the lean operation, being able to provide a sufficient ΔP to improve the jet penetration.
- The delay between the ST and the start of ejection (SOE) increases as the mixture becomes lean, requiring further advance of the ST to reach the combustion phasing criterion as the fuel-air equivalence ratio decreases. For the leanest case (ϕ=0.75), only PC3 meets the combustion phasing criterion.
- The imaging analysis showed that the jet composition significantly changes as the mixture becomes lean, being abundant in OH radicals at stoichiometric mixture, and decreasing its quantity as the mixture becomes lean for all PCs tested. Moreover, the lower PC pressure also decreases the temperature of the gases being ejected, corroborated by the lower contrast of the schlieren images.

- In addition to the jet composition, the decrease in the fuel-air equivalence ratio also modified the MC ignition location and the flame propagation pattern. The lower jet penetration in virtue of the lean mixture progressively decreased the ignition spots, the turbulence induced by the jet, and the energy contained in the jet. The MC ignition location then changed from a large fraction of the MC to a small fraction region close to the PC orifice exit, and the MC combustion takes longer and the flame propagates from the region close to the orifice to the rest of the MC in the lean cases.

- The leanest case (ϕ=0.75) presented flame-quenching when passing through the orifice for all PCs tested, likely due to its larger flame thickness caused by the dilution and, to a lesser extent, the lower PC pressure.

Finally, the effect of the EGR rate on the PC combustion, jet characteristics, and MC ignition was assessed, and the main conclusions were:

- The maximum admissible EGR rate to achieve combustion was 20% both for PC1 and PC3 geometries;

- Regardless of the PC geometry, the PC pressure rise rate and PC maximum pressure during PC combustion decreased as the EGR rate increased as a result of the lower heat-released rate. As a result of the lower ΔP between chambers, the jet tip penetration was reduced as the EGR rate increased.

- Schlieren and OH* chemiluminescence images combined with PC and MC in-cylinder pressure indicated that the PC flame front was quenched at the orifice for the 10 and 20% EGR cases, which do not occur for the 0% EGR case.

- The geometrical parameter $A_e/V_{PC}N$ did not present a substantial impact on the MC ignition pattern or the presence of active radials on the jet. However, it changed the delay between the ST and the start of ejection (SOE) because of the different flow restriction.

From the studies varying the equivalence ratio and the EGR rate, the flame properties for the different mixture conditions were estimated according to the PC conditions, and the Da number and the relation between the orifice diameter (d_o) and the laminar flame thickness (δ_L) were proposed to evaluate the flame-quenching phenomenon at the PC orifice. The Table 5.12 shows

the flame properties, the dimensionless d_o/δ_L parameter, the Da number, and an indication if the imaging data suggests that the PC flame front quenched or not when passing through the orifice. Figure 5.47 shows graphically both the d_o/δ_L (left-hand side) and the Da number (right-hand side), as well as if the flame quenched (blue symbol) or not (red symbol) at the orifice. It was identified that the quenching threshold (transition region) for methane-air mixtures in the PC geometry tested in the RCEM was around 84 and 93 d_o/δ_L, given that in this range there are cases in which there was no flame quenching (PC1 ϕ=0.80 and PC2 ϕ=0.90) and cases in which the flame quenching was observed (PC3 ϕ=0.90). Below this range, all cases presented flame quenching at the orifice, and above this range, no flame quenching was observed. Contrary to what was supposed in 4.5, the Da number has not proved to be a reliable parameter for identifying flame quenching of the jet exiting the PC orifice, possibly because it is a parameter that varies spatially and then should be calculated locally, and due to the difficulty in properly determining the parameters used to calculate the Da number (here estimated from the in-cylinder pressure and mixture conditions).

Table 5.12: Summary of the flame properties for the equivalence ratio and EGR rate sweep for PC1, PC2, and PC3.

PC	ϕ [-]	**EGR** [%]	δ_L [µm]	S_L [cm/s]	d_o [mm]	d_o/δ_L [-]	**Da** [-]	**Quenching** [-]
PC1	1.00	0	14.9	58.0	2.72	182	3.64	No
	0.90	0	20.1	41.5		135	2.23	No
	0.80	0	32.4	34.5		84	1.68	No
	0.75	0	35.8	30.1		76	3.62	Yes
	1.00	0	21.3	36.2		128	1.62	No
	1.00	10	45.9	23.7		59	0.92	Yes
	1.00	20	48.9	20.7		56	6.06	Yes
PC2	1.00	0	15.8	47.1	2.22	141	2.83	No
	0.90	0	24.1	35.2		92	1.86	No
	0.80	0	34.6	32.8		64	2.95	Yes
	0.75	0	36.6	22.7		61	1.36	Yes
PC3	1.00	0	14.7	46.4	2.24	153	3.00	No
	0.90	0	24.0	36.0		93	2.91	Yes
	0.80	0	29.1	29.8		77	1.59	Yes
	0.75	0	36.9	24.9		61	1.10	Yes
	1.00	0	14.7	46.4		153	2.93	No
	1.00	10	34.0	27.1		66	0.83	Yes
	1.00	20	51.7	18.8		43	0.51	Yes

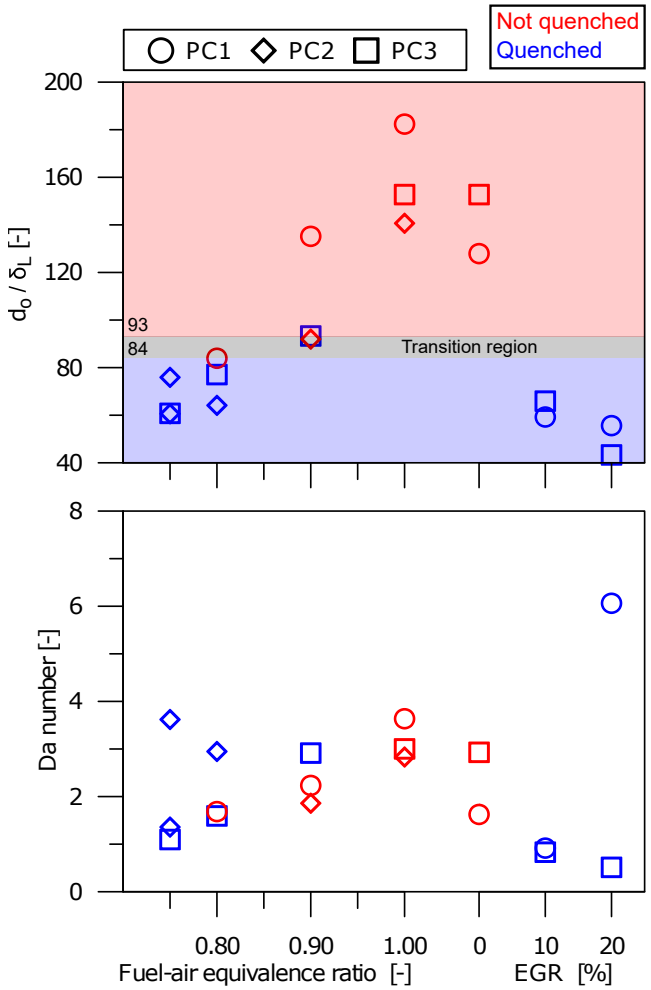

Figure 5.47: Ratio between orifice diameter and laminar flame thickness, and Da number for different equivalence ratio and EGR rate.

References

[1] Benajes, J. et al. "Evaluation of the passive pre-chamber ignition concept for future high compression ratio turbocharged spark-ignition engines". In: *Applied Energy* 248 (2019), pp. 576–588. DOI: 10.1016/j.apenergy.2019.04.131.

[2] Novella, R., Gomez-Soriano, J., Martinez-Hernandiz, P.J., Libert, C., and Rampanarivo, F. "Improving the performance of the passive pre-chamber ignition concept for spark-ignition engines fueled with natural gas". In: *Fuel* 290.December 2020 (2021), p. 119971. DOI: 10.1016/j.fuel.2020.119971.

[3] Macian, V., Bermudez, V., Payri, R., and Gimeno, J. "NEW TECHNIQUE FOR DETERMINATION OF INTERNAL GEOMETRY OF A DIESEL NOZZLE WITH THE USE OF SILICONE METHODOLOGY". In: *Experimental Techniques* 27.2 (2003), pp. 39–43. DOI: 10.1111/j.1747-1567.2003.tb00107.x.

[4] Macián, V., Salvador, F. J., De la Morena, J., and Pagano, V. "Combustion analysis of a stratified pre-chamber ignition system by means of a zero-dimensional turbulence and flame speed model". In: *Combustion and Flame* 232 (2021). DOI: 10.1016/j.combustflame.2021.111526.

[5] Novella, R., Gomez-Soriano, J., Barbery, I., and Libert, C. "Numerical analysis of the passive pre-chamber ignition concept for light duty applications". In: *Applied Thermal Engineering* 213 (2022), p. 118610. DOI: 10.1016/j.applthermaleng.2022.118610.

[6] Silva, Mickael et al. "Computational assessment of effects of throat diameter on combustion and turbulence characteristics in a pre-chamber engine". In: *Applied Thermal Engineering* 212.May (2022), p. 118595. DOI: 10.1016/j.applthermaleng.2022.118595.

[7] Woschni, G. "A Universally Applicable Equation for the Instantaneous Heat Transfer Coefficient in the Internal Combustion Engine". In: (1967). DOI: 10.4271/670931.

[8] Heywoood, John B. *Internal Combustion Engine Fundamentals*. Second ed. New York, N.Y.: McGraw Hill, 2018, p. 1056.

[9] Bardis, Konstantinos, Xu, Guoqing, Kyrtatos, Panagiotis, Wright, Yuri M., and Boulouchos, Konstantinos. "A Zero Dimensional Turbulence and Heat Transfer Phenomenological Model for Pre-Chamber Gas Engines". In: *SAE Technical Papers*. Vol. 2018-April. 2018, pp. 1–28. DOI: 10.4271/2018-01-1453.

[10] Chiodi, Marco and Bargende, Michael. "Improvement of engine heat-transfer calculation in the three-dimensional simulation using a phenomenological heat-transfer model". In: *SAE Technical Papers* 724 (2001). DOI: 10.4271/2001-01-3601.

[11] Gordon, S and McBride, B J. "Computer program for calculation of complex chemical equilibrium compositions rocket performance incident and reflected shocks, and Chapman-Jouguet detonations". In: *NASA Report SP-273, Interim Revision* (1976).

[12] Tinaut, F. V., Reyes, M., Giménez, B., and Pastor, J. V. "Measurements of OH* and CH* chemiluminescence in premixed flames in a constant volume combustion bomb under autoignition conditions". In: *Energy and Fuels* 25 (2011), pp. 119–129. DOI: 10.1021/ef1013456.

[13] Hu, Yue, Tan, Jianguo, Lv, Liang, and Li, Xiangdong. "Investigations on quantitative measurement of heat release rate using chemiluminescence in premixed methane-air flames". In: *Acta Astronautica* 164 (2019), pp. 277–286. DOI: 10.1016/j.actaastro.2019.07.019.

[14] Tu, Po-Wen et al. "Numerical Investigation of GDI Injector Nozzle Geometry on Spray Characteristics". In: *SAE Technical Papers*. Vol. 2015-Septe. September. 2015. DOI: 10.4271/2015-01-1906.

[15] Park, Junkyu, Kim, Donghwan, and Park, Sungwook. "Effects of Nozzle L/D on Near-Field Development and Macroscopic Spray Characteristics of Common-Rail Diesel Sprays". In: *International Journal of Automotive Technology* 21.3 (2020), pp. 657–666. DOI: 10.1007/s12239-020-0063-2.

[16] Ailaboina, Akhil and Saha, Kaushik. "On Modeling of Spray G ECN Using ROI-Based Eulerian-Lagrangian Simulation". In: *Frontiers in Mechanical Engineering* 8.July (2022), pp. 1–22. DOI: 10.3389/fmech.2022.880635.

[17] DeBonis, James and Scott, James. "A large-eddy simulation of a turbulent compressible round jet". In: *7th AIAA/CEAS Aeroacoustics Conference and Exhibit*. Vol. 40. 7. Reston, Virigina: American Institute of Aeronautics and Astronautics, 2001. DOI: 10.2514/6.2001-2254.

[18] Uzun, Ali and Hussaini, M. Yousuff. "Investigation of high frequency noise generation in the near-nozzle region of a jet using large eddy simulation". In: *Theoretical and Computational Fluid Dynamics* 21.4 (2007), pp. 291–321. DOI: 10.1007/s00162-007-0048-z.

[19] Law, Chung K. *Combustion Physics*. Cambridge University Press, 2006. DOI: 10.1017/CBO9780511754517.

[20] Novella, Ricardo et al. "Experimental and Numerical Analysis of Passive Pre-Chamber Ignition with EGR and Air Dilution for Future Generation Passenger Car Engines". In: *SAE Technical Papers*. Vol. 2020-April. April. 2020, pp. 1–18. DOI: 10.4271/2020-01-0238.

[21] Siebers, Dennis L. and Higgins, Brian. "Flame Lift-Off on Direct-Injection Diesel Sprays Under Quiescent Conditions". In: *SAE Technical Papers*. 2001. DOI: 10.4271/2001-01-0530.

Chapter 6

Complementary studies on multi-orifices pre-chambers

6.1 Introduction

This chapter of the PhD. thesis is focused on describing the results obtained with a multi-orifice passive pre-chamber operating in a single-cylinder optical engine [1]. In this study, conducted during a pre-doctoral stay at the Institute of Sciences and Technologies for Sustainable Energy and Mobility (STEMS), the natural flame luminosity optical technique and an in-cylinder-pressure-based analysis are applied to both quantitatively and qualitatively assess the jet ejection and main chamber combustion development.

This study arises from the limited number of experimental studies using optical techniques to assess passive pre-chambers and relies on the effect of the orifice diameter on the jet characteristics and main chamber combustion parameters. Additionally, a conventional spark ignition system (spark plug) is taken as a reference case.

The chapter begins with a description of the optical setup, the pre-chamber geometries, the image processing methodology, and the operating points tested. Then, the pre-chamber ignition system is compared to the conventional spark ignition system to illustrate the main differences in the combustion development. Next, the effect of the orifice diameter, the relative air/fuel ratio (λ), and the spark timing are discussed. After that, the effect of

the spark timing was assessed for the PC geometries tested. Finally, the key conclusions of this study are then outlined.

6.2 Materials and methods

6.2.1 Engine characteristics and optical setup

The experiments were performed in a single-cylinder naturally-aspirated 4-stroke SI optical engine. The cylinder head has a pent-roof-shaped combustion chamber with a central spark plug and four valves. A low-pressure direct injection (DI) system was used to inject the fuel directly into the main chamber. The main characteristics of the engine can be found in Table 6.1.

Table 6.1: Engine specifications.

Property	**Unit**	**Value**
Engine base type	–	4-stroke SI
Bore x Stroke	mm	72 x 60
Swept volume	cm^3	244.3
Compression Ratio SI	–	9.0:1
Compression Ratio PCSI	–	8.6:1
Fuel injection system	–	DI @ 6.5 bar
Start of injection	CAD	315 BTDC
Valve timing @1mm lift	CAD	IVO = 6 BTDC IVC = 50 ABDC EVO = 41 BBDC EVC = 1 ATDC

The bottom optical access to the combustion chamber is obtained by elongation of the regular metallic piston with a hollow cylinder (Bowditch design) and the use of a cylindrical sapphire window with a diameter of 54 mm on the flat top piston. Unlubricated Teflon-bronze composite piston rings seal the combustion chamber while ensuring no window oil contamination. The one-side oblong opening on the extended piston allows the installation of a 45-degree UV-coated mirror to redirect the image orthogonally to the piston axis. A schematic view of the optically accessible engine setup is illustrated on the left-hand side of Figure 6.1.

The flame natural luminosity was recorded by a Photron FASTCAM SA-X2 high-speed camera mounted with a NIKKOR 18-105mm f/3.5-5.6 zoom lens (in this study the focal length and aperture used were 105 mm and f/5.6,

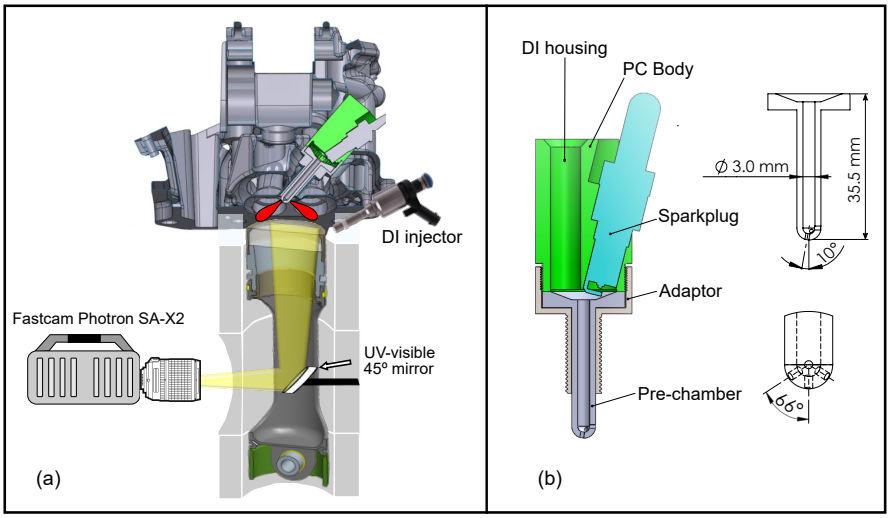

Figure 6.1: Illustrative representation of (a) the optical engine setup and (b) the PC layout.

respectively). The frame rate was set to 10,000 FPS, which is equivalent to 1.2 CAD resolution at 2000 rpm and resulted in an exposure time of 100μs. A region of interest of 512x512 pixels resulted in a spatial resolution of 6.3 pixels per millimeter. Given the characteristic time of the jet penetration, an even higher temporal resolution would be desirable; however the trade-off between shutter speed and frame rate was the limiting factor due to the low luminosity intensity produced by the jet ejection process.

As the results and conclusions made in this study rely on macro phenomena (jet tip penetration and burned area), a higher frame rate to obtain sharper images is desired but not mandatory. It was preferred to set the frame rate as high as possible while maintaining a suitable luminosity and signal-to-noise ratio. Furthermore, as the jet tip is always moving away from its previous position, its ultimate location (at the end of the exposure time) is the main data point. In other words, how the jet tip evolves during the exposure time is unknown, but its final position (at the end of the exposure time) can be correctly determined.

6.2.2 Pre-chamber geometries

As commonly used on experimental facilities to study the pre-chamber ignition concept, the conventional spark plug (12 mm thread diameter) was

replaced by the pre-chamber kit, which is composed by the pre-chamber itself, PC body, adaptor, spark plug (8mm thread diameter) and DI housing (not used in this study). Due to physical constraints, flexibility in use in both active and passive mode was chosen at the expense of installing a pressure sensor in the prechamber. A schematic view of the PC internal geometry and orifice configuration is illustrated on the right-hand side of Figure 6.1.

The design of the configuration used in this study includes an elongated section to avoid further modifications on the cylinder head and to properly set the PC orifices at the center of the combustion chamber. The share of pre-chamber volume located in the elongated section (3 mm duct) is 229.7 mm^3 (42% of the pre-chamber volume). The novelty proposed by the Institute of Sciences and Technologies for Sustainable Energy and Mobility (STEMS) consists of an exchangeable and free rotating (before assembly) pre-chamber, which allows an easy modification of the orifice layout, either by changing the inner part (which comprise the orifices), or simply rotating it to change the orifice orientation in the main chamber. In this way, the possibility of different orifice diameter and orientation combinations is greatly increased, improving the flexibility during the R&D phase. The orifices are straight and oriented with an angle to symmetrically distribute the hot gases into the main chamber, considering the inclination of the conventional spark plug.

In this study, three different pre-chamber geometries were experimentally evaluated. The overall layout (i.e., number of orifices, PC volume, orifice orientation, etc.) was kept the same, while three orifice diameters (1.0, 1.2 and 1.5 mm) were tested. The larger orifice diameter refers to the maximum diameter to maintain the flow throat area at the orifices, also the effective area (i.e. the product of the geometrical area and discharge coefficient) of the PC cross section area is always lower than the effective area of the orifices, therefore the orifices represent the smallest restriction area on all geometries. Although designed to minimize the increase of Top Dead Center (TDC) volume, the PCSI configuration causes a compression ratio reduction from 9.0 to 8.6, leading to a pressure difference at TDC of about 3.5 % (i.e., 1 bar at WOT). Table 6.2 summarizes the pre-chamber characteristics.

Table 6.2: Pre-chamber characteristics.

Property	**Unit**	**PC1**	**PC2**	**PC3**
Number of orifices	-		4	
PC volume	mm^3		549.9	
Orifice diameter	mm	1.0	1.2	1.5
Engine speed (N)	rpm		2000	
$A_n/(V_{pc}\, n)$	$(m/s)^{-1}$	0.171	0.247	0.386
Orifices flow area / PC volume	m^{-1}	5.7	8.2	12.9
Orifices flow area / PC cross-section area	-	0.4	0.6	1.0

6.2.3 Test cell instrumentation

The experiments were conducted in a fully equipped test cell, which enables the appropriate engine control and measurement of the critical parameters of the engine testing. To control engine speed and load, the engine was connected to an active dynamometer. The main chamber was equipped with a GH12D piezoelectric pressure transducer from AVL coupled to a FlexIFEM Piezo charge amplifier from AVL. The pressure signal was crank-angle resolved in every 0.1 crank-angle degrees (CAD) by an angular encoder. The intake pressure was measured with a manifold absolute pressure (MAP) sensor. The fuel and air mass flow rates were determined through a Brooks SLA5861 and a Sensyflow NW 25 thermal mass flowmeters, respectively. The exhaust oxygen concentration was obtained by a wide-band lambda sensor Bosch LSU 4.9 coupled to an ETAS Lambda Meter LA4 conditioner, then the actual air-to-fuel ratio could be calculated. An Engine Timing Unit (ETU) from AVL managed the ignition and injection settings. The sensors indicated above were all linked to a high-speed data acquisition system IndiModul from AVL, which provides the required information to the AVL IndiCom software to display real-time combustion parameters. 200 consecutive cycles were used to calculate averaged combustion parameters by means of a heat release analysis, as well as to evaluate the cycle-to-cycle variability. The temperatures of the intake and exhaust gases were measured by a low-frequency system employing type-K thermocouples. The engine coolant temperature, controlled by an AVL Coolant Conditioning system, was set at 60 ºC to minimize the wear of the Teflon-bronze piston rings.

6.2.4 Image processing

To obtain quantitative jet parameters and characterize the combustion itself, the raw images were processed through an in-house routine, briefly explained as follows. As illustrated in Figure 6.2, starting from the raw images (a), the first step is to locate the optical access and apply a geometrical mask to neglect any information outside of the piston window area (b). Then, some procedures such as gamma adjustment and background subtraction are used to increase the jet/flame contour detectability. Later, the image is divided into 4 sectors (one per orifice) and binarized based on a threshold limit, which is statistically determined with the likelihood ratio test (LRT) method for each sector of each frame [2]. To prevent pixels far from the jet from being wrongly considered part of the jet/flame, the binarized zone only allows interconnected pixels to be considered as part of the jet. Finally, the jet/flame contour is precisely determined at the intersection of the binary regions (c), and a jet contour mask can be applied to obtain an even clearer image (d). This procedure is replicated to each frame separately, then the jet tip penetration and the burning two-dimensional projected area (abbreviated as flame area) profiles are obtained with a resolution of 1.2 CAD.

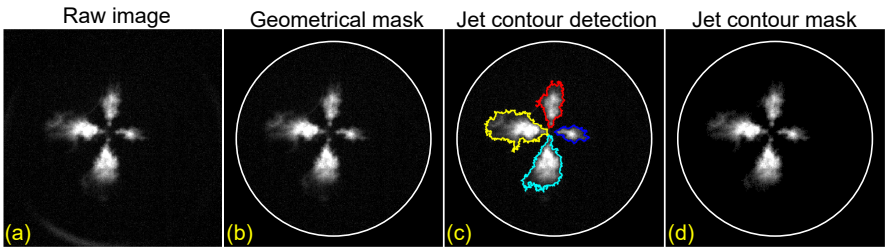

Figure 6.2: Steps during image processing.

The left-hand side of Figure 6.3 shows the jet penetration of each jet all over the 30 cycles in light colors and, the averaged jet penetration in dark colors. It is worth to mention that, since the pre-chamber is slightly offset from the center of the combustion chamber, the free length (axial distance between the orifice exit and the optical limit) is not the same for the four jets. This results in different maximum penetrations for each of the jets. The right-hand side of Figure 6.3 illustrates the main dimensions addressed during the post-processing. The jet tip penetration is the radial distance from the orifice exit to the furthest pixel within the jet/flame region. The jet penetration velocity is obtained by a backward finite difference approximation of each jet penetration, and the averaged jet penetration velocity is then calculated. To quantify the

overall flame development, an equivalent flame diameter is obtained assuming a circle of the same area as the total flame area (i.e. the sum of the four flame areas), allowing to estimate an equivalent radial flame propagation velocity and to compare it with the approximately spherical development of the flame front of the conventional SI case.

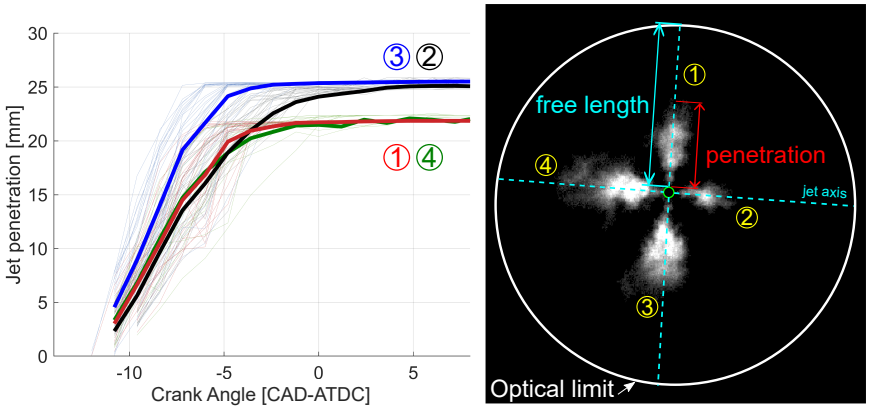

Figure 6.3: Methodology to calculate the jet tip penetration.

The image acquisition of the jet penetration is complex due to its fast movement and its low light emission. In this study using flame natural luminosity, the unavailability of prime lenses leads to the use of longer exposure times (and then a lower frame rate - FPS) to ensure enough luminosity to the camera sensor. As the image of each frame is the "light accumulation" from the opening to the closing of the diaphragm, depending on the jet penetration velocity, the use of a longer exposure time can lead to a smeared image and compromise the determination of geometrical aspects (e.g. jet contour). Therefore, as the jet penetration is susceptible, at some level, to the smear effect, reliable image segmentation and threshold determination are crucial to reduce this phenomenon.

In this sense, the image segmentation between background and jet/flame was based on the likelihood ratio test (LRT) algorithm, which is based on the assumption that each histogram (frequency of pixel intensity) can be considered as an estimation of the brightness probability density function [3]. After dividing the optical area of each frame into 4 sectors of 90º, the optimal threshold of each sector is statistically estimated based on the minimization of the probability of misclassifications between background and jet/flame area. A more detailed description of the theoretical development of the method, as

well as a comparison between other frequently used methods, can be found in previous publications [2, 3].

To ensure that the algorithm used for threshold determination (originally developed and validated for diesel spray imaging) is also valid for pre-chamber ignition imaging, Figure 6.4 shows, at the left-hand side, an example of the effectiveness of jet/flame tracking of the four jets exiting the pre-chamber, and a zoomed region of jet 1 with gamma correction for better visualization. In the right-hand side of Figure 6.4, the gray value (i.e. brightness) along the four axis represented at the left-hand side of Figure 6.4 are plotted. The bullet points represent the last intersection between the axis and the jet/flame contour (i.e. limit between background and jet/flame regions). The gray value at flame/jet border is right above the background noise value (pixels further than approx. 80 from center), which is the ideal case to ensure that there is no underestimation of the jet penetration. It is worth to mention that even if an isolated pixel presents a grey value higher than the threshold limit, only interconnected (and more than 20) pixels can be classified as jet/flame area, mitigating the misclassification of outlier pixels.

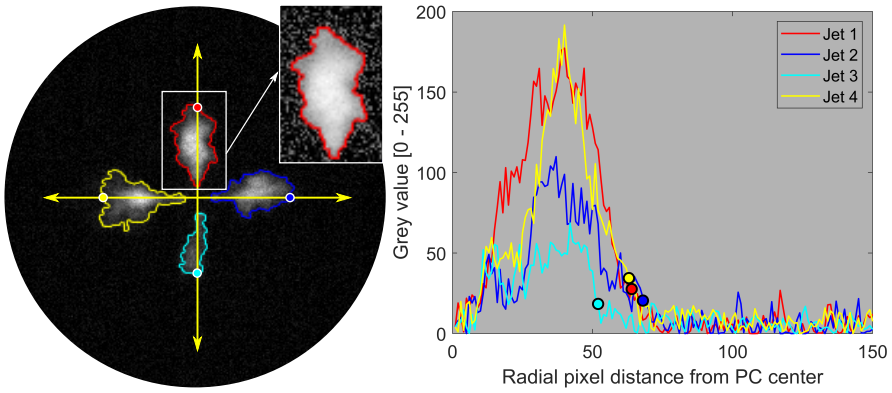

Figure 6.4: Flame contour (left) and the grey value along the jet axis (right).

6.2.5 Fuel injection system

In this study, the methane ($CH_4 \geq 99.95$ %) was used as a natural gas surrogate. There were PFI and DI injection strategies available, but the DI strategy was chosen since it has higher volumetric efficiency compared to the PFI one [4, 5]. Some fuel properties are listed in Table 6.3.

Table 6.3: Fuel characteristics.

Property	**Unit**	**Value**
Formula	-	CH_4
Stoichiometric air-to-fuel ratio	kg/kg	17.23
Molecular weight	kg/mol	16.042
Lower Heating Value	MJ/kg	50.0
Research Octane Number	-	120
Density @ $300K$ and 6.5 bar	kg/m^3	4.2269

The cylinder head was modified to accommodate a Siemens-Synerject Strata low-pressure air-assisted gasoline direct injector modified to use natural gas (without air assistance). The injection pressure was fixed at 6.5 bar (absolute), ensuring sonic nozzle conditions during the injection, because it was always placed early during the compression stroke, just after IVC. The duration of injection (DOI) was adjusted depending on the relative air-to-fuel mixture (lambda), and the start of injection (SOI) was fixed at 315 CAD-BTDC.

6.2.6 Methodology

The different pre-chamber geometries and the baseline conventional spark plug case were tested on the optically accessible SI engine at 2000 rpm under three mixture conditions and different spark timings (varying in intervals of 2 CAD). Given the optical constraints (luminosity and high angular resolution), higher engine speeds have not been tested. To faithfully reproduce the effect of residual gases in the PC combustion, no skip-fire operation was conducted. The engine operating conditions are tabulated in Table 6.4.

After the engine oil and coolant reach steady-state temperature by means of the dedicated conditioning systems, the engine was motored at the testing engine speed for 5 minutes and the steady-state was confirmed again. Still in the pre-testing procedure, the DOI to meet the three lambda conditions were determined (in a maximum of 400 combustion cycles to avoid excessive ring wear). Once the pre-testing procedure was completed, the engine is motored to the testing engine speed, and then 400 consecutive combustion cycles are performed. Given the discontinuity of going from motored to combustion operation, only the last 200 consecutive cycles were used to calculate the averaged combustion parameters. For the imaging data, the last 30 cycles were acquired.

Table 6.4: Matrix for optical engine experiments.

Engine Speed [rpm]	**Orifice diameter** [mm]	**Lambda** [-]	**DOI** [CAD]	**ST** [CAD BTDC]
2000	1.0	0.9	240	[22;18]
		1.0	215	[22;14]
		1.1	200	[22;16]
	1.2	0.9	240	[20;14]
		1.0	215	[22;14]
		1.1	200	[24;16]
	1.5	0.9	240	[20;12]
		1.0	215	[22;14]
		1.1	200	[24;16]
	SI	0.9	240	[20;14]
		1.0	215	[22;14]
		1.1	200	[22;16]

6.3 Results

In this section, the pre-chamber spark-ignition (PCSI) strategy is first compared with the typical SI configuration. Then, the effect of the pre-chamber orifice diameter, air-fuel ratio, and spark timing are further discussed. Some results are shown versus crank angle after ST to emphasize the variable "jet ejection delay" between chambers because the sparking timing varies from case to case and it may be challenging to detect the differences caused by orifice diameter without a common starting point. Some results are shown versus crank angle after ST to emphasize the variable "jet ejection delay" between chambers because the spark timing varies from case to case and it may be challenging to detect the differences caused by orifice diameter without a common starting point.

6.3.1 SI and PCSI ignition method comparison

Before discussing in detail the effect of the pre-chamber orifice diameter, it is worthy to analyze the impact of the PCSI system in the combustion process. Figure 6.5 shows the in-cylinder pressure and the Rate of Heat Released (RoHR) for the SI case and the three PC geometries tested (orifice diameter of 1.0, 1.2 and 1.5 mm), all operating with stoichiometric mixture and maximum brake-torque (MBT) timing (ST=-20 for SI and PCSI 1.0mm; ST=-16 for PCSI 1.2 and 1.5 mm).

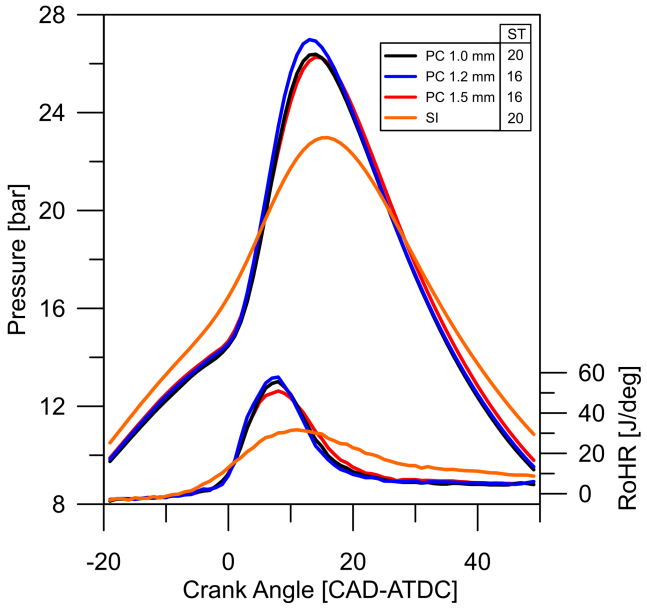

Figure 6.5: In-cylinder pressure and RoHR comparative between SI and PCSI with 1.0, 1.2, and 1.5 mm orifice diameter at $\lambda = 1.0$ and MBT.

It can be observed that the three PCSI cases presented a higher peak of in-cylinder pressure in comparison with the SI case. This behavior is explained by the faster heat released (also depicted at the bottom of Figure 6.5) provided by the pre-chamber ignition system, leading the PCSI case to burn the fuel when the combustion chamber has a smaller volume than the SI case, thus reaching higher in-cylinder peak pressure. The slightly higher pressure during the compression stroke for the SI case is due to the slightly higher compression ratio (absence of the extra volume of the PC) and, to a lesser extent, to the better scavenging process (more fresh mixture trapped).

Figure 6.6 presents the natural luminosity evolution of a conventional SI (top) and a pre-chamber SI (bottom) combustion, both at stoichiometric mixture and spark advance of 20 CAD BTDC. In this comparison, the PCSI concept is represented by the geometry with orifice diameter of 1.5 mm and, for the sake of preserving the same initial piston position, the spark timing is 4 CAD more advanced than the MBT timing. When the first visible jet is detected on the PCSI case (-10.8 CAD), a spherical-shaped flame front can already be seen on the SI case. From that point onwards, the multiple ignition sites generated by the jets lead to a faster combustion propagation for the PCSI case in comparison to the conventional SI case, having more luminous area from -6 CAD and quickly reaching the optical limit.

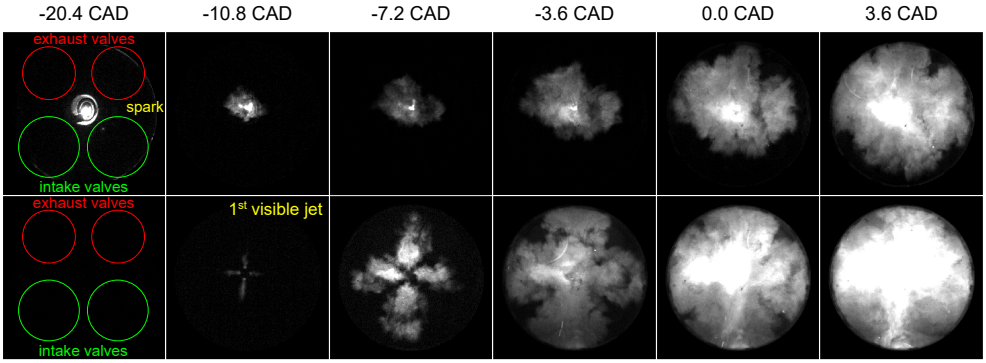

Figure 6.6: Flame development comparison between SI and PCSI (1.5 mm orifice) at $\lambda = 1.0$ and ST=-20 CAD using broadband flame chemiluminescence.

Figure 6.7 depicts the equivalent flame propagation velocity over crank angle position for the PCSI and SI cases at stoichiometric conditions and MBT timing, as well as the advanced PC 1.5 mm case presented in Figure 6.6. Here, the term "equivalent" is used to emphasize that the flame propagation velocity for the PCSI case is obtained considering a spherical combustion evolution, which is an approximation that allows the comparison with the SI case (which is in fact spherical). Although not entirely correct from a physical point of view (i.e. the flame structure is not circular at the early stage of combustion), the peak of equivalent flame propagation velocity of the PCSI case is more than twice the velocity calculated for the SI case, and is located about 2.4 CAD after the first visible jet, i.e. when the main chamber has already been ignited and wrinkled flames are observed on the outer part of the jet.

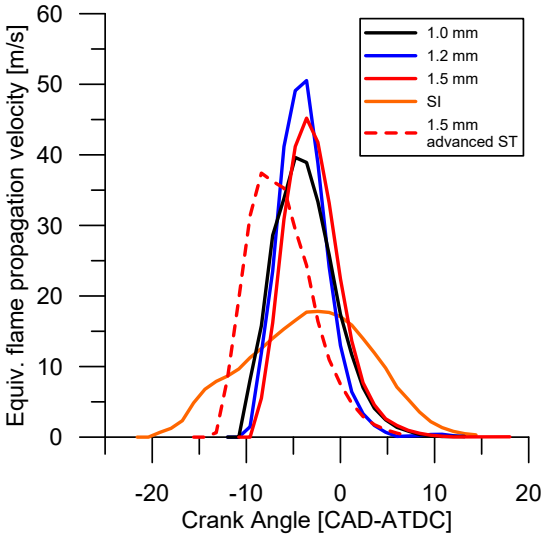

Figure 6.7: Equivalent flame propagation velocity: a comparison between SI and PCSI with different diameter of orifices operating at $\lambda = 1.0$ and MBT, and advanced ST for 1.5 mm case.

6.3.2 Effect of orifice diameter and air-fuel ratio on the PCSI concept

Once the main characteristics of the PCSI combustion in relation to the conventional spark ignition system were presented, the effect of the orifice diameter, relative air-fuel ratio (lambda) and spark timing in the main-chamber combustion development are going to be discussed afterward.

Figure 6.8 shows the combustion evolution by means of the flame natural luminosity for the PCs with orifice diameter of 1.0, 1.2, and 1.5 mm at $\lambda = 1.0$ and ST=-18 CAD. The same ST was chosen to ensure identical thermodynamic conditions for all geometries at ST. For the sake of visibility, the maximum luminous intensity was adjusted over time, but it remained the same for each column.

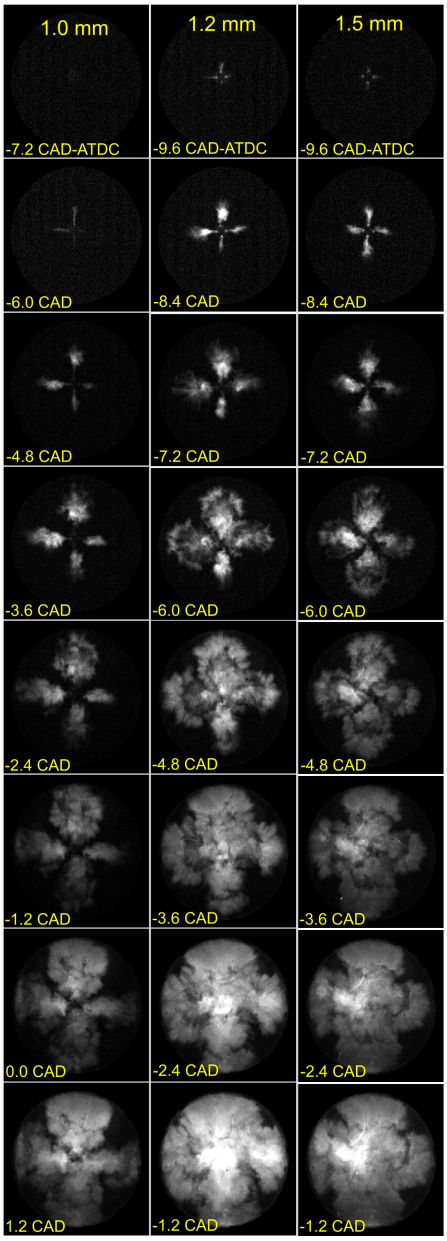

Figure 6.8: Jet penetration and flame development: a comparison between different diameters of orifices of the PCSI operating at $\lambda = 1.0$ and ST=-18 CAD-ATDC using broadband flame chemiluminescence imaging.

Comparing the different orifice diameters, 1.2 and 1.5 mm cases present the first luminous flame practically at the same crank-angle position (around -9.6 and -8.4 CAD), whereas 1.0 mm presented the same jet structure about 3.6 CAD later. Aside from the phasing of 1.0 mm case, the three PC configurations present a very similar jet macrostructure and flame development after jet ejection. It is important to note that the images are a two-dimensional representation of a three-dimensional phenomenon, therefore the jet impingement on the piston must be considered. First, narrow jets coming from the PC penetrate about 25 to 30% of the total visible distance in the main chamber. Then, the main chamber combustion starts and the enflamed area increases on the outer part of these jets towards the periphery of the combustion chamber, driven mainly by the bulk flow. Next, the enflamed area reaches the piston crown and spreads (-6 CAD-ATDC on 1.2 and 1.5 mm cases and -1.2 CAD-ATDC on 1.0 mm case). Finally, the combustion rapidly expands towards the cylinder walls, reaching the optical limit first on the jet tip, while it propagates at a lower velocity in the region between the jets. Moreover, the bulk flow and associated convection induced by the jet clearly influences the main chamber flame propagation, which develops faster on the jet axis centerline in comparison with the radial direction (region between the jets). And, furthermore, there is a superposition of the flame front propagation and the charge motion generated by the jet momentum.

The instant in which the reacting jets are ejected from PC to MC is mainly determined by the combination of two factors: (1) the time for the flame front to sweep all the PC length (i.e. flame propagation velocity) and (2) the rate of gas discharge through nozzles, which will "drag out" the flame front as the gases are exiting the PC. Since the spark timing is the same for the three geometries in Figure 6.8 and the PC with 1.0 mm orifices presents its first luminous jet around 3.6 CAD later, it was observed that the 1.0 mm case presented the slower combination of these two factors in comparison to the 1.2 and 1.5 mm cases, probably caused by the lower mass flow rate due to the smaller orifice diameter. Other factors that may also affect is that the lower flow area hinders the PC filling and scavenging processes, causing a higher concentration of residual gases and affecting the PC combustion.

Several factors, including the following, influence the main chamber combustion: time for the jet to reach the chamber wall, turbulence induced by the jet, orifice flame quenching, the area covered by the jet, etc. The outcome of all these factors (i.e., main chamber combustion) can be numerically assessed by the flame area. Figure 6.9 shows the flame area normalized by the total visible area for the three PC geometries at lambda 0.9, 1.0 and 1.1 at MBT.

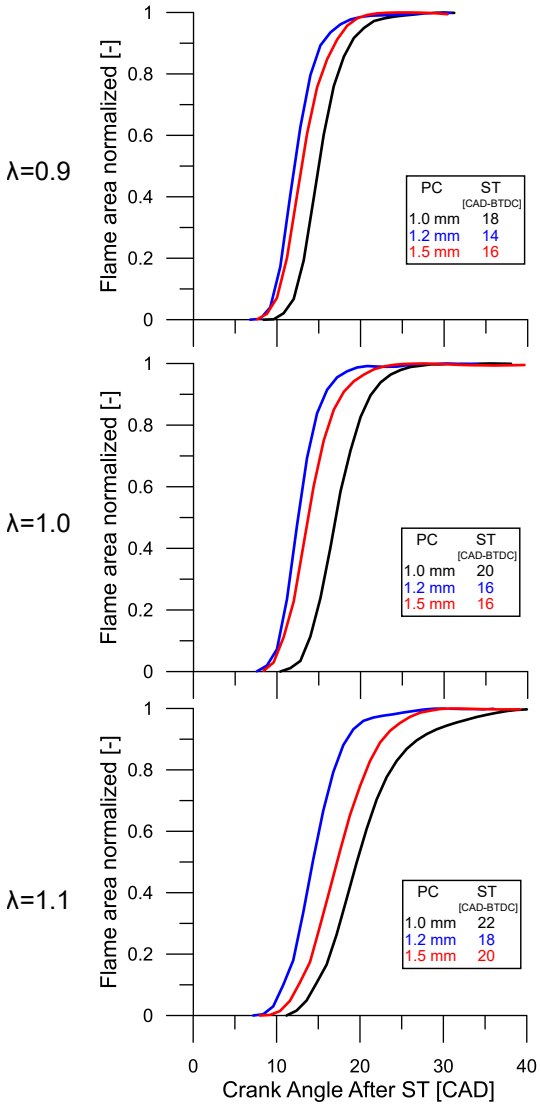

Figure 6.9: Flame area normalized: a comparison between different diameters of orifices of the PCSI operating at λ = 0.9, 1.0 and 1.1 and MBT.

Regardless the air-fuel ratio, the PC with an orifice diameter of 1.2 mm presented the fastest combustion, then 1.5 mm and finally 1.0 mm. Because of its faster combustion, the PC 1.2 mm requires the shortest spark advance to reach MBT condition. Moreover, the combustion process for PC 1.2 mm was less affected by the lean mixture.

The equivalent flame propagation velocity can be calculated from the flame area (assuming a circular flame propagation), and the main chamber combustion evolution for the different orifice diameters can be compared. As depicted in Figure 6.10, the PC with 1.2 mm orifice diameter presented the highest equivalent flame propagation velocity and the shorter interval between ST and maximum flame propagation velocity for the three mixture conditions tested. The PC with orifice diameter of 1.0 mm is clearly delayed in comparison to the 1.2 and 1.5 mm geometries, which can be explained by the mass flow restriction due to the smaller orifice diameter, requiring a higher pressure difference between PC and MC for ejection to occur, thus delaying the jet ejection. Additionally, the smaller flow area tends to reduce the area covered by the jet hot gases just after their ejection. The latter, however, is an assumption that is not supported by the optical data presented in this study because, in the case of flame quenching at the orifice, the natural luminosity is not able to detect unreactive hot gases.

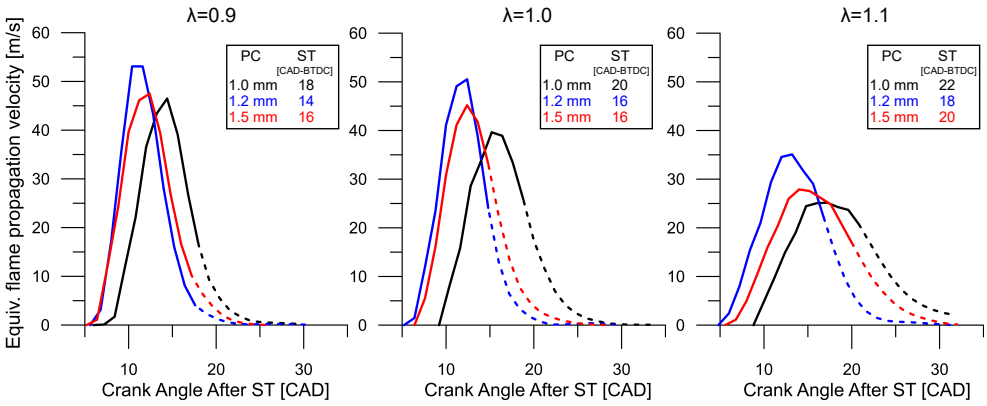

Figure 6.10: Equivalent flame propagation velocity: a comparison between different diameters of orifices of the PCSI operating at λ = 0.9, 1.0 and 1.1 and MBT. The instant in which part of the flame is outside the optical limit is indicated by dashed lines.

The flame tip velocity is represented versus the mean jet penetration in Figure 6.11. Sequential images of the 1.2 mm case are shown in the figure to illustrate the jet structure. As it can be observed, the maximum flame tip velocity does not occur right after the first luminous jet has been detected, but 2 or 3 frames later (when the MC has already been ignited and the flame front is propagating across it), dropping its velocity when approaching the optical limit. It is worth noting that when the flame boundaries start to

locally exceed the optically accessible area (23 mm from the orifice exit), the computed decay in flame velocity is due to the flame area growth outside the piston window and bears limited quantitative significance [6]. On the one hand, the momentum generated by the jet pushes the charge towards the cylinder walls and combined with the conventional turbulent flame front, these two overlapped motion phenomena cause the higher jet/flame velocity. On the other hand, since the natural luminosity technique relies on the luminosity generated by the high-temperature chemical reactions (i.e., combustion), this technique might not detect charge motion that is not burning or that has low light intensity.

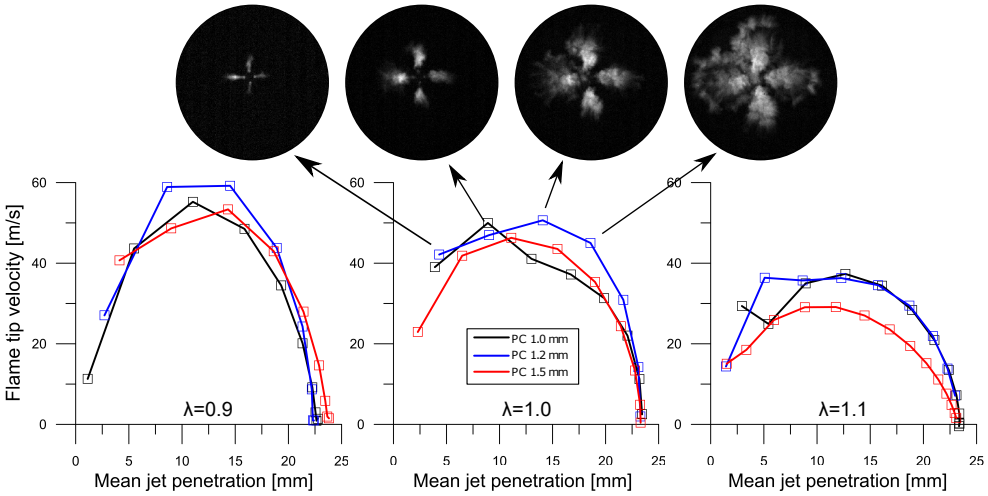

Figure 6.11: Jet tip velocity vs mean jet tip penetration: a comparison between different diameters of orifices of the PCSI operating at λ=0.9, 1.0 and 1.1 and MBT.

Overall, the different PC geometries did not present a significant difference in terms of maximum jet penetration velocity or a clear trend between them as the mixture is varied. However, as the mixture goes from rich to lean condition, the jet penetration velocity is reduced for all geometries tested. This behavior can be explained due to the lower pressure difference between PC and MC (during PC combustion) caused by the smaller amount of fuel in the PC and the slower pre-chamber combustion caused by the leaner mixture. Since the time taken by the initial jet to penetrate and initiate the main-chamber combustion is around 1 or 2 frames, there is a blind spot to precisely determine the time when the penetration starts. Therefore, an even higher

temporal resolution and a high-speed intensifier would help to determine the jet penetration velocity more accurately. Furthermore, an additional optical technique able to detect unreactive gas jets (e.g., high-speed infra-red or schlieren imaging) would be a valuable complement, even if with a significant increase in the complexity of the experimental arrangement.

Figure 6.12 reports the delay between the spark timing and the crank angle position where 10% of the heat is released, known as the flame development angle (ST-CA10), over the lambda for the three geometries at MBT condition. As can be noticed, the PC 1.2 mm presented the shortest flame development angle on all mixture conditions, then 1.5 mm, and lastly 1.0 mm. Overall, a clear upward trend in the flame development angle can be seen as the lambda increases, as expected.

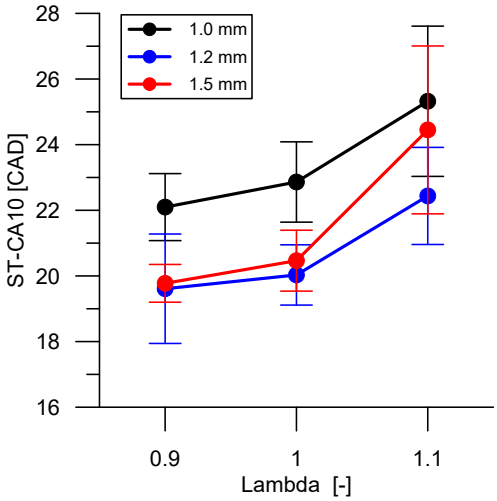

Figure 6.12: Flame development angle: a comparison between different diameters of orifices of the PCSI operating at λ=0.9, 1.0, and 1.1 at MBT condition.

In Figure 6.13, the flame development angle and the combustion duration crank angle intervals are plotted against the orifice diameter for the stoichiometric MBT case. Although the 1.0 mm orifice PC presents the higher flame development angle (delay), it exhibits the lowest overall MC combustion duration. Moreover, the combustion duration increases as the orifice diameter is larger. This behavior can be explained by the theoretical lower jet velocity and, consequently, shorter penetration, induced by the larger orifice diameter. As previously commented, due to the nonexistent or extremely low luminosity emitted by the initial jet, the entire jet may not be observed by using natural

flame luminosity. Moreover, as the outer portion of the combustion chamber is not optically accessible through the piston, the optical assessment reported in this study does not represent the entire combustion process.

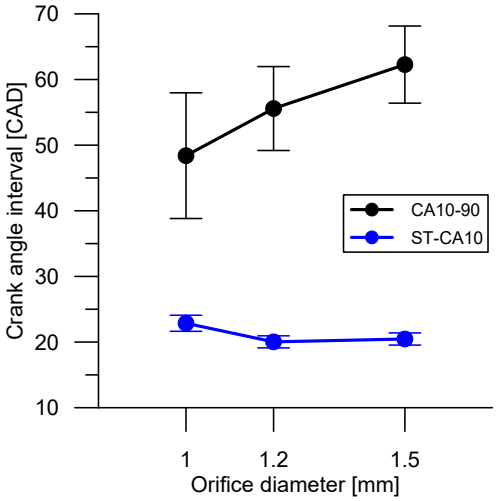

Figure 6.13: Combustion duration and flame development angle for different orifice diameters of the PCSI operating at λ=1.0 and MBT condition.

6.3.3 Spark timing sweep analysis

Figure 6.14 presents the effect of the spark timing (ST) on the in-cylinder pressure and RoHR for PC 1.2 mm at lambda 0.9, 1.0 and 1.1. The blue region highlights the 13 15 CAD and can be used as a guideline of the peak pressure location for the MBT condition. Starting from the most retarded spark timing, the maximum in-cylinder pressure increases and moves towards TDC as the spark timing is advanced. However, at a given moment, the maximum in-cylinder pressure no longer increases, and it starts to decrease if the ST continues to be advanced. It is plausible to assume that the PC filling is an ongoing process during the compression stroke; therefore, the earlier the spark timing, the higher the residual gas fraction and the smaller the amount of fuel available in the PC at this moment, probably worsening the PC combustion and generating less powerful jets towards the MC. As shown in Figure 6.14, this behavior is also noticed for the three levels of lambda tested. The peak of RoHR and the maximum in-cylinder pressure decreases as the air-fuel ratio increases as a result of the smaller amount of fuel and the lower laminar (and turbulent) flame speed.

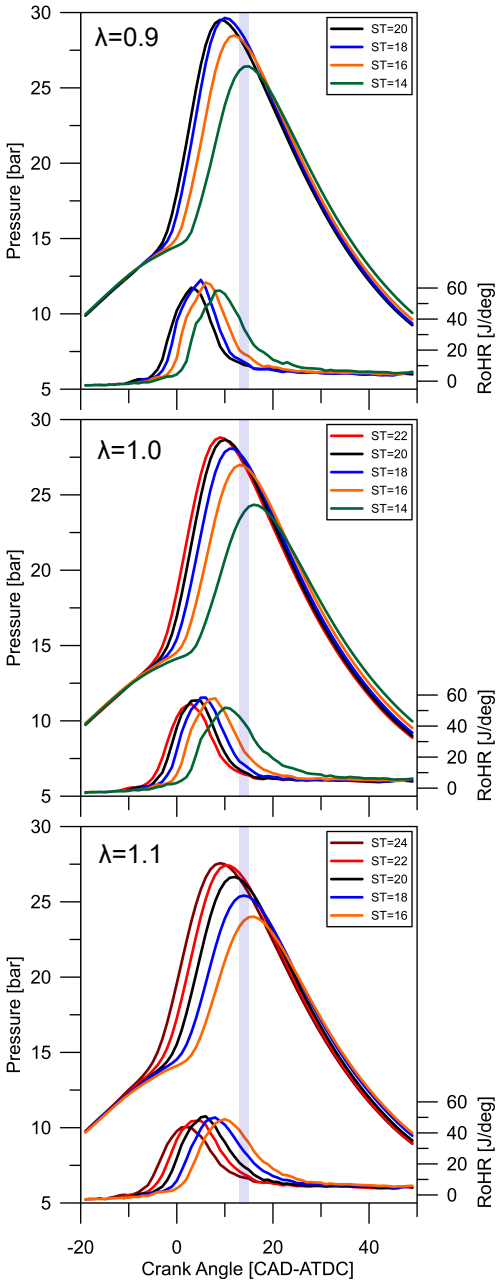

Figure 6.14: In-cylinder pressure and RoHR for different spark timings for the PC 1.2 mm operating at lambda 0.9 (top), 1.0 (center), and 1.1 (bottom). Blue rectangle highlights 13-15 CAD.

Following the same trend of the previously presented PC 1.2 mm, the effect of the spark timing (ST) on the in-cylinder pressure and RoHR for PC 1.0 and 1.5 mm at lambda 0.9, 1.0, and 1.1 is shown in Figure 6.15. From the top to the bottom, the three mixture conditions (lambda 0.9, 1.0, and 1.1) are shown. On the left-hand side, the results referred to PC 1.0 mm are traced, whereas on the right-hand side, those corresponding to PC 1.5 mm are provided. The blue region highlights the 13 to 15 CAD and can be used as a guideline for the peak pressure location for the MBT condition. For both 1.0 and 1.5 mm cases, the maximum in-cylinder pressure increases and is advanced as the spark timing is advanced. This behavior is also noticed for the three mixtures tested: lambda 0.9, 1.0, and 1.1. As the mixture is diluted with air, the peak of RoHR and the maximum in-cylinder pressure decreases as a result of the lower amount of fuel to be burned and the lower flame speed, as already indicated previously for the 1.2 mm case.

The effect of the spark timing on the normalized flame area and the flame development angle is depicted in Figure 6.16. As can be clearly seen, the flame area curve is advanced (shifted away from TDC) as the spark timing is advanced. Each respective flame development angle (ST-CA10) is plotted on the bottom right corner of the figure. For the 1.2 and 1.5 mm cases, the shorter ST-CA10 leads to a MBT condition. However, this trend was not observed for the 1.0 mm case, where the ST-CA10 does not show a clear trend and remains approximately constant for all the STs tested. A shorter ST-CA10 suggests a faster pre-chamber combustion that leads to a faster main chamber combustion. If it occurs at the right time, the optimum MBT condition is achieved.

To conclude with the effect of the spark timing on the different PC configurations and mixtures, Figure 6.17 shows the trend of the combustion center (CA50) as the ST is varied. As expected, the CA50 is retarded as the spark is retarded, except for the lean case with more advanced ST (24 and 22 CAD-BTDC), which due to the worse combustion stability, presents values that differ from the trend. Furthermore, it can be observed that the standard deviation of the CA50 is increased as the air-to-fuel ratio increases (note the change from the left graph to the one on the right). As a baseline, the CA50 for the SI case is also shown in Figure 6.17.

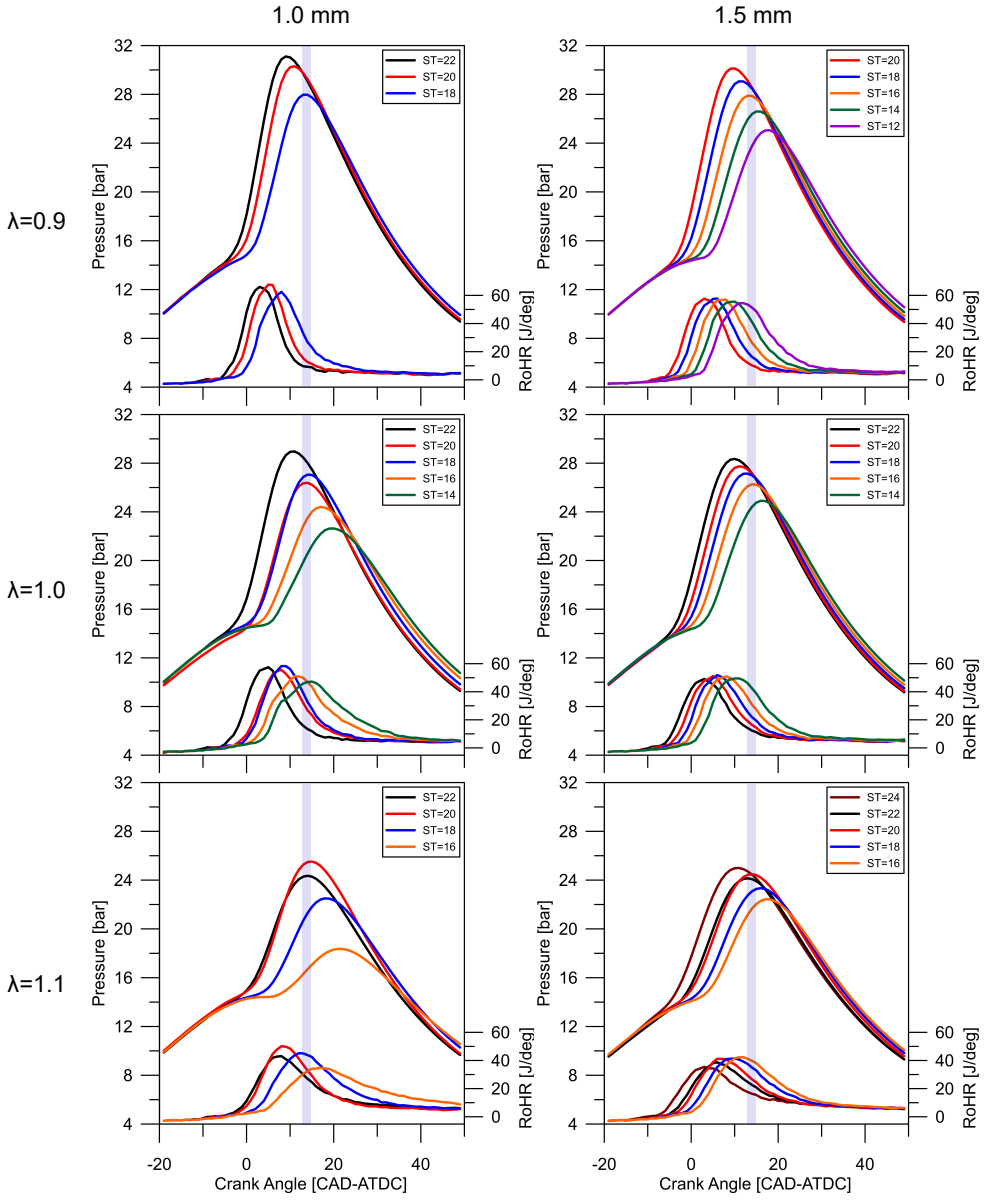

Figure 6.15: In-cylinder pressure and RoHR for different spark timings for the PC 1.5 mm operating at lambda 0.9 (top), 1.0 (center), and 1.1 (bottom). Blue rectangle highlights 13-15 CAD.

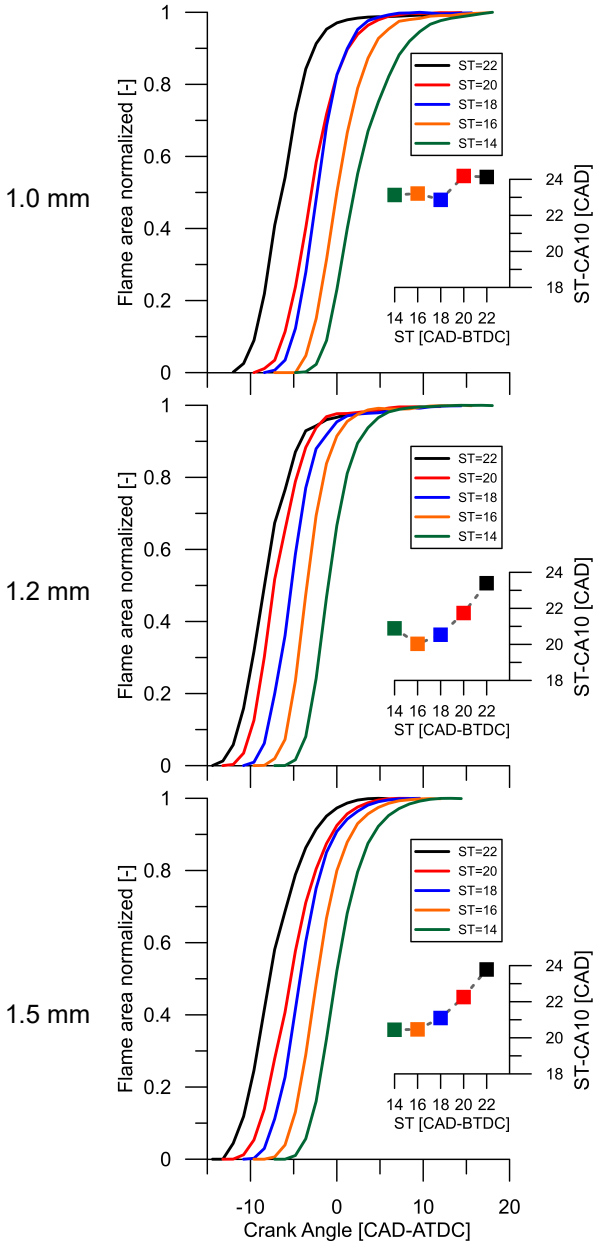

Figure 6.16: Normalized flame area and flame development angle for different spark timings for the PC 1.0, 1.2, and 1.5 mm operating at lambda=1.0.

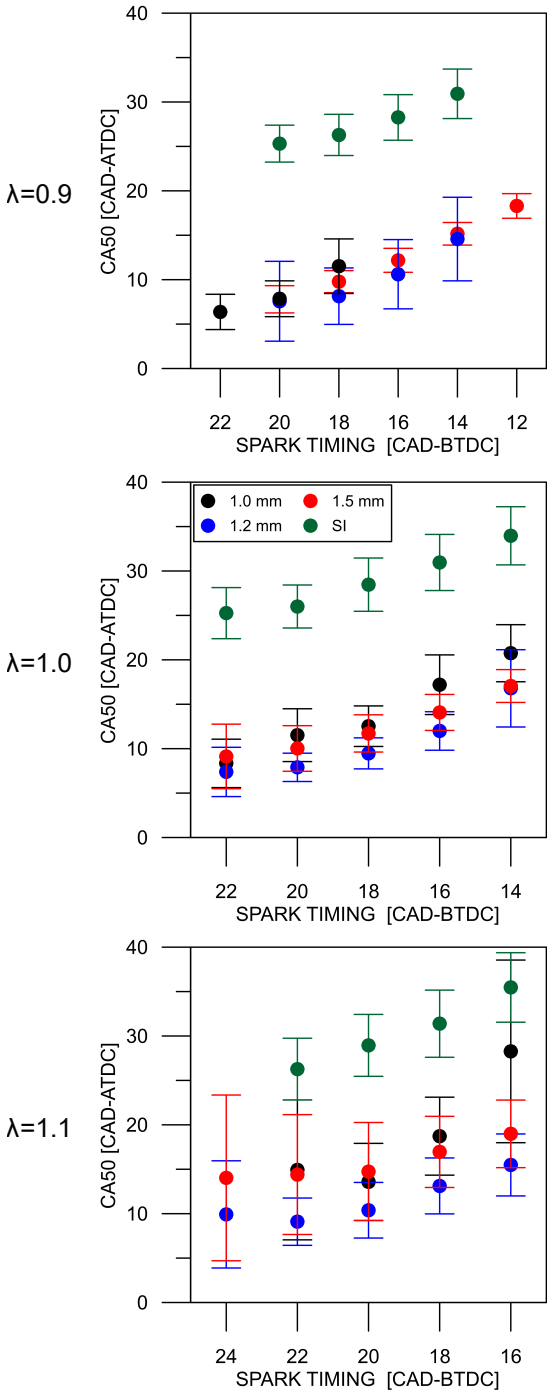

Figure 6.17: Effect of the spark timing and lambda on the CA50 for SI and PCSI with different diameters of orifices operating at lambda 0.9 (top), 1.0 (center), and 1.1 (bottom).

6.4 Summary and conclusions

In this study, an experimental assessment of the effect of the orifice diameter in an unscavenged passive pre-chamber is conducted in an optical engine. The jet characteristics and the main chamber combustion development were assessed by means of high-speed broadband chemiluminescence imaging and in-cylinder-pressure data in engine-like conditions. The results of this chapter allow a deep understanding of the local phenomena taking place in the combustion chamber when a passive pre-chamber is used. Moreover, the optical data can support 3D modeling development and validation.

First, the pre-chamber ignition concept was compared with the conventional spark plug, showing its potential to accelerate the main chamber combustion. Then, the effect of the orifice diameter and the air-to-fuel equivalence ratio (lambda) was thoroughly discussed. Finally, the relationship between the spark timing and some important combustion parameters is analyzed. The following conclusions are drawn from the experiments performed:

- The PC with orifices diameter of 1.0 mm presented the longest time between ST and the beginning of the jet ejection, requiring a more advanced ST than 1.2 and 1.5 mm cases to reach MBT condition for all lambda values;
- The PC with 1.2 mm orifice diameter presented the shortest flame development angle, followed by 1.5 and lastly 1.0 mm. This trend is observed for all lambdas. Additionally, the MBT case presented the shortest flame development angle for the 1.2 and 1.5 mm cases, becoming larger as the spark is advanced or retarded in relation to the MBT. For the 1.0 mm case, no clear trend was observed;
- Despite the longest flame development angle, the PC 1.0 mm presented the shortest main chamber combustion duration (CA10-90), which increases as the orifice diameter is increased thanks to the shorter jet penetration (lower ejection velocity);
- The position of the combustion center for all configurations of the PCSI concept was retarded as the spark advance was decreased, which is a similar trend compared to the typical SI configuration. In addition, the standard deviation increased as the air-fuel ratio increased;
- The jet penetration velocity and the equivalent flame propagation velocity decrease as the air-to-fuel ratio goes from rich to lean condition for all the pre-chamber configurations tested.

References

[1] Antolini, Jácson et al. “Effect of passive pre-chamber orifice diameter on the methane combustion process in an optically accessible SI engine”. In: *Fuel* 341 (2023), p. 126990. DOI: 10.1016/j.fuel.2022.126990.

[2] Macian, V., Payri, R., Garcia, A., and Bardi, M. “Experimental Evaluation of the Best Approach for Diesel Spray Images Segmentation”. In: *Experimental Techniques* 36.6 (2012), pp. 26–34. DOI: 10.1111/j.1747-1567.2011.00730.x.

[3] Pastor, José V., Arrègle, Jean, and Palomares, Alberto. “Diesel spray image segmentation with a likelihood ratio test”. In: *Applied Optics* 40.17 (2001), p. 2876. DOI: 10.1364/ao.40.002876.

[4] Catapano, F., Di Iorio, S., Sementa, P., and Vaglieco, B. M. “Analysis of energy efficiency of methane and hydrogen-methane blends in a PFI/DI SI research engine”. In: *Energy* 117 (2016), pp. 378–387. DOI: 10.1016/j.energy.2016.06.043.

[5] Catapano, Francesco, Iorio, Silvana Di, Sementa, Paolo, and Vaglieco, Bianca Maria. “Optimization of the compressed natural gas direct injection in a small research spark ignition engine”. In: *International Journal of Engine Research* 18.1-2 (2017), pp. 118–130. DOI: 10.1177/1468087417692505.

[6] Tornatore, Cinzia and Sjöberg, Magnus. “Optical Investigation of a Partial Fuel Stratification Strategy to Stabilize Overall Lean Operation of a DISI Engine Fueled with Gasoline and E30”. In: *Energies* 14.2 (2021), p. 396. DOI: 10.3390/en14020396.

Chapter 7

Conclusions and future works

7.1 Introduction

The purpose of this last chapter is to summarize the key findings from the present doctoral thesis, linking the conclusions presented throughout the chapters to the primary and secondary objectives originally suggested. Finally, some topics regarding pre-chamber ignition systems that eventually could not be addressed are suggested as future works.

7.2 Summary and conclusions

As detailed in Chapter 1, the main objective guiding the development of this PhD thesis has been to further understand the pre-chamber ignition concept. To accomplish this, sequential and complementary numerical and experimental studies were conducted in different experimental facilities and/or using different numerical tools.

First, during the literature review, it was identified that there was a lack of experimental studies under engine-like conditions that focused on understanding the jet characteristics and the mechanism behind the ignition of the air-fuel mixture in the main chamber. Furthermore, the design criteria to define the pre-chamber volume, orifice diameter, and other geometrical characteristics in the studies reported may raise the question of whether the results are representative of PC designs applied to internal combustion engines.

In this sense, given the flexibility of instrumentation and modification of the optical accesses, as well as the ability to replicate engine-like conditions, a Rapid Compression-Expansion Machine was chosen for the fundamental studies on single-orifice PC geometries. The use of single-orifice PC geometries lies in better jet visualization and avoiding jet-to-jet and jet-to-wall interaction. However, as most of the PC geometries applied on ICE currently are multi-orifices arrangements, it was proposed, within the scope of this thesis, a methodology to determine the geometrical parameters (i.e., PC volume and orifice diameter) of the "simplified" single-orifice pre-chamber to emulate a multi-orifice reference pre-chamber preserving as much as possible the jet characteristics. Among other conditions, this methodology proposes the conservation of the pressure difference between the PC and MC to preserve the characteristics of the mass flow processes (i.e. PC filling and jet ejection). The methodology was then numerically validated using a one-dimensional model to calculate the thermodynamic conditions on both chambers and the mass flow, and a one-dimensional spray model was employed to estimate a "hypothetical" penetration rate.

Then, once the methodology was numerically validated, the RCEM available at CMT Institute was redesigned to accommodate the single-orifice pre-chambers and provide full optical access to the main chamber. Furthermore, five different PC geometries were experimentally tested to assess the effect of different geometrical parameters (e.g. orifice diameter, PC volume, orifice length, etc.), fuel-air equivalence ratio, and EGR dilution on the jet characteristics and combustion development on both chambers. The analysis was supported by simultaneous high-speed OH* chemiluminescence and schlieren imaging, as well as in-cylinder pressure data for the pre- and main chambers.

Finally, one step further to the engine-like conditions, a multi-orifice PC arrangement installed in a single-cylinder optical engine was used to study the effect of the orifice diameter, the relative air-fuel ratio, and the spark timing on the MC combustion and jet characteristics. High-speed natural flame luminosity and in-cylinder pressure data were available during this study.

The most significant findings derived from this doctoral thesis are summarized in the following sub-sections, each one addressing a specific topic presented and discussed throughout the present document. These findings extended the understanding of the pre-chamber ignition concept and can be applied to the design of pre-chamber geometries for experimental facilities or directly for commercial internal combustion engines.

7.2.1 Reproducing a reference PC under simplified conditions

The first challenge in this PhD. thesis was to identify the key parameters to emulate a multi-orifice reference pre-chamber into a single-orifice pre-chamber configuration. Derived from a theoretical and numerical study, three relations between the geometrical and the engine operating parameters have been identified and presented: $A_e/V_{PC}N$, $d_0/(L^2N)$ and the Damköhler number. The first relation ensures a scaled energy flux in terms of enthalpy and kinetic energy associated with the mass flow between the reference and the simplified PC. In other words, it scales the flow area of the orifices according to the PC volume (and engine speed) to match the same pressure curve trace as the reference case. The second relation allows the preservation of the "relative" jet penetration rate (i.e. according to the distance between the orifice and wall) even at a different engine speed. The third relation is the well-known Damköhler number and it is used to match the chemical characteristics of the jet in terms of flame front quenching at the orifice. Finally, the conclusions derived from this theoretical and numerical study can be summarized as follows:

- The design criteria proposed in this study serve as a guideline to reproduce reference pre-chamber geometries under simplified conditions keeping as much as possible the flow conditions, the thermodynamic parameters, and the jet characteristics.
- The only way to simultaneously reproduce the thermodynamic conditions, the turbulence intensity and the integral scale, the characteristic chemical time, and the Damköhler number of a multi-orifice PC into a single orifice PC is to reproduce a "sector" of the reference multi-orifice PC, that is, the volume and the flow area are divided by the number of orifices. For any other choice, there will always be a compromise between faithfully reproducing the thermodynamic conditions (preserving $A_e/V_{PC}N$) and the relative jet penetration (preserving $d_0/(L^2N)$) or the flame quenching phenomenon (preserving the Damköhler number).
- For torch ignition systems (i.e., where the flame passes through the orifice), the Damköhler number should be at least equal or greater than the reference case, whereas for jet ignition systems (i.e., where the flame quenches at the orifice), the Damköhler number should be at least less or equal than the reference case.
- This methodology proposed can be used to transfer information among different engine sizes. For instance, the knowledge of pre-chambers for

large bore engines can be transferred to pre-chambers of passenger cars and vice versa, serving as a design tool for new pre-chamber geometries, regardless of its application.

7.2.2 Effect of the geometry on the pre-chamber ignition concept characteristics

After the definition of the methodology to reproduce the jet characteristics of a multi-orifice pre-chamber design into a "simplified" single-orifice pre-chamber design, the next step was to test different PC geometries to experimentally validate the effect of geometrical aspects on the PC combustion and jet ejection processes by using in-cylinder pressure-based and imaging analysis. The main findings of this study can be summarized as follows:

- Despite the PC volume, PC length, or orifice diameter, the pressure drop between PC and MC during the PC filling is preserved as long as the $A_e/V_{PC}N$ is preserved. In other words, three-dimensional aspects such as flow orientation, turbulence intensity, and mixture heterogeneity did not affect the pressure trace during the PC filling.

- During the PC combustion, however, variations in geometrical parameters (e.g., distance from the spark plug to the orifice, and PC body diameter) lead to a different PC pressure rise rate even preserving the $A_e/V_{PC}N$ parameter. It was identified that the higher distance from the spark plug to the orifice caused a longer PC combustion duration and, consequently, a lower and late peak of delta pressure and a late reactive (i.e. hot burnt gases) ejection.

- The length-to-diameter orifice ratio (L_o/d_o) was identified as the determinant factor of the jet angle. The higher the length-to-diameter orifice ratio, the lower the jet angle, and the slower the 2D flame area grows as the jet penetrates into the MC.

7.2.3 Effect of the global equivalence ratio on the pre-chamber ignition concept characteristics

The impact of the global equivalence ratio was then investigated with three different PC geometries: PC1, PC2, and PC3. The selection of these PC geometries was based on the combination of the different geometrical parameters that they include, allowing the assessment of the $A_e/V_{PC}N$ parameter, as well

as the orifice diameter and the PC volume. The equivalence ratio was swept from stoichiometric up to 0.75, this being the lean limit for the PC1 geometry.

The primary effect of the air-fuel mixture was in the in-cylinder pressure for both the pre- and main chambers, where the peak pressure decreased as the equivalence ratio decreased for all PC geometries tested. Nevertheless, when comparing the different PC geometries at the same mixture condition, the pressure drop from the PC to the MC during the PC combustion (i.e. jet ejection) increases as the $A_e/V_{PC}N$ decreases.

Regarding the jet ejection, the delay between the ST and the Start of Ejection (SOE) increased as the equivalence ratio decreased as a result of the lower laminar flame speed, which requires the use of earlier spark timings (similar to that observed in typical SI engines). In the leaner case tested, however, the exacerbated delay between ST and SOE impaired the combustion phasing for PC1 and PC2 geometries, and the PC3 was the only geometry that was able to ensure a proper MC combustion phasing for the ϕ=0.75 case. Moreover, the jet penetration rate decreases as the equivalence ratio is reduced as a result of the lower pressure drop between chambers during the jet ejection.

In terms of jet characteristics, the decrease of the equivalence ratio implied a reduction in the OH radical intensity for all pre-chambers tested. Moreover, the simultaneous schlieren and OH* chemiluminescence imaging coupled with the in-cylinder pressure data indicated that the flame front is more likely to quench when passing through the orifice as the equivalence ratio is decreased, mainly due to the thicker flame front thickness caused by the lean mixture. The laminar flame thickness has more than doubled from the stoichiometric to the leanest (ϕ=0.75) case for all PC pressure and temperature conditions. In order to quantify the flame quenching phenomenon, a dimensionless parameter, called the Péclet (Pe) number, relating the orifice diameter (d_o) to the laminar flame thickness (δ_L) was proposed to establish a threshold valid for the different PC geometries. The flame-quenching threshold falls in the range of 84 to 93 d_o/δ_L for the PC1, PC2 and PC3 geometries operating at different equivalence ratios. It is worth noting that the Da number was first used to analyze this flame quenching phenomenon, but to compute the Da number some other spatially dependent parameters must be estimated based on the in-cylinder pressure and mixture conditions, which is not the case in the Pe number. Therefore, as the Pe number depends less on variables calculated from experimental data and is less spatially dependent than Da number, this is the reason why flame quenching correlates better with the Pe number in the study performed.

The change in the jet characteristics also affected the MC ignition location and pattern. In addition to the reduction of the amount of radicals and intermediate species, the decrease of the PC peak pressure and the pressure drop to MC as the equivalence ratio decreases lead to a lower velocity and temperature of the gases being ejected to the MC. The higher jet penetration and the higher radical content of the stoichiometric cases led to a fast MC ignition across the entire surface of the jet (which covered the full length of the MC centerline), favoring the MC combustion to propagate from the jet centerline to the chamber walls, and from the jet tip (due to its larger area) to the orifice exit. As the equivalence ratio is decreased, the lower jet penetration associated with the low radical content and low temperature of the gases shifts the MC combustion propagation from the region close to the orifice exit to the region opposite to the orifice exit. The lower $A_e/V_{PC}N$ for the PC3 leads to a higher jet penetration even in the leanest case, enlarging the ignition area and favoring the MC combustion.

7.2.4 Effect of the EGR rate on the pre-chamber ignition concept characteristics

The impact of the EGR rate was then assessed with the PC1 and PC3 pre-chamber geometries, as a way of evaluating the EGR rate with different levels of the geometrical parameter $A_e/V_{PC}N$. The EGR rates tested were 0, 10, 20, and 25%, and the EGR-limit for combustion was 20% both for PC1 and PC3 (i.e., for the 25% EGR case, all repetitions resulted in misfire, whatever the spark timing).

Similar to that observed with the decreasing of the equivalence ratio, the EGR addition slowed down the PC combustion, decreasing the PC peak pressure during the jet ejection, as well as reducing the radical content and the temperature of the gases being ejected. The lower PC pressure rise rate led to a higher delay between the ST and the start of the jet ejection (SOE; somehow the "spark timing" of the main chamber), which required the advance of the ST as the EGR rate was increased. For the 20% EGR case, the excessive delay between ST and SOE impaired the combustion phasing for both PC geometries.

When comparing both pre-chambers, the one with the lowest $A_e/V_{PC}N$ parameter (PC3) presented a higher and early peak of PC heat release rate and greater delay between ST and SOE for all the EGR conditions tested. This result is due to the greater restriction imposed by the smaller orifice diameter for the ejection of the hot combustion gases of two PC with the same volume,

so reducing the energy lost in the form of enthalpy and increasing the PC pressure.

As pointed out by the flame properties calculations, the EGR dilution presented a great impact on the laminar flame thickness and the laminar flame velocity, by doubling the thickness and reducing about 40% of the laminar flame velocity from the 0 to 10% of EGR. As evidenced by the in-cylinder pressure measurements and the simultaneous schlieren and OH* chemiluminescence imaging, the flame characteristics worsening caused the PC flame front to quench at the orifice for the 10 and 20% EGR cases for both PC1 and PC3. The dimensionless parameter proposed to establish a threshold for the orifice flame quenching indicated that in all cases in which the flame quenching was observed the d_o/δ_L parameter is below 66, which is close to the threshold already established in the previous section for the equivalence ratio variations.

7.2.5 Effect of orifice diameter and air-fuel ratio on multi-orifice PC geometries

Complementing the studies using single-orifice PC geometries at the Rapid Compression-Expansion Machine, three different multi-orifice passive PC geometries were tested in an optical engine to assess the effect of the orifice diameter, the air-fuel ratio, and the spark timing. Not as flexible as an RCEM, the optical engine has the benefit of reproducing engine-like thermodynamic conditions while allowing the application of optical techniques combined with in-cylinder pressure measurements, therefore being one of the intermediate steps between simplified experimental facilities (e.g., RCEM) and the final application in a multi-cylinder metallic engine.

The three PC geometries tested have the same inner volume and geometry, differing only in the diameter of the four orifices: 1.0, 1.2, and 1.5 mm. In addition to the orifice diameter, the parametric study varied the relative air-fuel ratio from 0.9 to 1.1, and a spark sweep assessment was carried out for each PC configuration. After the analysis of the natural flame luminosity images along with a heat-released analysis, the most relevant contributions and findings are:

- The low natural flame luminosity emitted by the jet and the fast penetration into the main chamber are two important characteristics to be taken into account during optical studies of pre-chamber ignition systems. Therefore, the use of lenses with wide apertures is recommended to ensure a proper compromise between the small relative frame-to-frame

jet movement (obtained with a high FPS rate) and the high luminosity captured by the camera during the exposure time (obtained with a low FPS rate).

- The PC with 1.0 mm diameter orifices presented the longest delay between the ST and the beginning of the visible jet ejection for all conditions tested, thus requiring a more advanced ST to reach MBT when compared to the PC with 1.2 and 1.5mm diameter orifices. This result is in line with what was observed in the single-orifice PCs tested in the RCEM, and can be explained by the more restrictive flow area (i.e. smaller $A_e/V_{PC}N$), which slowed down the bulk flow exiting the PC and retarded the flame front appearance on the orifice.

- Regarding the delay between the ST and the 10% of mass fraction burnt in the main chamber, the PC with 1.2 mm diameter orifices presented the shortest delay for all air-fuel mixtures tested, followed by the PCs with 1.5 and 1.0 mm diameter orifices, respectively. The MBT case presented the shortest delay for the PCs with 1.2 and 1.5 mm diameter orifices, becoming longer as the ST was moved away from the MBT (either advancing or retarding).

- The main chamber combustion duration increased as the orifice diameter was increased. Since the entire combustion chamber is not optically accessible and the optical technique applied is limited, it is assumed that the hypothetical (because it was not measured) higher PC pressure (inferred assuming a lower $A_e/V_{PC}N$ parameter) for the smallest orifice diameter leads to an improved jet penetration throughout the combustion chamber.

- The spark timing sweep analysis pointed out that the center of combustion (crank angle position where 50% of the fuel is burnt) followed the same trend as the typical SI engine: retarded as the spark advance was decreased.

- Regarding the relative air-fuel ratio effect, it slowed down the jet penetration velocity and the equivalent flame propagation velocity as the relative air-fuel ratio was increased.

7.3 Future works

As an emerging topic, much attention has been paid to the pre-chamber ignition concept in the last few years and several complementary studies have

been done since the beginning of the present PhD. thesis. However, there are still relevant topics about the pre-chamber ignition concept to be further explored, whether in fundamental research or practical problems on implementing this technology in passenger car engines or optimizing its use in large-bore engines. To continue exploring this important topic, the following proposals might be relevant for future studies:

- Extend the assessment of the jet characteristics in the proposed RCEM setup for different experimental conditions, including different geometrical aspects (inner PC geometry, PC volume, orifice diameter, and orifice shape) and boundary conditions (initial temperature, initial pressure, compression ratio, and fuels).
- To further investigate the three-dimensional aspects taking place in the PC such as the flow field, the turbulence intensity, and the air-fuel mixture distribution, aiming to identify the key parameters to extend the PC range operation in engines for passenger cars.
- To deepen the knowledge regarding the flame quenching at the orifice, by extending the experimental matrix for this phenomenon at different thermodynamic conditions, equivalence ratio, EGR rate, orifice diameter, and fuels. Moreover, CFD studies can contribute with detailed information about the flow properties, allowing the estimation of local flame quenching parameters (e.g. Damköhler number).
- To investigate the jet-to-jet and the jet-to-wall interactions under engine-like conditions may contribute to the understanding of the main chamber ignition in commercial engine applications.
- As the passive pre-chamber architecture shares the same ignition issues as typical SI engines under lean or EGR-diluted operations, the use of combustion improvers (small quantities of hydrogen, for instance) in the PC can improve the early flame development and ensure a more stable PC combustion at diluted cases.
- The application of laser-based optical techniques can significantly contribute to the understanding of the jet mixing with the main chamber fresh charge, and the jet interaction with piston and chamber walls. Planar laser-induced fluorescence (PLIF) optical technique, for instance, can give insights about the flame front contour and the visualization of the turbulence structures.

Global Bibliography

Adams, T. G. "Theory and Evaluation of Auxiliary Combustion (Torch) Chambers". In: *SAE Prepr.* 780631. 1978, pp. 2328–2339. DOI: 10.4271/780631 (cited on page 101).

Adams, Tim G. "Torch ignition for combustion control of lean mixtures". In: *SAE Technical Papers* (1979). DOI: 10.4271/790440 (cited on pages 19–21, 26).

Ailaboina, Akhil and Saha, Kaushik. "On Modeling of Spray G ECN Using ROI-Based Eulerian-Lagrangian Simulation". In: *Frontiers in Mechanical Engineering* 8.July (2022), pp. 1–22. DOI: 10.3389/fmech.2022.880635 (cited on page 137).

Albert, James S. et al. "Human impacts outpace natural processes in the Amazon". In: *Science* 379.6630 (2023). DOI: 10.1126/science.abo5003 (cited on page 2).

Almatrafi, Fahad, Hlaing, Ponnya, Echeverri Marquez, Manuel, Ben Houidi, Moez, and Johansson, Bengt. "Narrow-Throat Pre-Chamber Combustion with Ethanol, a Comparison with Methane". In: *SAE Technical Paper Series* (2020). DOI: 10.4271/2020-01-2041 (cited on pages 25, 26).

Alvarez, Carlos Eduardo Castilla, Couto, Giselle Elias, Roso, Vinícius Rückert, Thiriet, Arthur Braga, and Valle, Ramon Molina. "A review of prechamber ignition systems as lean combustion technology for SI engines". In: *Applied Thermal Engineering* 128 (2018), pp. 107–120. DOI: 10.1016/j.applthermaleng.2017.08.118 (cited on page 7).

Antolini, Jácson et al. “Effect of passive pre-chamber orifice diameter on the methane combustion process in an optically accessible SI engine”. In: *Fuel* 341 (2023), p. 126990. DOI: 10.1016/j.fuel.2022.126990 (cited on pages 40, 41, 185).

Atis, Cyrus Ashok Arupratan, Ayele, Yidnekachew, Stuecken, Thomas, and Schock, Harold. “Effect of pre-chamber scavenging strategy on EGR tolerance and thermal efficiency of pre-chamber turbulent jet ignition systems”. In: *International Journal of Engine Research* (2022), p. 146808742211051. DOI: 10.1177/14680874221105162 (cited on page 19).

Attard, William P. and Blaxill, Hugh. “A single fuel pre-chamber jet ignition powertrain achieving high load, high efficiency and near zero NOx emissions”. In: *SAE International Journal of Engines* 5.3 (2012), pp. 734–746. DOI: 10.4271/2011-01-2023 (cited on page 19).

Attard, William P., Fraser, Neil, Parsons, Patrick, and Toulson, Elisa. “A Turbulent Jet Ignition pre-chamber combustion system for large fuel economy improvements in a modern vehicle powertrain”. In: *SAE Technical Papers* 3.2 (2010), pp. 20–37. DOI: 10.4271/2010-01-1457 (cited on pages 24–26).

Attard, William P., Kohn, Jacob, and Parsons, Patrick. “Ignition energy development for a spark initiated combustion system capable of high load, high efficiency and near zero NOx emissions”. In: *SAE Technical Papers* 3.2 (2010), pp. 481–496. DOI: 10.4271/2010-32-0088 (cited on pages 24–26).

Attard, William P. and Parsons, Patrick. “A normally aspirated spark initiated combustion system capable of high load, high efficiency and near Zero NOx emissions in a modern vehicle powertrain”. In: *SAE International Journal of Engines* 3.2 (2010), pp. 269–287. DOI: 10.4271/2010-01-2196 (cited on pages 24–26).

Attard, William P. et al. “Spark Ignition and Pre-Chamber Turbulent Jet Ignition Combustion Visualization”. In: *SAE Technical Papers*. 2012. DOI: 10.4271/2012-01-0823 (cited on page 40).

Bardis, Konstantinos, Xu, Guoqing, Kyrtatos, Panagiotis, Wright, Yuri M., and Boulouchos, Konstantinos. “A Zero Dimensional Turbulence and Heat Transfer Phenomenological Model for Pre-Chamber Gas Engines”. In: *SAE Technical Papers*. Vol. 2018-April. 2018, pp. 1–28. DOI: 10.4271/2018-01-1453 (cited on page 118).

Benajes, J., Pastor, J. V., García, A., and Monsalve-Serrano, J. "Redesign and Characterization of a Single-Cylinder Optical Research Engine to Allow Full Optical Access and Fast Cleaning during Combustion Studies". In: *Experimental Techniques* 42.1 (2018), pp. 55–68. DOI: 10.1007/s40799-017-0219-9 (cited on page 39).

Benajes, J. et al. "Evaluation of the passive pre-chamber ignition concept for future high compression ratio turbocharged spark-ignition engines". In: *Applied Energy* 248 (2019), pp. 576–588. DOI: 10.1016/j.apenergy.2019.04.131 (cited on pages 6, 92, 108, 111).

Bieker Georg. *A global comparison of the life-cycle greenhouse gas emissions of combustion engine and electric passenger cars - International Council on Clean Transportation*. 2021 (cited on page 5).

Biswas, Sayan. *Physics of Turbulent Jet Ignition*. Springer Theses. Springer International Publishing, 2018. DOI: 10.1007/978-3-319-76243-2 (cited on pages 19, 29).

Biswas, Sayan and Qiao, Li. "Prechamber Hot Jet Ignition of Ultra-Lean H2/Air Mixtures: Effect of Supersonic Jets and Combustion Instability". In: *SAE International Journal of Engines* 9.3 (2016), pp. 1584–1592. DOI: 10.4271/2016-01-0795 (cited on page 30).

Biswas, Sayan and Qiao, Li. "A Numerical Investigation of Ignition of Ultra-Lean Premixed H2/Air Mixtures by Pre-Chamber Supersonic Hot Jet". In: *SAE International Journal of Engines* 10.5 (2017). DOI: 10.4271/2017-01-9284 (cited on page 31).

Biswas, Sayan and Qiao, Li. "Ignition of ultra-lean premixed hydrogen/air by an impinging hot jet". In: *Applied Energy* 228.March (2018), pp. 954–964. DOI: 10.1016/j.apenergy.2018.06.102 (cited on page 31).

Biswas, Sayan, Tanvir, Saad, Wang, Haifeng, and Qiao, Li. "On ignition mechanisms of premixed CH 4 /air and H 2 /air using a hot turbulent jet generated by pre-chamber combustion". In: *Applied Thermal Engineering* 106 (2016), pp. 925–937. DOI: 10.1016/j.applthermaleng.2016.06.070 (cited on pages 29, 30, 37, 82, 101).

Biswas, Sayan, Zhang, Pei, Wang, Haifeng, and Qiao, Li. "Propagation and extinction behavior of methane/air premixed flames through straight and converging-diverging microchannels". In: *Applied Thermal Engineering* 148.July 2018 (2019), pp. 1395–1406. DOI: 10.1016/j.applthermaleng.2018.07.049 (cited on page 31).

Blöschl, Günter et al. “Changing climate shifts timing of European floods”. In: *Science* 357.6351 (2017), pp. 588–590. DOI: 10.1126/science.aan2506 (cited on page 2).

Bolla, Michele et al. “Numerical Simulations of Pre-Chamber Combustion in an Optically Accessible RCEM”. In: *SAE Technical Paper Series* (2019). DOI: 10.4271/2019-01-0224 (cited on pages 34, 38).

Bolla, Michele et al. “Numerical study of turbulence and fuel-air mixing within a scavenged pre-chamber using RANS and LES”. In: *SAE Technical Papers* 2019-April.April (2019), pp. 1–11. DOI: 10.4271/2019-01-0198 (cited on pages 34, 38).

Boretti, Alberto. “Plug-in hybrid electric vehicles are better than battery electric vehicles to reduce CO 2 emissions until 2030”. In: *International Journal of Energy Research* 46.14 (2022), pp. 20136–20145. DOI: 10.1002/er.8313 (cited on page 5).

Brandstetter, Walter. “The Volkswagen lean burn PC-engine concept”. In: *SAE Technical Papers* (1980). DOI: 10.4271/800456 (cited on pages 19–21, 26).

Bueschke, Wojciech, Szwajca, Filip, and Wislocki, Krzysztof. “Experimental Study on Ignitability of Lean CNG/Air Mixture in the Multi-Stage Cascade Engine Combustion System”. In: *SAE Technical Papers* 2020 (2020), pp. 1–13. DOI: 10.4271/2020-01-2084 (cited on pages 34, 37).

Bunce, Michael and Blaxill, Hugh. “Sub-200 g/kWh BSFC on a Light Duty Gasoline Engine”. In: *SAE Technical Papers*. Vol. 2016-April. April. 2016. DOI: 10.4271/2016-01-0709 (cited on page 6).

Bunce, Michael et al. “Pre-chamber Combustors: An Enabling Technology for High Efficiency, Low CO2 Engine Operation”. In: *Energy, Environment, and Sustainability*. Springer Singapore, 2022, pp. 133–173. DOI: 10.1007/978-981-16-8717-4_7 (cited on page 7).

Bureshaid, Khalifa, Shimura, Ray, Feng, Dengquan, Zhao, Hua, and Bunce, Mike. “Experimental Studies of the Effect of Ethanol Auxiliary Fueled Turbulent Jet Ignition in an Optical Engine”. In: *SAE International Journal of Engines* 12 (2019). DOI: 10.4271/03-12-04-0026 (cited on page 40).

Calvin, Katherine et al. *IPCC, 2023: Climate Change 2023: Synthesis Report. Contribution of Working Groups I, II and III to the Sixth Assessment Report of the Intergovernmental Panel on Climate Change [Core Writing Team, H. Lee and J. Romero (eds.)]. IPCC, Geneva, Switzerland.* Tech. rep. Intergovernmental Panel on Climate Change, 2023, pp. 1–163. DOI: 10.59327/IPCC/AR6-9789291691647 (cited on pages 2, 3).

Catapano, F., Di Iorio, S., Sementa, P., and Vaglieco, B. M. "Analysis of energy efficiency of methane and hydrogen-methane blends in a PFI/DI SI research engine". In: *Energy* 117 (2016), pp. 378–387. DOI: 10.1016/j.energy.2016.06.043 (cited on page 192).

Catapano, Francesco, Iorio, Silvana Di, Sementa, Paolo, and Vaglieco, Bianca Maria. "Optimization of the compressed natural gas direct injection in a small research spark ignition engine". In: *International Journal of Engine Research* 18.1-2 (2017), pp. 118–130. DOI: 10.1177/1468087417692505 (cited on page 192).

Chinnathambi, Prasanna, Thelen, Bryce, Cook, Dave, and Toulson, Elisa. "Performance metrics for fueled and unfueled turbulent jet igniters in a rapid compression machine". In: *Applied Thermal Engineering* 182.August 2020 (2021), p. 115893. DOI: 10.1016/j.applthermaleng.2020.115893 (cited on pages 34, 36).

Chinnathambi, Prasanna, Thelen, Bryce, Naylor, Michael, Cook, Dave, and Toulson, Elisa. "Performance Assessment of a Single Jet, Dual Diverging Jets, and Dual Converging Jets in an Auxiliary Fueled Turbulent Jet Ignition System". In: *SAE Technical Papers* 2018-April.x (2018), pp. 1–13. DOI: 10.4271/2018-01-1135 (cited on pages 34, 36).

Chiodi, Marco and Bargende, Michael. "Improvement of engine heat-transfer calculation in the three-dimensional simulation using a phenomenological heat-transfer model". In: *SAE Technical Papers* 724 (2001). DOI: 10.4271/2001-01-3601 (cited on page 118).

Convergent Science. *CONVERGE 2.4 Manual*. 2020 (cited on page 75).

Costa, Roberto Berlini Rodrigues da et al. "Development of a homogeneous charge pre-chamber torch ignition system for an SI engine fuelled with hydrous ethanol". In: *Applied Thermal Engineering* 152 (2019), pp. 261–274. DOI: 10.1016/j.applthermaleng.2019.02.090 (cited on pages 41, 45).

Council Directive of the European Communities. *Directive 91/441: amending Directive 70/220/EEC on the approximation of the laws of the Member States relating to measures to be taken against air pollution by emissions from motor vehicles*. 1991 (cited on page 16).

Cruz, Igor William Santos Leal, Alvarez, Carlos Eduardo Castilla, Teixeira, Alysson Fernandes, and Valle, Ramon Molina. "Zero-dimensional mathematical model of the torch ignited engine". In: *Applied Thermal Engineering* 103 (2016), pp. 1237–1250. DOI: 10.1016/j.applthermaleng.2016.05.017 (cited on page 45).

Date, Tasuku, Yagi, Shizuo, Ishizuya, Akira, and Fujii, Isao. "Research and development of the Honda CVCC engine". In: *SAE Technical Papers* (1974). DOI: 10.4271/740605 (cited on pages 20, 22, 26).

Davis, G. C., Krieger, R. B., and Tabaczynski, R. J. "Analysis of the flow and combustion processes of a three-valve stratified charge engine with a small prechamber". In: *SAE Technical Papers* (1974), pp. 3534–3550. DOI: 10.4271/741170 (cited on pages 20, 22, 26).

DeBonis, James and Scott, James. "A large-eddy simulation of a turbulent compressible round jet". In: *7th AIAA/CEAS Aeroacoustics Conference and Exhibit*. Vol. 40. 7. Reston, Virigina: American Institute of Aeronautics and Astronautics, 2001. DOI: 10.2514/6.2001-2254 (cited on page 150).

Desantes, J. M., Payri, R., Salvador, F. J., and Gil, A. "Development and validation of a theoretical model for diesel spray penetration". In: *Fuel* 85.7-8 (2006), pp. 910–917. DOI: 10.1016/j.fuel.2005.10.023 (cited on page 75).

Desantes, J.M., Pastor, J.V., García-Oliver, J.M., and Pastor, J.M. "A 1D model for the description of mixing-controlled reacting diesel sprays". In: *Combustion and Flame* 156.1 (2009), pp. 234–249. DOI: 10.1016/j.combustflame.2008.10.008 (cited on pages 74, 75, 84).

Desantes, José M, López, J Javier, Gil, Antonio, and Antolini, Jácson. "Theoretical development and experimental validation of a methodology to reproduce multi-orifice pre-chamber jets in an optical accessible RCEM". In: *SIA Powertrain & Power Electronics 2021*. 2021 (cited on pages 34, 38, 45).

Desantes, José M, López, J Javier, Molina, Santiago, and López-Pintor, Darío. "Design of synthetic EGR and simulation study of the effect of simplified formulations on the ignition delay of isooctane and n-heptane". In: *Energy Conversion and Management* 96 (2015), pp. 521–531. DOI: 10.1016/j.enconman.2015.03.003 (cited on page 61).

Desantes, Jose M., Arregle, Jean, Lopez, J. Javier, and Cronhjort, Andreas. "SCALING LAWS FOR FREE TURBULENT GAS JETS AND DIESEL-LIKE SPRAYS". In: *Atomization and Sprays* 16.4 (2006), pp. 443–474. DOI: 10.1615/AtomizSpr.v16.i4.60 (cited on page 98).

Desantes, José M., Bermúdez, Vicente, López, J. Javier, and López-Pintor, Darío. "Experimental validation of an alternative method to predict high and low-temperature ignition delays under transient thermodynamic conditions for PRF mixtures using a Rapid Compression-Expansion Machine". In: *Energy Conversion and Management* 129 (2016), pp. 23–33. DOI: 10.1016/j.enconman.2016.09.089 (cited on page 61).

Desantes, José M., López, J. Javier, Molina, Santiago, and López-Pintor, Darío. "Theoretical development of a new procedure to predict ignition delays under transient thermodynamic conditions and validation using a Rapid Compression–Expansion Machine". In: *Energy Conversion and Management* 108 (2016), pp. 132–143. DOI: 10.1016/j.enconman.2015.10.077 (cited on page 64).

Desantes, José M., López, J. Javier, Novella, Ricardo, and Antolini, Jácson. "Pre-chamber ignition systems: A methodological proposal to reproduce a reference case in a simplified experimental facility for fundamental studies". In: *International Journal of Engine Research* 22.11 (2021), pp. 3358–3371. DOI: 10.1177/1468087420971115 (cited on page 45).

Desantes, Jose Maria, Novella, Ricardo, De La Morena, Joaquin, and Pagano lng, Vincenzo. "Achieving Ultra-Lean Combustion Using a Pre-Chamber Spark Ignition System in a Rapid Compression-Expansion Machine". In: *SAE Technical Papers*. Vol. 2019-April. April. 2019. DOI: 10.4271/2019-01-0236 (cited on pages 34, 38, 61).

Distaso, Elia et al. "Experimental and Numerical Analysis of a Pre-Chamber Turbulent Jet Ignition Combustion System". In: *SAE Technical Papers*. Vol. 2019. 2019. DOI: 10.4271/2019-24-0018 (cited on page 42).

Distaso, Elia et al. "Analysis of the combustion process in a lean-burning turbulent jet ignition engine fueled with methane". In: *Energy Conversion and Management* 223 (2020). DOI: 10.1016/j.enconman.2020.113257 (cited on pages 39, 41, 42).

Echeverri Marquez, Manuel et al. "Optical Diagnostics of Pre-Chamber Combustion with Flat and Bowl-In Piston Combustion Chamber". In: *SAE Technical Papers*. 2021. DOI: 10.4271/2021-01-0528 (cited on page 43).

Echeverri Marquez, Manuel et al. "Visualization of Pre-Chamber Combustion and Main Chamber Jets with a Narrow Throat Pre-Chamber". In: *SAE Technical Paper Series* (2022). DOI: 10.4271/2022-01-0475 (cited on page 44).

Empresa de Pesquisa Energética. *Brazilian Energy Balance 2023 Year 2022*. Rio de Janeiro, 2023 (cited on page 6).

Environmental Protection Agency (EPA). *Technical Amendments for Marine Spark-Ignition Engines and Vessels*. 2010 (cited on page 16).

Environmental Protection Agency (EPA). *Revised 2023 and later model year light-duty vehicle greenhouse gas emissions standards*. 2021 (cited on page 16).

Environmental Protection Agency (EPA). *The 2020 EPA Automotive Trends Report: Greenhouse Gas Emissions, Fuel Economy, and Technology since 1975*. 2022 (cited on page 18).

Environmental Protection Agency (EPA). *Smog Vehicle Emissions*. 2023 (cited on page 17).

European Automobile Manufacturers' Association (ACEA). *Fuel types of new passenger cars in the EU*. 2023 (cited on pages 16, 17).

European Parliament. *Regulation (EC) No. 715/2007: on type approval of motor vehicles with respect to emissions from light passenger and commercial vehicles (Euro 5 and Euro 6) and on access to vehicle repair and maintenance information*. 2007 (cited on page 16).

European Parliament. *Regulation (EC) No. 443/2009: setting emission performance standards for new passenger cars as part of the Community's integrated approach to reduce CO2 emissions from light-duty vehicles*. 2009 (cited on page 16).

European Parliament. *Regulation (EU) 2019/631: setting CO2 emission performance standards for new passenger cars and for new light commercial vehicles*. 2017 (cited on page 16).

European Parliament. *Amending Regulation (EU) 2019/631 as regards strengthening the CO2 emission performance standards for new passenger cars and new light commercial vehicles in line with the Union's increased climate ambition*. 2021 (cited on page 16).

Fernandes, Heder, Pimenta, Charles Quirino, Rodrigues, Wanderson Navegantes, De Souza Montemor, Raphael Bezerra, and Barros, José Eduardo Mautone. "Experimental Investigation of Internal Exhaust Gas Recirculation on a Variable Valve Actuation Spark Ignition Engine Operating with Gasoline and Ethanol". In: *SAE Technical Papers* Part F127082.October (2016). DOI: 10.4271/2016-36-0399 (cited on page 18).

Fischer, Michael, Kreutziger, Philipp, Sun, Yong, and Kotrba, Adam. "Clean EGR for Gasoline Engines – Innovative Approach to Efficiency Improvement and Emissions Reduction Simultaneously". In: *SAE Technical Papers*. Vol. 2017-March. March. 2017. DOI: 10.4271/2017-01-0683 (cited on page 18).

Frasci, Emmanuele et al. "Comprehensive model for energetic analyses of a series hybrid-electric vehicle powered by a passive Turbulent Jet Ignition engine". In: *Energy Conversion and Management* 269.May (2022), p. 116092. DOI: 10.1016/j.enconman.2022.116092 (cited on page 7).

Gaydon, A. G. *The Spectroscopy of Flames*. Vol. 80. 12. Dordrecht: Springer Netherlands, 1974, pp. 3169–3169. DOI: 10.1007/978-94-009-5720-6 (cited on page 68).

Gentz, Gerald, Gholamisheeri, Masumeh, and Toulson, Elisa. "A study of a turbulent jet ignition system fueled with iso-octane: Pressure trace analysis and combustion visualization". In: *Applied Energy* 189 (2017), pp. 385–394. DOI: 10.1016/j.apenergy.2016.12.055 (cited on pages 34, 36).

Gentz, Gerald, Thelen, Bryce, Toulson, Elisa, Litke, Paul, and Hoke, John. "Combustion Visualization, Performance, and CFD Modeling of a Pre-Chamber Turbulent Jet Ignition System in a Rapid Compression Machine". In: *SAE International Journal of Engines* 8.2 (2015), pp. 538–546. DOI: 10.4271/2015-01-0779 (cited on pages 34, 36).

Gentz, Gerald et al. "A study of the influence of orifice diameter on a turbulent jet ignition system through combustion visualization and performance characterization in a rapid compression machine". In: *Applied Thermal Engineering* 81 (2015), pp. 399–411. DOI: 10.1016/j.applthermaleng.2015.02.026 (cited on pages 34–36).

Gholamisheeri, Masumeh, Givler, Shawn, and Toulson, Elisa. "Large eddy simulation of a homogeneously charged turbulent jet ignition system". In: *International Journal of Engine Research* 20.2 (2019), pp. 181–193. DOI: 10.1177/1468087417742834 (cited on pages 34, 36).

Gholamisheeri, Masumeh, Givler, Shawn, and Toulson, Elisa. "RANS and LES of a Turbulent Jet Ignition System Fueled with Iso-Octane". In: *Flow, Turbulence and Combustion* Ic (2019). DOI: 10.1007/s10494-019-00049-5 (cited on pages 34, 36).

Gholamisheeri, Masumeh, Thelen, Bryce, Gentz, Gerald, and Toulson, Elisa. "CFD Modeling of an Auxiliary Fueled Turbulent Jet Ignition System in a Rapid Compression Machine". In: *SAE Technical Papers*. March. 2016. DOI: 10.4271/2016-01-0599 (cited on pages 34, 36).

Gholamisheeri, Masumeh, Thelen, Bryce, and Toulson, Elisa. "CFD Modeling and Experimental Analysis of a Homogeneously Charged Turbulent Jet Ignition System in a Rapid Compression Machine". In: *SAE Technical Paper Series* (2017). DOI: 10.4271/2017-01-0557 (cited on page 36).

Gholamisheeri, Masumeh, Thelen, Bryce C., Gentz, Gerald R., Wichman, Indrek S., and Toulson, Elisa. "Rapid compression machine study of a premixed, variable inlet density and flow rate, confined turbulent jet". In: *Combustion and Flame* 169 (2016), pp. 321–332. DOI: 10.1016/j.combustflame.2016.05.001 (cited on page 34).

Gholamisheeri, Masumeh, Wichman, Indrek S., and Toulson, Elisa. "A study of the turbulent jet flow field in a methane fueled turbulent jet ignition (TJI) system". In: *Combustion and Flame* 183 (2017), pp. 194–206. DOI: 10.1016/j.combustflame.2017.05.008 (cited on pages 34, 36).

Glassman, Irvin and Yetter, Richard A. *Combustion*. 4 ed. Vol. 59. Elsevier, 2008. DOI: 10.1016/B978-0-12-088573-2.X0001-2 (cited on page 68).

Gordon, S and McBride, B J. "Computer program for calculation of complex chemical equilibrium compositions rocket performance incident and reflected shocks, and Chapman-Jouguet detonations". In: *NASA Report SP-273, Interim Revision* (1976) (cited on page 121).

Gruden, Dusan. "Combustion and exhaust emission of an engine using the porsche-stratified- charge-chamber-system". In: *SAE Technical Papers* (1975). DOI: 10.4271/750888 (cited on pages 21, 23, 26).

Gussak, L. A. "High chemical activity of incomplete combustion products and a method of prechamber torch ignition for avalanche activation of combustion in internal combustion engines". In: *SAE Technical Papers* (1975). DOI: 10.4271/750890 (cited on pages 22, 26).

Hensinger, D. M., Maxson, J. A., Hom, K., and Oppenheim, A. K. "Jet plume injection and combustion". In: *SAE Technical Papers*. 1992. DOI: 10.4271/920414 (cited on pages 23, 26).

Heywoood, John B. *Internal Combustion Engine Fundamentals*. Second ed. New York, N.Y.: McGraw Hill, 2018, p. 1056 (cited on pages 16, 18, 66, 91, 101, 117).

Hlaing, Ponnya et al. "A Study of Lean Burn Pre-Chamber Concept in a Heavy Duty Engine". In: *SAE Technical Papers* 2019-September (2019), pp. 1–13. DOI: 10.4271/2019-24-0107 (cited on pages 25, 26).

Hsiang, Solomon et al. "Estimating economic damage from climate change in the United States". In: *Science* 356.6345 (2017), pp. 1362–1369. DOI: 10.1126/science.aal4369 (cited on page 2).

Hu, Yue, Tan, Jianguo, Lv, Liang, and Li, Xiangdong. "Investigations on quantitative measurement of heat release rate using chemiluminescence in premixed methane-air flames". In: *Acta Astronautica* 164 (2019), pp. 277–286. DOI: 10.1016/j.actaastro.2019.07.019 (cited on page 125).

IEA. *Energy Statistics Data Browser*. 2023 (cited on pages 1, 2).

IEA. *Global CO2 emissions from transport by sub-sector in the Net Zero Scenario, 2000-2030*. 2023 (cited on page 4).

IEA. *Energy consumption in transport by fuel in the Net Zero Scenario, 1975-2030* (cited on page 4).

Institute, Energy. "Statistical Review of World Energy 2023". In: *BP Energy Outlook 2023* 70.73 (2023), pp. 8–20 (cited on page 1).

Intergovernmental Panel on Climate Change (IPCC). *Climate Change 2022 - Mitigation of Climate Change*. Ed. by Intergovernmental Panel on Climate Change (IPCC). Cambridge University Press, 2023. DOI: 10.1017/9781009157926 (cited on page 2).

International Council on Clean Transportation. "European Stage V non-road emission standards". In: November (2016) (cited on page 16).

International Energy Agency. *World Energy Outlook 2022*. Tech. rep. Paris, 2022, p. 524 (cited on page 5).

Ju, Dehao, Huang, Zhong, Li, Xiang, Zhang, Tingting, and Cai, Weiwei. "Comparison of open chamber and pre-chamber ignition of methane/air mixtures in a large bore constant volume chamber: Effect of excess air ratio and premixed pressure". In: *Applied Energy* 260.December 2019 (2020), p. 114319. DOI: 10.1016/j.apenergy.2019.114319 (cited on page 31).

Kalwar, Ankur and Agarwal, Avinash Kumar. "Optical Diagnostics for Gasoline Direct Injection Engines". In: *Energy, Environment, and Sustainability*. Ic. Springer Singapore, 2022, pp. 201–241. DOI: 10.1007/978-981-16-8418-0_7 (cited on page 68).

Lacis, Andrew A., Schmidt, Gavin A., Rind, David, and Ruedy, Reto A. "Atmospheric CO 2 : Principal Control Knob Governing Earth's Temperature". In: *Science* 330.6002 (2010), pp. 356–359. DOI: 10.1126/science.1190653 (cited on page 1).

Law, Chung K. *Combustion Physics*. Cambridge University Press, 2006. DOI: 10.1017/CBO9780511754517 (cited on page 151).

Lemmon, Eric W., McLinden, Mark O., and Friend, Daniel G. "Thermophysical Properties of Fluid Systems". In: *NIST Chemistry WebBook*. Ed. by P.J. Linstrom and W.G. Mallard. Gaithersburg MD: National Institute of Standards and Technology. Chap. NIST Stand. DOI: https://doi.org/10.18434/T4D303 (cited on page 66).

Lezanski, T., Kesler, M., Rychter, T., Teodorczyk, A., and Wolanski, P. "Performance of Pulsed Jet Combustion (PJC) System in a research engine". In: *SAE Technical Papers* 412 (1993). DOI: 10.4271/932709 (cited on pages 23, 26).

Li, Fubai, Zhao, Ziqing, Wang, Boyuan, and Wang, Zhi. "Experimental study of pre-chamber jet ignition in a rapid compression machine and single-cylinder natural gas engine". In: *International Journal of Engine Research* (2019), pp. 1–15. DOI: 10.1177/1468087419883783 (cited on pages 34, 36).

Li, Fubai, Zhao, Ziqing, Wang, Zhi, and Wang, Boyuan. "Experimental and Numerical Study of a Methane-Fueled Pre-chamber System in Rapid Compression Machine". In: *Combustion Science and Technology* 193.9 (2021), pp. 1463–1494. DOI: 10.1080/00102202.2019.1699547 (cited on pages 34, 36, 45).

Li, Xiang et al. "Pre-chamber turbulent jet ignition of methane/air mixtures with multiple orifices in a large bore constant volume chamber: effect of air-fuel equivalence ratio and pre-mixed pressure". In: *Frontiers in Energy* 13.x (2019), pp. 483–493. DOI: 10.1007/s11708-019-0631-1 (cited on pages 30, 31).

Liu, Peilin, Zhong, Lijia, Zhou, Lei, and Wei, Haiqiao. "The ignition characteristics of the pre-chamber turbulent jet ignition of the hydrogen and methane based on different orifices". In: *International Journal of Hydrogen Energy* 46.74 (2021), pp. 37083–37097. DOI: 10.1016/j.ijhydene.2021.08.201 (cited on pages 30–32).

Liu, Wei, Qi, Yunliang, Zhang, Ridong, Zhang, Qihang, and Wang, Zhi. "Investigation on end-gas auto-ignition and knock characteristics of iso-octane over wide thermodynamic conditions under jet ignition using a rapid compression machine". In: *Fuel* 313.September 2021 (2022), p. 122665. DOI: 10.1016/j.fuel.2021.122665 (cited on pages 19, 34, 37).

Macian, V., Bermudez, V., Payri, R., and Gimeno, J. "NEW TECHNIQUE FOR DETERMINATION OF INTERNAL GEOMETRY OF A DIESEL NOZZLE WITH THE USE OF SILICONE METHODOLOGY". In: *Experimental Techniques* 27.2 (2003), pp. 39–43. DOI: 10.1111/j.1747-1567.2003.tb00107.x (cited on page 111).

Macian, V., Payri, R., Garcia, A., and Bardi, M. "Experimental Evaluation of the Best Approach for Diesel Spray Images Segmentation". In: *Experimental Techniques* 36.6 (2012), pp. 26–34. DOI: 10.1111/j.1747-1567.2011.00730.x (cited on pages 190, 192).

Macián, V., Salvador, F. J., De la Morena, J., and Pagano, V. "Combustion analysis of a stratified pre-chamber ignition system by means of a zero-dimensional turbulence and flame speed model". In: *Combustion and Flame* 232 (2021). DOI: 10.1016/j.combustflame.2021.111526 (cited on pages 28, 34, 38, 61, 112).

Malé, Quentin et al. "Large Eddy Simulation of Pre-Chamber Ignition in an Internal Combustion Engine". In: *Flow, Turbulence and Combustion* 103.2 (2019), pp. 465–483. DOI: 10.1007/s10494-019-00026-y (cited on page 82).

Marquez, Manuel Alejandro Echeverri et al. "A Pathway to Ultra-Lean IC Engine Combustion: The Narrow Throat Pre-chamber". In: *Engines and Fuels for Future Transport*. 2022. Chap. 8, pp. 175–203. DOI: 10.1007/978-981-16-8717-4_8 (cited on pages 18, 26).

Martínez, María, Altantzis, Christos, Wright, Yuri M., Martí-Aldaraví, Pedro, and Boulouchos, Konstantinos. "Computational study of the Premixed Charge Compression Ignition combustion in a Rapid Compression Expansion Machine: Impact of multiple injection strategy on mixing, ignition and combustion processes". In: *Fuel* 318.February (2022), p. 123388. DOI: 10.1016/j.fuel.2022.123388 (cited on page 61).

Mastorakos, Epaminondas et al. "Fundamental Aspects of Jet Ignition for Natural Gas Engines". In: *SAE International Journal of Engines* 10.5 (2017), pp. 2017–24–0097. DOI: 10.4271/2017-24-0097 (cited on page 101).

Millo, Federico et al. "Experimental and Numerical Investigation of a Passive Pre-Chamber Jet Ignition Single-Cylinder Engine". In: *SAE Technical Paper Series*. 2021. DOI: 10.4271/2021-24-0010 (cited on page 42).

Minarcin, Monika A., Rask, Eric, and Smith, Matthew R. "Challenges and Opportunities in Adoption of Hybrid Technologies in Medium and Heavy Duty Applications". In: *SAE Technical Papers*. Vol. 2711. 2011. DOI: 10.4271/2011-01-2251 (cited on page 5).

Moreira, T. A. A. et al. "Design and Construction Methodology of a Stratified Torch Ignition System". In: *SAE Technical Papers*. 2013. DOI: 10.4271/2013-36-0562 (cited on page 45).

Murase, E., Ono, S., Hanada, K., and Oppenheim, Antoni K. "Pulsed combustion jet ignition in lean mixtures". In: *SAE Technical Papers*. 412. 1994. DOI: 10.4271/942048 (cited on pages 23, 26).

Noguchi, M., Sanda, S., and Nakamura, N. "Development of toyota lean burn engine". In: *SAE Technical Papers* (1976). DOI: 10.4271/760757 (cited on pages 19–21, 26).

Nordelöf, Anders, Messagie, Maarten, Tillman, Anne Marie, Ljunggren Söderman, Maria, and Van Mierlo, Joeri. "Environmental impacts of hybrid, plug-in hybrid, and battery electric vehicles—what can we learn from life cycle assessment?" In: *International Journal of Life Cycle Assessment* 19.11 (2014), pp. 1866–1890. DOI: 10.1007/s11367-014-0788-0 (cited on page 5).

Nori, Venkata and Seitzman, Jerry. "Evaluation of Chemiluminescence as a Combustion Diagnostic Under Varying Operating Conditions". In: *46th AIAA Aerospace Sciences Meeting and Exhibit*. Reston, Virigina: American Institute of Aeronautics and Astronautics, 2008, pp. 1–14. DOI: 10.2514/6.2008-953 (cited on page 68).

Novella, R., Gomez-Soriano, J., Barbery, I., and Libert, C. "Numerical analysis of the passive pre-chamber ignition concept for light duty applications". In: *Applied Thermal Engineering* 213 (2022), p. 118610. DOI: 10.1016/j.applthermaleng.2022.118610 (cited on page 112).

Novella, R., Gomez-Soriano, J., Martinez-Hernandiz, P.J., Libert, C., and Rampanarivo, F. "Improving the performance of the passive pre-chamber ignition concept for spark-ignition engines fueled with natural gas". In: *Fuel* 290.December 2020 (2021), p. 119971. DOI: 10.1016/j.fuel.2020.119971 (cited on pages 7, 27, 108).

Novella, Ricardo, De la Morena, Joaquín, Pagano, Vincenzo, and Pitarch, Rafael. "Optical evaluation of orifice orientation and number effects on active pre-chamber spark ignition combustion". In: *Fuel* 338.December 2022 (2023), p. 127265. DOI: 10.1016/j.fuel.2022.127265 (cited on pages 34, 38).

Novella, Ricardo et al. "Experimental and Numerical Analysis of Passive Pre-Chamber Ignition with EGR and Air Dilution for Future Generation Passenger Car Engines". In: *SAE Technical Papers*. Vol. 2020-April. April. 2020, pp. 1–18. DOI: 10.4271/2020-01-0238 (cited on page 171).

Oppenheim, A K et al. "Combustion by Pulsed Jet Plumes - Key to Controlled Combustion Engines". In: *SAE Technical Papers*. 1989. DOI: 10.4271/890153 (cited on pages 22, 26).

Oppenheim, A. K. "Prospects for combustion in piston engines". In: *SAE Technical Papers* 724 (2002). DOI: 10.4271/2002-01-0999 (cited on page 23).

Oppenheim, A. K., Teichman, K., Hom, K., and Stewart, H. E. "Jet ignition of an ultra-lean mixture". In: *SAE Technical Papers* (1978), pp. 2416–2428. DOI: 10.4271/780637 (cited on pages 22, 23, 26).

Park, Junkyu, Kim, Donghwan, and Park, Sungwook. "Effects of Nozzle L/D on Near-Field Development and Macroscopic Spray Characteristics of Common-Rail Diesel Sprays". In: *International Journal of Automotive Technology* 21.3 (2020), pp. 657–666. DOI: 10.1007/s12239-020-0063-2 (cited on page 137).

Pastor, J.V., Lopez, J. Javier, García-Oliver, J.M., and Pastor, José M. "A 1D model for the description of mixing-controlled inert diesel sprays". In: *Fuel* 87.13-14 (2008), pp. 2871–2885. DOI: 10.1016/j.fuel.2008.04.017 (cited on pages 74, 75, 84).

Pastor, José V., Arrègle, Jean, and Palomares, Alberto. "Diesel spray image segmentation with a likelihood ratio test". In: *Applied Optics* 40.17 (2001), p. 2876. DOI: 10.1364/ao.40.002876 (cited on pages 69, 191, 192).

Pastor, José V., Micó, Carlos, Lewiski, Felipe, Tejada, Francisco J., and Tornatore, Cinzia. "A Synergic Application of High-Oxygenated E-Fuels and New Bowl Designs for Low Soot Emissions: An Optical Analysis". In: *Applied Sciences (Switzerland)* 13.14 (2023). DOI: 10.3390/app13148560 (cited on page 6).

Pastor, José V., Olmeda, Pablo, Martín, Jaime, and Lewiski, Felipe. "Methodology for optical engine characterization by means of the combination of experimental and modeling techniques". In: *Applied Sciences (Switzerland)* 8 (2018). DOI: 10.3390/app8122571 (cited on page 39).

Payri, Raul, Salvador, F. J., Bracho, Gabriela, and Viera, Alberto. "Differences between single and double-pass schlieren imaging on diesel vapor spray characteristics". In: *Applied Thermal Engineering* 125 (2017), pp. 220–231. DOI: 10.1016/j.applthermaleng.2017.06.140 (cited on page 67).

Photron. *FASTCAM SA5 Hardware Manual*. 2014 (cited on page 69).

Photron. *FASTCAM SA-X2 Hardware Manual*. 2019 (cited on page 73).

Prisacariu, Emilia et al. "Calculating and Setting Up A Schileren System". In: *Turbo* VII.2 (2020), pp. 25–34 (cited on page 67).

Qin, Fei et al. "Detailed numerical simulation of transient mixing and combustion of premixed methane/air mixtures in a pre-chamber/main-chamber system relevant to internal combustion engines". In: *Combustion and Flame* 188 (2018), pp. 357–366. DOI: 10.1016/j.combustflame.2017.10.006 (cited on page 84).

Rajasegar, Rajavasanth, Niki, Yoichi, García-Oliver, Jose Maria, Li, Zheming, and Musculus, Mark P.B. "Fundamental insights on ignition and combustion of natural gas in an active fueled pre-chamber spark-ignition system". In: *Combustion and Flame* 232.x (2021). DOI: 10.1016/j.combustflame.2021.111561 (cited on pages 28, 39, 40, 44).

Reitz, R. D. et al. "IJER editorial: The future of the internal combustion engine". In: *International Journal of Engine Research* 21.1 (2020), pp. 3–10. DOI: 10.1177/1468087419877990 (cited on page 4).

Ribeiro, Camilo Bastos, Rodella, Fernando Henrique Cavalcante, and Hoinaski, Leonardo. "Regulating light-duty vehicle emissions: an overview of US, EU, China and Brazil programs and its effect on air quality". In: *Clean Technologies and Environmental Policy* 24.3 (2022), pp. 851–862. DOI: 10.1007/s10098-021-02238-1 (cited on page 5).

Ricardo, Harry R. "RECENT RESEARCH WORK ON THE INTERNAL-COMBUSTION ENGINE". In: SAE Technical Paper 220001, 1922. DOI: 10.4271/220001 (cited on pages 19, 20, 26).

Robinet, C., Higelin, P., Moreau, B., Pajot, O., and Andrzejewski, J. "A new firing concept for internal combustion engines: "i'APIR"". In: *SAE Technical Papers* 724 (1999). DOI: 10.4271/1999-01-0621 (cited on pages 23, 26).

Rohwer, Johannes, Han, Taehoon, Shah, Ashish, and Rockstroh, Toby. "Investigations into EGR dilution tolerance in a pre-chamber ignited GDI engine". In: *International Journal of Engine Research* (2022), p. 146808742210847. DOI: 10.1177/14680874221084777 (cited on page 6).

Rounce, David R. et al. "Global glacier change in the 21st century: Every increase in temperature matters". In: *Science* 379.6627 (2023), pp. 78–83. DOI: 10.1126/science.abo1324 (cited on page 2).

Salaun, Erwan et al. "Optical Investigation of Ignition Timing and Equivalence Ratio in Dual-Fuel CNG/Diesel Combustion". In: *SAE Technical Papers* 2016-April.April (2016). DOI: 10.4271/2016-01-0772 (cited on page 61).

Sampath, Ramgopal et al. "Study on the Pre-Chamber Fueling Ratio Effect on the Main Chamber Combustion Using Simultaneous PLIF and OH* Chemiluminescence Imaging". In: *SAE International Journal of Advances and Current Practices in Mobility* 3.1 (2020), pp. 2020–01–2024. DOI: 10.4271/2020-01-2024 (cited on page 42).

Sanal, Sangeeth, Echeverri Marquez, Manuel, Silva, Mickael, Cenker, Emre, and Im, Hong G. "A Numerical Study on the Effect of a Pre-Chamber Initiated Turbulent Jet on Main Chamber Combustion". In: *SAE Technical Paper Series* 1 (2022), pp. 1–8. DOI: 10.4271/2022-01-0469 (cited on page 43).

Schlatter, Stephanie, Schneider, Bruno, Wright, Yuri M., and Boulouchos, Konstantinos. "Comparative study of ignition systems for lean burn gas engines in an optically accessible rapid compression expansion machine". In: *SAE Technical Papers* 6 (2013). DOI: 10.4271/2013-24-0112 (cited on pages 34, 37).

Sementa, Paolo, Catapano, Francesco, Di Iorio, SILVANA, Todino, Michele, and Vaglieco, Bianca Maria. "Turbulent Jet Ignition Effect on Exhaust Emission and Efficiency of a SI Small Engine Fueled with Methane and Gasoline". In: *SAE Technical Paper Series*. Vol. 1. 2020. DOI: 10.4271/2020-24-0013 (cited on page 41).

Sementa, Paolo, Catapano, Francesco, Di Iorio, Silvana, Todino, Michele, and Vaglieco, Bianca Maria. "Analysis of the Combustion Process of SI Engines Equipped with Non-Conventional Ignition System Architecture". In: *SAE Technical Papers*. 2020. DOI: 10.4271/2020-37-0035 (cited on page 41).

Sementa, Paolo, Catapano, Francesco, Di Iorio, Silvana, and Vaglieco, Bianca Maria. "Experimental Investigation of a Fueled Prechamber Combustion in an Optical Small Displacement SI Methane Engine". In: *SAE Technical Papers*. 2019. DOI: 10.4271/2019-24-0170 (cited on page 41).

Sementa, Paolo, Tornatore, Cinzia, Catapano, Francesco, Di Iorio, Silvana, and Vaglieco, Bianca Maria. "Custom-Designed Pre-Chamber: Investigating the Effects on Small SI Engine in Active and Passive Modes". In: *Energies* 16.13 (2023), p. 5097. DOI: 10.3390/en16135097 (cited on pages 19, 41).

Sementa, Paolo et al. "Exploring the potentials of lean-burn hydrogen SI engine compared to methane operation". In: *International Journal of Hydrogen Energy* 47.59 (2022), pp. 25044–25056. DOI: 10.1016/j.ijhydene.2022.05.250 (cited on page 6).

Settles, G. S. *Schlieren and Shadowgraph Techniques*. Berlin, Heidelberg: Springer Berlin Heidelberg, 2001. DOI: 10.1007/978-3-642-56640-0 (cited on page 66).

Shah, Ashish, Tunestal, Per, and Johansson, Bengt. "Effect of Pre-Chamber Volume and Nozzle Diameter on Pre-Chamber Ignition in Heavy Duty Natural Gas Engines". In: *SAE Technical Papers*. Vol. 2015-April. April. 2015. DOI: 10.4271/2015-01-0867 (cited on page 45).

Shah, Ashish, Tunestal, Per, and Johansson, Bengt. "Scalability Aspects of Pre-Chamber Ignition in Heavy Duty Natural Gas Engines". In: *SAE Technical Papers*. group 1. 2016. DOI: 10.4271/2016-01-0796 (cited on pages 7, 45).

Shapiro, Evgeniy et al. "Experimental and numerical analysis of pre-chamber combustion systems for lean burn gas engines". In: *SAE Technical Papers* 2019-April.April (2019), pp. 1–11. DOI: 10.4271/2019-01-0260 (cited on pages 34, 38).

Siebers, Dennis L. and Higgins, Brian. "Flame Lift-Off on Direct-Injection Diesel Sprays Under Quiescent Conditions". In: *SAE Technical Papers*. 2001. DOI: 10.4271/2001-01-0530 (cited on page 174).

Silva, Mickael et al. "Computational assessment of effects of throat diameter on combustion and turbulence characteristics in a pre-chamber engine". In: *Applied Thermal Engineering* 212.May (2022), p. 118595. DOI: 10.1016/j.applthermaleng.2022.118595 (cited on page 112).

Song, Ruitao, Gentz, Gerald, Zhu, Guoming, Toulson, Elisa, and Schock, Harald. "A control-oriented model of turbulent jet ignition combustion in a rapid compression machine". In: *Proceedings of the Institution of Mechanical Engineers, Part D: Journal of Automobile Engineering* 231.10 (2017), pp. 1315–1325. DOI: 10.1177/0954407016670303 (cited on page 34).

Sys, Christa, Vanelslander, Thierry, Adriaenssens, Mathias, and Van Rillaer, Ive. "International emission regulation in sea transport: Economic feasibility and impact". In: *Transportation Research Part D: Transport and Environment* 45 (2016), pp. 139–151. DOI: 10.1016/j.trd.2015.06.009 (cited on page 5).

Tanamura, Masashi et al. "A Fundamental Study on Combustion Characteristics in a Pre-Chamber Type Lean Burn Natural Gas Engine". In: *SAE Technical Papers* (2019). DOI: 10.4271/2019-24-0123 (cited on pages 34, 39).

Tang, Qinglong et al. "Simultaneous Negative PLIF and OH* Chemiluminescence Imaging of the Gas Exchange and Flame Jet from a Narrow Throat Pre-Chamber". In: *SAE Technical Papers*. 2020. DOI: 10.4271/2020-01-2080 (cited on pages 40, 42).

Tang, Qinglong et al. "Optical diagnostics on the pre-chamber jet and main chamber ignition in the active pre-chamber combustion (PCC)". In: *Combustion and Flame* 228 (2021), pp. 218–235. DOI: 10.1016/j.combustflame.2021.02.001 (cited on pages 40, 42, 43).

Tang, Qinglong et al. "Study on the effects of narrow-throat pre-chamber geometry on the pre-chamber jet velocity using dual formaldehyde PLIF imaging". In: *Combustion and Flame* 240 (2022), p. 111987. DOI: 10.1016/j.combustflame.2022.111987 (cited on pages 27, 43).

Tanoue, Kimitoshi, Kimura, Takanori, Jimoto, Taishu, Hashimoto, Jun, and Moriyoshi, Yasuo. "Study of prechamber combustion characteristics in a rapid compression and expansion machine". In: *Applied Thermal Engineering* 115 (2017), pp. 64–71. DOI: 10.1016/j.applthermaleng.2016.12.079 (cited on pages 34, 35, 39).

Technologies, Gamma. *Engine Performance Application Manual*. 2021 (cited on page 74).

Technologies, Gamma. *Flow Theory Manual*. 2021 (cited on page 74).

Thelen, Bryce C. and Toulson, Elisa. "A computational study on the effect of the orifice size on the performance of a turbulent jet ignition system". In: *Proceedings of the Institution of Mechanical Engineers, Part D: Journal of Automobile Engineering* 231.4 (2017), pp. 536–554. DOI: 10.1177/0954407016659199 (cited on pages 34, 36).

Thelen, Bryce Charles, Gentz, Gerald, and Toulson, Elisa. "Computational Study of a Turbulent Jet Ignition System for Lean Burn Operation in a Rapid Compression Machine". In: *SAE Technical Papers*. Vol. 2015-April. April. 2015. DOI: 10.4271/2015-01-0396 (cited on pages 34, 36).

Thelen, Bryce Charles and Toulson, Elisa. "A Computational Study of the Effects of Spark Location on the Performance of a Turbulent Jet Ignition System". In: *SAE Technical Papers* (2016). DOI: 10.4271/2016-01-0608 (cited on pages 34, 36).

Tian, Jiangping, Cui, Zechuan, Ren, Zhongyong, Tian, Hua, and Long, Wuqiang. "Experimental study on jet ignition and combustion processes of natural gas". In: *Fuel* 262.July 2019 (2020), p. 116467. DOI: 10.1016/j.fuel.2019.116467 (cited on pages 30, 32, 82).

Tinaut, F. V., Reyes, M., Giménez, B., and Pastor, J. V. "Measurements of OH* and CH* chemiluminescence in premixed flames in a constant volume combustion bomb under autoignition conditions". In: *Energy and Fuels* 25 (2011), pp. 119–129. DOI: 10.1021/ef1013456 (cited on page 125).

Tornatore, Cinzia, Marchitto, Luca, Sabia, Pino, and De Joannon, Mara. "Ammonia as Green Fuel in Internal Combustion Engines: State-of-the-Art and Future Perspectives". In: *Frontiers in Mechanical Engineering* 8.July (2022), pp. 1–16. DOI: 10.3389/fmech.2022.944201 (cited on page 6).

Tornatore, Cinzia, Marchitto, Luca, and Valentino, Gerardo. "Technologies for Knock Mitigation in SI Engines—A Review". In: *Engines and Fuels for Future Transport*. Springer Singapore, 2022. Chap. 13, pp. 325–349. DOI: 10.1007/978-981-16-8717-4_13 (cited on page 18).

Tornatore, Cinzia and Sjöberg, Magnus. "Optical Investigation of a Partial Fuel Stratification Strategy to Stabilize Overall Lean Operation of a DISI Engine Fueled with Gasoline and E30". In: *Energies* 14.2 (2021), p. 396. DOI: 10.3390/en14020396 (cited on page 202).

Toulson, Elisa, Schock, Harold J., and Attard, William P. "A Review of Pre-Chamber Initiated Jet Ignition Combustion Systems". In: *SAE Technical Paper Series* (2010). DOI: 10.4271/2010-01-2263 (cited on pages 7, 19).

Tu, Po-Wen et al. "Numerical Investigation of GDI Injector Nozzle Geometry on Spray Characteristics". In: *SAE Technical Papers*. Vol. 2015-Septe. September. 2015. DOI: 10.4271/2015-01-1906 (cited on page 137).

Turkish, Michael C. "3 - Valve stratified charge engines: Evolvement, analysis and progression". In: *SAE Technical Papers* (1974), pp. 3483–3503. DOI: 10.4271/741163 (cited on pages 20, 22).

Turns, Stephen R. *An introduction to combustion: concepts and applications*. 2nd. Vol. 499. McGraw-Hill, 2000, p. 411 (cited on page 101).

U.S. Department of Energy. *2022 Light-Duty Vehicle Registration Counts by State and Fuel Type*. 2023 (cited on page 16).

U.S. Energy Information Administration. *Annual Energy Outlook 2022*. 2022 (cited on page 6).

U.S. Energy Information Administration. *Electricity explained*. 2023 (cited on page 6).

Uzun, Ali and Hussaini, M. Yousuff. "Investigation of high frequency noise generation in the near-nozzle region of a jet using large eddy simulation". In: *Theoretical and Computational Fluid Dynamics* 21.4 (2007), pp. 291–321. DOI: 10.1007/s00162-007-0048-z (cited on page 150).

Validi, AbdoulAhad, Schock, Harold, and Jaberi, Farhad. "Turbulent jet ignition assisted combustion in a rapid compression machine". In: *Combustion and Flame* 186 (2017), pp. 65–82. DOI: 10.1016/j.combustflame.2017.07.032 (cited on pages 34, 36).

Valle, R. M., Cândido De Sá, D. C., and Ramalho Filho, F. A. "Constructive parameters analysis of combustion pre-chamber adapted in torch-ignition system of otto cycle engine". In: *SAE Technical Papers* (2003). DOI: 10.4271/2003-01-3713 (cited on page 45).

Varde, K. S. and Lubin, M. J. "The roll of connecting nozzle and the flame initiation point in the performance of a dual chamber stratified charge engine". In: *SAE Technical Papers* (1974). DOI: 10.4271/741161 (cited on page 21).

Vedharaj, S. "Advanced Ignition System to Extend the Lean Limit Operation of Spark-Ignited (SI) Engines—A Review". In: *Alternative Fuels and Advanced Combustion Techniques as Sustainable Solutions for Internal Combustion Engines*. Springer Singapore, 2021. Chap. 10, pp. 217–255. DOI: 10.1007/978-981-16-1513-9_10 (cited on page 18).

Vera-Tudela, Walter, Barro, Christophe, and Boulouchos, Konstantinos. "Investigations on spark pre-chamber ignition and subsequent turbulent jet main chamber ignition in a novel optically accessible test rig". In: *International Journal of Engine Research* (2021), pp. 1–13. DOI: 10.1177/14680874211019849 (cited on pages 32, 33).

Wallington, Timothy J., Anderson, James E., Dolan, Rachael H., and Winkler, Sandra L. "Vehicle Emissions and Urban Air Quality: 60 Years of Progress". In: *Atmosphere* 13.5 (2022). DOI: 10.3390/atmos13050650 (cited on page 5).

Wei, Fuxing et al. "Visualization study on lean combustion characteristics of the premixed methanol by the jet ignition of an ignition chamber". In: *Fuel* 308.July 2021 (2022). DOI: 10.1016/j.fuel.2021.122001 (cited on page 32).

Wellander, Rikard et al. "Study of the Early Flame Development in a Spark-Ignited Lean Burn Four-Stroke Large Bore Gas Engine by Fuel Tracer PLIF". In: *SAE International Journal of Engines* 7 (2014), pp. 2014–01–1330. DOI: 10.4271/2014-01-1330 (cited on pages 40, 41).

Wolanski, Piotr, Gut, Zbigniew, Niedziela, Witold, Przastek, Janusz, and Siwiec, Stanislaw. "Study of combustion dynamics in the research engine". In: *SAE Technical Papers* 412 (1997). DOI: 10.4271/972829 (cited on pages 23, 26).

Woschni, G. "A Universally Applicable Equation for the Instantaneous Heat Transfer Coefficient in the Internal Combustion Engine". In: (1967). DOI: 10.4271/670931 (cited on page 117).

Wyczalek, F. A., Harned, J. L., Maksymiuk, S., and Blevins, J. R. "EFI prechamber torch ignition of lean mixtures". In: *SAE Technical Papers* (1975). DOI: 10.4271/750351 (cited on pages 21, 23, 26).

Xu, Guoqing, Kotzagianni, Maria, Kyrtatos, Panagiotis, Wright, Yuri M., and Boulouchos, Konstantinos. "Experimental and numerical investigations of the unscavenged prechamber combustion in a rapid compression and expansion machine under engine-like conditions". In: *Combustion and Flame* 204 (2019), pp. 68–84. DOI: 10.1016/j.combustflame.2019.01.025 (cited on pages 34, 37).

Zhou, Lei, Liu, Peilin, Zhong, Lijia, Feng, Zhonghui, and Wei, Haiqiao. "Experimental observation of lean flammability limits using turbulent jet ignition with auxiliary hydrogen and methane in pre-chamber". In: *Fuel* 305.March (2021), p. 121570. DOI: 10.1016/j.fuel.2021.121570 (cited on page 31).

Zhou, Lei et al. "Effects of different hole structures of pre-chamber with turbulent jet ignition on the flame propagation and lean combustion performance of a single-cylinder engine". In: *Fuel* 308.August 2021 (2022), p. 121902. DOI: 10.1016/j.fuel.2021.121902 (cited on page 6).


UNIVERSITAT
POLITÈCNICA
DE VALÈNCIA
CMT
Clean Mobility & Thermofluids
December 2024